

Lamb Wave Propagation and Material Characterization of
Metallic and Composite Aerospace Structures for
Improved Structural Health Monitoring (SHM)

by

Shashank Pant

A thesis submitted to the Faculty of Graduate and Postdoctoral Affairs in
partial fulfillment of the requirements for the degree of

Doctor of Philosophy
in
Aerospace Engineering

Carleton University
Ottawa, Ontario

© 2014
Shashank Pant

ABSTRACT

The use of Lamb waves, which are ultrasonic guided waves, have shown potential for detecting damage in composite specimens as a part of a Structural Health Monitoring (SHM) system. Damage in a structure can be detected by analyzing the difference between the phase/group velocity and the loss of amplitude of Lamb waves on damaged versus un-damaged specimens. The propagation characteristics of Lamb waves are described in the form of dispersion curves, which are plots of phase/group velocities versus the frequency-thickness product generated by solving the Lamb wave equations. Such dispersion curves are used to select proper Lamb wave modes, excitation frequency, transducer sizing, and signal generation/acquisition hardware.

The most commonly used methods for solving the Lamb wave equations for composite laminates consist of using laminated plate theory or 3D linear elasticity by assuming an orthotropic and/or higher symmetry. This assumption may not be true, if the actuators and sensors in an orthotropic or transversely isotropic laminates are installed in a non-principal direction. Therefore, this dissertation presents a full derivation and experimental validation of Lamb wave equations for n-layered monoclinic composite laminates. The derivation is based on linear 3D elasticity by considering the displacement fields in all three directions and by using the partial wave technique in combination with the Global Matrix (GM) approach. A robust method for numerically solving the Lamb wave equations is also presented. The presented method is verified experimentally by analyzing the propagation of Lamb waves in two different composite laminates constructed out of unidirectional carbon-fibre epoxy prepreg (Cycom G40-800/5276-1) and fibre-metal laminate (GLARE 3-3/4). The experimentally verified carbon-fibre epoxy laminate is further analyzed to study the effects of changes in the material properties such as

E_{11} , E_{22} , G_{12} , and density on the Lamb waves' propagation characteristics. The analysis is performed by using the experimentally verified Lamb wave equations to generate the phase velocity dispersion and slowness curves by reducing E_{11} , E_{22} , G_{12} , and density with the intent of representing defects.

In order to accurately generate the Lamb wave dispersion curves, proper material properties such as stiffness and Poisson's ratio are required. Therefore, this dissertation also presents a one-sided *in-situ* method based on the ultrasonic wave velocity measurements to determine the stiffness properties of isotropic and transversely isotropic material. The technique consists of generating and receiving quasi-longitudinal and quasi-transverse waves at different propagation angles and using a non-linear least square technique to inversely calculate the stiffness constants. The method is experimentally verified on an isotropic aluminum Al 7050-T7451 with two different thicknesses and a transversely isotropic (Cycom 977-2-12k-HTA) composite sample fabricated using 24 plies of unidirectional prepregs.

ACKNOWLEDGEMENTS

First and foremost, I would like to thank my supervisors and my mentors Dr. Jeremy Laliberté, Dr. Marcias Martinez, and Prof. Paul V. Straznicky for giving me an opportunity to pursue this PhD research. Without their support and guidance, I would have never been able to successfully complete this research. In addition to my supervisors, I would like to extend my sincere thanks to:

- Dr. Bruno Rocha, National Research Council Canada (NRC), for providing guidance in both analytical and experimental work.
 - Dr. Yuu Ono, Systems and Computer Engineering, Carleton University, for providing direction in ultrasonic experimental setup and analysis.
 - Mike Brothers, Mark Genest, and Dr. Catalin Mandache at NRC for performing C-scan on the composite test panel and for providing the ultrasonic transducers and equipment.
 - Tom Benak for providing guidance in the lab, Matt Harrison for fabricating the composite panels, Michel Delannoy for instrumenting piezoelectric transducers, and Tom Kay for cutting the composite panels at NRC.
 - Dr. Nezhir Mrad, Defence R&D Canada, Department of National Defence, for providing the Acellent system and Dr. David Backman, NRC for providing the lab space.
 - Darun Barazanchy for fabricating the composite test panels at Delft University of Technology (TU Delft).
 - Steve Truttman for running the tensile tests, Stephan Biljan for 3-D printing, Alex Proctor and Kevin Sangster for helping out in the machine shop at Carleton University.
 - All the faculty and staff in the Department of Mechanical and Aerospace Engineering at Carleton University for guiding/helping me during my studies.
-

- The Natural Sciences and Engineering Research Council of Canada (NSERC) and the Ontario Graduate Scholarship (OGS) program for providing the financial support.
- My good friends Jeeva Selvadurai, Fady Habib, and Mario Mahendran for their continuing support.

Lastly, I would like to thank my wife Sabina for providing her utmost support and motivation.

Dedicated to my parents and grandparents.....

TABLE OF CONTENTS

Abstract.....	ii
Acknowledgements.....	iv
Table of Contents	vii
List of Tables.....	xi
List of Figures.....	xii
Nomenclature.....	xviii
Subscript.....	xx
Superscript.....	xx
Acronyms	xxi
Chapter 1: Introduction and Background.....	1
1.1 Composite Airframe Damage Detection and Monitoring.....	5
1.1.1 Typical damage types found in laminated composites.....	10
1.1.1.1 Delamination.....	10
1.1.1.2 Damaged fibres	11
1.1.1.3 Matrix cracking.....	13
1.1.1.4 Porosity/voids.....	14
1.1.1.5 Matrix damage due to improper cure.....	14
1.1.1.6 Resin rich and resin starved areas.....	15
1.1.1.7 Cracks/fractures.....	15
1.1.1.8 Matrix damage due to environmental degradation.....	16
1.1.1.9 Disbond	17
1.1.2 NDE methods for composites	18
1.1.2.1 Visual inspection	19
1.1.2.2 Tap-testing.....	21
1.1.2.3 Ultrasound	22
1.1.2.3.1 Pulse-echo	23
1.1.2.3.2 Through-transmission	25

1.1.2.3.3	Back-scattering.....	26
1.1.2.3.4	Phased-array.....	26
1.1.2.4	Liquid penetrant.....	27
1.1.2.5	Eddy current.....	28
1.1.2.6	Radiography.....	29
1.1.2.7	Infrared thermography.....	30
1.1.2.8	Laser shearography.....	32
1.1.3	SHM for composites.....	33
1.1.3.1	Damage detection techniques.....	34
1.1.3.1.1	Acousto-ultrasonic.....	34
1.1.3.1.2	Acoustic emission.....	35
1.1.3.1.3	Vibration-based.....	36
1.1.3.1.4	Other methods.....	37
1.1.3.2	Sensing technologies.....	38
1.1.3.2.1	Strain gage.....	38
1.1.3.2.2	Optical fibre sensors.....	39
1.1.3.2.3	Piezoelectric transducers.....	41
1.1.3.2.4	Micro-electro-mechanical systems.....	43
1.1.3.2.5	Surface mountable crack sensor.....	43
1.1.3.2.6	Comparative vacuum monitoring sensor.....	44
1.1.3.3	Signal processing.....	45
1.2	Research Motivation, Objective, and Scope.....	50
1.3	Contributions to Science and Technology.....	55
1.4	Thesis Overview.....	59
Chapter 2:	Ultrasonic Waves.....	61
2.1	Bulk Waves.....	61
2.2	Guided Waves.....	63
2.2.1	Rayleigh waves.....	63
2.2.2	Lamb waves.....	64
2.2.3	Previous research on lamb waves in composite laminates.....	68

2.2.4	Derivation of lamb wave equations.....	74
2.2.4.1	Stress-strain relationship for composite laminate.....	76
2.2.4.2	Lamb wave equations for single monoclinic lamina	80
2.2.4.3	Lamb wave equations for n-layered laminate	89
2.2.4.3.1	Transfer Matrix approach.....	90
2.2.4.3.2	Global Matrix approach	93
2.2.5	Numerical solution of lamb wave dispersion curves.....	98
2.2.6	Software to generate the lamb wave dispersion curve.....	100
2.2.7	Experimental validation.....	103
2.2.7.1	Comparison with the classical laminated plate theory	112
	Chapter 2 Summary	114
	Chapter 3: Effects of Lamina Properties on Lamb Waves.....	115
3.1	Existing Research	116
3.2	Effects of Changes in the Material Properties.....	118
3.2.1	Method	119
3.2.2	Results	121
3.2.2.1	Unidirectional laminate.....	121
3.2.2.2	Cross-ply laminate.....	130
3.2.2.3	Quasi-isotropic laminate.....	137
3.2.2.4	Summary of the results.....	145
	Chapter 3 Summary	147
	Chapter 4: Material Characterization.....	148
4.1	Ultrasonic Wave Theory	148
4.2	Search Algorithm to Find Elastic Constants	159
4.2.1	Sensitivity analysis for isotropic material.....	160
4.2.2	Sensitivity analysis for unidirectional composite laminate	166
4.3	Experimental Verification.....	174
4.3.1	Experimental setup and data acquisition	176

4.3.2	Experimental results for isotropic Al 7050-T7451	179
4.3.3	Experimental results for transversely isotropic.....	180
	Chapter 4 Summary	184
	Chapter 5: Thesis Conclusions	185
	Chapter 6: Future Recommendations	189
	References	192
	Appendix A: Constants for Coefficient (D_i).....	203
	Appendix B: Constants for the Stiffness Matrix [c'_{ij}]	205
	Appendix C: Convergence Study of Isotropic Ti-6Al-4V	206
	Appendix D: Convergence Study of Unidirectional Laminate	209

LIST OF TABLES

Table 1: Specimen type, layup, and material.....	103
Table 2: Material properties used to generate the dispersion curve.....	107
Table 3: Material properties for Cytec G40-800/5276-1 prepreg.....	119
Table 4: Laminate type and layup sequence	120
Table 5: Suggested Lamb wave modes to detect damage associated with E_{11} , E_{22} , G_{12} , and density	145
Table 6: Measured QL and QT velocities and propagation angles of Al 7050-T7451 specimen.....	179
Table 7: Measured material properties of Al 7050-T7451	180
Table 8: Summary of the measured QL and QT velocities of the transversely isotropic specimen	181
Table 9: Measured material properties of transversely isotropic sample.....	182
Table 10: Change in QL and QT velocities due to ± 0.5 mm thickness variation for $\theta_{12} = 0^\circ$	182
Table 11: Change in QL and QT velocities due to ± 0.5 mm thickness variation for $\theta_{12} = 90^\circ$..	183
Table D1: Material properties used for the sensitivity study [L. Wang et al., 2007b].....	209

LIST OF FIGURES

Figure 1: Increase in the use of composite materials in aircraft over time [IHS, 2014].....	2
Figure 2: HOLSIP based approach	8
Figure 3: Typical damage types found in laminated composites	10
Figure 4: Tap-testing instruments [D. Roach, 2007].....	21
Figure 5: Electro-mechanical tap-testing systems.....	22
Figure 6: Schematic of pulse-echo ultrasonic technique with A-scan display.....	24
Figure 7: Schematic of pitch-catch/through-transmission ultrasonic technique.....	25
Figure 8: Principle of backscatter ultrasonic [J. R. Lhota et al., 1994]	26
Figure 9: Phased array beam focusing at (a) an angle and (b) normal incidence [N. Dube, 2007]27	
Figure 10: Damage detection using eddy current.....	29
Figure 11: Schematic of thermography inspection technique	31
Figure 12: (a) Schematic of laser shearography and (b) Concentration of fringes due to defect...33	
Figure 13: Signal features of acoustic emission [W. J. Staszewski et al., 2004].....	36
Figure 14: Bonded metallic strain gage [National Instruments, 2013].....	39
Figure 15: FBG sensing concept [W. J. Staszewski et al., 2004].....	40
Figure 16: PZT and PVDF piezoelectric sensors [A. Raghavan, 2007].....	42
Figure 17: Reaction of piezoelectric element to the applied load/voltage [APC International, 2011].....	43
Figure 18: SMCS with an interrogator unit [M. Martinez et al., 2012].....	44
Figure 19: Schematic of CVM sensor [D. Roach, 2009]	45
Figure 20: Signal processing flowchart.....	46
Figure 21: Mother wavelets $\psi(t)$: (a) Daubechies (db6), (b) Mexican hat, (c) Gaussian, and (d) Morlet [M. M. Reda Taha et al., 2006].....	48

Figure 22: Lamb wave propagation in (a) time domain, (b) frequency-domain, (c) time-space domain, and (d) frequency-wavenumber domain [Z. Tian et al., 2014].....	49
Figure 23: Commonly used signal processing tools [W. J. Staszewski et al., 2004]	50
Figure 24: Through-thickness propagation of longitudinal and shear waves	62
Figure 25: Surface displacement pattern in Rayleigh wave [J. D. N. Cheeke, 2002].....	64
Figure 26: Lamb wave dispersion curve for 2024-T6 aluminum plate	65
Figure 27: Comparison of non-dispersive and dispersive wave [V. Giurgiutiu, 2008].....	65
Figure 28: Propagation of Lamb wave modes (a) symmetrical and (b) anti-symmetrical	67
Figure 29: Upward and downward travelling partial waves for a single anisotropic layer.....	75
Figure 30: Generalized co-ordinate system with local fibre orientation	77
Figure 31: Thin monoclinic plate with thickness of $2h$	81
Figure 32: N-layered composite laminate showing k -th layer [V. Giurgiutiu, 2008]	90
Figure 33: N-layered monoclinic plate showing partial waves [B. Pavlakovic, 1997]	94
Figure 34: Global Matrix for a five-layered monoclinic plate with two vacuum half-spaces.....	96
Figure 35: Global Matrix with zero surface stress boundary condition	97
Figure 36: Flow chart to numerically solve Lamb wave equations using Global Matrix approach	99
Figure 37: MATLAB GUI to generate Lamb wave dispersion curves.....	101
Figure 38: MATLAB GUI showing the isotropic material input.....	102
Figure 39: GUI for n-layered anisotropic material with text file containing the material properties	102
Figure 40: Ultrasonic C-scan image of carbon-fibre panel	104
Figure 41: Dimension and location of transducers of carbon-fibre epoxy laminate.....	105
Figure 42: Dimension and location of transducers of GLARE panel.....	105
Figure 43: 200 kHz actuator signal in (a) Time domain and (b) Frequency domain	106
Figure 44: Experimental setup to generate and receive Lamb waves	106
Figure 45: Custom MATLAB software developed to extract phase and group velocity data	107

Figure 46: Dispersion curve for carbon-fibre epoxy at (a) 0°, (b) 45°, and (c) 90° sensor orientations, where solid lines represent the theoretically generated Lamb wave dispersion curves	109
Figure 47: Dispersion curve for GLARE at (a) 0°, (b) 20°, (c) 45°, (d) 70°, and (e) 90° sensor orientations, where solid lines represent the theoretically generated Lamb wave dispersion curves	110
Figure 48: Comparison of 3D linear elasticity and classical laminate plate theory for Lamb wave travelling in (a) 0°, (b) 45°, and (c) 90°.	112
Figure 49: Effects of reducing E_{11} on the dispersion characteristic of A_o and S_o waves for unidirectional laminate.....	122
Figure 50: Effects of reducing E_{22} on the dispersion characteristic of A_o and S_o waves for unidirectional laminate.....	123
Figure 51: Effects of reducing G_{12} on the dispersion characteristic of A_o and S_o waves for unidirectional laminate.....	125
Figure 52: Effects of reducing density on the dispersion characteristic of A_o and S_o waves for unidirectional laminate.....	127
Figure 53: Effects of (a) E_{11} , (b) E_{22} , (c) G_{12} , and (d) density on the slowness of fundamental anti-symmetric Lamb wave propagating in the unidirectional laminate.....	128
Figure 54: Effects of (a) E_{11} , (b) E_{22} , (c) G_{12} , and (d) density on the slowness of fundamental symmetric Lamb wave propagating in the unidirectional laminate.....	129
Figure 55: Effects of reducing E_{11} on the dispersion characteristic of A_o and S_o waves for cross-ply laminate.....	130
Figure 56: Effects of reducing E_{22} on the dispersion characteristic of A_o and S_o waves for cross-ply laminate.....	132
Figure 57: Effects of reducing G_{12} on the dispersion characteristic of A_o and S_o waves for cross-ply laminate	133
Figure 58: Effects of reducing density on the dispersion characteristic of A_o and S_o waves for cross-ply laminate.....	134
Figure 59: Effects of (a) E_{11} , (b) E_{22} , (c) G_{12} , and (d) density on the slowness of fundamental anti-symmetric Lamb wave propagating in the cross-ply laminate.....	135
Figure 60: Effects of (a) E_{11} , (b) E_{22} , (c) G_{12} , and (d) density on the slowness of fundamental symmetric Lamb wave propagating in the cross-ply laminate.....	136

Figure 61: Effects of reducing E_{11} on the dispersion characteristic of A_o and S_o waves for quasi-isotropic laminate	137
Figure 62: Effects of reducing E_{22} on the dispersion characteristic of A_o and S_o waves for quasi-isotropic laminate	139
Figure 63: Effects of reducing G_{12} on the dispersion characteristic of A_o and S_o waves for quasi-isotropic laminate	141
Figure 64: Effects of reducing density on the dispersion characteristic of A_o and S_o waves for quasi-isotropic laminate.....	142
Figure 65: Effects of (a) E_{11} , (b) E_{22} , (c) G_{12} , and (d) density on the slowness of fundamental anti-symmetric Lamb wave propagating in the quasi-isotropic laminate.....	143
Figure 66: Effects of (a) E_{11} , (b) E_{22} , (c) G_{12} , and (d) density on the slowness of fundamental symmetric Lamb wave propagating in the quasi-isotropic laminate.....	144
Figure 67: Orthotropic plate with the associate coordinates.....	149
Figure 68: Modes of ultrasonic wave propagations at various wedge angles	152
Figure 69: Anisotropic plate with rotated coordinate.....	154
Figure 70: Propagation of phase and group velocity vectors in non-principal direction	158
Figure 71: Non-linear least square method to calculate isotropic material constants.....	161
Figure 72: Initial convergence summary of Al 2024-T6 elastic stiffness (E)	162
Figure 73: Initial convergence summary of Al 2024-T6 shear stiffness (G).....	162
Figure 74: Initial convergence summary of Al 2024-T6 Poisson's ratio (μ)	163
Figure 75: An improved method to calculate isotropic material stiffness constants.....	164
Figure 76: Convergence of Al 2024-T6 elastic stiffness (E) after implementing improved algorithm	165
Figure 77: Convergence of Al 2024-T6 shear stiffness (G) after implementing improved algorithm	165
Figure 78: Convergence of Al 2024-T6 Poisson's ratio (μ) after implementing improved algorithm	166
Figure 79: Flow chart to calculate stiffness constants of a unidirectional composite laminate...	167
Figure 80: Initial convergence summary of E_{11}	168

Figure 81: Initial convergence summary of E_{22}	168
Figure 82: Initial convergence summary of G_{12}	169
Figure 83: Initial convergence summary of μ_{12}	169
Figure 84: Initial convergence summary of μ_{23}	170
Figure 85: Improved method to find stiffness constant of transversely isotropic material	171
Figure 86: Convergence summary of E_{11} after implementing improved algorithm	172
Figure 87: Convergence summary of E_{22} after implementing improved algorithm	172
Figure 88: Convergence summary of G_{12} after implementing improved algorithm.....	173
Figure 89: Convergence summary of μ_{12} after implementing improved algorithm.....	173
Figure 90: Convergence summary of μ_{23} after implementing improved algorithm.....	174
Figure 91: Schematic of the immersion method.....	175
Figure 92: Experimental (a) schematic and (b) setup to generate and gather ultrasonic waves..	176
Figure 93: Custom MATLAB GUI showing initial pulse, QL and QT waves generated by 15° wedge.....	177
Figure 94: Method followed to fabricate the custom wedges.....	178
Figure C1: Initial convergence of Ti-6Al-4V elastic stiffness (E).....	206
Figure C2: Convergence of Ti-6Al-4V elastic stiffness (E) after implementing improved algorithm	206
Figure C3: Initial convergence of Ti-6Al-4V shear stiffness (G)	207
Figure C4: Convergence of Ti-6Al-4V shear stiffness (G) after implementing improved algorithm	207
Figure C5: Initial convergence of Ti-6Al-4V Poisson's ratio (μ).....	208
Figure C6: Convergence of Ti-6Al-4V Poisson's ratio (μ) after implementing improved algorithm	208

Figure D1: Initial convergence of elastic stiffness (E_{11})	209
Figure D2: Convergence of elastic stiffness (E_{11}) after implementing improved algorithm	209
Figure D3: Initial convergence of elastic stiffness (E_{22})	210
Figure D4: Convergence of elastic stiffness (E_{22}) after implementing improved algorithm	210
Figure D5: Initial convergence of shear stiffness (G_{12}).....	211
Figure D6: Convergence of shear stiffness (G_{12}) after implementing improved algorithm.....	211
Figure D7: Initial convergence of Poisson's ratio (μ_{12}).....	212
Figure D8: Convergence of Poisson's ratio (μ_{12}) after implementing improved algorithm	212
Figure D9: Initial convergence of Poisson's ratio (μ_{23}).....	213
Figure D10: Convergence of Poisson's ratio (μ_{23}) after implementing improved algorithm.....	213

NOMENCLATURE

Symbols	Description	Units
A	Anti-symmetric Lamb wave	
λ_B	Bragg wavelength	m
Λ_{il}	Christoffel matrix components	
ω	Circular wave frequency	Rad/s
s_{ij}	Compliance elastic constants	m^2/N
T	Coordinate transformation matrix	
ρ	Density	kg/m^3
x_i	Direction	Unit less
n_j	Directional unit vector	Unit less
u_i	Displacement	m
U_i	Displacement amplitude	m
V_q	Displacement amplitude ratio	Unit less
W_q	Displacement amplitude ratio	Unit less
n_{eff}	Effective refractive index	Unit less
λ_i	Eigenvalue	
f	Frequency	Hz
T_g	Glass transition temperature	$^{\circ}C$
Z	Global matrix	
Λ	Grating period	m
c_g	Group velocity	m/s
i	Imaginary number	Unit less
E	Longitudinal elastic constant	N/m^2
L	Longitudinal wave	

c_L	Longitudinal wave velocity	m/s
ϕ	Material orientation angle	Degrees
inv	Matrix inverse	
c_p	Phase velocity	m/s
h	Plate half-thickness	m
μ	Poisson's ratio	Unit less
χ_q	Representation for direction vector k_3	
G	Shear elastic constant	N/m^2
SH	Shear horizontal wave	
SV	Shear vertical wave	
c_{ij}	Stiffness elastic constants	N/m^2
ε_{ij}	Strains	Unit less
σ_{ij}	Stresses	N/m^2
SW	Surface waves	
S	Symmetric Lamb wave	
d_k	Thickness of k -th layer	m
t	Time	s
c_T	Transverse wave velocity	m/s
Φ	Vertical wave incident angle	Degrees
k	Wavenumber	s^{-1}
θ	Wave propagation direction	Degrees
λ	Wavelength	m

SUBSCRIPT

Symbols **Description**

ij	2 nd order tensor
1,2,3	Direction
k	k -th layer
L	Longitudinal wave
n	Order of the Lamb wave mode
q	Partial wave number
Q	Quasi wave
ε	Strain
σ	Stress
T	Transverse wave
i,j	Vector

SUPERSCRIPT

Symbols **Description**

-	Bottom layer
°	Degree
*	Local coordinate system
-1	Matrix inverse
'	Monoclinic stiffness matrix found by multiplying the orthotropic matrix
+	Top layer
→	Vector

ACRONYMS

AE	Acoustic Emission
BVID	Barely Visible Impact Damage
CAA	Civil Aviation Authority
CATT	Computer Aided Tap Tester
CBM	Condition Based Maintenance
CCD	Charge Coupled Device
CLPT	Classical Laminated Plate Theory
CT	Computed Tomography
CVM	Comparative Vacuum Monitoring
FAA	Federal Aviation Administration
FBG	Fibre Bragg Grating
FEM	Finite Element Method
FT	Fourier Transform
GA	Genetic Algorithms
GM	Global Matrix
GUI	Graphical User Interface
HOLSIP	Holistic Structural Integrity Philosophy
IFT	Inverse Fourier Transform
LHS	Left Hand Side
LL	Limit Load
MEMS	Micro-Electro-Mechanical Systems
NDE	Non-Destructive Evaluation
NLS	Nonlinear Least Square
NRC	National Research Council Canada
PMC	Polymer Matrix Composite
PoD	Probability of Detection
PVDF	Polyvinylidene Fluoride
PZT	Lead Zirconate Titanate

RHS	Right Hand Side
SAFE	Semi-Analytical Finite Element
SHM	Structural Health Monitoring
SMCS	Surface Mountable Crack Sensor
STFT	Short-Time Fourier Transform
TM	Transfer Matrix
TU Delft	Delft University of Technology
UL	Ultimate Load
UV	Ultraviolet
WT	Wavelet Transform

CHAPTER 1: INTRODUCTION AND BACKGROUND

In recent years Fibre Reinforced Polymer Matrix Composites (PMCs) have become one of the materials of choice for many aerospace structural components; these advanced composites are made out of polymer matrix combined with glass, aramid (Kevlar®), boron, and carbon fibre reinforcements. Polymer matrix composites have the ability to tailor the properties of composites to the loading of the aerospace parts, which may result in components that are lighter, stronger, and more resistant to corrosion and fatigue damage than traditional aluminum alloys. Initially, PMCs were found in secondary (non-safety critical) aircraft structures such as fairings, hatches, and cowlings. As confidence in the durability and damage tolerance of these materials increased, airframe manufacturers began to use them in more highly loaded structures. Eventually, this led to several significant military and civil aircraft applications such as the Beech Starship all-composite turboprop aircraft, Boeing 777 composite empennage, Airbus A300 empennage, Hawker-Siddley Harrier, Raytheon Premiere I all-composite fuselage, and the Bell-Boeing V-22 Osprey. These important milestones have led to widespread adoption of PMCs in another wave of civil and military aircraft including the Lockheed Martin F-35 and F-22, Learjet 85, Bombardier CSeries, Boeing 787, Airbus A380, Airbus A350 XWB, etc. These aircraft contain a significant fraction of composite materials, in some cases approaching 50% of the total structural weight as shown in Figure 1.

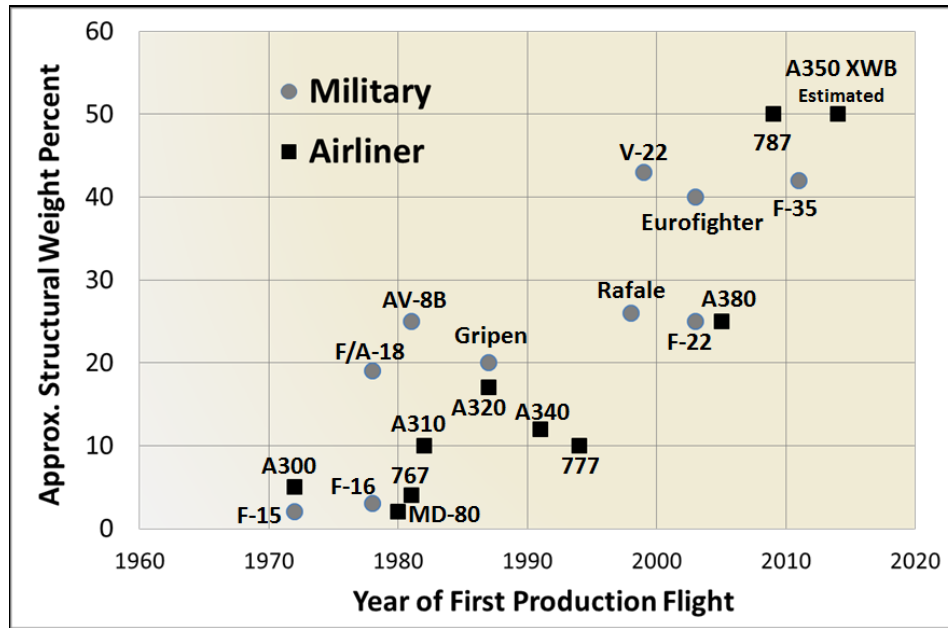


Figure 1: Increase in the use of composite materials in aircraft over time [IHS, 2014]

Despite enhancements in specific strength and stiffness, susceptibility to hidden and Barely Visible Impact Damage (BVID) in composites is still a major concern for operators and civil/military aviation safety regulators. This type of damage may occur during manufacturing, maintenance, or in service and is usually caused by manufacturing defects, bird strikes, runway debris, and dropped tools, which may lead to voids, delamination, fibre breakage, and matrix cracking. Such damage usually occurs below the surface, where visual inspections are limited, thus requiring expensive and lengthy Non-Destructive Evaluation (NDE) techniques such as tap-testing, thermography, x-ray, ultrasonic, liquid penetrant testing, etc. According to Federal Aviation Administration (FAA) advisory circulars for composite aircraft structures [AC 20-107B, 2009], impact damage can significantly reduce the structural performance, which requires attention in the damage threat assessment to identify damage severity and detectability for design and maintenance. This is because if undetected, the damage may grow as a result of local

buckling caused by compressive load during service, which may lead to catastrophic failure of the structure. To avoid such catastrophic failure, composite structures have to be inspected at regular intervals and repaired when the damage is detected [W. J. Staszewski, 2002]. These repairs increase the life cycle cost in two ways - direct cost associated with the repairs, and indirect cost due to loss of revenue induced by having the aircraft temporarily taken out of service for the duration of the repair. Therefore, a reliable and low-cost approach for damage detection in composites is needed to ensure that the total life cycle cost does not become a limiting factor for their use [S. S. Kessler, 2002a].

Most aerospace structures are designed for *safe-life* (designed to surpass the required service life through rigorous fatigue testing), *fail-safe* (having multiple load paths in case one of the components fail) or *damage-tolerance* (damage is assumed to exist from initial manufacturing and periodic inspections and maintenance are needed to detect and repair such damage before it reaches a critical size). In general, aircraft maintenance strategies can be divided into three different categories, which are: *reactive*, *preventive*, and *predictive* [A. Wilson, 2002]. *Reactive* maintenance refers to repair after failure and is commonly used in aircraft maintenance, in which damage/defect detected by flight crew or maintenance personnel are promptly addressed and repaired to maintain safe flight. *Preventive* maintenance refers to periodic inspections using NDE techniques and as needed repairs, which can either be based on time or number of flight cycles. *Preventive* maintenance is widely employed in aerospace structural components with the *damage-tolerance* approach to maintain safety, prolong component life, and decrease downtime. However, it can be labour intensive and can be a waste of resources if the component is found to be structurally sound. *Preventive* maintenance can also be a cause of

accidental damage during routine maintenance and at times damage that are missed or occur during repairs may still cause catastrophic failure. Such was the case of China Airlines Flight 611, in which the improperly repaired tail strike damage led to the in-flight breakup of the aircraft killing all on board [IASA, 2005]. A similar example is the Japan Airlines Flight 123 where an improperly repaired rear pressure bulkhead gave way in flight causing explosive decompression killing 520 people with only 4 survivors [Aviation Safety Network, 1985]. *Predictive* maintenance refers to regularly monitoring the condition of the safety critical structural components in order to improve safety, reduce downtime due to unnecessary inspections, and extend the maintenance intervals. *Predictive* is a Condition Based Maintenance (CBM) approach, in which the component is taken out of service only when it is required. A part of *predictive* maintenance approach to monitor the condition of a structure is called Structural Health Monitoring (SHM). Some of the advantages of using *predictive* over other two maintenance strategies include: service life extension, reduction in downtime, the ability to take corrective actions to avoid failure, decrease in overall life cycle cost, and reduction in human errors. However, *predictive* maintenance is still in the research and developmental phase, thus a lot of work needs to be done to prove its viability [T. R. Hay, 2004].

The following sections provide a brief description regarding typical damage found in composite laminates, commonly used NDE techniques as a part of *preventive* maintenance to find such damage, and SHM systems that are currently being developed as a part of future *predictive* maintenance strategy.

1.1 COMPOSITE AIRFRAME DAMAGE DETECTION AND MONITORING

The modern, optimized composite aircraft structures require careful monitoring and inspections to identify damage and take corrective action as needed to ensure continued safe operation. Composite aircraft structures are no different than metallic structures in this regard; the only difference is what types of damage pose the greater risk and what inspection methods are needed to identify them. For example, in metallic structures, operators are primarily concerned with corrosion, fatigue cracking under tensile loads, tensile overload, creep, and stress corrosion cracking. In composite structures, operators are concerned with delamination growth from compression fatigue, discrete source impact damage, manufacturing defects, hygrothermal degradation, and fibre failures among others. These types of damage usually occur below the surface and may go undetected during routine inspections. Therefore, the certification authorities require demonstration of adequate safety levels in presence of such hidden damage. For composites additional testing and substantiation is often required due to differences in manufacturing and possible service damage as compared to metallic counterpart. For example, certification authorities will not approve fully-bonded primary composite structures unless:

“...the limit load capacity must be substantiated by one of the following methods—(i) The maximum disbands of each bonded joint consistent with the capability to withstand the loads in paragraph (a)(3) of this section must be determined by analysis, tests, or both. Disbands of each bonded joint greater than this must be prevented by design features; or (ii) Proof testing must be conducted on each production article that will apply the critical limit design load to each critical bonded joint; or (iii) Repeatable and reliable non-destructive inspection techniques must be established that ensure the strength of each joint.” [FAA-23.573 pg. 234, 2002]

Currently, there are no economical NDE techniques capable of satisfying point (iii) above. Similarly, proof testing, as recommended in (ii) of every production article is generally impractical and not desirable for aircraft manufacturers. For the most part, manufacturers use design features (e.g. mechanical fasteners in bonded joints) and thus follow recommendation (i). In addition to the challenges presented by the lack of reliable and repeatable NDE techniques required to satisfy point (iii), composite structures are affected by several potential damage conditions such as disbonds, inclusions, resin rich/starved areas, fibre breakage, core crushing (in the case of honeycomb material), impact damage, and environmental degradation effects, which are discussed in Section 1.1.1. Some of these conditions are promoted by loading and usage, while others are a function of environmental exposure during the usage of the structure. These damage conditions can have adverse effects on the material properties, causing a significant change in the values initially considered during the design, verification, and certification process of the structure.

As more and more aircraft with composite structures replace aging metallic aircraft, operators will be further looking for ways to save inspection and maintenance costs associated with the use of composite structures. The cost of inspecting primary composites structures can be as high as 30% of the acquisition and operation costs [Y. Bar-Cohen, 2000a]. One of the causes for this high inspection cost is due to the damage created by low-velocity impacts, which can occur anytime during the aircraft service life and anywhere within the structure. This critical flaw type requires detection and as needed repair as soon as possible rather than postponing it to the next scheduled maintenance cycle. Conducting a point-by-point search using conventional NDE can be very costly and time consuming because the aircraft has to be temporarily removed from

service. Therefore, there is always going to be a need for a low-cost system that can be used to rapidly inspect large areas without any removal of structural components to minimize operational downtime [Y. Bar-Cohen, 2000b].

One of the methods to reduce such inspection cost and maintain safety is by using Structural Health Monitoring (SHM) techniques, which may form part of a Holistic Structural Integrity Process (HOLSIP) as shown in Figure 2. Structural health monitoring is defined as technologies that can be used to monitor, detect, and identify damage in structures to maintain safety, reliability, and reduce the overall maintenance cost [H. Sohn et al., 2003]. In a typical SHM system, the structure is monitored using on-board sensors continuously or at discrete intervals. The data gathered by the sensors can be processed on-board or sent to the ground control station for evaluation. The evaluation results are then used to identify damage occurrence and inform the operator about the location, nature, and severity of the damage. This will be a major shift from the current interval-based to condition-based maintenance, in which the aircraft is taken out of service only when the maintenance and repair is needed based on operator's decision. This will also reduce the associated cost of using NDE because damaged areas are often hard to localize requiring the entire aircraft structure to be inspected, which might involve tearing down some components. A reliable SHM system can increase the design life of a structure or the original design itself can be made less conservative, hence saving weight.

As mentioned earlier, SHM in conjunction with other systems such as *usage monitoring* and *structural condition & history* can be a part of a HOLSIP approach (Figure 2). Holistic structural integrity process is a system engineering based approach which aims at developing physics based models that combine structural loading, initial structural conditions, environmental effects, and material properties at the initiation of the structure's life and the evolution of these same properties as they change in time due to damage such as: corrosion, delamination, impact, etc. Holistic structural integrity process was founded upon the idea that all failure mechanisms involved in the degradation of the structure are interconnected [D. W. Hoepfner, 2011]. As shown in Figure 2, the *usage monitoring* acquires operational loads such as temperature, humidity, speed, and manoeuvres. Whereas, *structural conditions & history* represents collection of initial structural information such as design, analysis, testing, material properties data, maintenance/repair records, and previous flight history, which serve as a database to be used in a physics-based nucleation model in order to determine the remaining component life.

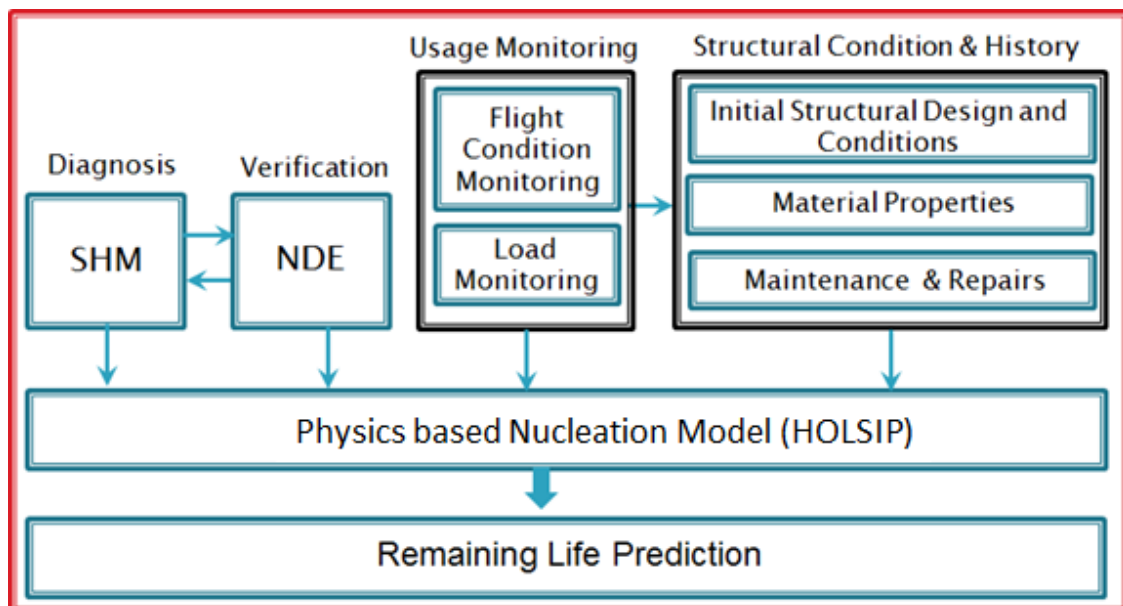


Figure 2: HOLSIP based approach

Before an SHM system can be installed in an aircraft for monitoring and evaluation, it has to be certified by the civil and military aviation authorities. The certification process may include safety assessment, verification, and validation. Some of the certification requirements are suggested in [ARP6461, 2013]. As a minimum, an SHM system should be able to detect damage exceeding a prescribed threshold, as set by the established Probability of Detection (PoD) with associated confidence levels traditionally used in NDE. Results from the well-established NDE techniques can be used as a feedback to improve an SHM system or set the damage detection level [ARP6461, 2013]. As the reliability of the SHM increases it can be used in conjunction with NDE, *usage monitoring*, *structural initial condition*, and *structural history* to be a part of HOLSIP (Figure 2). Holistic Structural Integrity Process can be used to forecast the remaining life of the structure by measuring the past and current state of the structure using SHM and *usage monitoring*, estimating anticipated future operational loads, and by using physics based models and past experiences. Data from *usage monitoring* can also be used to develop a data-based model to predict the future loading on similar aircraft experiencing analogous loading conditions [C. R. Farrar et al., 2007].

As far as SHM for composite is concerned, the system should be able to detect damage that can be detrimental to the structural integrity and may jeopardize safety of a composite structure. Some of the typical damages that are detrimental to a composite structure are discussed in the following section.

1.1.1 TYPICAL DAMAGE TYPES FOUND IN LAMINATED COMPOSITES

This section provides a brief description of typical damage types that are found in laminated composite materials as shown in Figure 3, some of which may have a detrimental effect on the structural integrity.

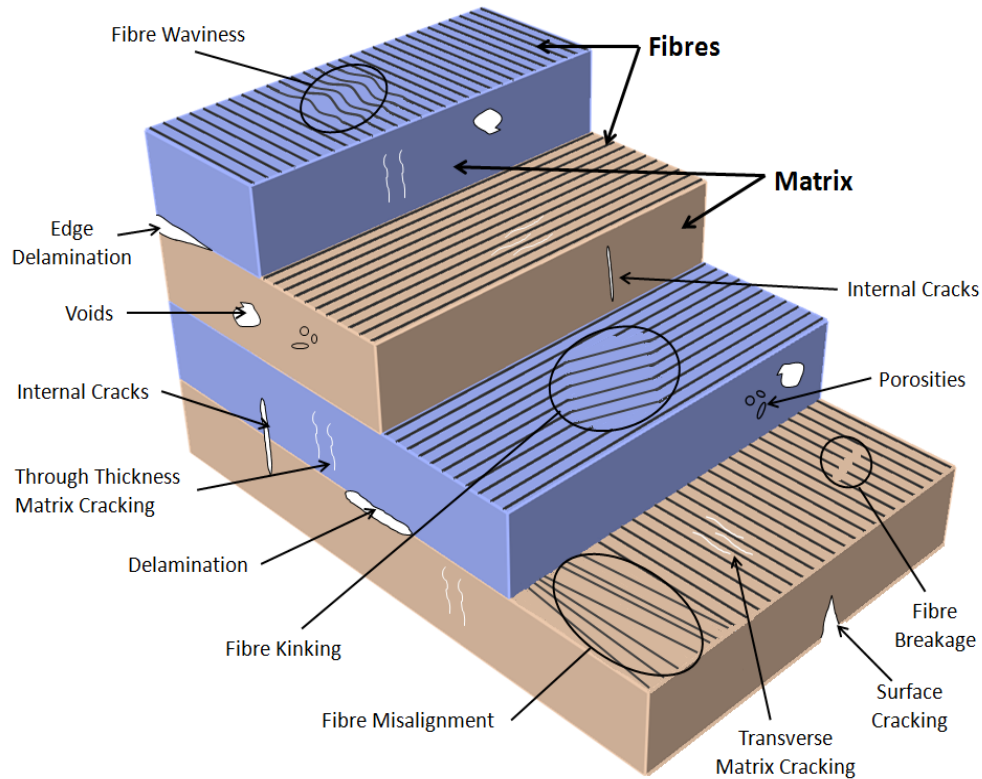


Figure 3: Typical damage types found in laminated composites

1.1.1.1 Delamination

Delamination is the separation of two adjacent plies and is one of the most worrisome failure modes in laminated composites. This type of damage is due to matrix properties having lower fracture toughness, strength, and resistance against inter-laminar shear and transverse tension as compared to the reinforcement constituent. Thermal stresses and resin cure shrinkage during

manufacturing can give rise to the residual/inter-laminar stresses that can be high enough to cause delamination due to the mismatch between the properties of two adjacent layers [V. V. Bolotin, 1996]. Delamination can also be caused due to contaminations such as fragments of backing paper and peel ply left behind during layup and processing steps. The causes of delamination in-service are due to temperature cycling, local loads, impacts, and fatigue. Failure due to delamination often initiates from free edges, surface defects, and stress concentrations, which leads to the loss of overall stiffness/strength and under compressive loading leads to reduce buckling load limits [A. N. Vorontsov et. al, 1989].

1.1.1.2 Damaged fibres

Since fibres carry majority of the applied tensile and in-plane shear loads, damage in fibres can have detrimental effects on the overall strength of the composite structure. Typical damages associated with fibres are: misalignment, waviness, kinking, and fracture/breakage. Misalignment and waviness are introduced during manufacturing process, whereas kinking and fracture/breakage occur during service.

Misalignment is caused during processing, cutting, draping/laying up the composite fabric/prepreg, when the fibres are aligned off-axis to the desired design direction. This can be caused by operator's error during hand lay-up or by poor path followed by an automated fibre/tape lay-up robot.

Waviness is formed due to mismatch in the thermal expansion between fibre and matrix or composite and the tool plate during cool down [D. Kugler et al., 2001]. The through-thickness temperature gradient causes higher volumetric shrinkage of the matrix and since the coefficient of thermal expansion of the fibre is significantly lower; the lamina orientated in different direction tries to slip with respect to each other. If this slippage is restricted by the stiff fibres in the neighboring plies, the load is transferred between individual plies by interface tractions, thus creating waviness [K. Vanclooster et al., 2009]. Shear stresses can be induced because of the offset angle between the fibres and the loading axis created due to waviness. The shear stress produces shear strains, which leads to greater misalignment of fibres, hence higher shear stresses. Therefore, waviness reduces the compressive strength of a composite [M. R. Wisnom, 1993].

Kinking is the localized shear deformation in a band across the thickness due to micro-buckling of fibres created by compressive loads. Within kink band, fibres experience significant rotation, while the matrix undergoes large shear deformations. Therefore, resistance to kinking is controlled by the shear stiffness of the matrix. Initial imperfections such as fibre misalignment, waviness, improper resin impregnation, and porosity have significant influence in the formation of kink band [Z. Yongbo et al., 2011].

Fibre breakage occurs when the applied stress is greater than the fracture strength of the composite. Majority of the time, failure due to fibre breakage occurs in steps. First, the fibre with an existing damage fails, which in turn, increases the load concentration in the surrounding

intact fibres. Since the load distribution is now higher for the remaining fibres, the next weak fibre tends to fail. This process will repeat until the entire structure fractures. Fibre breakage is generally caused in service due to foreign-object impact, lightning strike, applied load, erosion, scratches, and abrasion.

1.1.1.3 Matrix cracking

Matrix cracking occurs in the through-thickness and transverse directions and can run perpendicular and parallel to the fibres respectively. Matrix cracking is usually the first damage to occur when a composite laminate is subjected to a quasi-static/cyclic tensile loading [P. Gayathri et al., 2010]. The through-thickness cracks occur because of the significantly lower matrix strength/stiffness as compared to the reinforcement. This causes strain magnification within the matrix in the off-axis ply direction. Since the strain to failure of the off-axis ply is significantly lower than that of the ply aligned to the loading direction, the through-thickness cracking is developed. Similarly, transverse cracks appear due to a mismatch between the in-plane Poisson's ratio of the plies in the loaded and off-axis directions [S. Abrate, 1991]. This type of damage usually occurs during service as a result of tensile, fatigue, and impact loading and is affected by the polymer matrix [H. Hu, 2007]. Despite being one of the most common forms of damage in composites, matrix cracking itself, does not lead to a structural failure; however, it can initiate other critical failure modes such as delamination and fibre breakage.

1.1.1.4 Porosity/voids

The terms porosity and voids are interchangeably used to describe trapped moisture and volatiles in a composite matrix. Porosity refers to a concentration of micro-voids; whereas void is a single isolated entrapment of moisture/volatile. Porosity and voids are usually created during manufacturing process due to [F. C. Campbell, 2010]:

- Entrapment of air/moisture during mixing of matrix and preparation/storage of prepreg.
- Release of volatiles during resin cure.
- Improper curing cycle temperature, pressure and/or vacuum levels.

Porosity and voids affect compressive, shear, and bending strengths, which are dominated by the matrix properties. They also act as stress concentration points and possible damage initiation sites [A. M. Rubin et al., 1994].

1.1.1.5 Matrix damage due to improper cure

Improper curing is a matrix-dominated defect because during the cure cycle the resin changes its physical state from liquid to rubbery to glassy. Incomplete/non-uniform curing creates parts with thickness variation causing residual stress build up, thus affecting the stiffness and toughness of the composites, whereas over-curing can lead to matrix cracking or burning. Improper cure can also entrap volatiles, which can lead to void formation [V. Antonucci et al., 2005].

1.1.1.6 Resin rich and resin starved areas

Resin rich areas are generally formed in a part with chamfered edges and angled corners. During liquid composite moulding process, the fibres are compressed during mold closure; this compressive pressure pulls the fibres at the outside corners tighter forming a gap between the fibres and the mold surface. After infusion, if the accumulated resin within the gap is not forced out; resin-rich areas are formed. Resin rich areas can also be formed due to uneven tooling surfaces and improper compaction during cure [C. Dong, 2011].

Resin starved areas on the other hand are formed when resin fails to fully impregnate the fibres. This occurs when excessive moulding pressure is applied during curing causing the resin to bleed off, or insufficient amount of resin is applied to fully wet out the dry fibres. In resin-starved areas, the fibres are exposed to the outside environment, which makes them susceptible to fibre breakage, thus reducing the strength of the part [Netcomposites, 2013].

1.1.1.7 Cracks/fractures

Cracks are defined as damages that are present in one or more layers without reaching the opposite surface, whereas a fracture extends through entire layers of the laminate. Cracks are common in composites arising during manufacturing and due to in-service loading. During manufacturing, cracks can form during curing as a consequence of thermal and/or residual stresses. Processing steps such as drilling, trimming and machining can introduce inter-laminar cracking. In service, cracks are formed due to impact, over-torqued fasteners or due to fastener

pull through. Cracks can affect moisture absorption by providing more space for the moisture to enter the laminate and can also act as a stress concentration point.

1.1.1.8 Matrix damage due to environmental degradation

Composites are susceptible to environmental degradation such as chemical contamination, ultraviolet (UV) radiation, moisture absorption, and temperature fluctuations. Surface damage can occur due to adverse interaction of chemicals commonly used in aircraft such as fuel, hydraulic fluids, de-icing agents, washing detergent, paint, and paint strippers [A. Baker et al., 2004]. Similarly, UV radiation can also create surface damage by altering the chemical structure of the exposed matrix by molecular chain scission (breaking of molecular bonds) and chain crosslinking. Chain scission lowers the molecular weight of the matrix thus reducing the strength and heat resistance, whereas chain crosslinking increase brittleness resulting in micro-cracking [B. G. Kumar et al., 2002].

Moisture absorption is a diffusion process where the matrix absorbs water from a humid environment mostly through the faces of the structure, which can be accelerated by elevated temperatures and applied stresses. Composites absorb water by two methods - the unbound and the bound method. In the unbound method, the water molecules are free to move through the voids filling the free space. Effects caused by the unbound method can be reversible upon drying, provided no permanent damage has been done due to thermal cycling or hygroscopic swelling. In the bound method water molecules attach themselves to the matrix polymer chain via hydrogen bonding disrupting the inter-chain bonding, which creates swelling and plasticizing

of the polymer matrix. Swelling can reduce mechanical interlocking between the fibre and the matrix during cool down due to variations in thermal expansion rates causing internal stress [M. R. Vanlandingham et al., 1999]. Plasticization of the matrix can have a dual effect, it can aid in reducing the residual stresses while reducing the glass transition temperature (T_g). Reduction in T_g can affect the service temperature limit [S. Wang et al., 2002].

Temperature fluctuations can have detrimental effects when combined with moisture absorption and presence of voids. The stiffness and strength of composites can decrease significantly when exposed to temperatures exceeding T_g . Also at high temperatures the trapped volatiles within the matrix may be released. The volatiles can expand creating high pressures within the matrix voids/cracks increasing the stress within the surrounding matrix and/or fibre creating permanent damage. At low temperatures, water trapped in the void/cracks may freeze and expand in volume, thus creating pressure on the surrounding material resulting in matrix cracking and delamination. Severe thermal damage can also be caused by lightning strike, inducing cracking and delamination [A. Baker et al., 2004].

1.1.1.9 Disbond

Disbond is referred to as a separation of the adhesively bonded material from another material [A. Baker et al., 2004]. This type of damage is dependent on the integrity of the adhesive layer and is affected by the presence of manufacturing defects as well as service loading. Manufacturing defects include: poor surface preparation, contamination, improper curing,

inaccurate applied pressure, geometrical mismatch between the adherents, and trapped air/moisture in the adhesive mixture. Poor surface preparation is one of the leading causes of adhesively bonded joint failures. Creation of porosity and voids can also degrade the adhesive properties as well as create stress concentration during loading. During service, disbond can occur due to impact damage, environmental degradation such as moisture ingress, and aging of the adhesive layer [FAA-AR-09-4, 2009].

The main concern for the composite aircraft operator as imposed by the regulatory agencies is to detect and repair damage discussed above in order to stop them from growing and causing catastrophic failure of the structure. Some of commonly used NDE methods to find such damage are discussed in the following section.

1.1.2 NDE METHODS FOR COMPOSITES

To maintain airworthiness, aircraft are currently inspected and maintained based on calendar or flight hours. The checklists of parts to be inspected and the approved inspection methods are generally provided by the airframe manufacturers, parts vendors, and the civil aviation administration authorities (e.g. Transport Canada). The inspections are performed using *routine* inspection, for example pre-flight visual examination or *detailed* inspection such as A, B, C, and D checks, increasing in inspection cycle and details requiring NDE techniques. Maintenance personnel conducting such inspections require proper training, which may range from simple with little expertise to highly trained and certified technicians using specific NDE technique. The

operator training guidelines for some of the NDE techniques as provided by different organization can be found in:

- SNT-TC-1A, The American Society for Nondestructive Testing, *Recommended Practice, Personnel Qualification and Certification in Nondestructive Testing.*
- ATA-105 Aviation Transport Association, *Guidelines for Training and Qualifying Personnel in Nondestructive Testing Methods.*
- AIA-NAS-410, Aerospace Industries Association, *National Aerospace Standard, NAS Certification and Qualification of Nondestructive Test Personnel.*
- ISO 9712, International Organization for Standards, *Nondestructive Testing Qualification and Certification of Personnel.*

Some of the most commonly used NDE techniques for detecting damage in composite airframes are discussed in the following sections.

1.1.2.1 Visual inspection

Visual inspection as defined by FAA [FAA-AC-43-204, 1997] is the process of judging the condition of the inspected unit using the unaided eye alone, or with various aids as sensing mechanism. Visual inspection is the oldest and most frequently used aircraft inspection technique which accounts for 80% of the overall inspections on large transport aircraft. Depending on the complexity, visual inspection has been broken down by FAA into four levels.

Level 1 *walk-around*, is conducted from the ground level for inspecting broad area of the aircraft for overall condition. Level 2 *general*, is the inspection performed on the exterior, some interior components, selected hatches, installations or assembly to detect obvious damage. Level 3 *detailed*, is inspection requiring surface preparation and the use of inspection aids. Level 4 *special-detailed*, is intensive examination requiring disassembly and cleaning to find specific fault or damage [FAA-AC-43-204, 1997]. Similar levels have also been used by other aviation administration; for example Civil Aviation Authority (CAA) [CAA-CAP562, 2005] suggests an inspection distance of 2 m for *general* and 0.3 m for *detailed* visual inspection.

Instruments such as magnifying lenses, borescopes, mirrors, and flash lights provide additional aid during visual inspection. Even though visual inspection is the most economical, rapid, and flexible method for aircraft inspections, it is highly dependent on human factors and working environment. Personnel conducting visual inspection require vision acuity, colour vision, and proper posture. Proper posture such as coordinated head, hand and body movements without any interference from aircraft parts and structures can be impossible to maintain at all times. Working environment such as inadequate lighting, glare, surface reflections, temperature, weather, and noise level, all play a significant role in reducing the inspector's ability to detect damage [C. G. Drury et al., 2002]. In composite the damage are even harder to detect. This is because flight and ground crews are experienced in detecting damage such as dents created by impact or tears in metallic structure. However, in composite the impact damage may not appear on the surface. Thus, such damage can go unreported even by highly experience crew members and can have significant impact in the structural rigidity [L. Cook, 2009].

1.1.2.2 Tap-testing

Coin and hammer tap-testing are one of the oldest methods of inspecting laminated, sandwich, and bonded composite structures. Tap-testing methods are widely used as quick evaluation procedure to detect delamination, disbond, and poor cure. In this method the operator lightly taps the structure with a coin (approx. 25 mm in diameter, size of a Canadian/US 25 cents coin) or a small hammer (max 2 ounces) some of which are shown in Figure 4 and listens to the sound radiated by the structure. The characteristics of the impact due to tapping depend on the local stiffness of the structure in response to the coin or hammer used, which can be altered due to the presence of damage. The acoustic response is compared with that of a healthy structure which produces *ring* as compared to the *flat* or *dead* response by the presence of damage [FAA-1C-43.13-1B, 2009].



Figure 4: Tap-testing instruments [D. Roach, 2007]

Some of the disadvantages of tap-testing include: limited to thin skins and the need to tap the entire structure for damage localization. Tap-testing is also highly dependent on inspector's ability to hear and interpret the results. Therefore, any adverse working environment such as background noise can have negative impact on the ability to detect damage. Recent advancements have been made in order to automate and reduce human errors by instrumenting the traditional tap hammer with force transducer to record the force-time history. Some of the notable devices that are used in the aerospace industry of such sort are Boeing tap hammer (RD³), which was developed by Boeing and licensed to Wichitech (Figure 5a), Computer-Aided Tap Tester (CATT), which was developed by Iowa State University and licensed to Advanced Structural Imaging Inc. (Figure 5b), and Woodpecker by Bittech Inc (Figure 5c).



Figure 5: Electro-mechanical tap-testing systems

1.1.2.3 Ultrasound

Ultrasonic technique is commonly used for detecting internal damage in composite structures such as delamination, matrix cracking, disbond, fibre breakage, voids, and inclusions both during quality assurance and in-service. In this technique, short pulses of ultrasound typically between 500 kHz to 20 MHz frequency are transferred into the specimen; however, for composite 10

MHz or less is commonly used due to high attenuation [A. Kapadia, 2011]. Damage detection using ultrasound is based on the principle that the wave gets scattered, reflected, and transmitted at different velocity and amplitude when an interface with different acoustic impedance is encountered along its propagation path. Data from ultrasound testing are typically displayed in A-scan, B-scan, and C-scan formats. In A-scan format, the ultrasonic signal strength is plotted against the elapsed time, which can be used to detect and locate the damage by comparing the signal amplitude reflected by the damage with the known reflector such as back wall or front wall of the specimen. In B-scan format, the time-of-flight of ultrasonic signal is displayed in the vertical axis against the transducer's location, which can be used to determine the damage depth and size along the scan direction. In C-scan format, the time-of-flight or signal amplitude of A-scan is recorded at different points, which are displayed in greyscale or in color images representing signal amplitude over the specimens' two-dimensional plan-view. C-scan is generally produced by automated computer scanning system by immersing the specimen under fluid, which records the signal amplitude through the entire thickness of the specimen [NDT Resource Center, 2013a].

Some of the most commonly used ultrasonic techniques are pulse-echo, through-transmission, back-scattering, and phased-array, which are discussed in the following sections.

1.1.2.3.1 Pulse-echo

In this technique, a transducer sends an ultrasonic pulse into the specimen; the pulse gets echoed back due to the change in acoustic impedance encountered in the presence of damage

or front and back wall of the specimen. The reflected/echoed signal is picked up by either the same transducer or a second one located on the same surface; thus, requiring access to only one side of the specimen. Delay lines are generally added to get the proper top surface reflection and detect near surface damage in order to minimize the dead zone (area directly under the top surface). Referring to Figure 6, an initial pulse (P) is sent into the specimen via a piezoelectric transducer. The same transducer is used to pick up the reflected signal from the front wall (a) and the back wall (c) along the regions free of damage. In the presence of damage, the reflected signal from the damage (b) is shown in between the front and back wall echo signals. Depending on the time of arrival and the amount of energy reflected by the damage, the through-thickness location and damage severity can be found.

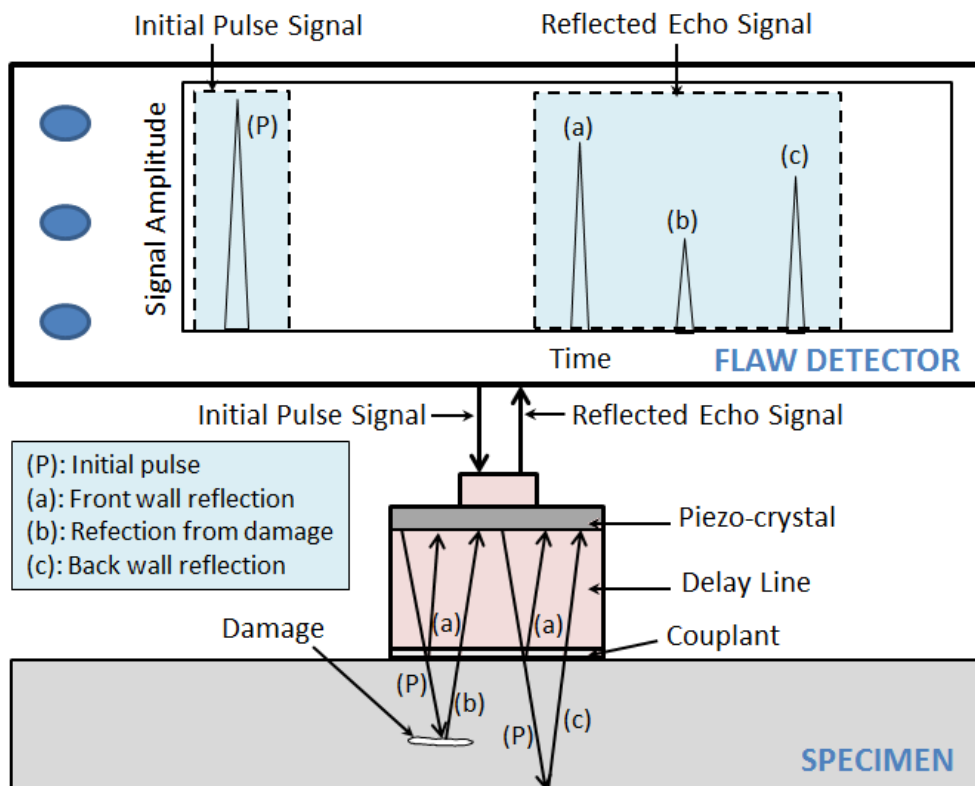


Figure 6: Schematic of pulse-echo ultrasonic technique with A-scan display

1.1.2.3.2 Through-transmission

In this technique (referring to Figure 7), a transmitter (T) sends out an ultrasonic pulse (P) into the specimen. After travelling through the thickness, the signal is picked up by a receiver (R), facing directly on the opposite side. Presence of damage along the ultrasound path results in either total or partial loss of the transmitted sound, thus reducing the energy received by the transducer. Damage intensity can be found by examining the difference between the received signal amplitude of a damaged region (b) and an undamaged region (a). Through-transmission is preferred over pulse-echo technique to detect near-surface damage and damage that are poor reflectors; however, the through-transmission method requires simultaneous access to both sides of the specimen and does not provide the through-thickness location of the damage.

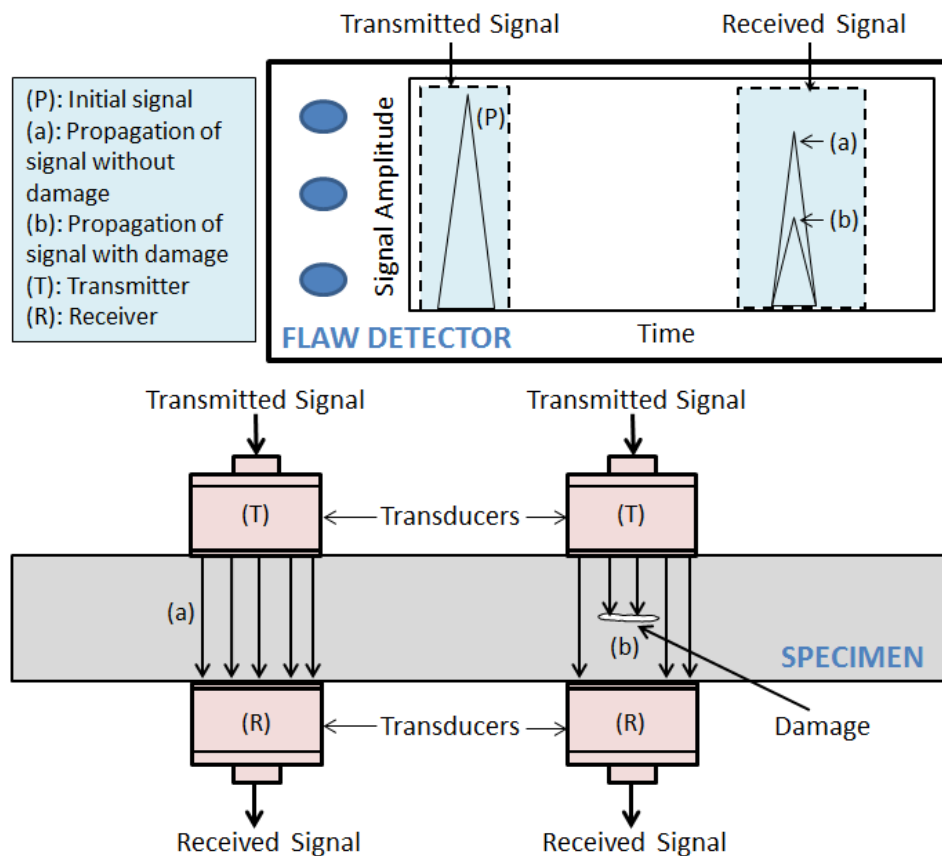


Figure 7: Schematic of pitch-catch/through-transmission ultrasonic technique

1.1.2.3.3 Back-scattering

This technique is similar to the pulse-echo; however, the angle of incidence of the ultrasound beam is non-zero, which aids in inspecting areas that are not accessible with the conventional pulse-echo or through-transmission techniques. If the back surface is uniform, the signal is not backscattered as compared to the back surface with irregularities, where a greater amount of energy is backscattered and can be detected by the transducer as shown in Figure 8 [J. R. Lhota et al., 1994].

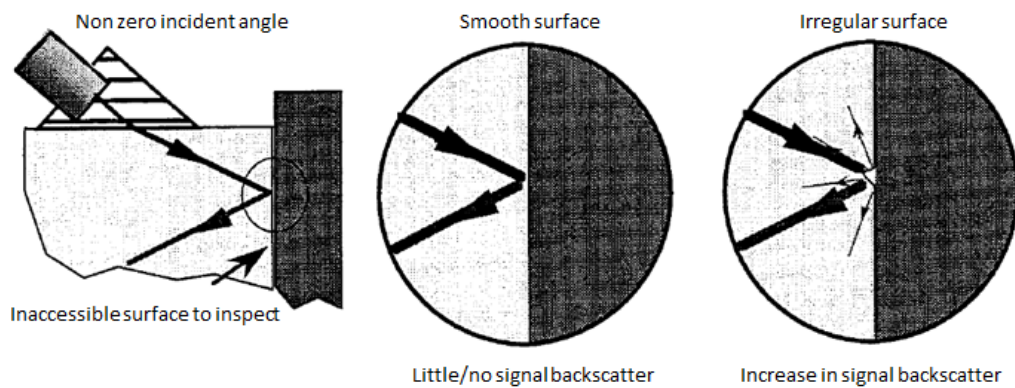


Figure 8: Principle of backscatter ultrasonic [J. R. Lhota et al., 1994]

1.1.2.3.4 Phased-array

In this technique, multiple small individual transducers arranged typically in a strip, ring, or circular pattern are used instead of a single or paired transducers such as in the case of pulse-echo and through-transmission techniques. Transducer assembly of as many as 256 small elements can be pulsed separately at desired intervals, which can have a constructive and destructive interference effect on the outgoing ultrasonic wave front. This effect of strategically adding or canceling the wave energy in a desired way is used to steer and shape the ultrasonic beam, while reducing beam spreading and improving energy focusing as shown in Figure 9. The constructive and destructive effect of the multiple waves create a single primary wave front,

which gets reflected due to the presence of damage and back wall along its propagation path. The reflected signals are picked up by the same or different transducers and the information can be presented in the standard A, B, or C-scan formats. A single phased array system can sweep the ultrasonic beam linearly or through a range of reflected angles and focus the energy at different depths, thus improving the flexibility as compared to the conventional transducers [M. Anderson, 2012].

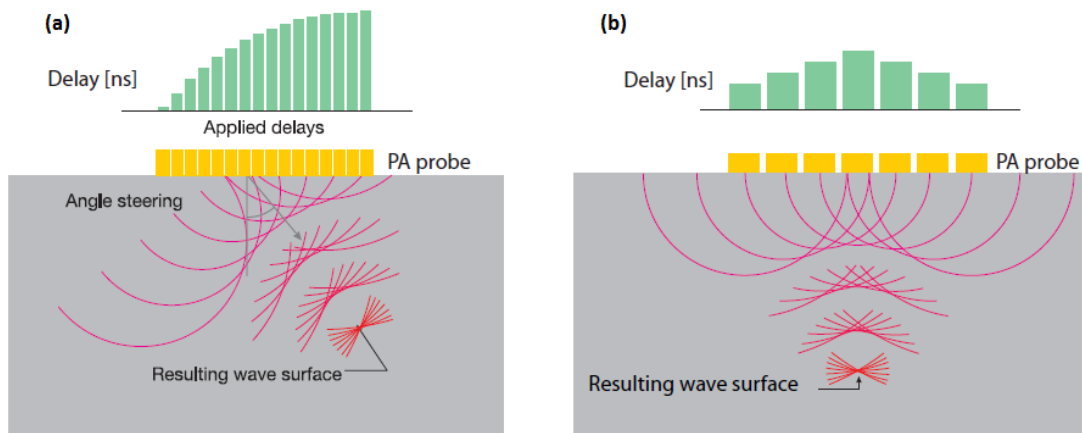


Figure 9: Phased array beam focusing at (a) an angle and (b) normal incidence [N. Dube, 2007]

1.1.2.4 Liquid penetrant

Liquid penetrant is one of the most commonly used NDT methods to detect surface/sub-surface cracks and discontinuities because of its versatility and cost-effectiveness. This method makes the discontinuities easier to detect by increasing the contrast between the flaw and the background. In this method, the surface is first prepared to be free of contaminants such as oil, water, and grease. Liquid penetrant dye is then applied by dipping, pouring, spraying, or brushing onto the parts' surface; thus, allowing the dye to penetrate into the cracks/discontinuities (dwell time). Excess penetrant is then removed using water-soluble penetrant, low-pressure coarse water spray or wiped out with a damp cloth. A thin layer of light-

colored developer is applied to the surface by means of dry powders, dipping, or spraying, which absorbs the excess penetrant and also spreads above and around the defects improving visibility. Liquid penetrants are selected on basis of their penetrating ability and dyes are selected for their brilliance. Colored dyes are used for visible light, whereas fluorescent dyes are used to be viewed under ultraviolet light. Post-cleaning is important to remove any residual penetrant material in order to avoid any moisture absorption by composites [P. E. Mix, 2005].

1.1.2.5 Eddy current

Eddy current inspection is based on the principle of electromagnetic induction, in which, an application of alternating current passed through a coil develops a primary magnetic field, which in turn generates eddy current when brought in close proximity to a conductive material. The change of eddy current to the applied alternating current is monitored as a change in impedance of the test coil providing a fast contact free inspection. Presence of crack or damage in a conductive material obstructs the flow of eddy current lengthening its path, which in turn decreases the secondary magnetic field and thereby increasing the coil impedance as shown in Figure 10. This changes the eddy current's phase and amplitude, which can be detected, amplified, and displayed by an eddy current flaw detector [P. E. Mix, 2005].

This method is widely used for detecting cracks and corrosion in metal; however, it is limited to composite material displaying electrical conductivity. As in the case of carbon fibre polymer composites, even though the matrix is nonconductive, carbon fibre exhibits low electrical conductivity. Therefore, eddy current method has been used to detect variation in fibre volume

fraction, fibre orientation, fibre breakage, and low velocity impact damage in carbon fibre composites [X. E. Gros et al., 1998].

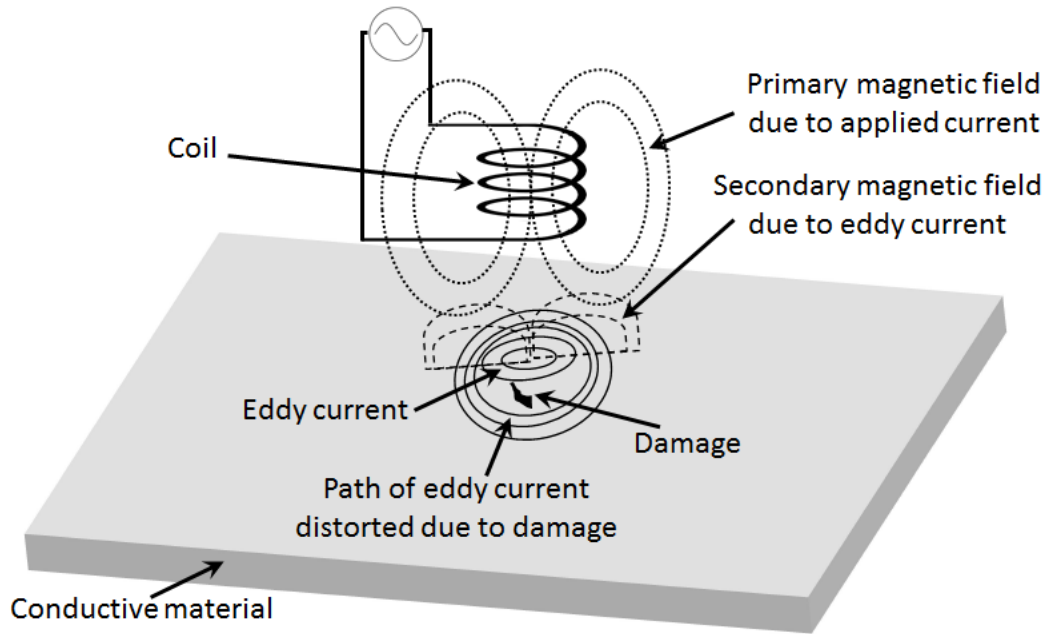


Figure 10: Damage detection using eddy current

1.1.2.6 Radiography

In radiography, a shadow image (radiograph or shadowgraph) of a material/structure is produced using high energy radiation such as x-rays or gamma-rays that are able to penetrate the object and disclose any discontinuities. The penetration and absorption characteristics differ for materials with different densities, changes in thickness, or both. Such difference in density and thickness is captured in a shadowgraph showing regions with varying contrasts. Unlike metals, composite are highly transparent to x-ray requiring low energy as compared to the metallic counterpart. Damage such as voids, cracks, entrapment of foreign material during manufacturing, and impact damage can be detected using this method. However, due to the

radiation risk, extensive operator training is needed and also no quantitative information regarding the location of the damage is provided [P. Vaara et al., 2012].

An improvement upon the film x-ray can be found with the Computed Tomography (CT) technique, which produces 2-D and 3-D cross-sectional images of an object from the x-ray images. In this method the part is placed on a computer controlled rotating platform, where the x-ray images are taken at different positions as the part is rotated full 360 degrees. Computer software is used to produce sliced cross-sectional images of the part, revealing its geometrical characteristics, sub-surface defects, discontinuities, and change in density [NDT Resource Center, 2014].

1.1.2.7 Infrared thermography

Infrared thermography is based on the measurement of radiated thermal energy. The method can detect subsurface damage by monitoring the temperature difference over the specimen's surface with an infrared camera. This technique provides a non-contact method to inspect large areas of composite structures to detect disbonds, delaminations, voids, matrix cracks, foreign object inclusions, and impact damage [ASTM E2533-09, 2009]. Thermography is divided into two modes - *passive* and *active*. *Passive* mode depends on the part's temperature being already indifferent with the surrounding providing a qualitative estimate of the damage. Whereas in the *active* mode, an external source is used to induce thermal contrasts between the defective and healthy areas to measure surface temperature response over time providing a controlled

measurement. Commonly used *active* modes are pulsed/transient thermography and lock-in thermography [P. Vaara et al., 2012].

In pulsed/transient thermograph the sample is rapidly heated using a pulse heat source such as flash lamp, induction heater, or hot-air gun. An infrared camera is then used to measure the surface temperature variation over time. Presence of defects offers resistance to the thermal front; hence, the area above the defect has a lower cooling rate as shown in Figure 11. Defects appear on the surface as areas of higher temperature as compared to the surrounding areas without defects. Since the thermal front requires a longer time to reach defects deep within the thickness, deeper defects are observed at a later time. Thus, by using a temperature-time profile of the surface, defect and its approximate depth can be found [A. Manohar, 2012].

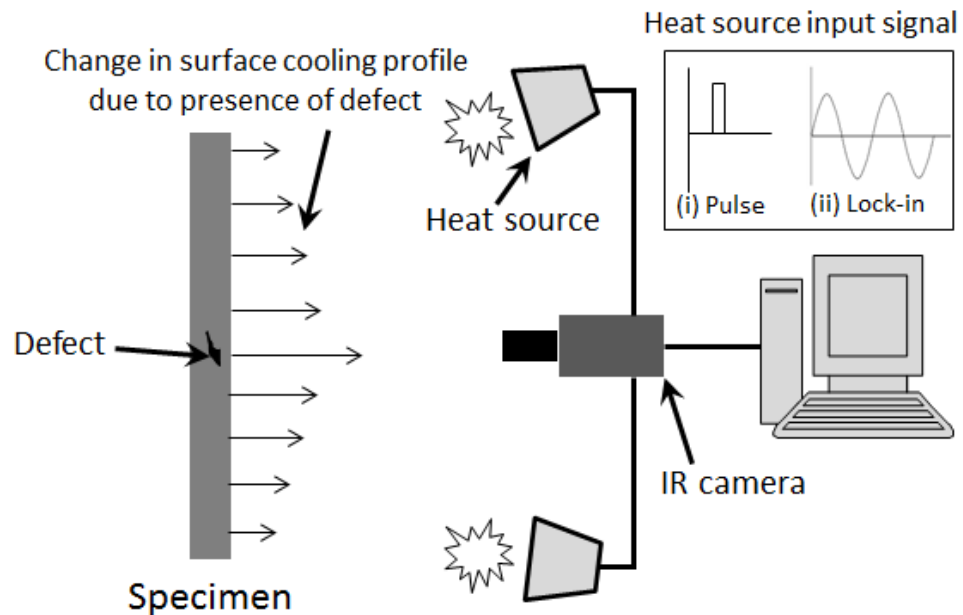


Figure 11: Schematic of thermography inspection technique

Lock-in thermography uses the same setup as pulse thermography but instead of applying an instantaneous pulse, it uses a continuously fluctuating heat to measure the variation in surface temperature as shown in Figure 11. This technique is effective in detecting defects in thick composites and is based on measuring the phase lag/shift between the applied periodic heat source and the surface temperature of the specimen. The lag/shift is caused by some of the heat wave getting reflected upon encountering a defect [X. P. V. Maldague, 2002].

1.1.2.8 Laser shearography

Shearography is an optical method based on the principle that a difference in strain causes a relative phase shift between two points due to the change in the optical path. In this method the surface of a test sample is illuminated using laser and images are taken using a Charge Coupled Device (CCD) camera via an optical shearing element as shown in Figure 12a. The shearing element allows for a superposition of two laterally displaced (shear) images called shearogram [Y. Y. Hung et al., 1979]. The two images are taken at different loading conditions, which could be static or dynamic causing difference in strain. Some of the commonly used methods to induce strain are: pressure, vacuum, thermal, and vibrational. The difference between two images results in an interference fringe pattern, which is directly related to the difference in strain.

Presence of defect induces higher strain directly on the surface above the damage as compared to the surrounding areas without damage. This difference in strain can be seen as concentration of fringes as shown in Figure 12b. Even though shearography measures the surface strains, both surface and internal flaws can be detected unless the flaw is hidden deep from the surface not

affecting the surface deformation. Stereography provides a fast, contact-free and full-field evaluation of a composite specimen to detect subsurface imperfections such as disbonds, delaminations, wrinkles, porosity, foreign object inclusions, and impact damage [Y. Y. Hung, 1999].

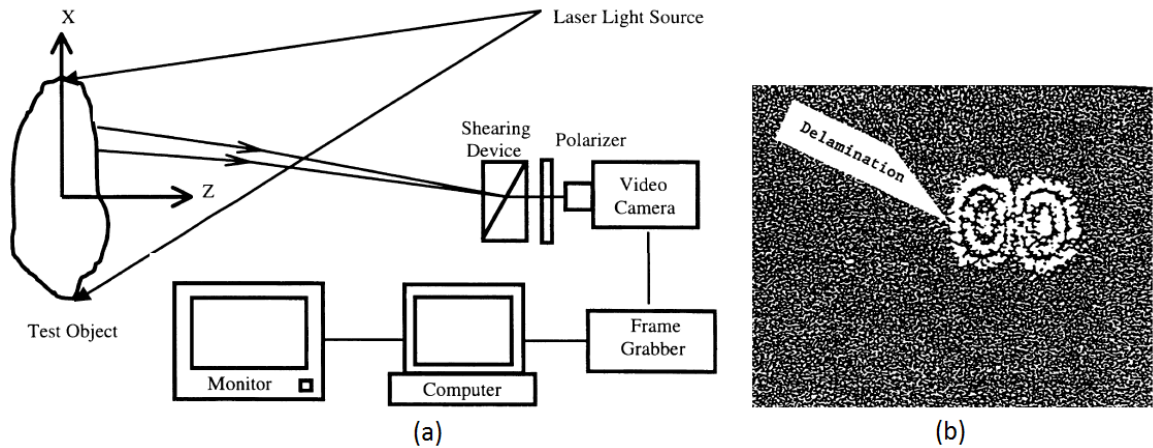


Figure 12: (a) Schematic of laser shearography and (b) Concentration of fringes due to defect
[Y. Y. Hung, 1999]

The aforementioned NDE methods can be both costly and time consuming. Also, the aircraft has to be taken out of service to conduct such evaluations. Therefore, the use of SHM system as discussed in the following section can be a part of the future CBM philosophy for damage detection/monitoring so that the aircraft is taken out of service only when a repair is needed.

1.1.3 SHM FOR COMPOSITES

This section provides a brief description of some of the most widely used SHM techniques for damage detection in composite materials.

1.1.3.1 Damage detection techniques

Some of the most commonly used SHM techniques can be grouped into two categories - *active* and *passive*. An *active* approach is where an actuator sends a diagnostic signal, which is picked up by neighboring sensors for analysis such as in acousto-ultrasonic. This method is useful for detecting internal and external cracks in the material. In a *passive* approach, sensors are used in the listening mode and pick up signals that are generated due to environmental changes and damage growth such as in acoustic emission, vibration, and energy-based methods. This method is effective in monitoring changes in the structure due to external loads, impacts, changes in temperature, etc. [M. M. Derriso et al., 2006]. The following sections describe some of the most commonly used damage detection techniques, which are based on *active* and *passive* damage detection approaches.

1.1.3.1.1 Acousto-ultrasonic

Acousto-ultrasonic is an *active* approach in which stress waves are introduced into a structure by a probe/transmitter at one point and sensed by another probe/sensor at a different point. Propagations of acousto-ultrasonic waves are difficult to analyze because of high-frequency excitation resulting in exciting mixed wave modes such as longitudinal, shear, Rayleigh, or Lamb waves [W. J. Staszewski et al., 2004]. In acousto-ultrasonic benign ultrasonic stress waves that resemble the waves similar to acoustic emission are generated externally by a pulsed/periodic source without disrupting the material. The waves are generated within the structure where post-processing is done similar to the acoustic emission technique. Once launched inside the material, the waves are modified by the presence of damage [J. J. Scholey et al., 2010]. Acousto-ultrasonic waves are launched periodically at predetermined interval and rates. Knowing the

nature and location of the sources, characterization of the material medium between the source and the receiver can be performed. The effect measured in acousto-ultrasonic is relative attenuation and change in wave velocity. When properly measured, any variation of the acousto-ultrasonic signal will depend primarily on material factors that govern attenuation in composite material such as microstructure, fibre damage, porosity, bond quality, presence of micro-cracks, and cure state [A. Vary et al., 1990].

1.1.3.1.2 Acoustic emission

The Acoustic Emission (AE) is a *passive* approach and is based on the fact that materials can store certain amount of elastic or plastic energy before fracturing. The application of external force exceeding this level can cause the material to rapidly release the stored energy creating AE signals. Sources of AE include fracture, plastic deformation, impacts, etc. [R. D. Finlayson et al., 2000]. In a composite material AE may be released due to crack propagation, matrix cracking, fibre fracture, fibre debonding, and delamination [R. G. Liptai, 1972]. The energy emitted from the damage can be registered in forms of burst or continuous acoustic signals. A number of specific signal features are used for damage detection and location. The features are signal duration, maximum amplitude, single threshold level, signal energy, number of threshold crossings, arrival time, and signal energy as shown in Figure 13 [W. J. Staszewski et al., 2004]. The release of AE can be registered using piezoelectric transducers. An array of multiple sensors can be used to triangulate the location of damage by analyzing the time-of-flight of the signal. Acoustic emission is highly sensitive to detect newly formed crack surfaces and damages [J. J. Scholey et al., 2010].

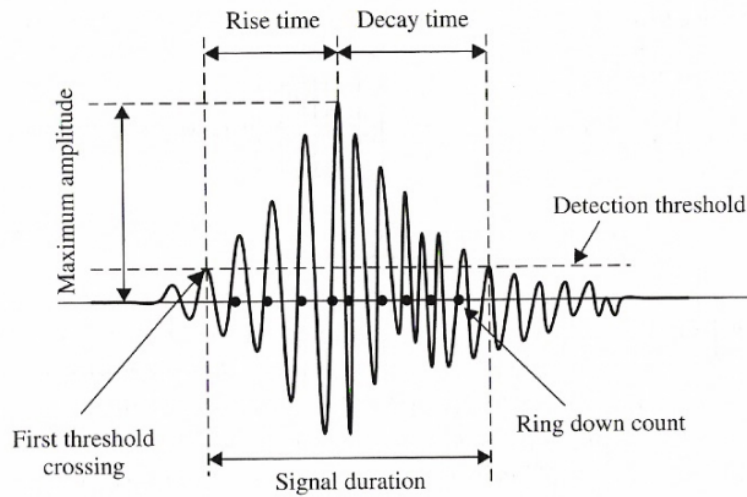


Figure 13: Signal features of acoustic emission [W. J. Staszewski et al., 2004]

1.1.3.1.3 *Vibration-based*

Vibration-based methods rely on the modification in structural modal parameters such as natural frequencies, mode shapes, and modal damping due to the presence of damage. The modal parameters are directly related to physical parameters such as mass, stiffness, and damping. Therefore, any changes to the physical parameters due to the presence of damage affect the modal properties of a structure. Usually, the presence of damage will decrease the mass and stiffness and increase the damping ratio. Mass is less sensitive to damage; whereas damping is most sensitive to damage [Y. Zou et al., 2000].

The capacity to locate damage is limited by using natural frequencies and mode shapes because natural frequencies and mode shapes are global parameters, which can only be associated with local responses at high frequencies. Methods based on natural frequency shift can be divided

into two categories - the *forward* and the *inverse* problem. The *forward* problem consists of determining the natural frequency changes due to known damage cases (including location, extension and type). In this case, damage is usually modeled numerically or analytically. Gathered data can then be compared with the analytical data to determine damage location and extent. The effectiveness of this method depends on the accuracy of the structural model and proper material properties, which is difficult to implement on complex structures. Because of the need for baseline undamaged structural modal parameters, the *forward* method requires large data storage capacity for a complete structure. In the *inverse* problem, damage parameters such as crack length, type and location are determined using the changes in the natural frequency [D. Montalvao et al., 2006]. Due to low sensitivity to damage, change in natural frequency requires high levels of damage and highly accurate measurement techniques for reliable results. It has been found that long cracks or delamination can affect the natural frequency for which the size of damage must be at least 10% of the area monitored in order for it to be reliably detectable [S. W. Dowling et al., 1998].

1.1.3.1.4 Other methods

Some of the other methods used are based on: energy, strain, resistance, and vacuum. In the energy method, the level of impact energy and force is used to relate damage detection and severity. Damage occurs in composites above a certain energy threshold. It has been found that global measurements of contact force and dissipated energy under impact can be related to fibre breakage and delamination growth [J. D. Pearson et al., 2007]. The strain based method relies on measuring strain close to the crack locations, which provide direct measurements of damage evolution. This method can also be used to distinguish between strain caused by

external loads or from damage evolution by monitoring and comparing strain data from close to the crack and far from it, since the strain far from the crack is unaffected by the damage evolution [Ch. E. Katsikeros et al., 2009]. Resistance and vacuum based methods are described in Section 1.1.3.2.5 and Section 1.1.3.2.6 respectively.

1.1.3.2 Sensing technologies

Sensors play an important role in any SHM systems. They are used to acquire data regarding the structure's response to the presence of damage. Some of the most commonly used sensors for damage detection in composites as a part of an SHM system are described in this section.

1.1.3.2.1 Strain gage

In a strain gage sensor, the electrical resistance of the gage varies in proportion to the applied load. This change in resistance due to application of force/pressure is measured by the change in electrical resistance of the gage using a Wheatstone bridge circuit. The most commonly used strain gage is the bonded metallic strain gage, which consists of a very fine wire arranged in a grid pattern to maximize the strain over the wires in the parallel directions as shown in Figure 14. The cross-sectional area of the grid is minimized to reduce the shear and Poisson's effect. The grid is bonded onto a thin backing such as Kapton, which is then directly attached on to the specimen. The sensitivity of a strain gage to the applied strain is expressed as the Gage Factor (GF), which is the ratio of change in electrical resistance over the change in strain [National Instruments, 2013]. Strain gages are generally used for hot spot monitoring.

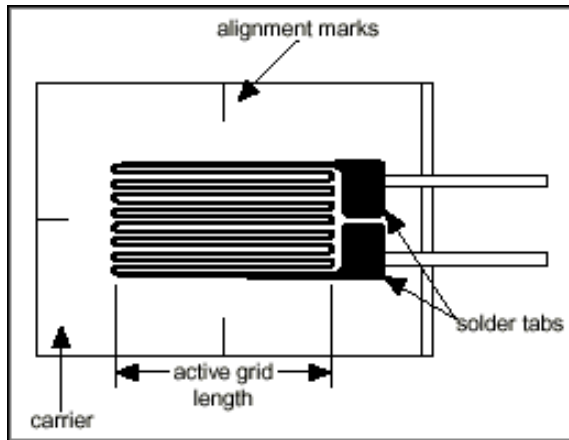


Figure 14: Bonded metallic strain gage [National Instruments, 2013]

1.1.3.2.2 *Optical fibre sensors*

Optical fibres are commonly used for data transmission in telecommunication. In recent years, they have been increasingly used for sensing strain, vibration, temperature, and pressure both for testing purposes and in SHM applications. Optical fibres have a high refractive index core surrounded by lower refractive index cladding. Light is guided through the fibres due to total internal reflection. Their small cross-section, low mass, and immunity to electromagnetic interference suggest they can be embedded into composite structures. Fibre optic sensors can be multiplexed, so that many sensors can be accessed via a single fibre optic cable [W. J. Staszewski et al., 2004].

Fibre Bragg Grating (FBG) sensors are one of the most commonly used optical sensors. The gratings, which are close parallel lines typically between 1 mm to 25 mm long, consist of periodic regions of higher and lower refractive indices printed into the core of a fibre. Broadband light passing through the grating is partially reflected from the grating at particular

wavelength called the Bragg wavelength. Interference between the individual grating planes results in a narrow wavelength range of light being reflected, which will be in phase and amplified. The remaining wavelengths are transmitted through the grating. The reflection wavelength of the FBG is determined by the spacing between the individual grating planes, which are pre-set. The reflected component can be determined by the Bragg wavelength by [M. Majumder et al., 2008]:

$$\lambda_B = 2n_{eff} \Lambda \quad (1.1)$$

Where, λ_B = Bragg wavelength, n_{eff} = effective refractive index and Λ = grating period

When the load is applied to the structure, the grating is strained, which shifts the band of wavelengths at which the Bragg grating reflects. Strain can be quasi-static or dynamic (stress wave events caused by impact) [W. J. Staszewski et al., 2004]. Figure 15 shows the basics of FBG sensors.

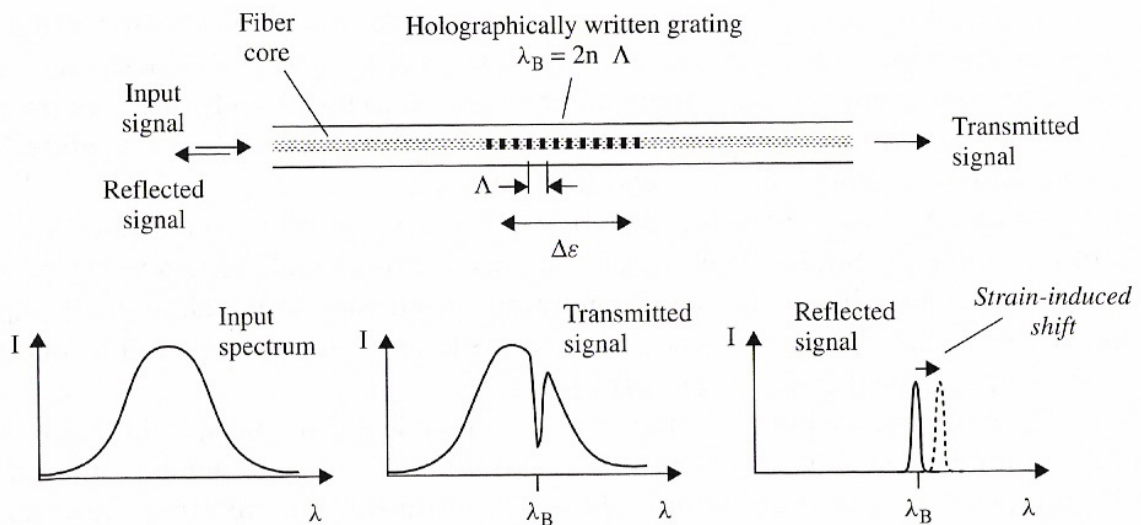


Figure 15: FBG sensing concept [W. J. Staszewski et al., 2004]

Interrogation units are required for reading the Bragg wavelength shift of the FBGs induced due to measured physical parameters like strain and temperature. The choice of the interrogation method depends on several factors such as type and range of parameter being measured, required accuracy and sensitivity, number of sensors, and overall cost [M. Majumder et al., 2008]. Some of the disadvantages associated with using the optical fibres are the inherent fragility, low survivability, and reliability in systems subjected to impact loads, limited angular changes in the fibre path, connection, installation and alignment, moisture degradation, and repairability. The major draw-back for using the optical fibres is the use expensive interrogation equipment.

1.1.3.2.3 Piezoelectric transducers

Piezoelectric materials display coupled mechanical and electrical properties. Piezoelectric material can generate charge when subjected to mechanical stress and conversely elongate or contract when subjected to an electric field. Piezoelectric materials are widely used in SHM due to their ability to simultaneously act as sensors and actuators. Their miniature size and weight are negligible compared to the host structures. Therefore, their integration into the structure creates very minimal change in the overall structural performance [G. Park et al., 2003]. There are several materials that exhibit the piezo-effect. However, Lead Zirconate Titanate (PZT) and Polyvinylidene Fluoride (PVDF) as shown in Figure 16 are most commonly used for SHM applications. PZT is a ceramic, which is brittle in nature but can perform equally well as actuator and sensor. PVDF is a polymer film, which is flexible, lightweight, and can be constructed in various shapes and sizes. It has been found that PVDF cannot perform as well as PZT when used as an actuator. Therefore, PVDF materials are mostly used for sensing applications [J. M. Park et

al., 2005]. Both PZT and PVDF sensors can be either surface mounted or embedded in the composite structures.



Figure 16: PZT and PVDF piezoelectric sensors [A. Raghavan, 2007]

The piezoelectric PZT and PVDF sensors are generally polarized (poled) through the thickness direction (3-direction), which is also the direction in which the voltage is applied or sensed. The poling is done by aligning the ferroelectrics domain by exposing the element to a strong direct current field at temperature slightly below the Curie point. When the applied electric field is removed, the dipoles are locked into the near aligned configuration. Application of tension or compression on the poled piezoelectric element changes the dipole moment, thus creating voltage and vice-versa as shown in Figure 17 [APC International, 2011]. Therefore, when used as an actuator, the applied high frequency voltage causes the element to lengthen and contract creating waves within the structure. When used as a sensor, the strain caused by the propagating wave over the sensor area induces voltage across the element [A. Raghavan, 2007].

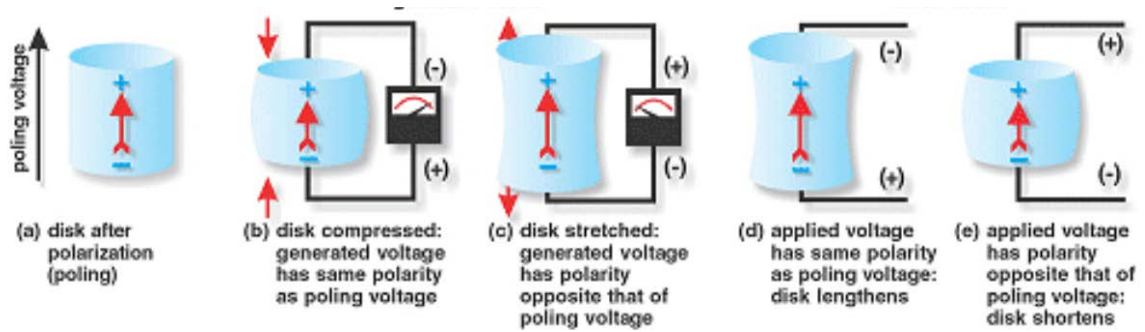


Figure 17: Reaction of piezoelectric element to the applied load/voltage [APC International, 2011]

1.1.3.2.4 *Micro-electro-mechanical systems*

Micro-Electro-Mechanical Systems (MEMS) or micro-machines integrate mechanical elements, sensors, actuators, and electronics typically onto silicon substrates as one package. Using MEMS, it is possible to incorporate micro-scale devices such as actuators and various types of sensors such as inertial, force, optical, piezoelectric, and magnetic that can be used for SHM applications [V. K. Goel et al., 2008]. It is also possible to integrate microelectronics, which can process the information gathered from the sensors and relay it wirelessly. Due to their miniature size MEMS can be either surface mounted or even embedded into composite structure [S. Beeby et al., 2004].

1.1.3.2.5 *Surface mountable crack sensor*

Surface Mountable Crack Sensor (SMCS) was developed at National Research Council Canada (NRC), in which a conductive paint is applied over the surface to be monitored with an insulating substrate to isolate the electrical sensing circuit from the base material. When the crack propagates through the conductive paint, the overall resistance changes and can be detected by an interrogator unit as a change in voltage as shown in Figure 18. If the circuit is broken, the

voltage signal on the SMCS will be zero corresponding to the complete propagation of crack through the sensing element [M. Martinez et al., 2012].

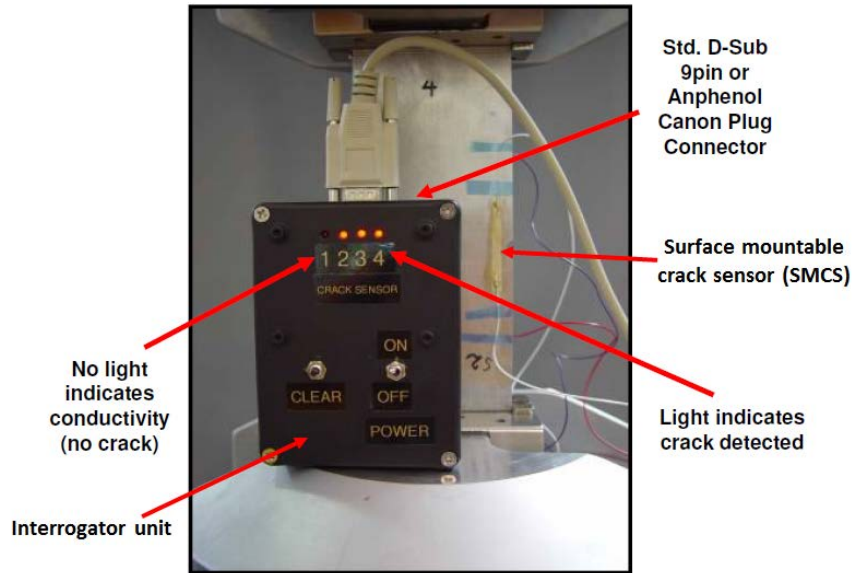


Figure 18: SMCS with an interrogator unit [M. Martinez et al., 2012]

1.1.3.2.6 Comparative vacuum monitoring sensor

Comparative Vacuum Monitoring (CVM) sensor is based on the principle that a small volume maintained at a low vacuum pressure is extremely sensitive to air ingress and leakage caused by formation of cracks. When the sensors are attached to the structure, the channels and the structure form a manifold alternately at low vacuum and atmospheric pressure as depicted in Figure 19 by (V) and (A) respectively. When vacuum is applied it remains stable if there are no cracks. Alternatively, when a crack develops, air will flow from the adjacent atmospheric channel through the crack into the vacuum channel producing a measurable change in the vacuum level (Figure 19). Therefore, the CVM can detect surface cracks only when they interact with the vacuum chamber [D. Roach, 2009].

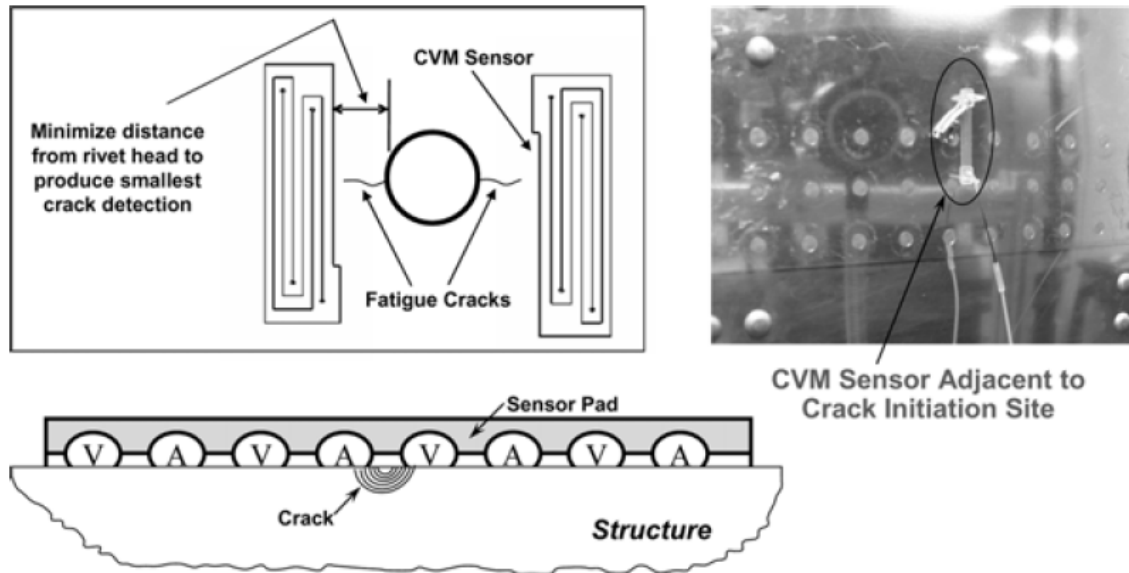


Figure 19: Schematic of CVM sensor [D. Roach, 2009]

1.1.3.3 Signal processing

Signal processing plays a crucial role in implementing and operating any damage identification and assessment system. Feasibility and effectiveness of any SHM system entirely rely on extracting essential features from acquired raw data through various sensors and translate the information by conducting a diagnosis or prognosis of damage location and severity. The most challenging part in signal processing is to extract from the raw data proper information that is sensitive to the damage and discard any environmental and operational noises [Z. Su et al., 2004]. A typical signal processing flow chart is shown in Figure 20.

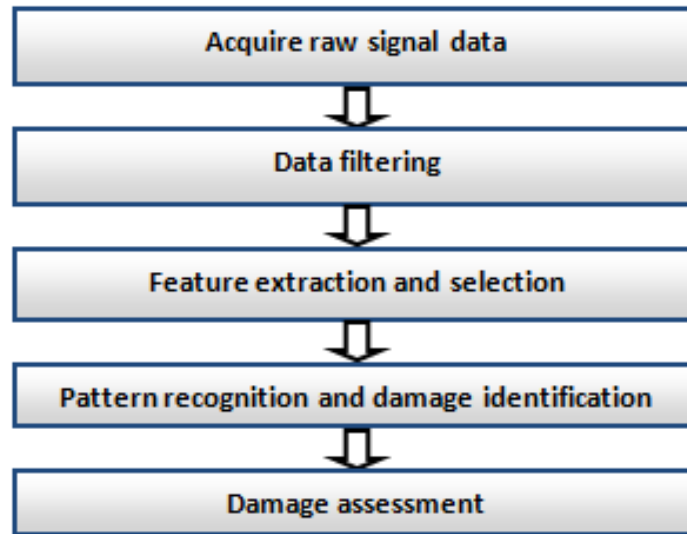


Figure 20: Signal processing flowchart

The first step of signal processing for damage detection is acquiring the raw signal data from various sensors that are usually deployed in arrays. The gathered raw data carry the required information regarding the structural damage plus noises due to environmental, electrical, and mechanical interference. So the second process is to filter out most of the unwanted features. This can be done by smoothing the signal by applying digital filters. The third process is to select the types of features to extract from the filtered data and choose the appropriate method for extraction. The types of features to extract depend on the chosen damage detection technique described in Section 1.1.3.1. Some of the most commonly used feature extraction techniques are done in *time-domain*, *frequency-domain*, *time-frequency-domain*, and *frequency-wavenumber-domain*.

In *time-domain*, the signal amplitude is plotted against elapsed time. Signal features such as peaks or zero-crossings are tracked between two sensors of known separation. Finding the time

it took for the signal to reach from one sensor to another, the time-of-flight of that signal can be determined. The approximate distance between the sensor and the damage can be found by multiplying the time-of-flight by the velocity of the wave. In *frequency-domain* analysis the *time-domain* signal is converted into *frequency-domain* using Fourier Transform (FT), which provides the information regarding the frequency of the waves that make up the signal and their corresponding strengths. Signal information can be easily converted from *time-domain* to *frequency-domain* and vice-versa using Fourier Transform and Inverse Fourier Transform (IFT) respectively. This method is used to find the frequency content of a signal but does not provide information regarding the position of that frequency, i.e. the spatial information of the wave is lost. Short-Time Fourier Transform (STFT) has been used to find the frequency and spatial information of a wave. This is done by windowing technique in which the signal is cut into small sections onto which the Fourier analysis is performed. In this way the frequency content of that small section can be found by preserving the spatial information. One drawback of STFT is that the time window is same for all frequencies, which results in trade-off between spatial resolution and frequency information [Y. Lingyu et al., 2005]. This deficiency can be overcome by using Wavelet Transform (WT), which uses the *time-frequency-domain* analysis. Wavelets are a family of orthogonal basic functions, which are not limited to sines and cosines as in the case of FT and STFT. WT decomposes a signal into a set of basic functions that are localized in both time and frequency. The basic function $\psi(t)$ is referred to as mother wavelet (Figure 21), which is scaled and shifted to produce the maximum number of wavelet coefficients within the full time span for time localization. The scaled and shifted versions of the mother wavelet are called daughter wavelets [M. M. Reda Taha et al., 2006]. Some of the mother wavelet functions are shown in Figure 21.

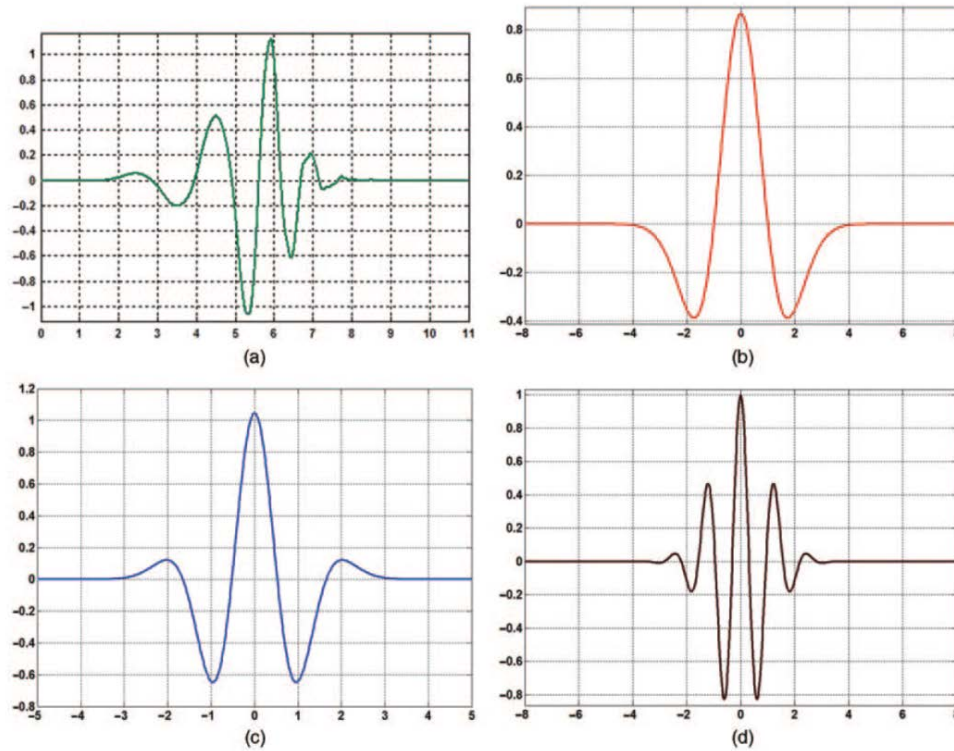


Figure 21: Mother wavelets $\psi(t)$: (a) Daubechies (db6), (b) Mexican hat, (c) Gaussian, and (d) Morlet [M. M. Reda Taha et al., 2006]

In the *frequency-wavenumber-domain*, the Fourier and the inverse Fourier transforms are extended to frequency-wavenumber spectrum, which can be interpreted as an alternative representation of the time-space wavefield. *Frequency-wavenumber-domain* has been used to extract components of higher Lamb wave modes present in a signal, which are generally not provided by *time-domain* and *frequency-domain* analysis. The time-space wavefield is shown in Figure 22 (c), which is transformed into the *frequency-wavenumber-domain* shown in Figure 22 (d) along with the theoretically predicted Lamb wave dispersion curves. It can be seen that the theoretically predicted Lamb modes matches well with the signal extracted in the *frequency-wavenumber-domain* shown in Figure 22 (d), where the higher Lamb wave modes are

identifiable [Z. Tian et al., 2014]. Similar analysis can also be performed in *space-wavenumber-domain*.

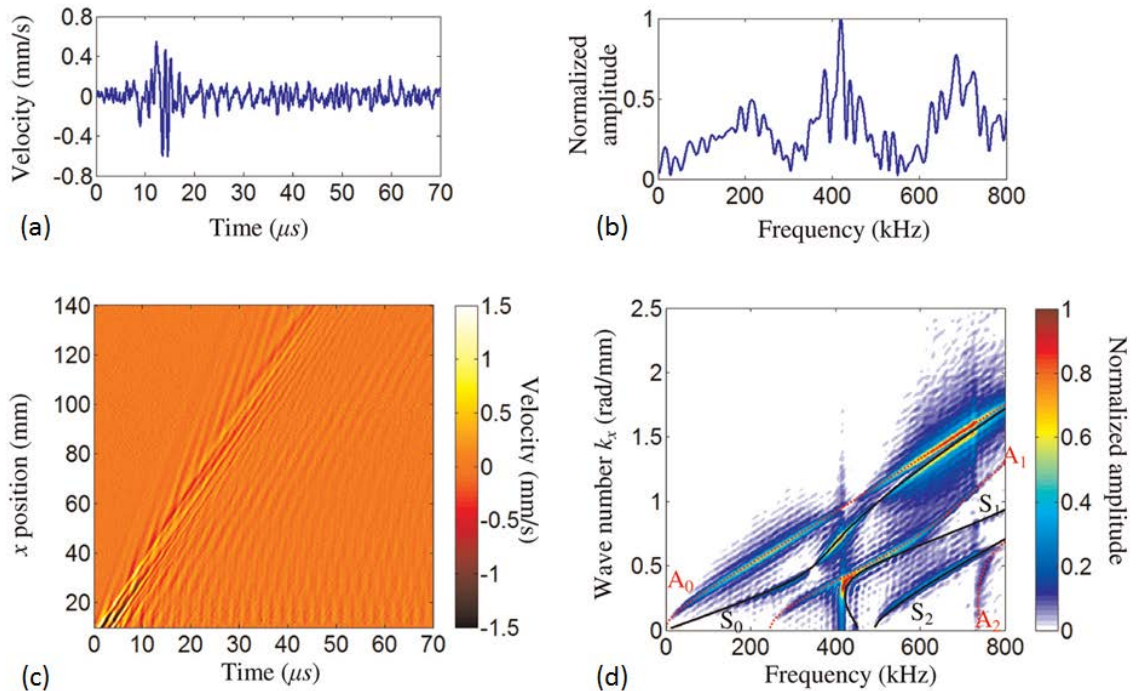


Figure 22: Lamb wave propagation in (a) time domain, (b) frequency-domain, (c) time-space domain, and (d) frequency-wavenumber domain [Z. Tian et al., 2014]

The extracted features are usually combined in patterns; therefore, the fourth process is the pattern recognition and damage identification in which diverse damage conditions are considered. This process is usually performed using software tools for which various methods and algorithms are available. Some of the most widely used software tools for pattern recognition and damage identification are shown in Figure 23. The final course of action is using the outcome information from the pattern recognition process to assess damage severity. The assessment results are then passed on to the operator for further analysis and decision-making regarding the structural health [W. J. Staszewski et al., 2004].

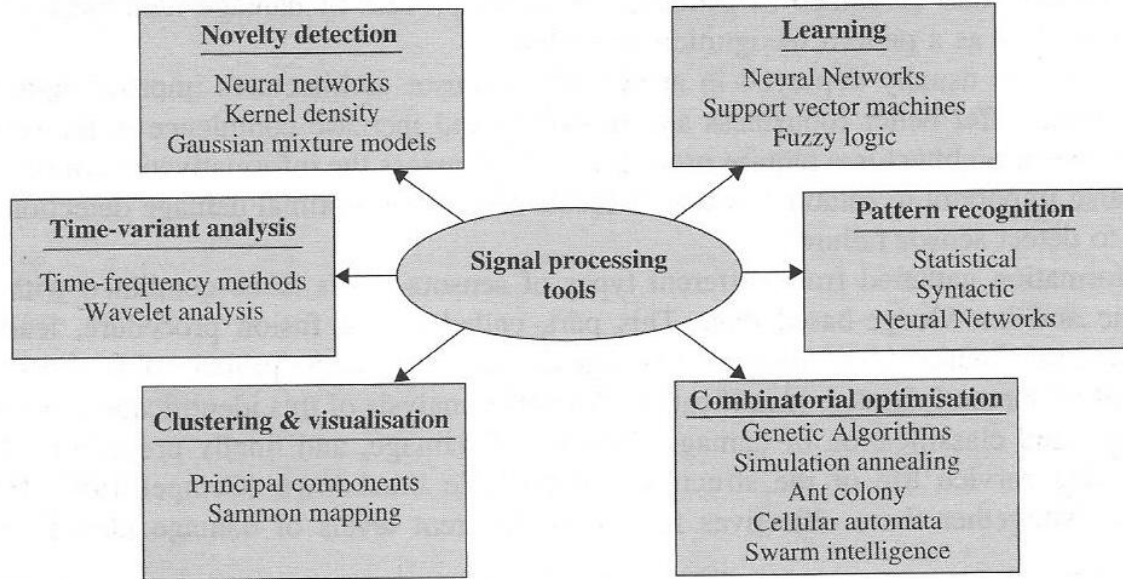


Figure 23: Commonly used signal processing tools [W. J. Staszewski et al., 2004]

It is to be noted that signal processing and damage detection algorithm are complex. Therefore, comprehensive study of various signal processing techniques and damage detection algorithms are beyond the scope of this thesis.

1.2 RESEARCH MOTIVATION, OBJECTIVE, AND SCOPE

As previously discussed, the use of composite materials in an aircraft structure has greatly increased over the last few decades. However, one of the major concerns over the use of composite is its susceptibility to hidden and impact damage, which can create delamination, fibre breakage, matrix cracking, among others described in Section 1.1.1. Such damages usually occur below the surface requiring expensive and lengthy Non-Destructive Evaluation (NDE) techniques discussed in Section 1.1.2. As reported earlier, the cost of NDE techniques can be as

high as 30% of the acquisition and operational costs. Over and above excessive time and cost, NDE methods have inherent limitations such as the ones described in [ASTM E2533-09, 2009] as:

- Visual and tap-testing are completely dependent on the inspector's ability to view, hear, and interpret the results, which may be prone to errors.
- Conventional ultrasonic method requires point by point inspection on a relatively flat and smooth surface.
- Radiography requires access to both sides and is prone to radiation hazards.
- Thermography may cause heat damage to the polymer matrix.
- Leak testing may have detrimental effect due to liquid ingress.
- Shearography requires sufficiently large defect to cause difference in surface strain.

The use of Structural Health Monitoring (SHM) on an aircraft has been envisioned to minimize cost and time associated with the current NDE techniques. An automated SHM system may also minimize human errors and there is always a potential of investment cost savings if the SHM system can detect damage in its early stage before a catastrophic failure. Currently as mandated by FAR 25.571, the civil aircraft regulation authorities require that the composite structures should be able to carry Ultimate Load (UL) in the presence of non-visible manufacturing defects and Barely Visible Impact Damage (BVID) under no detrimental damage growth philosophy. For visible damage such as disbanded stringer and facesheets, the structure should be able to sustain the Limit Load (LL) without failure until the damage is found and repaired, assuming one missed inspection (two routine inspection/maintenance interval requirements). For immediately visible damage such as one caused by rotating components, bird strikes, blown tires, in-flight hail, etc., in which case, the crew are aware of the damage and will attempt to land as soon as

possible/practical, the airframe must support the continued safe flight requirement of 70% LL without failure [A. J. Fawcett et al., 2006]. Structural health monitoring system that can provide early damage detection can potentially find a non-detectable damage making it detectable, thereby reducing the UL and LL requirements. This in-turn reduces the required strength to sustain the UL and LL; thus, saving weight and increasing the time between maintenance intervals. An automated SHM system may also minimize human errors and there is always a potential of investment cost savings if the SHM system can detect damage in its early stage before it grows to a critical size causing catastrophic failure [L. E. Mujica et al. 2008]. Once proven reliable, the SHM system can be used as a part of Condition-Based Maintenance (CBM) in which the aircraft is taken out of service only when damage is present and confirmed by a SHM system. A reliable SHM system can also be integrated in the next generation aircraft and can be incorporated from the design phase so that the design itself can be made less conservative, hence saving weight. The potential benefits of using SHM systems are tremendous; however, proving its reliability is a major issue and there is still no widely accepted definition of PoD levels for SHM as there is for NDE. Some of the SHM methods described in Section 1.1.3 have been actively investigated by both industry and academia.

This research is based on using guided Lamb waves, which is a part of an *active* approach acousto-ultrasonic SHM technique described in Section 1.1.3.1.1. Lamb waves are ultrasonic guided waves propagating in thin plate like structures bounded by two surfaces, such as aircraft skin. Unlike conventional ultrasonic NDE techniques (Section 1.1.2.3), which are based on point by point inspections, Lamb waves can travel long distances through-thickness even in composite with high attenuation. So using Lamb waves, significant portion of a structure can be evaluated

by measuring the wave characteristic such as velocity and amplitude. Lamb waves have been widely explored for SHM applications, particularly when related to smart structures with permanently embedded or bonded sensors. The high number of proposed experiments and demonstrated SHM applications using Lamb waves are related to the advancement in electronics and computational capabilities enabling the generation, acquisition, and processing of Lamb waves even at high frequencies in MHz range. However, for the proper application of Lamb waves as a part of a SHM system, the understanding of the underlying physics behind the Lamb waves and their complex multi-mode propagation characteristics within the host material is essential for sensor sizing, optimizing sensor placement, selecting proper Lamb wave modes, and excitation frequency.

Lamb waves are dispersive, i.e. the propagation velocity is dependent on excitation frequency and can travel independently in two distinct symmetric and anti-symmetric modes. The propagation characteristic is provided in dispersion curves, which are plots of phase/group velocity vs. frequency-thickness product. Dispersion curves are generated numerically by solving the Lamb wave equations. Lamb wave equations for isotropic material are well established; such is not the case for composites. In composites, the wave velocity depends on the propagation angle and lay-up. Therefore, it is necessary to take into account the anisotropy caused by rotating the lamina during stacking and the propagation of wave in any arbitrary direction. The goal of this research was to obtain an in depth understanding of the physics behind Lamb wave propagation in composite structures. For this purpose, the Lamb wave equations for an n-layered composite laminate were derived analytically by taking into account the material anisotropy and waves travelling in all three axes. The analytical equations were solved

numerically to generate the dispersion curves. The numerically generated dispersion curves were tested against the experimental results for verification purposes. Lamb waves were selected over other *passive* approaches described in Section 1.1.3.1, such as Acoustic Emission (AE), vibration, and strain-based due to their on-demand interrogation capabilities. As mentioned earlier, in a *passive* approach the structure has to be monitored continuously and in real-time to detect damage evolution/growth, which requires carrying all the associated hardware on board the aircraft, thus increasing complexity and weight. Whereas, in an *active* Lamb waves based SHM approach, the interrogation can be done on-demand when the aircraft is on the ground relieving the burden of carrying the associated hardware during flight. On top of providing an on-demand interrogation, Lamb wave was chosen also because of the readily available equipment at Carleton University and National Research Council Canada (NRC) for experimental verification because of their low-cost. For experimental verification, Lamb waves were generated using piezoelectric transducers described in Section 1.1.3.2.3, which were used interchangeably as actuators and sensors. Using the experimentally verified analytical solution, the effects of Lamb waves propagation due to change in stiffness constants were also studied for different laminate types for selecting proper Lamb wave modes.

Lastly, the research also addressed ways to measure the material properties using non-destructive ultrasonic technique with access to only one side of the specimen. This part of the research was conducted because of the major challenge encountered for generating the Lamb wave dispersion curves when material properties are not known in advance. In the case of composites, oftentimes this information is not readily available in the literature. Measuring the material properties can be expensive and may be destructive using the conventional mechanical

testing such as tensile and shear. Therefore, the final objective of this research was to measure the material properties of an isotropic metallic and transversely isotropic composite using non-destructive *in-situ* technique based on ultrasonic wave velocity.

The scope of this research was not to develop a Lamb wave based SHM system, optimize sensor selection/placement, study interaction between sensor and host structure, improve signal processing/damage detection technique, and to experimentally detect and localize damage. The objective was to aid in improving the understanding of Lamb wave propagation in composite laminates to be used as a part of a SHM system. Outcome of this research can be used to measure stiffness properties, which are inputs for accurately generating the Lamb wave dispersion curves. Dispersion curves can be used to study the effects on the propagation characteristic of Lamb waves due to presence of defect/damage. Accurate dispersion curves are also needed for selecting proper Lamb wave modes, their corresponding excitation frequency, which in turn govern piezoelectric transducer sizing and associated hardware to generate/receive Lamb waves for damage detection.

1.3 CONTRIBUTIONS TO SCIENCE AND TECHNOLOGY

Following are the contributions made through this research to the enhancement of SHM research based on Lamb wave acousto-ultrasonic techniques and material characterization using ultrasonic waves:

1. Derived and experimentally verified Lamb wave equations for an n-layered monoclinic composite laminates based on linear 3D elasticity by considering displacement fields in all three co-ordinates, which takes into account the interaction of waves travelling in all three directions.
 - i. First, the equation was presented for a single-layered monoclinic composite lamina and was compared with the commonly used classical laminate plate theory. This part of the research was presented and published in the proceedings of the 19th International Conference on Composites Materials:
 - S. Pant, J. Laliberté, M. Martinez (2013), Structural health monitoring (SHM) of composite aerospace structures using Lamb waves, The 19th International Conference on Composite Materials, Montreal.
 - ii. The equation for a single-layered monoclinic lamina was then generalized and assembled using a Global Matrix approach for an n-layered laminate. A robust method was proposed for assembling and numerically solving the Lamb wave equations for an n-layered composite laminate. The numerical solution was verified on two different composite laminates to prove its prediction and robustness. This part of the research was accepted for publication in the Journal of Composites Structures:
 - S. Pant, J. Laliberté, M. Martinez, B. Rocha (2014), Derivation and experimental validation of Lamb wave equations for an n-layered anisotropic composite laminate, Composite Structures, 111:566-579.

2. The effect on the Lamb wave propagation/dispersion due to changes in the material properties such as E_{11} , E_{22} , G_{12} , and density were analyzed for unidirectional, cross-ply, and quasi-isotropic laminates. The analysis was performed by using the derived equations and proposed numerical methods to generate the Lamb wave phase velocity dispersion and slowness curves for each laminate. This was done by reducing E_{11} , E_{22} , G_{12} , and density with the intent of representing defects and variability during manufacturing and in service. This part of the research was submitted for consideration to the Journal of Intelligent Material Systems and Structures:

- S. Pant, J. Laliberté, M. Martinez, B. Rocha, D. Ancrum (Submitted March 2014), Effects of composite lamina properties on Lamb wave dispersion characteristics, Journal of Intelligent Material Systems and Structures, In-Review.

3. A one-sided *in-situ* method for determining the material constants was investigated based on the ultrasonic wave propagation within the material. First the analytical equations were derived for isotropic metallic and transversely isotropic composite laminates. Then, an inverse method based on the non-linear least square technique was used to calculate the stiffness constants from the ultrasonic wave velocities. Sensitivity analysis was performed by randomly perturbing the velocity data and observing its effect on the calculated stiffness constants. An improved algorithm was proposed and tested to reduce the effect of these random errors. The method was experimentally verified to find the material constant for isotropic aluminum and transversely-isotropic unidirectional composite laminate. This part of the research was submitted for consideration to the Journal of Ultrasonic:

- S. Pant, J. Laliberté, M. Martinez, B. Rocha, (Submitted May 2014), Characterizing isotropic and transversely isotropic material properties using ultrasonic wave velocities, Journal of Ultrasonic, In-Review.

4. The method discussed in (3) was further analyzed to find the material properties of an orthotropic laminate. The analytical equations derived for a transversely isotropic laminates were expanded to account for orthotropic symmetry by considering the wave propagation in a non-principal axis. Only the analytical expressions were derived in this part of the work.

The information provided in this research can be put to practice in multiple ways as a part of a Lamb wave based SHM system. First the method described to measure the material properties can be used to find the stiffness constants of an existing structure with access to only one-side. The information can then be used to analytically solve the Lamb wave equations and select the proper mode (symmetric or anti-symmetric) based on the critical damage type to be detected. Once the proper mode is selected, the excitation frequency range can be determined to minimize dispersion. Knowing the excitation range, the piezoelectric transducers can be tuned for that particular frequency range for optimal generation and gathering of Lamb waves. Also the selected Lamb wave mode and frequency range in turns dictates the requirements for the Lamb wave signal generation and processing unit.

1.4 THESIS OVERVIEW

Chapter 2 presents a brief description of ultrasonic bulk (longitudinal and transverse) waves and guided (Rayleigh and Lamb) waves followed by a detail theoretical aspect of Lamb wave propagation. First, previous research performed on the Lamb wave from Horace Lamb, who discovered the wave back in 1917 to more recent ones are presented with the emphasis on the propagation characteristic of Lamb wave in composite material. A step by step derivation of Lamb wave for monoclinic and higher symmetry material is presented followed by a robust numerical method to solve the derived equations in order to generate the Lamb wave dispersion curves. The numerically generated dispersion curve is verified experimentally for two different composite laminates.

In Chapter 3, the effect on the Lamb wave propagation/dispersion due to changes in the material properties are analyzed for three different composite laminate types typically used in aerospace applications. The analysis is performed by obtaining the characteristic Lamb wave phase velocity dispersion and slowness curves for each laminate types by reducing E_{11} , E_{22} , G_{12} , and density with the intent of representing defects. Since Lamb waves' velocity in composite laminate varies with the propagation direction, the laminates are analyzed at 0° , 20° , 45° , 70° , and 90° propagation angles. A program developed in MATLAB is used to generate the analytically derived dispersion curves for the fundamental anti-symmetric and symmetric Lamb wave modes.

In Chapter 4, a one-sided *in-situ* method based on the ultrasonic wave time-of-flight measurement is explored for isotropic and transversely isotropic material. The method consists of generating and receiving quasi-longitudinal and quasi-transverse waves at different propagation angles using angled wedges. An improved inverse method based on the non-linear least square technique is presented and validated using sensitivity analysis. The sensitivity analysis is performed by randomly perturbing the velocity data and observing its effect on the calculated stiffness constants. The method is then experimentally verified on isotropic and transversely isotropic samples.

Finally, Chapter 5 summarizes the results of this research and Chapter 6 provides recommendations for future work that can be carried out from the information provided in this dissertation.

CHAPTER 2: ULTRASONIC WAVES

Ultrasonic waves are defined as acoustic waves having frequencies greater than 20 kHz, which is the limit of human hearing. Bulk waves and guided waves are two types of ultrasonic waves commonly used for NDE/SHM applications. In this chapter a brief description of bulk waves is provided with emphasis on the guided Lamb waves. A full derivation of Lamb wave equations for n-layered monoclinic composite laminates based on linear 3D elasticity is presented and verified experimentally. A robust method for numerically solving the Lamb wave equations is also presented.

2.1 BULK WAVES

Bulk or fundamental waves propagate inside an object and are independent of structural shapes and boundaries. Bulk waves travel with constant speed regardless of frequency and hence are considered to be non-dispersive. In general, two types of bulk waves exist, which are: longitudinal pressure waves (P -waves) and shear waves (S -waves). The direction of particle motion in the longitudinal waves and shear waves is along the wave propagation direction and perpendicular to it respectively as shown in Figure 24 [I. Ihara, 2008].

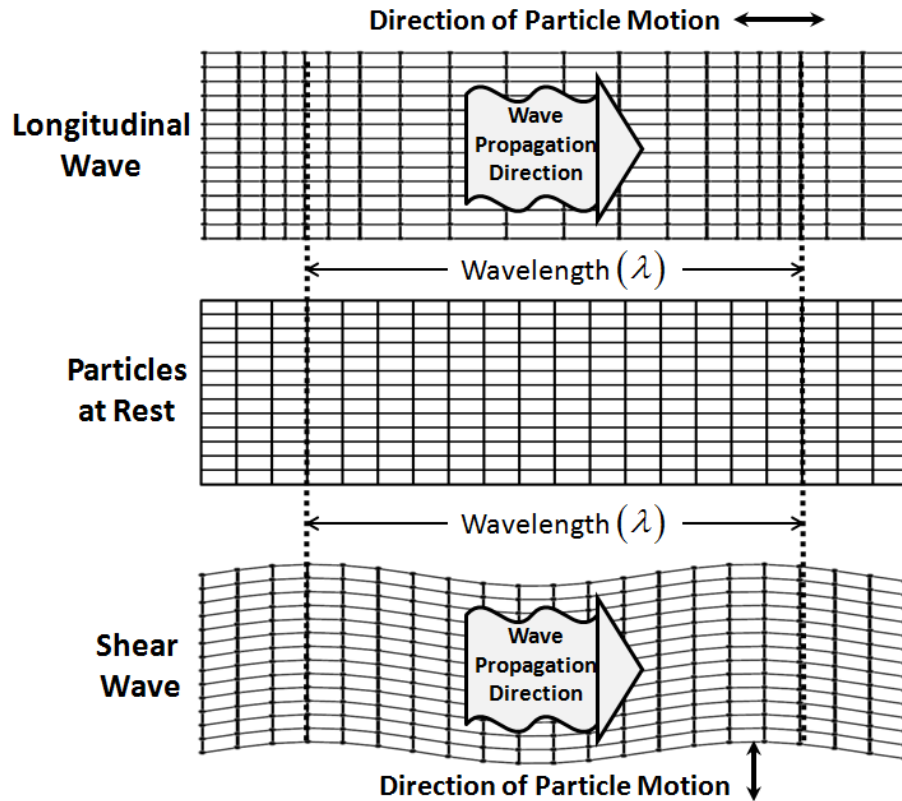


Figure 24: Through-thickness propagation of longitudinal and shear waves

Ultrasonic bulk waves can travel long distances in solid media with a decrease in energy over distance. Propagating waves are scattered, reflected, or absorbed when travelling through different material boundaries (e.g. changes in density, crystal orientation, bonded interfaces, etc.), which changes the waves' amplitude and velocity. Damage can be detected using the information regarding wave attenuation, velocity, reflection, and refraction [J. D. N. Cheeke, 2002]. Bulk waves are primarily used for NDE applications as described in Section 1.1.2.3 and their behaviours are well documented in the literature [J. D. N. Cheeke, 2002].

2.2 GUIDED WAVES

Guided waves are propagating wave packets which are the results of the superposition of longitudinal and shear modes. Unlike bulk waves, guided waves require a boundary for propagation. Guided waves have infinite number of modes for propagation and are highly sensitive to defects. Rayleigh and Lamb waves are the most commonly used guided waves for SHM applications [W. J. Staszewski et al., 2004], which are described in the following sections.

2.2.1 RAYLEIGH WAVES

Rayleigh waves are surface waves created due to elastic perturbations propagating near the free boundary of a solid. Figure 25 shows the pattern of displacement of Rayleigh waves. In Rayleigh waves, the longitudinal and shear wave motions are coupled together and travel at a common velocity [I. A. Viktorov, 1967]. The displacements are restrained between one to two Rayleigh wavelengths of the surface. The mechanism of propagation is complex as the trajectories of the surface particles displacements are ellipses (Figure 25). Rayleigh waves can couple with a medium surrounding the surface of the body both liquid and air which affects the amplitude and velocity of the wave. The wave amplitude decreases rapidly with depth and the rate of decrease depends on the wavelength. When defects are present on the surface over which Rayleigh waves are propagating, the waves get scattered, as are longitudinal and transverse (shear) waves propagating into the depth of the medium. Thus, Rayleigh waves are mostly used to detect surface defects [W. J. Staszewski et al., 2004].

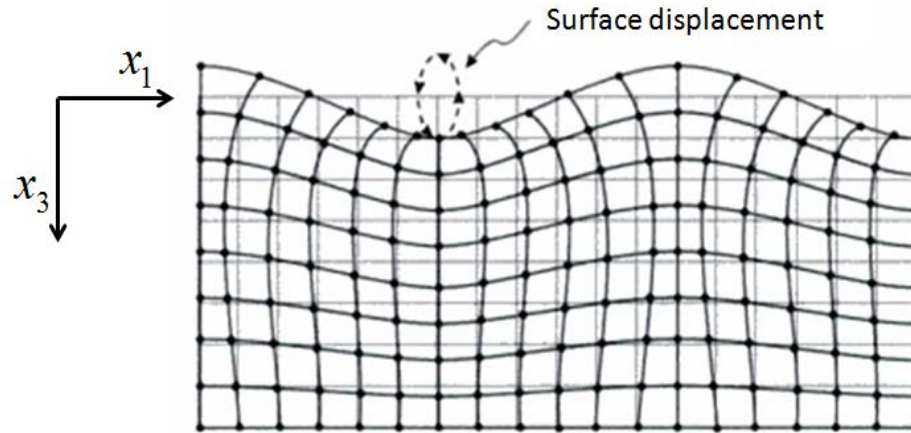


Figure 25: Surface displacement pattern in Rayleigh wave [J. D. N. Cheeke, 2002]

2.2.2 LAMB WAVES

Lamb waves are elastic perturbations propagating in a thin solid plate with free boundaries, for which the displacement occur both in the direction of the wave propagation and perpendicular to it [I. A. Viktorov, 1967]. Lamb waves are superposition of longitudinal waves (P -waves) and shear waves (S -waves). Lamb waves can exist simultaneously in two independently propagating symmetric (S_n) and anti-symmetric (A_n) modes. For a finite plate thickness at acoustic frequency (f), there exist a number of such symmetric and anti-symmetric Lamb wave modes. These modes differ from one another by their phase and group velocities as well as their distribution of the displacements and stresses through the thickness of the plate [W. J. Staszewski et al., 2004]. The propagation characteristics of the waves are given in the form of dispersion curves, illustrating the change in plate-mode phase and group velocities as a function of frequency-thickness product as shown in Figure 26.

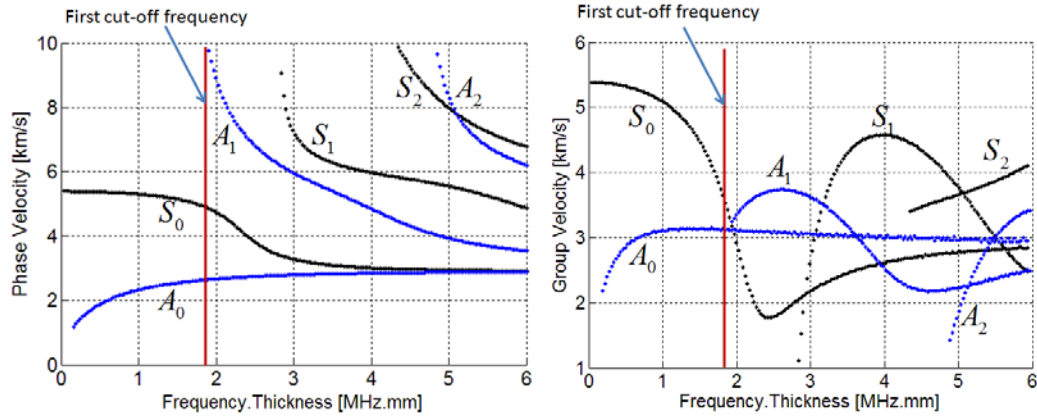


Figure 26: Lamb wave dispersion curve for 2024-T6 aluminum plate

As shown in Figure 26, Lamb waves can exist simultaneously in two modes - symmetric (S_n) and anti-symmetric (A_n) modes for which the particle displacements are shown in Figure 28. The subscript (n) is an integer indicating the order of the mode or the number of inflexion points found in the wave deformation field across the thickness. In Figure 26, S_0 and A_0 represents the fundamental symmetric and anti-symmetric Lamb modes, which are the ones commonly used for damage detection. This is because higher modes represented by $S_{1,2,3\dots}$ and $A_{1,2,3\dots}$ in Figure 26 are present only at higher frequency-thickness products and are very dispersive as shown in Figure 27 i.e, the propagation velocity depends on the excitation frequency.

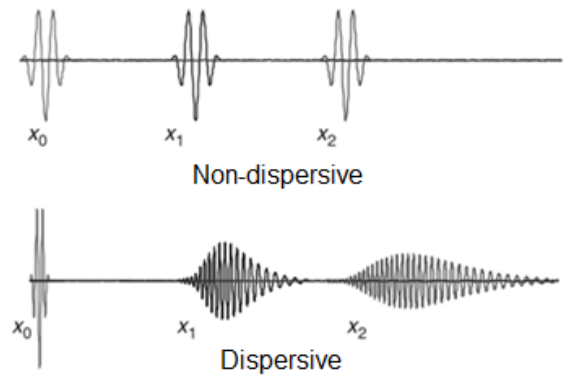


Figure 27: Comparison of non-dispersive and dispersive wave [V. Giurgiutiu, 2008]

As shown in Figure 26 Lamb wave's mode cut-off occurs at specific frequency-thickness products for higher modes. At these points the phase velocity approaches infinity as the group velocity tends to zero. The excitation of the higher-order modes complicates the signal analysis as more than one mode will be present at any given frequency-thickness product. Therefore, the frequency-thickness product below the first cut-off point is commonly used for damage detection application. It can be noted from Figure 26, that at very high frequency-thickness products all the Lamb wave modes are converging to a single velocity (Rayleigh wave velocity). This is because at very high frequencies the wavelength becomes so small that the propagation of the wave is restricted to only the top and bottom most surfaces, thus behaving as a Rayleigh wave. This behaviour is predicted by the relevant Lamb wave characteristic equations and is represented by the dispersion curves, i.e., propagation velocity versus frequency-thickness product curves such as one provided in Figure 26. The dispersive behaviour and the characterization of the displacement fields of the different waves and modes are essential for the selection of the proper excitation frequency, sensors, sensor dimensions/types, associated sensor systems, signal generation/acquisition, and data processing [B. Rocha et al., 2010].

The propagation of Lamb waves in composite material is even more complex due to anisotropy. Parameters of composite materials such as fibre volume fractions, layup, type of matrix and reinforcements strongly influence the velocity of propagating waves as discussed later in Chapter 3. Waves in composite plates propagate in each direction with different velocities; also, the shape of the wave front changes with the frequency [Z. Su et al., 2006]. Waves tend to travel at higher velocities in composites with higher fibre volume fraction because of the higher

stiffness along the fibre direction. The phase/group velocity also depends on the orientation angle of the reinforcing fibres [I P. Kudela et al., 2008].

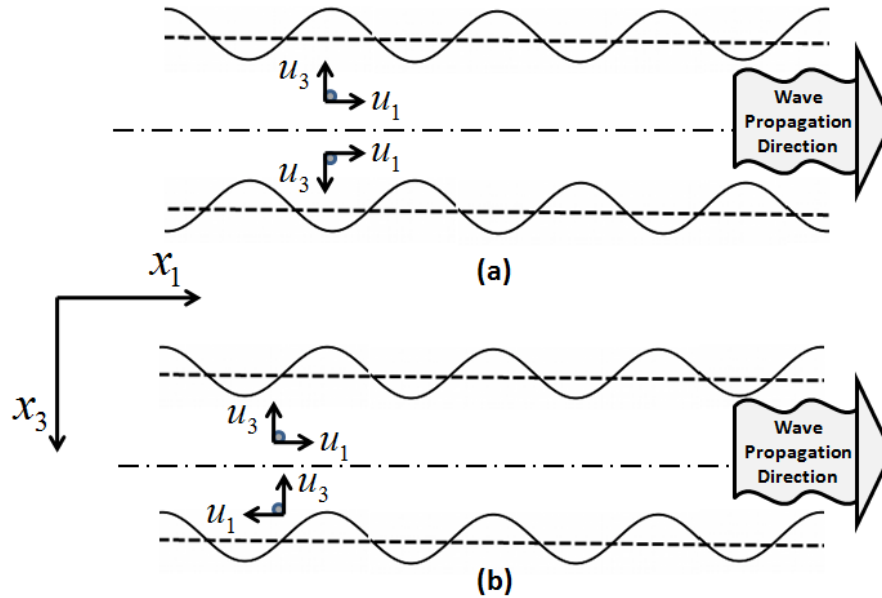


Figure 28: Propagation of Lamb wave modes (a) symmetrical and (b) anti-symmetrical

For practical applications input signals that excite the fundamental anti-symmetric (A_o) and symmetric (S_o) Lamb waves are usually considered. Damage can be detected by analyzing the difference between the phase/group velocity and the loss of amplitude of Lamb waves on damaged versus un-damaged specimens. The Lamb wave's phase and group velocity is directly related to structural stiffness, so as a wave travelling across an area of reduced stiffness slows down. Another phenomenon associated with damage is that upon reaching a region of dissimilar boundaries, a portion of the wave is reflected proportionally to the difference in their stiffness and density (impedance). From these two pieces of information, good correlation with damage location and magnitude can be determined [S. S. Kessler et al., 2002b].

For the design of an SHM system based on Lamb waves, the understanding of the underlying physics behind the Lamb waves and their multi-mode propagation characteristics within the host material is essential and is provided in the following sections.

2.2.3 PREVIOUS RESEARCH ON LAMB WAVES IN COMPOSITE LAMINATES

The existence of Lamb waves was originally proven mathematically by Horace Lamb [H. Lamb, 1917] based upon the Rayleigh wave equations developed by Lord Rayleigh [J. W. S. Rayleigh, 1885]. The difference between Rayleigh and Lamb waves as mentioned earlier are the boundary conditions affecting their propagation characteristic. Rayleigh waves propagate in a medium with one nearby free surface boundary; whereas the propagation of Lamb waves is guided by two nearby parallel free surfaces.

Propagation characteristics of Lamb waves for isotropic materials are well defined in the literature from Mindlin [R. D. Mindlin, 1960a], Viktorov [I. A. Viktorov, 1967] to Rose [J. L. Rose, 1999]; however, this is not the case for composite materials. Most of the theoretical analysis development enabling the precise application of Lamb waves has been performed mainly for isotropic materials, or for anisotropic materials with orthotropic and higher levels of symmetry. The simplest method to generate the Lamb wave dispersion curves as compared with other methods is by using the effective stiffness approach, in which the geometrically weighted average of the constituent properties are used as the average material constants for the entire laminate [C. T. Sun, 1968]. Another simpler method is by using the first order Classical Laminated Plate Theory (CLPT) based on linear strain distribution through the thickness and

neglecting transverse shear; however, the first order CLPT fails to accurately predict Lamb wave dispersion characteristics at higher frequencies. Therefore, the CLPT has been preceded by higher-order plate theories [L. Wang et al., 2007a] in which the through-thickness deformation is assumed to be a quadratic or higher functions of the through-thickness direction and taking into account the transverse shear deformation as suggested by Whitney [J. M. Whitney et al., 1973] to better predict the dispersion characteristics. Despite being computationally efficient, CLPT and higher-order theories are only approximations and fail to accurately predict the Lamb wave modes at higher frequencies [L. Wang et al., 2007a]. Datta [S. K. Datta et al., 1988] provided another approximation method for a multi-layered transversely isotropic material based on the stiffness method presented by Shah [A. H. Shah et al., 1982] in which the displacement distribution through the thickness was approximated by polynomial interpolation functions and showed that the method agreed with the exact solution for an isotropic and transversely isotropic plate. An additional hybrid method includes the use of Semi-Analytical Finite Element (SAFE), which uses the Finite Element Method (FEM) to discretize the cross-section and describes the displacement along the wave propagation direction with the use of analytical simple harmonic functions [M. Calomfirescu, 2008]. To date the exact method for characterising Lamb waves' propagation in composites is by using linear 3D elasticity and partial wave technique in which the principle of superposition of upward and downward travelling plane waves are assumed in order to satisfy the associated boundary conditions. Some of the notable researches regarding the Lamb wave dispersion relationship are described in the following paragraphs.

Solie [L. P. Solie et al., 1973] used the partial wave technique for a single-layered cubic symmetry material using Mindlin boundary conditions ($\sigma_{xz} = u_z = 0$ or $\sigma_{zz} = u_x = 0$) [R. D. Mindlin, 1960b] to obtain the decoupled flexural/shear-vertical (SV), dilatational/longitudinal (P) and shear-horizontal (SH) modes dispersion curves and showed that the SH mode decouples from the P and SV modes when the wave is not propagating along the planes of symmetry. Chimenti [D. E. Chimenti et al., 1985] presented the method for calculating leaky (immersed in fluid) Lamb waves propagating along the principal direction for a unidirectional composite laminate with transversely isotropic symmetry using a two-step process based on alternating layered media (modelling fibre and matrix as separate media) and effective stiffness (approximating overall through-thickness properties as a weighted sum of fibre and matrix layers). The method was experimentally verified for the Lamb wave travelling along the fibre direction by observing the change in magnitude of the plane-wave reflection from a composite plate immersed in a fluid by varying the incident angle and the excitation frequency. Tang [B. Tang et al., 1989] obtained the dispersion behavior for the (S_o) and (A_o) waves for composite laminates based on the approximate shear deformation theory for unidirectional, symmetric cross-ply, and symmetric quasi-isotropic laminate and found a good correlation between the approximate theory and the experimental data for low frequency, long wavelength region. Dayal [V. Dayal et al., 1989] provided the leaky Lamb wave equations for symmetric and anti-symmetric modes for a single-layered monoclinic symmetry using effective stiffness and the partial wave technique. The equations were experimentally verified on an isotropic and a balanced symmetric laminate, where excellent agreement was observed between the theory and the experimental results for the isotropic material but only satisfactory agreement for the composite laminate. Nayfeh [A. H. Nayfeh, 1989] provided analytical equations for the

symmetric and anti-symmetric Lamb waves propagating in the principal planes (decoupling the shear-horizontal mode) in a single-layered monoclinic plate and later Nayfeh [A. H. Nayfeh, 1991] extended this derivation to incorporate a solution to an n-layered lamina with monoclinic and orthotropic symmetry, based on the Transfer Matrix (TM) approach introduced by Thompson [W. T. Thompson, 1950], which relates the displacements and stresses at top and bottom of each individual layers, to form a transfer matrix for the entire laminate.

Li [Y. Li et al., 1990] developed a set of analytical dispersion equations for a single-layered monoclinic and orthotropic stress-free laminate using partial wave technique and provided numerical examples to illustrate the difference between isotropic and orthotropic dispersion behaviour. Liu [G. R. Liu et al., 1990] investigated the dispersion behaviour of the fundamental Lamb wave modes propagating in an arbitrary direction on transversely isotropic laminates based on 3D linear elasticity theory and Transfer Matrix approach. Liu also calculated the through-thickness strain energy distribution for Lamb wave modes on a unidirectional and hybrid (carbon/epoxy and glass/epoxy) using the real part of the stress and strain. Potel [C. Potel et al., 1993] presented the leaky quasi-longitudinal and quasi-transverse wave equations for a multi-layered monoclinic symmetric media based on the slowness vector and Transfer Matrix approach. Potel also suggested the method to generate Lamb wave solution with a vacuum boundary condition for the wave propagation in the axis of symmetry decoupling the shear-horizontal mode. Lowe [M. J. S. Lowe, 1995] presented the coupling between the longitudinal and shear waves giving rise to the plate wave for an n-layered orthotropic laminate based on both the Transfer Matrix and Global Matrix originally presented by Knopoff [L. Knopoff, 1964] in which all of the equations from each layer are assembled to form a global

matrix that describes the displacement and stress fields associated with the wave propagation in the entire laminate. Lowe also presented methods to numerically generate the Lamb wave dispersion curve.

Xi [Z. C. Xi et al., 2001] investigated the dispersion characteristic of Lamb waves for monoclinic symmetry using a through-thickness quadratic interpolation shape function and presented slowness curves for composite laminates. Xi also suggested for discretizing the through-thickness element, the element should be smaller than one-quarter and one-eighth of the wavelength when quadratic and linear shape functions respectively are used. Neau [G. Neau, 2003] studied the dispersion relationship in an orthotropic single-layered laminate based on 3D linear elasticity using partial wave technique and slowness vector. Neau used Newton-Raphson method to numerically generate the slowness and dispersion curves and extended the purely elastic case to study attenuation behaviour of A_o and S_o Lamb modes due to viscoelastic effect on a unidirectional composite laminate. Lowe [M. J. S. Lowe et al., 2004] developed a computer program named DISPERSE, which can generate the Lamb wave dispersion curve in an n-layered orthotropic laminate using the Global Matrix approach for both vacuum and liquid interface. Wang [L. Wang et al., 2007] provided the Lamb wave dispersion solution for infinite wave modes for symmetric laminates based on group velocity by assuming the displacement as function of the thickness direction for monoclinic symmetry using 3-D linear elasticity and Transfer Matrix approach. Wang separated the symmetric and anti-symmetric Lamb modes by considering only upper or lower half of the symmetric laminate and by imposing a stress and displacement condition at the mid-plane for symmetric mode as $(u_z = \sigma_{yz} = \sigma_{xz} = 0)$ and or anti-symmetric

mode as $(u_x = u_y = \sigma_{zz} = 0)$. Verma [K. L. Verma, 2008] presented the Lamb wave dispersion relation in a single-layered monoclinic plate for the wave propagating in the off-principal axes based on 3D linear elasticity.

The previous research described above shows that most work regarding the analytical derivation to characterize the propagation and dispersion of Lamb waves has been done for orthotropic and higher symmetry for an n-layered composite laminate. The prior research also involved several simplifications and approximations (characterizing the wave propagation only in specific directions, considering symmetric laminates and others mentioned previously). Adopting an orthotropic hypothesis may not be accurate if the actuators and sensors in an orthotropic or transversely isotropic laminate are installed in a non-principal direction. This gives rise to the lower monoclinic symmetry for which the solution is provided mostly for a single layer. Therefore, this thesis presents a full derivation of Lamb wave equations for n-layered monoclinic composite laminates based on linear 3D elasticity. The solution considers the effective coupling between the Lamb waves and the horizontal shear waves by considering the displacement fields along all three directions. The method uses the partial wave technique in combination with the Global Matrix approach to numerically solve the Lamb wave equations. A robust step-by-step solution to generate the Lamb wave dispersion curves is presented and subsequently verified experimentally.

2.2.4 DERIVATION OF LAMB WAVE EQUATIONS

Lamb wave equation for an isotropic medium is solved by Helmholtz decomposition in which a three dimensional displacement vector is decomposed into a sum of curl-free and divergence-free vector fields. This decomposition produces two simpler equations, one for the longitudinal wave using curl-free decomposition and another for the transverse wave using divergence-free conditions. The combination of longitudinal and transverse waves give rise to two distinct waves the symmetric and the anti-symmetric Lamb waves for which the characteristic equations are provided as:

Symmetric Lamb wave

$$\frac{\tan(qh)}{\tan(ph)} = \frac{-4k^2 pq}{(q^2 - k^2)^2} \quad (2.1)$$

Anti-symmetric Lamb wave

$$\frac{\tan(qh)}{\tan(ph)} = \frac{-(q^2 - k^2)^2}{4k^2 pq} \quad (2.2)$$

Where, $p^2 = \left(\frac{\omega^2}{c_L^2} - k^2 \right)$, $q^2 = \left(\frac{\omega^2}{c_T^2} - k^2 \right)$, k = wavenumber, ω = circular frequency, h = plate half-thickness, c_L and c_T are longitudinal and transverse wave velocities respectively

However, in an anisotropic medium such as a laminated composite, the application of Helmholtz decomposition does not help in simplifying the Lamb wave equations. The most general method

for solving the propagation of Lamb waves in an anisotropic media is by using the partial wave technique. In this technique, the principle of superposition of three upward and three downward travelling plane waves is assumed to satisfy the associated boundary conditions. The bounded upper and lower surfaces reflect the waves and the combination of these reflections going towards the upper or lower interfaces results in the propagating guided waves (Figure 29). Six waves consist of two quasi-longitudinal ($L+/-$), two quasi-transverse vertical ($SV+/-$), and two quasi-transverse horizontal ($SH+/-$) waves, which are present in a single layer (Figure 29). Positive and negative sign denotes that the wave is travelling down or up respectively as shown in Figure 29. The combination of all six waves defines a single guided wave mode [J. L. Rose, 1999].

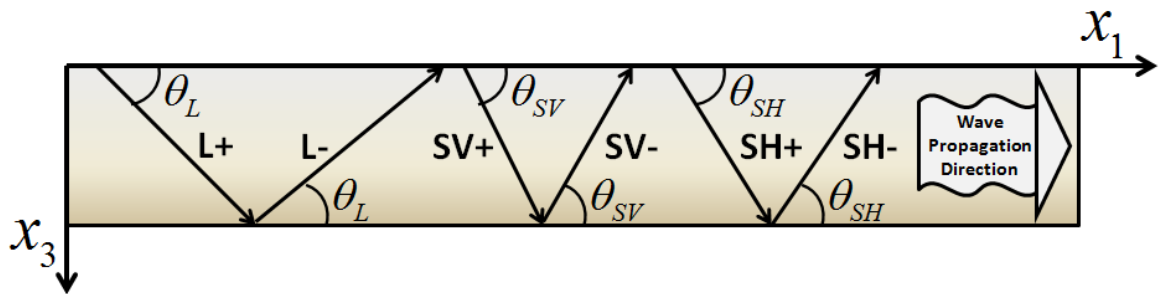


Figure 29: Upward and downward travelling partial waves for a single anisotropic layer

This section provides a full derivation of Lamb waves for an n-layered composite material with monoclinic symmetry based on partial wave techniques. First, the equations for Lamb waves are derived for a single monoclinic lamina, which are then generalized for an n-layered laminate.

2.2.4.1 Stress-strain relationship for composite laminate

The stress-strain relationship in the Cartesian co-ordinate system for an anisotropic solid medium assuming linear behavior can be written in a tensor form as:

$$\begin{aligned}\sigma_{ij} &= c_{ijkl} \varepsilon_{kl} \\ \varepsilon_{ij} &= s_{ijkl} \sigma_{kl}\end{aligned}\tag{2.3}$$

Where, σ_{ij} = stress tensor, ε_{kl} = strain tensor, c_{ijkl} and s_{ijkl} are the stiffness and compliance tensors respectively both containing material elastic constants

Strain in terms of displacement u_i is given by:

$$\varepsilon_{ij} = \frac{1}{2} \left(\frac{\partial u_i}{\partial x_j} + \frac{\partial u_j}{\partial x_i} \right)\tag{2.4}$$

The general equation of motion without considering body forces can be written as:

$$\frac{\partial \sigma_{ij}}{\partial x_j} = \rho \frac{\partial^2 u_i}{\partial t^2}\tag{2.5}$$

Using Eqn. (2.3) and (2.4); Eqn. (2.5) can be rewritten in terms of displacement as:

$$c_{ijkl} \frac{\partial^2 u_k}{\partial x_j \partial x_l} = \rho \frac{\partial^2 u_i}{\partial t^2}\tag{2.6}$$

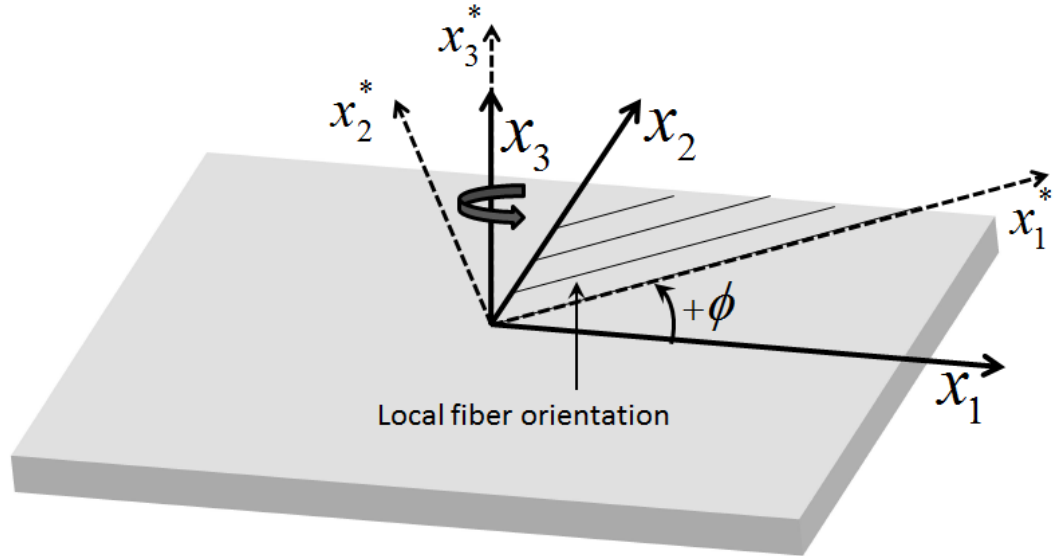


Figure 30: Generalized co-ordinate system with local fibre orientation

In composite materials, the fibres are oriented at desired angles for optimal performance. Due to different orientations, the material can behave differently in various directions. Depending on how the fibres are orientated (planes of symmetry), composite materials can be categorized as triclinic, monoclinic, orthotropic, transversely isotropic, and isotropic [L. P. Kollár et al., 2003]. The general co-ordinate system used to describe the planes of symmetry is shown in Figure 30, where x_3 represents the thickness direction. Since composite laminates are constructed by stacking individual lamina at different local orientations, transformation of each layer's properties from its local orientation to a common global system leads to a significant simplification in the analysis as suggested by Nayfeh [A. H. Nayfeh, 1995]. Figure 30 shows the coordinate system for composite lamina, where $[x_1, x_2, x_3]$ and $[x_1^*, x_2^*, x_3^*]$ represent the global and local coordinate systems respectively. The transformation of the stiffness tensor from the local (x_i^*) to global (x_i) coordinate can be performed by orthogonal transformation assuming that the rotation takes place along the thickness axis ($x_3; x_3^*$), positive counter-clockwise as

shown in Figure 30. Method presented by Kollár [L. P. Kollár et al., 2003] is used for finding the relationship between stress and strain provided below.

The stresses in the global system can be calculated from the local system in a matrix form by:

$$\{\sigma\} = [T_\sigma] \{\sigma^*\} \quad (2.7)$$

Where, $\{\sigma\}$ and $\{\sigma^*\}$ are [6x1] stress vector representing global and local stresses respectively, whereas $[T_\sigma]$ is a [6x6] stress transformation matrix

Taking into account that the local coordinate (x_3^*) coincides with the global coordinate (x_3) and ϕ is the angle of rotation around x_3 axis positive counter-clockwise (Figure 30), the stress transformation matrix $[T_\sigma]$ is given by:

$$[T_\sigma] = \begin{bmatrix} c^2 & s^2 & 0 & 0 & 0 & 2cs \\ s^2 & c^2 & 0 & 0 & 0 & -2cs \\ 0 & 0 & 1 & 0 & 0 & 0 \\ 0 & 0 & 0 & c & -s & 0 \\ 0 & 0 & 0 & s & c & 0 \\ -cs & cs & 0 & 0 & 0 & c^2 - s^2 \end{bmatrix} \quad (2.8)$$

Where $c = \cos \phi$ and $s = \sin \phi$

Similarly, strains in the global system can be calculated from the local system in a matrix form by:

$$\{\varepsilon\} = [T_\varepsilon] \{\varepsilon^*\} \quad (2.9)$$

Where, $\{\varepsilon\}$ and $\{\varepsilon^*\}$ are [6x1] strain vector representing global and local strains respectively, $[T_\varepsilon]$ is a [6x6] strain transformation matrix

Taking into account the aforementioned simplifications performed for stresses, the strain transformation matrix $[T_\varepsilon]$ can be written as:

$$[T_\varepsilon] = \begin{bmatrix} c^2 & s^2 & 0 & 0 & 0 & cs \\ s^2 & c^2 & 0 & 0 & 0 & -cs \\ 0 & 0 & 1 & 0 & 0 & 0 \\ 0 & 0 & 0 & c & -s & 0 \\ 0 & 0 & 0 & s & c & 0 \\ -2cs & 2cs & 0 & 0 & 0 & c^2 - s^2 \end{bmatrix} \quad (2.10)$$

Where $c = \cos \phi$ and $s = \sin \phi$

The stress strain relationship for the global system can be found using:

$$\begin{aligned} \{\sigma\} &= [c]\{\varepsilon\} \\ \{\varepsilon\} &= [s]\{\sigma\} \end{aligned} \quad (2.11)$$

Where, $[c]$ and $[s]$ are stiffness and compliance matrices respectively for the global system

The stiffness matrix can be transformed from local to global system by:

$$[c] = [T_\sigma][c^*][T_\varepsilon]^{-1} \quad (2.12)$$

Similarly, the compliance matrix can be transformed from local to global system using:

$$[s] = [T_\varepsilon][s^*][T_\sigma]^{-1} \quad (2.13)$$

2.2.4.2 Lamb wave equations for single monoclinic lamina

Composite materials typically used for aerospace applications such as woven and unidirectional prepregs or fabrics exhibit monoclinic and higher degrees of symmetries. Therefore, the Lamb wave equations derived here assumes monoclinic symmetry for which the stress-strain relationship given in Eqn. (2.3) can be expanded as:

$$\begin{Bmatrix} \sigma_{11} \\ \sigma_{22} \\ \sigma_{33} \\ \sigma_{23} \\ \sigma_{13} \\ \sigma_{12} \end{Bmatrix} = \begin{bmatrix} c_{11} & c_{12} & c_{13} & 0 & 0 & c_{16} \\ c_{12} & c_{22} & c_{23} & 0 & 0 & c_{26} \\ c_{13} & c_{23} & c_{33} & 0 & 0 & c_{36} \\ 0 & 0 & 0 & c_{44} & c_{45} & 0 \\ 0 & 0 & 0 & c_{45} & c_{55} & 0 \\ c_{16} & c_{26} & c_{36} & 0 & 0 & c_{66} \end{bmatrix} \begin{Bmatrix} \varepsilon_{11} \\ \varepsilon_{22} \\ \varepsilon_{33} \\ 2\varepsilon_{23} \\ 2\varepsilon_{13} \\ 2\varepsilon_{12} \end{Bmatrix} \quad (2.14)$$

For the derivation of the representative equations for Lamb wave in a monoclinic material, displacement fields in all three directions are considered as compared to just considering the wave travelling along the propagating directions. This method provides a full picture of the wave propagating in all three directions within the structure including the symmetric, anti-symmetric, shear-horizontal, and any waves that satisfy the specified boundary conditions. For this, a plane wave travelling through a plate as shown in Figure 31 is considered, for which the displacement (u_i) is assumed as:

$$u_i = U_i e^{i(k_1 x_1 + k_2 x_2 + k_3 x_3 - \omega t)} \quad (2.15)$$

Where, U_i is displacement amplitude, k_i is wavenumber, x_i is direction, ω is angular frequency, and t is time

The wavevector \vec{k} , which defines the travelling direction of the wave is given by:

$$\vec{k} = [k_1, k_2, k_3]^T = [k_{12} \cos \theta_{12}, k_{12} \sin \theta_{12}, k_3]^T \quad (2.16)$$

Where, k_{12} is the wave vector along $(x_1 - x_2)$ plane and θ_{12} is the angle with respect to x_1 axis, positive counter clockwise (Figure 31).

Magnitude of \vec{k}_{12} is given by:

$$k_{12} = |\vec{k}_{12}| = \sqrt{k_1^2 + k_2^2} = \frac{\omega}{c_p} = \frac{2\pi}{\lambda} \quad (2.17)$$

Where, c_p is phase velocity of the wave travelling along $(x_1 - x_2)$ plane and λ is the wavelength

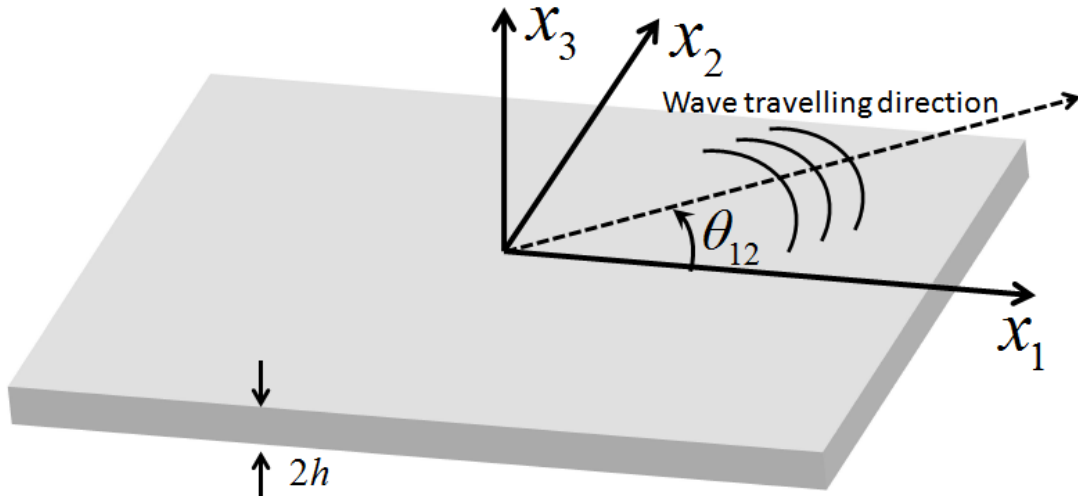


Figure 31: Thin monoclinic plate with thickness of $2h$

Expanding Eqn. (2.6), which is the general partial differential equation in terms of three displacements u_i provided in Eqn. (2.15) for a monoclinic material whose stiffness matrix is provided in Eqn. (2.14), gives:

For x_1 direction:

$$\begin{aligned} & c_{11} \frac{\partial^2 u_1}{\partial x_1^2} + c_{66} \frac{\partial^2 u_1}{\partial x_2^2} + c_{55} \frac{\partial^2 u_1}{\partial x_3^2} + 2c_{16} \frac{\partial^2 u_1}{\partial x_1 \partial x_2} + c_{16} \frac{\partial^2 u_2}{\partial x_1^2} + c_{26} \frac{\partial^2 u_2}{\partial x_2^2} + c_{45} \frac{\partial^2 u_2}{\partial x_3^2} \\ & + (c_{12} + c_{66}) \frac{\partial^2 u_2}{\partial x_1 \partial x_2} + (c_{13} + c_{55}) \frac{\partial^2 u_3}{\partial x_1 \partial x_3} + (c_{36} + c_{45}) \frac{\partial^2 u_3}{\partial x_2 \partial x_3} = \rho \frac{\partial^2 u_1}{\partial t^2} \end{aligned} \quad (2.18)$$

For x_2 direction:

$$\begin{aligned} & c_{16} \frac{\partial^2 u_1}{\partial x_1^2} + c_{26} \frac{\partial^2 u_1}{\partial x_2^2} + c_{45} \frac{\partial^2 u_1}{\partial x_3^2} + (c_{12} + c_{66}) \frac{\partial^2 u_1}{\partial x_1 \partial x_2} + c_{66} \frac{\partial^2 u_2}{\partial x_1^2} + c_{22} \frac{\partial^2 u_2}{\partial x_2^2} \\ & + c_{44} \frac{\partial^2 u_2}{\partial x_3^2} + 2c_{26} \frac{\partial^2 u_2}{\partial x_1 \partial x_2} + (c_{36} + c_{45}) \frac{\partial^2 u_3}{\partial x_1 \partial x_3} + (c_{23} + c_{44}) \frac{\partial^2 u_3}{\partial x_2 \partial x_3} = \rho \frac{\partial^2 u_2}{\partial t^2} \end{aligned} \quad (2.19)$$

For x_3 direction:

$$\begin{aligned} & (c_{13} + c_{55}) \frac{\partial^2 u_1}{\partial x_1 \partial x_3} + (c_{36} + c_{45}) \frac{\partial^2 u_1}{\partial x_2 \partial x_3} + (c_{36} + c_{45}) \frac{\partial^2 u_2}{\partial x_1 \partial x_3} \\ & + (c_{23} + c_{44}) \frac{\partial^2 u_2}{\partial x_2 \partial x_3} + c_{55} \frac{\partial^2 u_3}{\partial x_1^2} + c_{44} \frac{\partial^2 u_3}{\partial x_2^2} + c_{33} \frac{\partial^2 u_3}{\partial x_3^2} + 2c_{45} \frac{\partial^2 u_3}{\partial x_1 \partial x_2} = \rho \frac{\partial^2 u_3}{\partial t^2} \end{aligned} \quad (2.20)$$

Substituting displacement field u_i using Eqn. (2.15) into the expanded general equilibrium equations Eqn. (2.18) to (2.20); the general equilibrium equation can be reorganized in the form:

$$K_{ij}(k_3)U_j = 0 \quad (2.21)$$

The elements of K_{ij} for the monoclinic symmetry are given as:

$$\begin{aligned}
K_{11} &= c_{11}k_1^2 + c_{66}k_2^2 + c_{55}k_3^2 + 2c_{16}k_1k_2 - \rho\omega^2 \\
K_{12} = K_{21} &= c_{16}k_1^2 + c_{26}k_2^2 + c_{45}k_3^2 + (c_{12} + c_{66})k_1k_2 \\
K_{13} = K_{31} &= (c_{13} + c_{55})k_1k_3 + (c_{36} + c_{45})k_2k_3 \\
K_{22} &= c_{66}k_1^2 + c_{22}k_2^2 + c_{44}k_3^2 + 2c_{26}k_1k_2 - \rho\omega^2 \\
K_{23} = K_{32} &= (c_{36} + c_{45})k_1k_3 + (c_{23} + c_{44})k_2k_3 \\
K_{33} &= c_{55}k_1^2 + c_{44}k_2^2 + c_{33}k_3^2 + 2c_{45}k_1k_2 - \rho\omega^2
\end{aligned} \tag{2.22}$$

In the matrix form, Eqn. (2.22) can be written as:

$$\begin{bmatrix} K_{11} & K_{12} & K_{13} \\ K_{12} & K_{22} & K_{23} \\ K_{13} & K_{23} & K_{33} \end{bmatrix} \begin{Bmatrix} U_1 \\ U_2 \\ U_3 \end{Bmatrix} = \begin{Bmatrix} 0 \\ 0 \\ 0 \end{Bmatrix} \tag{2.23}$$

For a non-trivial solution to exist; $\det(K_{ij}) = 0$ must be true. Setting the determinant to be zero gives a polynomial solution in terms of k_3 as:

$$D_1k_3^6 + D_2k_3^4 + D_3k_3^2 + D_4 = 0 \tag{2.24}$$

The coefficients D_i are functions of $(k_1, k_2, \omega, \rho, c_{ij})$, and are provided in Appendix A.

Eqn. (2.24) provide three roots for k_3^2 , corresponding to one pair of quasi-longitudinal and two pairs of quasi-transverse modes. Altogether six roots of k_3 are present in pairs of two that are opposite of each other. Each pair represents an upward and downward travelling wave making the same angle with the x_1 axis (Figure 29). Representing the direction vector k_3 for each mode as χ_q , where $q=1,2,..6$, gives $\chi_2 = -\chi_1$, $\chi_4 = -\chi_3$ and $\chi_6 = -\chi_5$ [M. J. S. Lowe, 1995].

Applying traction free boundary conditions, which require the stresses to be zero at the top and bottom surfaces of the plate shown in Figure 31, gives:

$$\sigma_{33}(x_3 = \pm h) = \sigma_{13}(x_3 = \pm h) = \sigma_{23}(x_3 = \pm h) = 0 \quad (2.25)$$

Using the traction free boundary conditions, the stresses can be written in terms of stiffness and displacement as:

$$\begin{aligned} \sigma_{33} &= c_{13} \frac{\partial u_1}{\partial x_1} + c_{23} \frac{\partial u_2}{\partial x_2} + c_{33} \frac{\partial u_3}{\partial x_3} + c_{36} \left(\frac{\partial u_2}{\partial x_1} + \frac{\partial u_1}{\partial x_2} \right) \\ \sigma_{13} &= c_{45} \left(\frac{\partial u_2}{\partial x_3} + \frac{\partial u_3}{\partial x_2} \right) + c_{55} \left(\frac{\partial u_3}{\partial x_1} + \frac{\partial u_1}{\partial x_3} \right) \\ \sigma_{23} &= c_{44} \left(\frac{\partial u_2}{\partial x_3} + \frac{\partial u_3}{\partial x_2} \right) + c_{45} \left(\frac{\partial u_3}{\partial x_1} + \frac{\partial u_1}{\partial x_3} \right) \end{aligned} \quad (2.26)$$

Taking the partial derivative of the displacements given in Eqn. (2.15) and substituting into Eqn.

(2.26) above gives:

$$\begin{aligned} \sigma_{33} &= ie^{i(k_1 x_1 + k_2 x_2 + k_3 x_3 - \omega t)} (c_{13} U_1 k_1 + c_{23} U_2 k_2 + c_{33} U_3 k_3 + c_{36} U_2 k_1 + c_{36} U_1 k_2) \\ \sigma_{13} &= ie^{i(k_1 x_1 + k_2 x_2 + k_3 x_3 - \omega t)} (c_{45} U_2 k_3 + c_{45} U_3 k_2 + c_{55} U_3 k_1 + c_{55} U_1 k_3) \\ \sigma_{23} &= ie^{i(k_1 x_1 + k_2 x_2 + k_3 x_3 - \omega t)} (c_{44} U_2 k_3 + c_{44} U_3 k_2 + c_{45} U_3 k_1 + c_{45} U_1 k_3) \end{aligned} \quad (2.27)$$

Further simplification can be achieved by representing the displacements (u_1, u_2, u_3) as functions of single displacement amplitude (U_{1q}) , by defining the displacement component ratios as $V_q = U_{2q}/U_{1q}$ and $W_q = U_{3q}/U_{1q}$.

Where, V_q and W_q in terms of K_{ij} is given as

$$V_q = \frac{K_{11}(\chi_q)K_{23}(\chi_q) - K_{12}(\chi_q)K_{13}(\chi_q)}{K_{13}(\chi_q)K_{22}(\chi_q) - K_{12}(\chi_q)K_{23}(\chi_q)} \quad (2.28)$$

$$W_q = \frac{K_{11}(\chi_q)K_{23}(\chi_q) - K_{12}(\chi_q)K_{13}(\chi_q)}{K_{33}(\chi_q)K_{12}(\chi_q) - K_{13}(\chi_q)K_{23}(\chi_q)} \quad (2.29)$$

The total displacement can now be written in terms of V_q and W_q as:

$$\begin{aligned} u_1 &= \sum_{q=1}^6 U_{1q} e^{i(k_1 x_1 + k_2 x_2 + \chi_q x_3 - \omega t)} \\ u_2 &= \sum_{q=1}^6 V_q U_{1q} e^{i(k_1 x_1 + k_2 x_2 + \chi_q x_3 - \omega t)} \\ u_3 &= \sum_{q=1}^6 W_q U_{1q} e^{i(k_1 x_1 + k_2 x_2 + \chi_q x_3 - \omega t)} \end{aligned} \quad (2.30)$$

The total stress can also be simplified as:

$$\begin{aligned} \sigma_{33} &= i \sum_{q=1}^6 D_{1q} U_{1q} e^{i(k_1 x_1 + k_2 x_2 + \chi_q x_3 - \omega t)} \\ \sigma_{13} &= i \sum_{q=1}^6 D_{2q} U_{1q} e^{i(k_1 x_1 + k_2 x_2 + \chi_q x_3 - \omega t)} \\ \sigma_{23} &= i \sum_{q=1}^6 D_{3q} U_{1q} e^{i(k_1 x_1 + k_2 x_2 + \chi_q x_3 - \omega t)} \end{aligned} \quad (2.31)$$

Where,

$$\begin{aligned} D_{1q} &= k_1 (c_{13} + c_{36} V_q) + k_2 (c_{36} + c_{23} V_q) + c_{33} W_q \chi_q \\ D_{2q} &= c_{55} W_q k_1 + c_{45} W_q k_2 + \chi_q (c_{55} + c_{45} V_q) \\ D_{3q} &= c_{45} W_q k_1 + c_{44} W_q k_2 + \chi_q (c_{45} + c_{44} V_q) \end{aligned} \quad (2.32)$$

The stresses must go to zero at the top and bottom surfaces of the plate ($x_3 = \pm h$) as suggested by Eqn. (2.25), which can be simplified and expressed in the matrix form as:

$$\begin{bmatrix} D_{11}E_1 & D_{12}\bar{E}_1 & D_{13}E_3 & D_{14}\bar{E}_3 & D_{15}E_5 & D_{16}\bar{E}_5 \\ D_{21}E_1 & D_{22}\bar{E}_1 & D_{23}E_3 & D_{24}\bar{E}_3 & D_{25}E_5 & D_{26}\bar{E}_5 \\ D_{31}E_1 & D_{32}\bar{E}_1 & D_{33}E_3 & D_{34}\bar{E}_3 & D_{35}E_5 & D_{36}\bar{E}_5 \\ D_{11}\bar{E}_1 & D_{12}E_1 & D_{13}\bar{E}_3 & D_{14}E_3 & D_{15}\bar{E}_5 & D_{16}E_5 \\ D_{21}\bar{E}_1 & D_{22}E_1 & D_{23}\bar{E}_3 & D_{24}E_3 & D_{25}\bar{E}_5 & D_{26}E_5 \\ D_{31}\bar{E}_1 & D_{32}E_1 & D_{33}\bar{E}_3 & D_{34}E_3 & D_{35}\bar{E}_5 & D_{36}E_5 \end{bmatrix} \begin{Bmatrix} U_{11} \\ U_{12} \\ U_{13} \\ U_{14} \\ U_{15} \\ U_{16} \end{Bmatrix} = \begin{Bmatrix} 0 \\ 0 \\ 0 \\ 0 \\ 0 \\ 0 \end{Bmatrix} \quad (2.33)$$

Where, $E_q = e^{ix_q h}$, $\bar{E}_q = e^{-ix_q h}$

For symmetric Lamb mode, the displacement u_3 (Figure 28) is given by:

$$u_3(h) = -u_3(-h) \quad (2.34)$$

Substituting Eqn. (2.34) as u_3 in Eqn. (2.30); it can be realized that, in order for the relationship to be true, the conditions for displacement amplitudes should be $U_{11} = U_{12}$, $U_{13} = U_{14}$, and $U_{15} = U_{16}$.

Using the displacement amplitude relationship it can be seen that:

$$\begin{aligned} V_2 &= V_1; V_4 = V_3; V_6 = V_5 \\ W_2 &= -W_1; W_4 = -W_3; W_6 = -W_5 \end{aligned} \quad (2.35)$$

Using the above relationship, the properties of D_{ij} can be written as:

$$\begin{aligned}
 D_{12} &= D_{11}; D_{14} = D_{13}; D_{16} = D_{15} \\
 D_{22} &= -D_{21}; D_{24} = -D_{23}; D_{26} = -D_{25} \\
 D_{32} &= -D_{31}; D_{34} = -D_{33}; D_{36} = -D_{35}
 \end{aligned} \tag{2.36}$$

Therefore, Eqn. (2.33) can be rewritten as:

$$\begin{aligned}
 \left(D_{11}E_1 + D_{11}\bar{E}_1 \right)U_{11} + \left(D_{13}E_3 + D_{13}\bar{E}_3 \right)U_{13} + \left(D_{15}E_5 + D_{15}\bar{E}_5 \right)U_{15} &= 0 & \text{(a)} \\
 \left(D_{21}E_1 - D_{21}\bar{E}_1 \right)U_{11} + \left(D_{23}E_3 - D_{23}\bar{E}_3 \right)U_{13} + \left(D_{25}E_5 - D_{25}\bar{E}_5 \right)U_{15} &= 0 & \text{(b)} \\
 \left(D_{31}E_1 - D_{31}\bar{E}_1 \right)U_{11} + \left(D_{33}E_3 - D_{33}\bar{E}_3 \right)U_{13} + \left(D_{35}E_5 - D_{35}\bar{E}_5 \right)U_{15} &= 0 & \text{(c)} \\
 \left(D_{11}E_1 + D_{11}\bar{E}_1 \right)U_{11} + \left(D_{13}E_3 + D_{13}\bar{E}_3 \right)U_{13} + \left(D_{15}E_5 + D_{15}\bar{E}_5 \right)U_{15} &= 0 & \text{(d)} \\
 -\left(D_{21}E_1 - D_{21}\bar{E}_1 \right)U_{11} - \left(D_{23}E_3 - D_{23}\bar{E}_3 \right)U_{13} - \left(D_{25}E_5 - D_{25}\bar{E}_5 \right)U_{15} &= 0 & \text{(e)} \\
 -\left(D_{31}E_1 - D_{31}\bar{E}_1 \right)U_{11} - \left(D_{33}E_3 - D_{33}\bar{E}_3 \right)U_{13} - \left(D_{35}E_5 - D_{35}\bar{E}_5 \right)U_{15} &= 0 & \text{(f)}
 \end{aligned} \tag{2.37}$$

Adding Eqn. (2.37) (d) to (a), subtracting (e) from (b), (f) from (c), and dividing entire equations

by 2, Eqn. (2.37) can be reduced to the matrix form as:

$$\begin{bmatrix}
 D_{11}E_1 + D_{11}\bar{E}_1 & D_{13}E_3 + D_{13}\bar{E}_3 & D_{15}E_5 + D_{15}\bar{E}_5 \\
 D_{21}E_1 - D_{21}\bar{E}_1 & D_{23}E_3 - D_{23}\bar{E}_3 & D_{25}E_5 - D_{25}\bar{E}_5 \\
 D_{31}E_1 - D_{31}\bar{E}_1 & D_{33}E_3 - D_{33}\bar{E}_3 & D_{35}E_5 - D_{35}\bar{E}_5
 \end{bmatrix}
 \begin{Bmatrix}
 U_{11} \\
 U_{13} \\
 U_{15}
 \end{Bmatrix}
 =
 \begin{Bmatrix}
 0 \\
 0 \\
 0
 \end{Bmatrix} \tag{2.38}$$

Using the trigonometric identities for E_q and \bar{E}_q [A. H. Nayfeh, 1995] as:

$$\begin{aligned}
E_q + \bar{E}_q &= 2C_q = 2\cos(\chi_q h) \\
E_q - \bar{E}_q &= 2S_q = 2i\sin(\chi_q h)
\end{aligned} \tag{2.39}$$

Using identities given in Eqn. (2.39), Eqn. (2.38) can be simplified as:

$$\begin{bmatrix} D_{11} 2C_1 & D_{13} 2C_3 & D_{15} 2C_5 \\ D_{21} 2iS_1 & D_{23} 2iS_3 & D_{25} 2iS_5 \\ D_{31} 2iS_1 & D_{33} 2iS_3 & D_{35} 2iS_5 \end{bmatrix} \begin{Bmatrix} U_{11} \\ U_{13} \\ U_{15} \end{Bmatrix} = \begin{Bmatrix} 0 \\ 0 \\ 0 \end{Bmatrix} \tag{2.40}$$

In order for a non-trivial solution to exist, the determinant of Eqn. (2.40) should be zero. Finding the determinant of Eqn. (2.40) and setting it to zero, the symmetric Lamb wave dispersion equation for a single monoclinic layer can be found as:

$$\begin{aligned}
&(D_{11}D_{25}D_{33} - D_{11}D_{23}D_{35})\cos(\chi_1 h)\sin(\chi_3 h)\sin(\chi_5 h) \\
&+ (D_{35}D_{21}D_{13} - D_{13}D_{25}D_{31})\cos(\chi_3 h)\sin(\chi_1 h)\sin(\chi_5 h) \\
&+ (D_{31}D_{23}D_{15} - D_{15}D_{21}D_{33})\cos(\chi_5 h)\sin(\chi_1 h)\sin(\chi_3 h) = 0
\end{aligned} \tag{2.41}$$

In the above equation, D_{iq} is given by Eqn. (2.32), χ_q is the direction vector for each six waves propagating through the thickness as shown in Figure 29, and h is the plate half-thickness as shown in Figure 31.

Similar process can be followed for the anti-symmetric Lamb mode, in which the displacement u_3 (Figure 28) is given by:

$$u_3(h) = u_3(-h) \tag{2.42}$$

Substituting Eqn. (2.42) to u_3 in Eqn. (2.30), it can be realized that, in order for the relationship to be true, the conditions for displacement amplitudes should be $U_{12} = -U_{11}$, $U_{14} = -U_{13}$, and $U_{16} = -U_{15}$.

Following the process as described for the symmetric Lamb modes, the anti-symmetric Lamb wave dispersion equation for a single monoclinic layer can be found as:

$$\begin{aligned} & (D_{11}D_{25}D_{33} - D_{11}D_{23}D_{35})\sin(\chi_1h)\cos(\chi_3h)\cos(\chi_5h) \\ & + (D_{35}D_{21}D_{13} - D_{13}D_{25}D_{31})\sin(\chi_3h)\cos(\chi_1h)\cos(\chi_5h) \\ & + (D_{31}D_{23}D_{15} - D_{15}D_{21}D_{33})\sin(\chi_5h)\cos(\chi_1h)\cos(\chi_3h) = 0 \end{aligned} \quad (2.43)$$

Similar to the symmetric case, D_{iq} is given by Eqn. (2.32), χ_q is the direction vector for each six waves propagating through the thickness as shown in Figure 29, and h is the plate half-thickness as shown in Figure 31.

2.2.4.3 Lamb wave equations for n-layered laminate

Composite structures in general are made up of several lamina stacked together at different orientation angles. It is assumed that the anisotropic layers consist of linear elastic material with perfectly bonded interlaminar interface so that the displacements and stresses between the layers are continuous. In this thesis, two solution methods - Transfer Matrix (TM) and Global Matrix (GM), based on the 3D linear elasticity for generating the Lamb wave dispersion relationship for an n-layered laminate are explored in detail.

2.2.4.3.1 Transfer Matrix approach

Transfer Matrix (TM) approach discussed here is based on Nayfeh [A. H. Nayfeh, 1995]. This method in general relates the displacements and stresses at top and bottom of each individual layers to form a Transfer Matrix for the entire laminate.

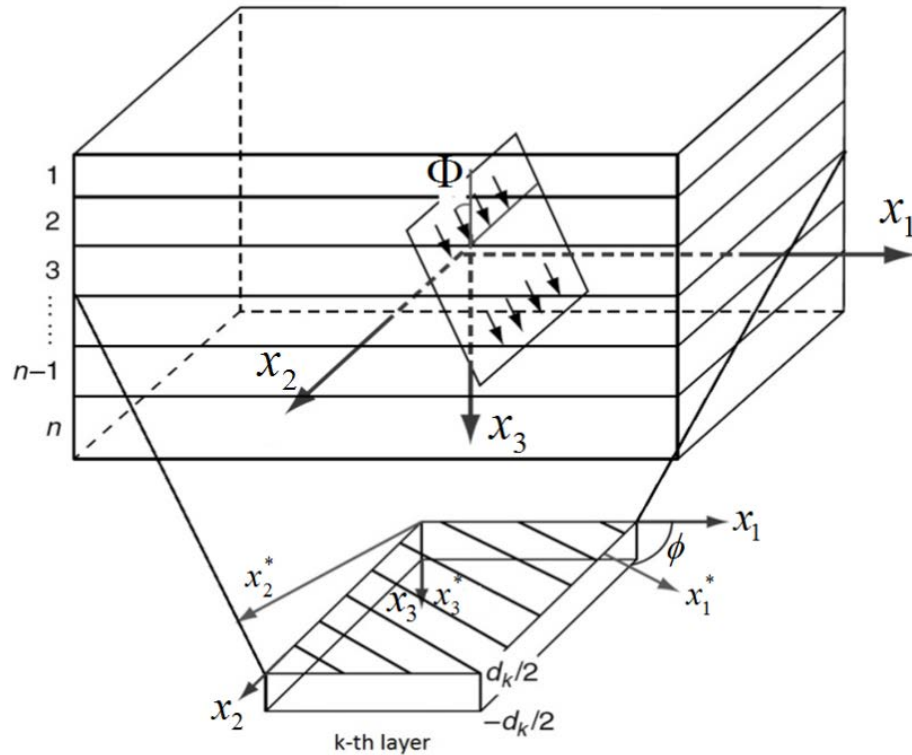


Figure 32: N-layered composite laminate showing k -th layer [V. Giurgiutiu, 2008]

For the TM approach, consider the k -th layer of an anisotropic plate shown in Figure 32, whose thickness is given as d_k . The displacement u_i and the stress σ_{ij} for this layer can be written using Eqn. (2.30) and (2.31) respectively as:

$$\begin{aligned}
(u_1, u_2, u_3)_k &= \sum_{q=1}^6 (1, V_q, W_q) U_{1q} e^{i(k_1 x_1 \sin \Phi + k_2 x_2 + \chi_q x_3 - \omega t)} \\
(\sigma_{33}, \sigma_{13}, \sigma_{23})_k &= \left[i \sum_{q=1}^6 (D_{1q}, D_{2q}, D_{3q}) U_{1q} e^{i(k_1 x_1 \sin \Phi + k_2 x_2 + \chi_q x_3 - \omega t)} \right]_k
\end{aligned} \tag{2.44}$$

Where, Φ is the incident angle (angle at which the vertical wave is excited), and the suffix k denotes the k -th layer as shown in Figure 32

Using the properties of (V_q, W_q, D_{iq}) , Eqn. (2.44) can be written in the matrix form as:

$$\begin{Bmatrix} u_1 \\ u_2 \\ u_3 \\ \sigma_{33} \\ \sigma_{13} \\ \sigma_{23} \end{Bmatrix}_k = \begin{bmatrix} 1 & 1 & 1 & 1 & 1 & 1 \\ V_1 & V_1 & V_3 & V_3 & V_5 & V_5 \\ W_1 & -W_1 & W_3 & -W_3 & W_5 & -W_5 \\ iD_{11} & iD_{11} & iD_{13} & iD_{13} & iD_{15} & iD_{15} \\ iD_{21} & -iD_{21} & iD_{23} & -iD_{23} & iD_{25} & -iD_{25} \\ iD_{31} & -iD_{31} & iD_{33} & -iD_{33} & iD_{35} & -iD_{35} \end{bmatrix}_k \begin{Bmatrix} U_{11} e^{i(k_1 x_1 \sin \Phi + k_2 x_2 + \chi_1 x_3 - \omega t)} \\ U_{12} e^{i(k_1 x_1 \sin \Phi + k_2 x_2 - \chi_1 x_3 - \omega t)} \\ U_{13} e^{i(k_1 x_1 \sin \Phi + k_2 x_2 + \chi_3 x_3 - \omega t)} \\ U_{14} e^{i(k_1 x_1 \sin \Phi + k_2 x_2 - \chi_3 x_3 - \omega t)} \\ U_{15} e^{i(k_1 x_1 \sin \Phi + k_2 x_2 + \chi_5 x_3 - \omega t)} \\ U_{16} e^{i(k_1 x_1 \sin \Phi + k_2 x_2 - \chi_5 x_3 - \omega t)} \end{Bmatrix}_k \tag{2.45}$$

Let the Left Hand Side (LHS) of the Eqn. (2.45), which contains the displacement and stress vectors be denoted as P_k , the 6x6 matrix on the Right Hand Side (RHS) be denoted as X_k , the displacement amplitude on the RHS as U_k , and the wave equation on the RHS as D_k . The RHS wave equation D_k can also be written as a diagonal matrix. Using the aforementioned notations P_k, X_k, U_k , and D_k ; Eqn. (2.45) can be written in the short form as:

$$\{P_k\} = [X_k][D_k]\{U_k\} \tag{2.46}$$

Eqn. (2.46) can be used to relate the displacements and stresses on the top to that of the bottom surface of the k -th layer.

The displacements and the stresses on the top layer can be denoted as:

$$\{P_k^+\} = [X_k][D_k^+]\{U_k\} \quad (2.47)$$

Similarly, the displacement and the stresses on bottom layer can be denoted as:

$$\{P_k^-\} = [X_k][D_k^-]\{U_k\} \quad (2.48)$$

The amplitude vector U_k can be rearranged in Eqn. (2.48) as:

$$\{U_k\} = [D_k^-]^{-1}[X_k]^{-1}\{P_k^-\} \quad (2.49)$$

Substituting Eqn. (2.49) into Eqn. (2.47) yields the relationship between the top and the bottom plate of k -th layer and is given as:

$$\{P_k^+\} = [X_k][D_k^+][D_k^-]^{-1}[X_k]^{-1}\{P_k^-\} \quad (2.50)$$

Multiplying $[D_k^+]$ by $[D_k^-]^{-1}$ yields $[D_k]$; letting $[X_k][D_k][X_k]^{-1}$ as $[A_k]$ the transfer matrix for k -th layer, Eqn (2.50) can be rewritten as:

$$\{P_k^+\} = [A_k]\{P_k^-\} \quad (2.51)$$

Using a similar process for each layer, the displacements and stresses on the bottom can be related to the top using the TM approach. The overall TM for an n -layered anisotropic plate can be found by multiplying individual transfer matrices from each layer as:

$$[A] = [A_1] \dots [A_k] \dots [A_n] \quad (2.52)$$

The overall transfer matrix can be written as:

$$\begin{Bmatrix} u_1^+ \\ u_2^+ \\ u_3^+ \\ \sigma_{33}^+ \\ \sigma_{13}^+ \\ \sigma_{23}^+ \end{Bmatrix} = \begin{bmatrix} A_{11} & A_{12} & A_{13} & A_{14} & A_{15} & A_{16} \\ A_{21} & A_{22} & A_{23} & A_{24} & A_{25} & A_{26} \\ A_{31} & A_{32} & A_{33} & A_{34} & A_{35} & A_{36} \\ A_{41} & A_{42} & A_{43} & A_{44} & A_{45} & A_{46} \\ A_{51} & A_{52} & A_{53} & A_{54} & A_{55} & A_{56} \\ A_{61} & A_{62} & A_{63} & A_{64} & A_{65} & A_{66} \end{bmatrix} \begin{Bmatrix} u_1^- \\ u_2^- \\ u_3^- \\ \sigma_{33}^- \\ \sigma_{13}^- \\ \sigma_{23}^- \end{Bmatrix} \quad (2.53)$$

For the Lamb wave propagation, stress-free boundary conditions can be applied at the top and bottom surfaces as: $(\sigma_{33}^+ = \sigma_{13}^+ = \sigma_{23}^+ = \sigma_{33}^- = \sigma_{13}^- = \sigma_{23}^- = 0)$, which leads to the simplification of

Eqn. (2.53) as:

$$\begin{Bmatrix} 0 \\ 0 \\ 0 \end{Bmatrix} = \begin{bmatrix} A_{41} & A_{42} & A_{43} \\ A_{51} & A_{52} & A_{53} \\ A_{61} & A_{62} & A_{63} \end{bmatrix} \begin{Bmatrix} u_1^- \\ u_2^- \\ u_3^- \end{Bmatrix} \quad (2.54)$$

For a non-trivial solution to exist requires matrix $[A]$ in Eqn. (2.54) to be a null matrix, which can be written as:

$$\begin{vmatrix} A_{41} & A_{42} & A_{43} \\ A_{51} & A_{52} & A_{53} \\ A_{61} & A_{62} & A_{63} \end{vmatrix} = \begin{Bmatrix} 0 \\ 0 \\ 0 \end{Bmatrix} \quad (2.55)$$

Solving Eqn. (2.55) numerically yields the Lamb wave dispersion curve.

2.2.4.3.2 Global Matrix approach

In the Global Matrix (GM) approach, all the equations from each layer are assembled to form a unified matrix that describes the displacement and stress fields associated with the wave

propagation. The GM method presented here is based on Knopoff [L. Knopoff, 1964]. The method consists of $X(n-1)$ equations for n layers, where X represents the number of assumed partial waves. The GM method is robust and remains stable for any frequency-thickness product because it does not rely on the coupling of the waves from one interface to another as compared to the TM approach [M. J. S. Lowe et al., 2004].

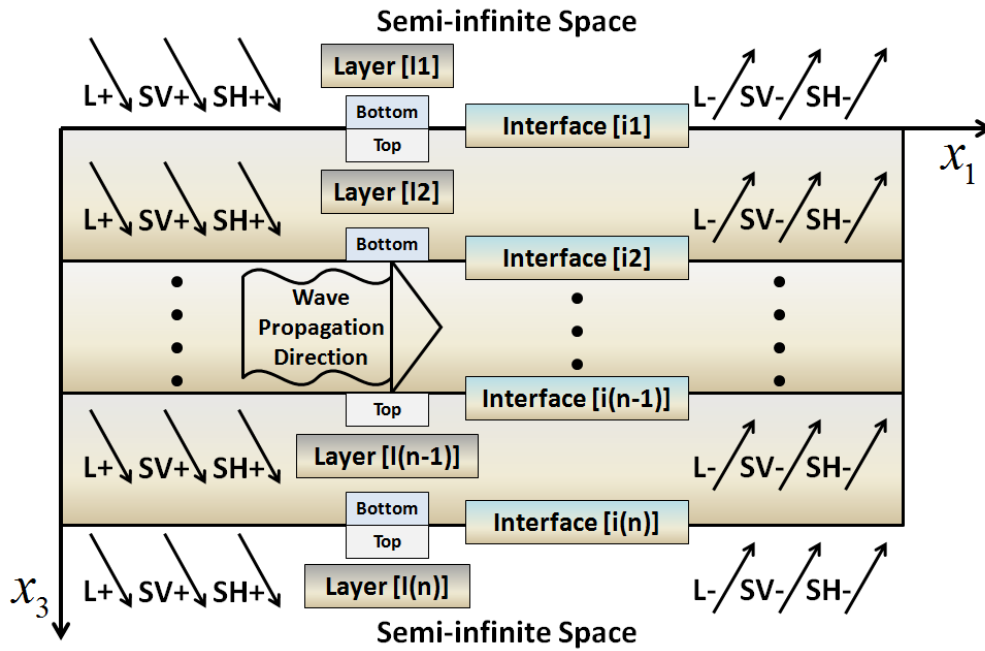


Figure 33: N-layered monoclinic plate showing partial waves [B. Pavlakovic, 1997]

As shown in Figure 33 for an n -layered monoclinic plate, each layer is assumed to have six partial waves denoted by $(L+/-)$, $(SV+/-)$, and $(SH+/-)$ representing quasi-longitudinal, quasi-transverse vertical, and quasi-transverse horizontal waves respectively. Positive and negative signs represent downward and upward travelling waves respectively. For the derivation of Lamb wave equation using GM approach, consider the second interface ($i2$), which consists of bottom surface of layer 2 ($I2$) and top surface of layer 3 ($I3$) as shown in Figure 33. The

displacements and stresses at the interface ($i2$) can be expressed using Eqn. (2.47) and (2.48) as:

$$\begin{aligned} \{P_{12,bot}\} &= \left[[X_{12,bot}] [D_{12,bot}] \right] \{U_{12,bot}\} \\ \{P_{13,top}\} &= \left[[X_{13,top}] [D_{13,top}] \right] \{U_{13,top}\} \end{aligned} \quad (2.56)$$

Let, the product of ($[X_k][D_k]$) be denoted as $[Z_k]$ and since the displacement and stresses are assumed to be continuous along the layers, Eqn. (2.56) can be expressed in a single matrix as:

$$\left[\begin{array}{cc} [Z_{12,bot}] & [-Z_{13,top}] \end{array} \right] \left\{ \begin{array}{c} \{U_{12,bot}\} \\ \{U_{13,top}\} \end{array} \right\} = \{0\} \quad (2.57)$$

A similar process can be carried out for all the layers to form the global unified matrix, which has $6(n-1)$ equations and $(6n)$ unknowns for six partial waves. Therefore, for the monoclinic layer shown in Figure 33 assuming five layers and four interfaces, the global matrix can be assembled as:

$$\left[\begin{array}{ccccc} [Z_{11,bot}] & [-Z_{12,top}] & [0] & [0] & [0] \\ [0] & [Z_{12,bot}] & [-Z_{13,top}] & [0] & [0] \\ [0] & [0] & [X_{13,bot}] & [-Z_{14,top}] & [0] \\ [0] & [0] & [0] & [Z_{14,bot}] & [-Z_{15,top}] \end{array} \right] \left\{ \begin{array}{c} \{U_{11}\} \\ \{U_{12}\} \\ \{U_{13}\} \\ \{U_{14}\} \\ \{U_{15}\} \end{array} \right\} = \{0\} \quad (2.58)$$

If the two semi-infinite half spaces (Figure 33) above and below the laminate are vacuum, Eqn. (2.58) can be modified to account for the absence of waves. This can be done by removing the sub-matrices corresponding to the top and bottom surface $[Z_{11,bot}]$ and $[-Z_{15,top}]$ from the GM.

It is to be noted that the stresses on the top and bottom most surfaces are zero; however, the

displacement on the aforementioned surfaces are not zero. Taken this into account, the new GM can now be modified as:

$$\begin{Bmatrix} P_{i1} \\ P_{i2} \\ P_{i3} \\ P_{i4} \end{Bmatrix} = \begin{bmatrix} [-Z_{12,top}] & [0] & [0] \\ [Z_{12,bot}] & [-Z_{13,top}] & [0] \\ [0] & [Z_{13,bot}] & [-Z_{14,top}] \\ [0] & [0] & [Z_{14,bot}] \end{bmatrix} \begin{Bmatrix} \{U_{12}\} \\ \{U_{13}\} \\ \{U_{14}\} \end{Bmatrix} \quad (2.59)$$

Where, P_{ik} is the displacement and stresses vector of layer- k

The GM presented in Eqn. (2.59) can be fully expanded as indicated in Figure 34.

		Top, Layer 2																						
Interface 1	u_1	$-Z_{11}$	$-Z_{12}$	$-Z_{13}$	$-Z_{14}$	$-Z_{15}$	$-Z_{16}$	0	0	0	0	0	0	0	0	0	0	0	0	0	0	0		
	u_2	$-Z_{21}$	$-Z_{22}$	$-Z_{23}$	$-Z_{24}$	$-Z_{25}$	$-Z_{26}$	0	0	0	0	0	0	0	0	0	0	0	0	0	0	0		
	u_3	$-Z_{31}$	$-Z_{32}$	$-Z_{33}$	$-Z_{34}$	$-Z_{35}$	$-Z_{36}$	0	0	0	0	0	0	0	0	0	0	0	0	0	0	0		
	σ_{33}	$-Z_{41}$	$-Z_{42}$	$-Z_{43}$	$-Z_{44}$	$-Z_{45}$	$-Z_{46}$	0	0	0	0	0	0	0	0	0	0	0	0	0	0	0		
	σ_{13}	$-Z_{51}$	$-Z_{52}$	$-Z_{53}$	$-Z_{54}$	$-Z_{55}$	$-Z_{56}$	0	0	0	0	0	0	0	0	0	0	0	0	0	0	0		
σ_{23}	$-Z_{61}$	$-Z_{62}$	$-Z_{63}$	$-Z_{64}$	$-Z_{65}$	$-Z_{66}$	0	0	0	0	0	0	0	0	0	0	0	0	0	0	0	0		
		Bottom, Layer 2						Top, Layer 3																
Interface 2	u_1	Z_{11}	Z_{12}	Z_{13}	Z_{14}	Z_{15}	Z_{16}	$-Z_{11}$	$-Z_{12}$	$-Z_{13}$	$-Z_{14}$	$-Z_{15}$	$-Z_{16}$	0	0	0	0	0	0	0	0	0		
	u_2	Z_{21}	Z_{22}	Z_{23}	Z_{24}	Z_{25}	Z_{26}	$-Z_{21}$	$-Z_{22}$	$-Z_{23}$	$-Z_{24}$	$-Z_{25}$	$-Z_{26}$	0	0	0	0	0	0	0	0	0		
	u_3	Z_{31}	Z_{32}	Z_{33}	Z_{34}	Z_{35}	Z_{36}	$-Z_{31}$	$-Z_{32}$	$-Z_{33}$	$-Z_{34}$	$-Z_{35}$	$-Z_{36}$	0	0	0	0	0	0	0	0	0		
	σ_{33}	Z_{41}	Z_{42}	Z_{43}	Z_{44}	Z_{45}	Z_{46}	$-Z_{41}$	$-Z_{42}$	$-Z_{43}$	$-Z_{44}$	$-Z_{45}$	$-Z_{46}$	0	0	0	0	0	0	0	0	0		
	σ_{13}	Z_{51}	Z_{52}	Z_{53}	Z_{54}	Z_{55}	Z_{56}	$-Z_{51}$	$-Z_{52}$	$-Z_{53}$	$-Z_{54}$	$-Z_{55}$	$-Z_{56}$	0	0	0	0	0	0	0	0	0		
σ_{23}	Z_{61}	Z_{62}	Z_{63}	Z_{64}	Z_{65}	Z_{66}	$-Z_{61}$	$-Z_{62}$	$-Z_{63}$	$-Z_{64}$	$-Z_{65}$	$-Z_{66}$	0	0	0	0	0	0	0	0	0	0		
								Bottom, Layer 3						Top, Layer 4										
Interface 3	u_1	0	0	0	0	0	0	Z_{11}	Z_{12}	Z_{13}	Z_{14}	Z_{15}	Z_{16}	$-Z_{11}$	$-Z_{12}$	$-Z_{13}$	$-Z_{14}$	$-Z_{15}$	$-Z_{16}$	0	0	0	0	0
	u_2	0	0	0	0	0	0	Z_{21}	Z_{22}	Z_{23}	Z_{24}	Z_{25}	Z_{26}	$-Z_{21}$	$-Z_{22}$	$-Z_{23}$	$-Z_{24}$	$-Z_{25}$	$-Z_{26}$	0	0	0	0	0
	u_3	0	0	0	0	0	0	Z_{31}	Z_{32}	Z_{33}	Z_{34}	Z_{35}	Z_{36}	$-Z_{31}$	$-Z_{32}$	$-Z_{33}$	$-Z_{34}$	$-Z_{35}$	$-Z_{36}$	0	0	0	0	0
	σ_{33}	0	0	0	0	0	0	Z_{41}	Z_{42}	Z_{43}	Z_{44}	Z_{45}	Z_{46}	$-Z_{41}$	$-Z_{42}$	$-Z_{43}$	$-Z_{44}$	$-Z_{45}$	$-Z_{46}$	0	0	0	0	0
	σ_{13}	0	0	0	0	0	0	Z_{51}	Z_{52}	Z_{53}	Z_{54}	Z_{55}	Z_{56}	$-Z_{51}$	$-Z_{52}$	$-Z_{53}$	$-Z_{54}$	$-Z_{55}$	$-Z_{56}$	0	0	0	0	0
σ_{23}	0	0	0	0	0	0	Z_{61}	Z_{62}	Z_{63}	Z_{64}	Z_{65}	Z_{66}	$-Z_{61}$	$-Z_{62}$	$-Z_{63}$	$-Z_{64}$	$-Z_{65}$	$-Z_{66}$	0	0	0	0	0	
														Bottom, Layer 4										
Interface 4	u_1	0	0	0	0	0	0	0	0	0	0	0	0	Z_{11}	Z_{12}	Z_{13}	Z_{14}	Z_{15}	Z_{16}	0	0	0	0	0
	u_2	0	0	0	0	0	0	0	0	0	0	0	0	Z_{21}	Z_{22}	Z_{23}	Z_{24}	Z_{25}	Z_{26}	0	0	0	0	0
	u_3	0	0	0	0	0	0	0	0	0	0	0	0	Z_{31}	Z_{32}	Z_{33}	Z_{34}	Z_{35}	Z_{36}	0	0	0	0	0
	σ_{33}	0	0	0	0	0	0	0	0	0	0	0	0	Z_{41}	Z_{42}	Z_{43}	Z_{44}	Z_{45}	Z_{46}	0	0	0	0	0
	σ_{13}	0	0	0	0	0	0	0	0	0	0	0	0	Z_{51}	Z_{52}	Z_{53}	Z_{54}	Z_{55}	Z_{56}	0	0	0	0	0
σ_{23}	0	0	0	0	0	0	0	0	0	0	0	0	Z_{61}	Z_{62}	Z_{63}	Z_{64}	Z_{65}	Z_{66}	0	0	0	0	0	

Figure 34: Global Matrix for a five-layered monoclinic plate with two vacuum half-spaces

For Lamb waves, the stresses are zero on the top and bottom surfaces. Solution to this boundary condition is performed by separating the sub-matrix of top and bottom layers in Eqn. (2.59) into their associated stresses and displacements to form a new matrix. After separation,

only the stress components at the top and bottom most surfaces are taken into account for obtaining the Lamb wave dispersion curves. Neglecting the displacement components from the top and bottom most layers of Eqn. (2.59), the new matrix can be expanded as indicated in Figure 35.

	Top, Layer 2																								
σ_{33}	$-Z_{41}$	$-Z_{42}$	$-Z_{43}$	$-Z_{44}$	$-Z_{45}$	$-Z_{46}$	0	0	0	0	0	0	0	0	0	0	0	0	0	0	0	0	U_{11}	0	
σ_{13}	$-Z_{51}$	$-Z_{52}$	$-Z_{53}$	$-Z_{54}$	$-Z_{55}$	$-Z_{56}$	0	0	0	0	0	0	0	0	0	0	0	0	0	0	0	0	0	U_{12}	0
σ_{23}	$-Z_{61}$	$-Z_{62}$	$-Z_{63}$	$-Z_{64}$	$-Z_{65}$	$-Z_{66}$	0	0	0	0	0	0	0	0	0	0	0	0	0	0	0	0	0	U_{13}	0
	Bottom, Layer 2						Top, Layer 3																		
u_1	Z_{11}	Z_{12}	Z_{13}	Z_{15}	Z_{15}	Z_{16}	$-Z_{21}$	$-Z_{22}$	$-Z_{23}$	$-Z_{24}$	$-Z_{25}$	$-Z_{26}$	0	0	0	0	0	0	0	0	0	0	U_{14}	0	
u_2	Z_{21}	Z_{22}	Z_{23}	Z_{16}	Z_{25}	Z_{26}	$-Z_{21}$	$-Z_{22}$	$-Z_{23}$	$-Z_{24}$	$-Z_{25}$	$-Z_{26}$	0	0	0	0	0	0	0	0	0	0	U_{15}	0	
u_3	Z_{31}	Z_{32}	Z_{33}	Z_{34}	Z_{35}	Z_{36}	$-Z_{31}$	$-Z_{32}$	$-Z_{33}$	$-Z_{34}$	$-Z_{35}$	$-Z_{36}$	0	0	0	0	0	0	0	0	0	0	U_{16}	0	
σ_{33}	Z_{41}	Z_{42}	Z_{43}	Z_{44}	Z_{45}	Z_{46}	$-Z_{41}$	$-Z_{42}$	$-Z_{43}$	$-Z_{44}$	$-Z_{45}$	$-Z_{46}$	0	0	0	0	0	0	0	0	0	0			
σ_{13}	Z_{51}	Z_{52}	Z_{53}	Z_{54}	Z_{55}	Z_{56}	$-Z_{51}$	$-Z_{52}$	$-Z_{53}$	$-Z_{54}$	$-Z_{55}$	$-Z_{56}$	0	0	0	0	0	0	0	0	0	0	U_{11}	0	
σ_{23}	Z_{61}	Z_{62}	Z_{63}	Z_{64}	Z_{65}	Z_{66}	$-Z_{61}$	$-Z_{62}$	$-Z_{63}$	$-Z_{64}$	$-Z_{65}$	$-Z_{66}$	0	0	0	0	0	0	0	0	0	0	U_{12}	0	
							Bottom, Layer 3						Top, Layer 4												
u_1	0	0	0	0	0	0	Z_{11}	Z_{12}	Z_{13}	Z_{14}	Z_{15}	Z_{16}	$-Z_{11}$	$-Z_{12}$	$-Z_{13}$	$-Z_{14}$	$-Z_{15}$	$-Z_{16}$	U_{13}	0					
u_2	0	0	0	0	0	0	Z_{21}	Z_{22}	Z_{23}	Z_{24}	Z_{25}	Z_{26}	$-Z_{21}$	$-Z_{22}$	$-Z_{23}$	$-Z_{24}$	$-Z_{25}$	$-Z_{26}$	U_{14}	0					
u_3	0	0	0	0	0	0	Z_{31}	Z_{32}	Z_{33}	Z_{34}	Z_{35}	Z_{36}	$-Z_{31}$	$-Z_{32}$	$-Z_{33}$	$-Z_{34}$	$-Z_{35}$	$-Z_{36}$	U_{15}	0					
σ_{33}	0	0	0	0	0	0	Z_{41}	Z_{42}	Z_{43}	Z_{44}	Z_{45}	Z_{46}	$-Z_{41}$	$-Z_{42}$	$-Z_{43}$	$-Z_{44}$	$-Z_{45}$	$-Z_{46}$	U_{16}	0					
σ_{13}	0	0	0	0	0	0	Z_{51}	Z_{52}	Z_{53}	Z_{54}	Z_{55}	Z_{56}	$-Z_{51}$	$-Z_{52}$	$-Z_{53}$	$-Z_{54}$	$-Z_{55}$	$-Z_{56}$	U_{11}	0					
σ_{23}	0	0	0	0	0	0	Z_{61}	Z_{62}	Z_{63}	Z_{64}	Z_{65}	Z_{66}	$-Z_{61}$	$-Z_{62}$	$-Z_{63}$	$-Z_{64}$	$-Z_{65}$	$-Z_{66}$	U_{12}	0					
													Bottom, Layer 4												
σ_{33}	0	0	0	0	0	0	0	0	0	0	0	0	Z_{41}	Z_{42}	Z_{43}	Z_{44}	Z_{45}	Z_{46}	U_{13}	0					
σ_{13}	0	0	0	0	0	0	0	0	0	0	0	0	Z_{51}	Z_{52}	Z_{53}	Z_{54}	Z_{55}	Z_{56}	U_{14}	0					
σ_{23}	0	0	0	0	0	0	0	0	0	0	0	0	Z_{61}	Z_{62}	Z_{63}	Z_{64}	Z_{65}	Z_{66}	U_{15}	0					
																			U_{16}	0					

Figure 35: Global Matrix with zero surface stress boundary condition

Solution for the Lamb wave propagation, hence the dispersion curves are obtained by finding a non-trivial solution of the above characteristic equation presented in Figure 35:

$$[Z]\{U\} = 0 \tag{2.60}$$

Where, $[Z]$ is the global matrix and $\{U\}$ is the amplitude vector.

Finding $|Z|=0$ numerically yields the Lamb wave dispersion curve, which is presented in the next section.

2.2.5 NUMERICAL SOLUTION OF LAMB WAVE DISPERSION CURVES

The numerical solution for the propagation of Lamb wave in anisotropic medium is similar to that of an isotropic medium as provided by Rose [J. L. Rose, 1999]. However, the longitudinal and transverse velocities are coupled together in the case of anisotropic media, which makes the solution complicated. Also at any given frequency there exist infinite wavenumbers both real and imaginary satisfying the Lamb wave equations. The Lamb wave equations are thus solved numerically in MATLAB to obtain the dispersion curves using both the Transfer and Global Matrix approaches. It was found that the Transfer Matrix approach was numerically unstable for the monoclinic laminate, thus only the Global Matrix approach was considered in this research. The flow chart of the solution process is shown in Figure 36. The dispersion curve (c_p vs. $f2h$) can be constructed using the steps shown in Figure 36 for various symmetric ($S_0, S_1, S_2, S_3, S_4, \dots$) and anti-symmetric ($A_0, A_1, A_2, A_3, A_4, \dots$) modes.

The group velocity c_g for the laminate can be approximated from phase velocity c_p using [V. Giurgiutiu, 2008]:

$$c_g = c_p^2 \left[c_p - (fd) \frac{dc_p}{d(fd)} \right]^{-1} \quad (2.61)$$

Where, $f = \frac{\omega}{2\pi}$ is the frequency of oscillation and d is the laminate thickness

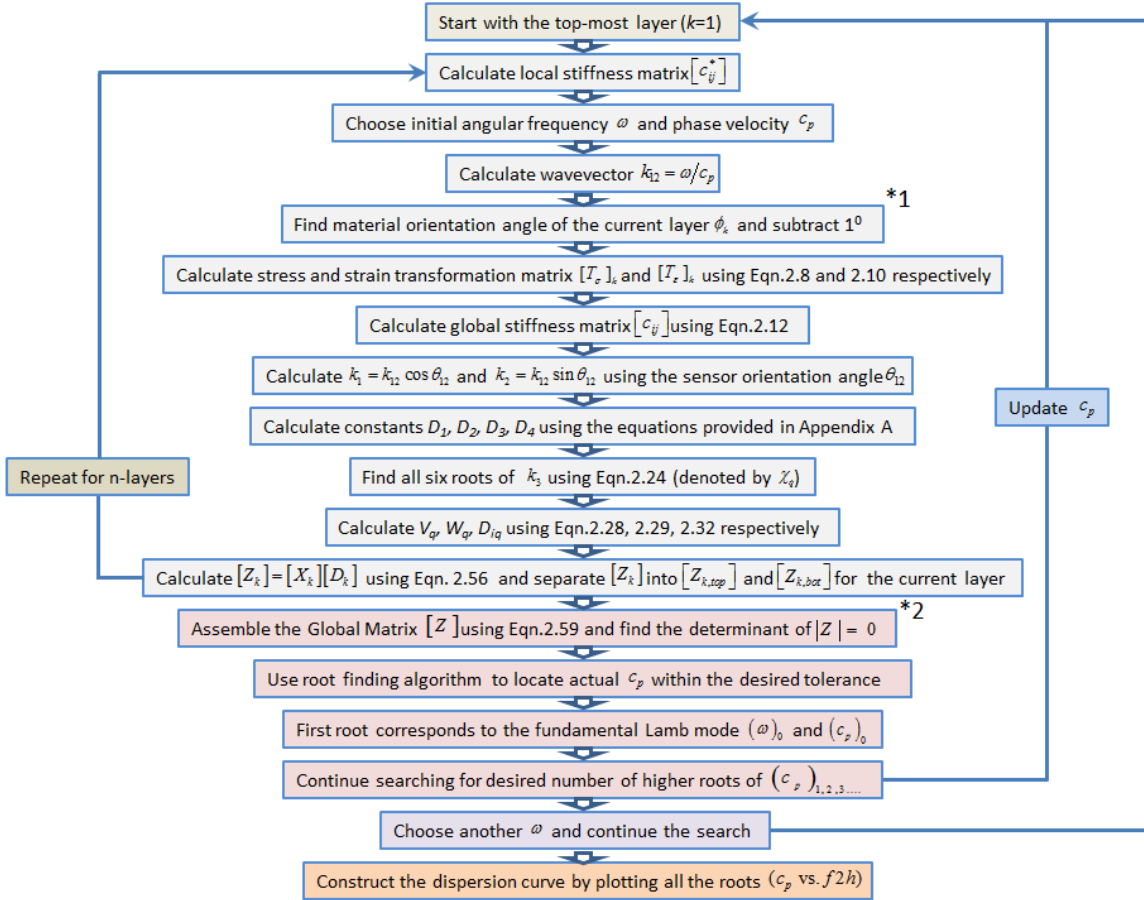


Figure 36: Flow chart to numerically solve Lamb wave equations using Global Matrix approach

Referring to Figure 36, *1 and *2 are described below:

*1: For orthotropic and higher symmetry materials during individual layer calculation; whenever the material orientation angle (fibre orientation angle within a layer) equals the sensor orientation angle (considered angle for wave propagation or the orientation angle between the wave source and sensor), the quasi-transverse horizontal wave decouples into pure shear horizontal wave. This reduces the total quasi waves from six to four and Eqn. (2.28) and (2.29) go to zero. As such, the Global Matrix approach became numerically unstable when six waves were combined with four waves due to the decoupling effect and no solution was found. Therefore, a simple solution is proposed by subtracting the material orientation by 1°, which ensures the six waves travelling along the plane at any given material and sensor

angles. The numerical stability was tested by subtracting the material orientation angle by 0.1° to 2° in 0.1° increments for different laminate configurations. It was found that minimum of 1° was required to maintain numerical stability of the solution. Subtracting 1° from the material orientation angle has very minimal effect on the overall stiffness of the laminate. This is because fibre misalignments occur frequently in composite manufacturing process and it has been reported that misalignments of $\pm 10^\circ$ produces only a 3% change in the laminate Young's Modulus [J. M. Berthelot, 1982].

*2: The numerical solution was found to be stable when the entire Global Matrix was divided by the largest term within the matrix before calculating its determinant.

Software that was developed in MATLAB to generate the Lamb wave dispersion curve using the procedure shown in Figure 36 is presented in the next section.

2.2.6 SOFTWARE TO GENERATE THE LAMB WAVE DISPERSION CURVE

In order to numerically solve the Lamb wave dispersion equations for both isotropic and monoclinic composite laminate, custom software was developed in MATLAB with a Graphical User Interface (GUI) as shown in Figure 37.

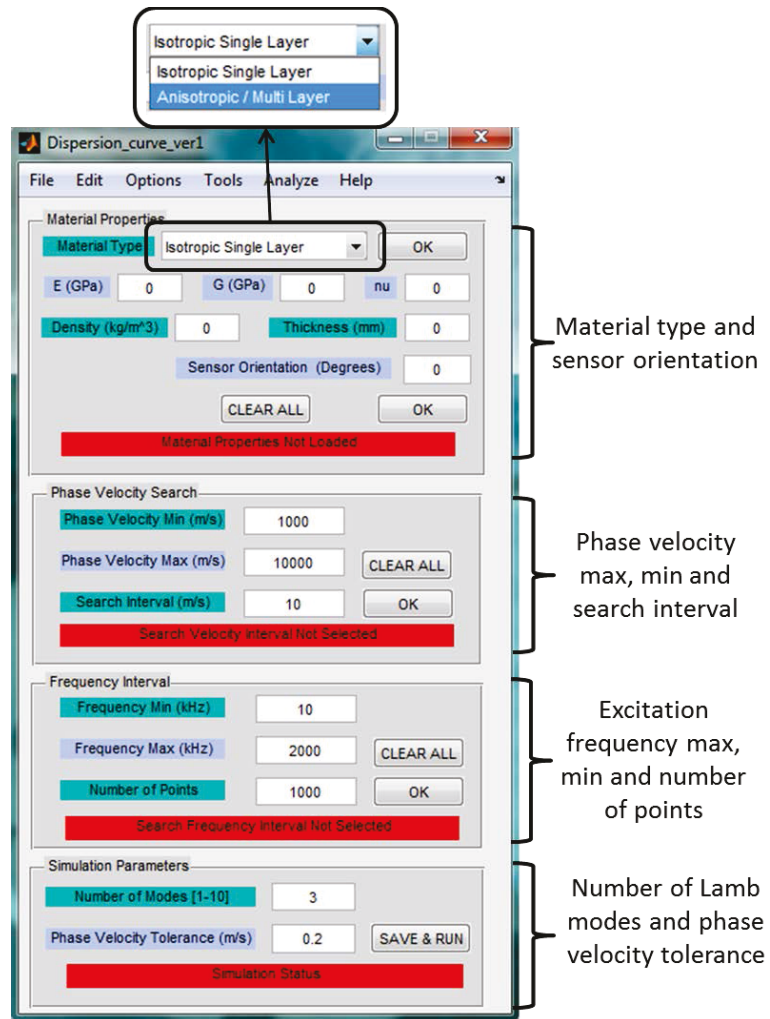


Figure 37: MATLAB GUI to generate Lamb wave dispersion curves

The software allows the user to select the type of material between an isotropic, a single layer anisotropic, multi-layered anisotropic, or combination of isotropic and anisotropic. For isotropic material the user can directly enter the material properties including the thickness on the main GUI as shown in Figure 38.

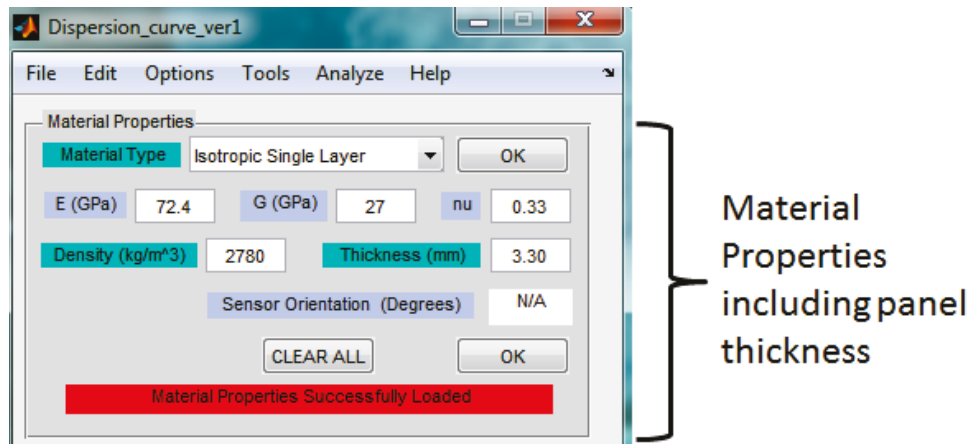


Figure 38: MATLAB GUI showing the isotropic material input

For a single/multi-layer anisotropic material user can input the number of lamina, choose the material properties for each lamina, their corresponding thickness, and the orientation in a separate window as shown in Figure 39. The material properties for each lamina can be selected from a text file as shown in Figure 39.

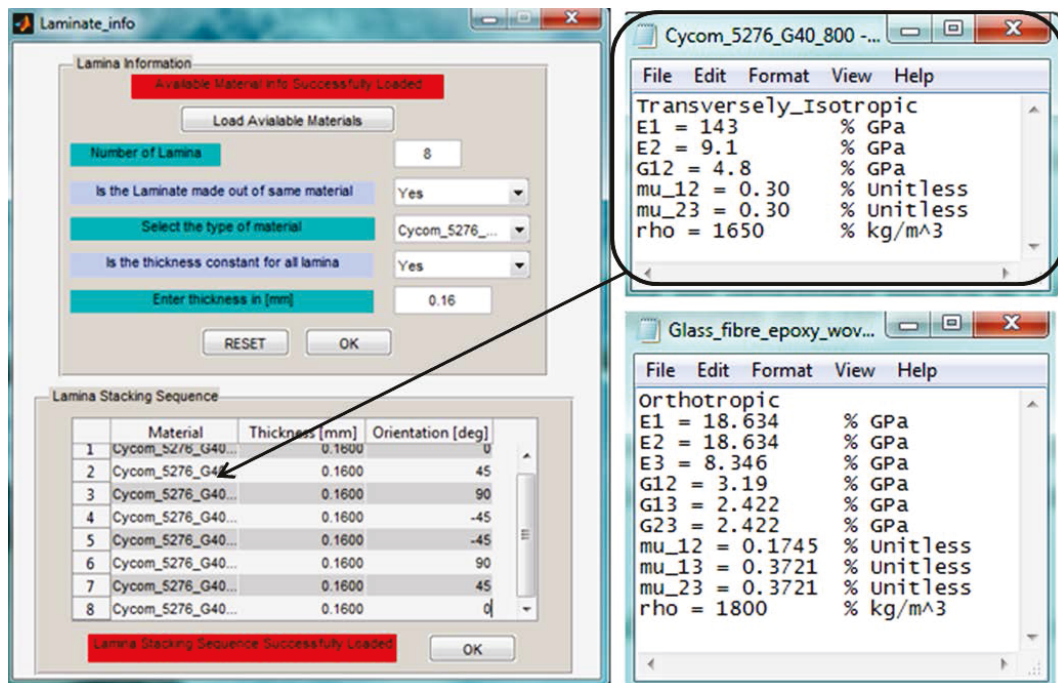


Figure 39: GUI for n-layered anisotropic material with text file containing the material properties

As shown in Figure 37, user can then proceed by inputting the search intervals for phase velocity and excitation frequency. For isotropic materials, the user can also choose the number of Lamb wave modes, which is not available for anisotropic material because the GM approach does not separate the Lamb modes into corresponding symmetric, anti-symmetric, and shear-horizontal waves. The output of the software is a text file containing frequency vs. phase/group velocity data, which can be further processed within MATLAB or in Excel.

2.2.7 EXPERIMENTAL VALIDATION

In order to verify the presented method to generate the Lamb wave dispersion curves for an n-layered composite laminate, two different composite panels were tested. The first specimen was constructed out of unidirectional carbon-fibre epoxy G40-800/5276-1 prepreg commonly used in the aerospace industry. The second specimen was a fibre-metal laminate (GLARE 3-3/4), which was constructed out of aluminum and unidirectional glass-fibre epoxy. The glass reinforced fibre-metal laminate (GLARE) was chosen to prove the versatility of the proposed method, since GLARE combines two completely different material types, one being isotropic (aluminum) and another being transversely isotropic (glass-fibre reinforced epoxy). Material type and layup information for both composites are provided in Table 1.

Table 1: Specimen type, layup, and material

Specimen	Layup	Ply Thickness	Material
Carbon-fibre epoxy composite	$[0/90/+45/-45]_{\text{SYM}}$	0.17 mm	G40-800/5276-1 Cytec Industries
GLARE 3-3/4	$[Al/0/90/Al/90/0/Al]$	Al: 0.33 mm Glass fibre: 0.127 mm	Al 2024-T3 S2 glass-fibre FM 94 resin

The carbon-fibre panel was inspected at NRC using a pulse-echo ultrasonic C-scan technique to identify any internal damage introduced during manufacturing and cutting. The C-scan image shown in Figure 40 reveals that there is no detectable internal damage present in the carbon-fibre panel. The GLARE panel was purchased pre-manufactured from a commercial supplier for a previous project and had already been found to be defect free [J. F. Laliberté, 2002].

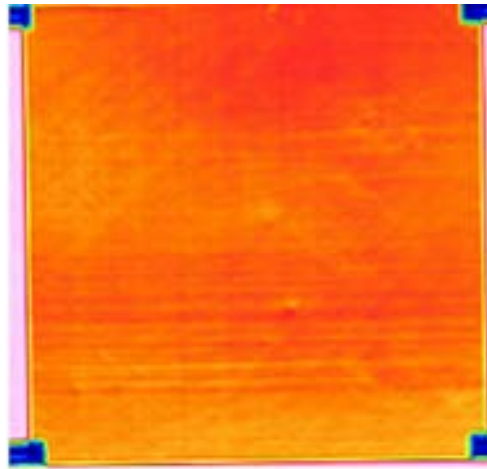


Figure 40: Ultrasonic C-scan image of carbon-fibre panel

The composite panels were instrumented with PZT transducers acquired from Acellent Technologies, Inc. and were permanently bonded onto the composite plate using M-Bond AE-10 adhesive from Vishay Micro-Measurements. Panel dimensions along with the transducer locations for carbon-fibre and GLARE are shown in Figure 41 and Figure 42 respectively. Sensor locations for the carbon-fibre panel were selected as a square pattern as compared to the circular pattern for GLARE because the carbon-fibre specimen was constructed to be used as a test panel for introducing and detecting discrete damage.

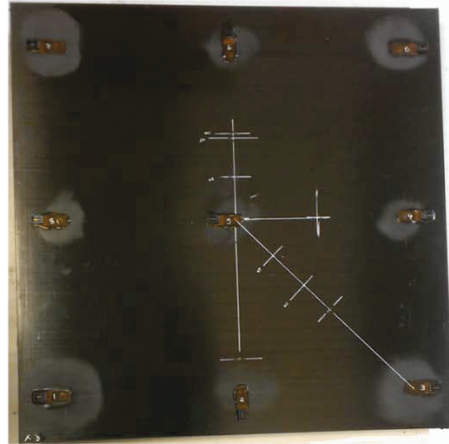
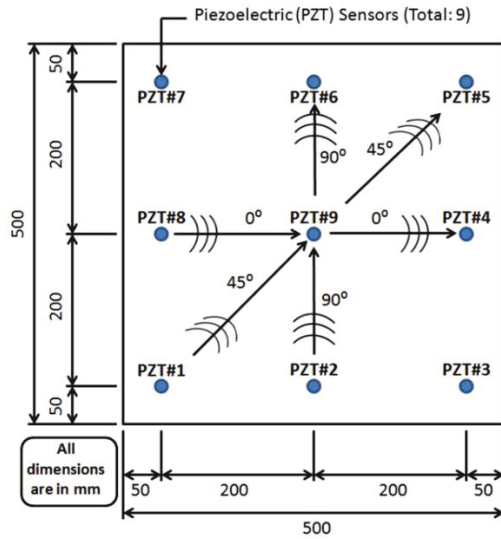


Figure 41: Dimension and location of transducers of carbon-fibre epoxy laminate

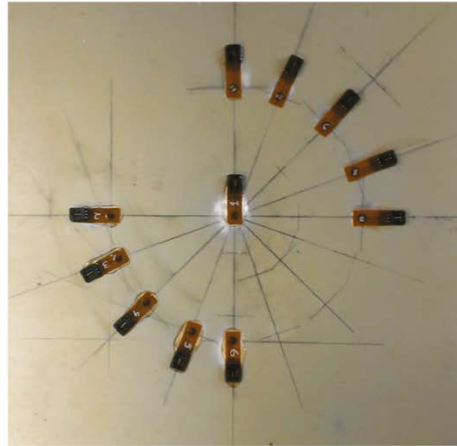
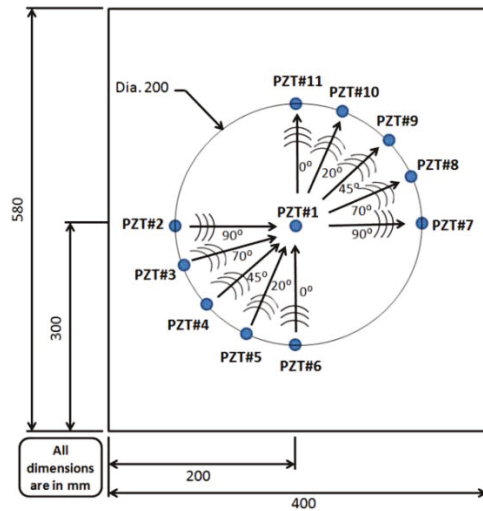


Figure 42: Dimension and location of transducers of GLARE panel

The installed PZTs were excited at different frequency intervals from 20 kHz to 500 kHz using five bursts of windowed sinusoidal waves at 35 V, which aids in focusing the excitation energy at the desired frequency as shown in Figure 43 for 200 kHz. The ultrasonic signals to excite Lamb

waves were generated using a Physical Acoustics Corp. ARB-1410 arbitrary waveform generator board and associated WaveGen1410 software.

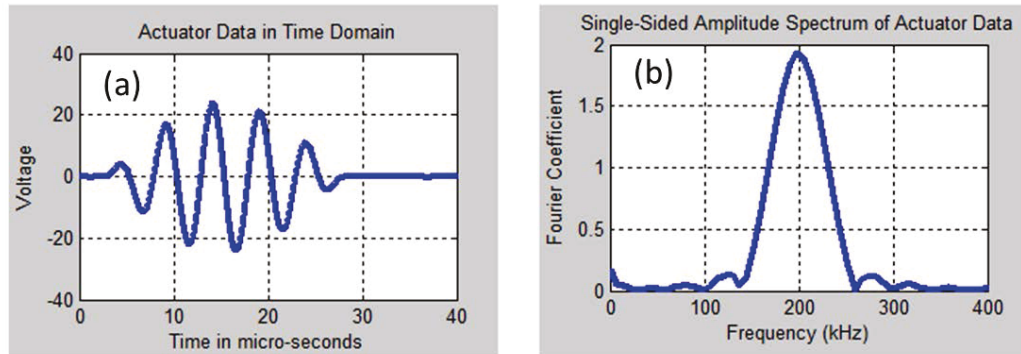


Figure 43: 200 kHz actuator signal in (a) Time domain and (b) Frequency domain

Signals were acquired at 125 MS/s and saved using a Tektronix TDS 5104 digital oscilloscope. Figure 44 shows the experimental setup in which the PZTs installed on the composite plate are connected to the signal generator and the oscilloscope. A similar procedure was followed to generate and gather Lamb waves in the GLARE panel. A MATLAB-based program shown in Figure 45 was also developed to process the acquired data from the oscilloscope in order to extract the relevant phase and group velocities.

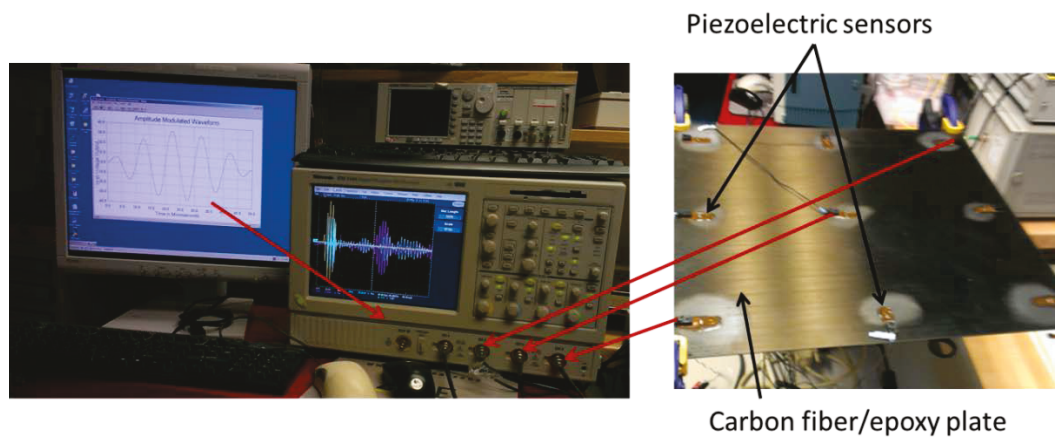


Figure 44: Experimental setup to generate and receive Lamb waves

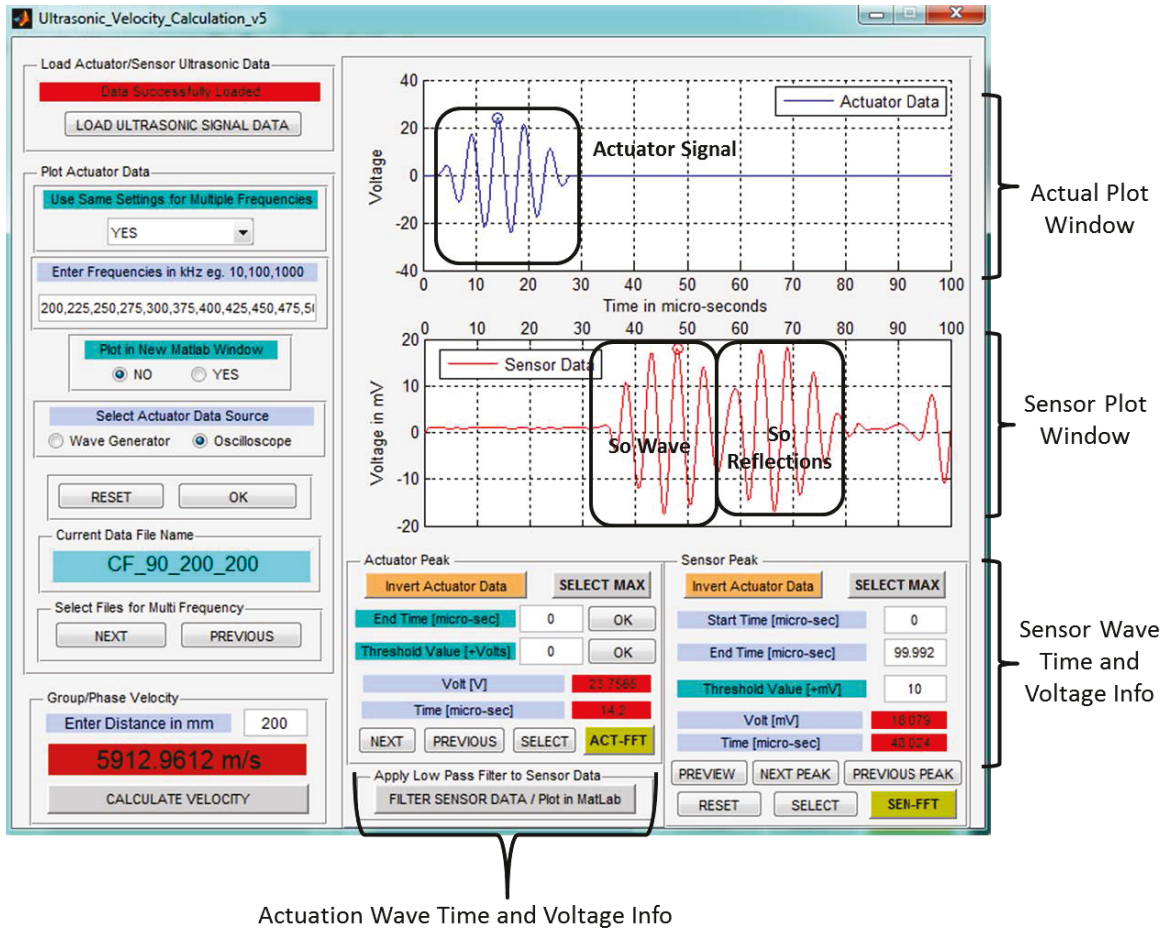


Figure 45: Custom MATLAB software developed to extract phase and group velocity data

As for the numerical solution, the material properties provided in Table 2 were used to generate the Lamb wave dispersion curves using the software described in Section 2.2.6.

Table 2: Material properties used to generate the dispersion curve

G40-800/5276-1 [K. Fayazbakhsh et al., 2013]	S2-FM94 [M. Hagenbeek, 2005]	Al 2024-T3 [ASM Al 2024-T3, 2013]
Transversely Isotropic	Transversely Isotropic	Isotropic
$E_{11} = 143$ GPa	$E_{11} = 50.6$ GPa	$E = 73.1$ GPa
$E_{22} = 9.1$ GPa	$E_{22} = 9.9$ GPa	$G = 28$ GPa
$G_{12} = 4.8$ GPa	$G_{12} = 3.7$ GPa	$\mu = 0.33$
$\mu_{12} = 0.3$	$\mu_{12} = 0.32$	Density = 2780 kg/m ³
$\mu_{23} = 0.3$	$\mu_{23} = 0.32$	
Density = 1650 kg/m ³	Density = 1980 kg/m ³	

The waves were excited and gathered at three different propagation angles of 0°, 45°, and 90° for the carbon-fibre panel and at six different angles of 0°, 20°, 45°, 70° and 90° for the GLARE panel. The transducers used to excite the waves for different angles are shown in Figure 41 and Figure 42 for carbon-fibre and GLARE panel, respectively. The phase and group velocities of the fundamental symmetric (S_0) and anti-symmetric (A_0) Lamb waves were extracted by tracking the peaks of each individual wave and the wave envelope respectively using a custom program developed in MATLAB as shown in Figure 45. The experiments were repeated on different days to confirm repeatability. No experimental data were available for comparing the shear-horizontal wave as the setup/transducers were unable to generate the shear-horizontal wave. A Butterworth low-pass filter was used to remove any high frequency noise and to smooth out the acquired signal. In order to eliminate the phase shift due to application of the low-pass filter and any time discrepancies between the signal generator and the PZT transducer, the waves were generated using one actuator and captured using two different sensors along the desired propagation angle. For example, for 0° propagation angle in GLARE (Figure 42), the waves were excited using PZT#6 and captured using PZT#1 and PZT#11. The process was repeated by switching the actuator and the second sensor, so that PZT#11 was now used as actuator and PZT#1 and PZT#6 were used to capture the wave. The wave velocities were calculated between the two sensor/capturing PZTs. The results presented here are the averaged velocities between the two reversed paths. Due to reflections from the boundaries as shown in Figure 45 only the first group of waves to arrive and being recognizable in the sensor signals were analyzed. For certain frequency ranges, (100-200) kHz for carbon-fibre and (100-150) kHz for GLARE, the corresponding acquired wave signals were discarded, since it was difficult to decipher and distinguish between the fundamental symmetric and anti-symmetric waves. Due to the tuning

effects relative to transducer dimensions, excited frequencies, and wavelengths at lower frequencies the anti-symmetric Lamb wave was dominant as compared to higher frequencies where the symmetric wave was the dominant one. Although, the propagation velocity of the fundamental symmetric wave mode is also higher than the anti-symmetric mode at lower frequencies, due to the tuning effect, the anti-symmetric mode is predominantly excited at such lower frequencies, with the symmetric mode not being recognizable in the sensor signals. The analytical and experimental dispersion curves for carbon-fibre panel and GLARE are shown in Figure 46 and Figure 47 respectively.

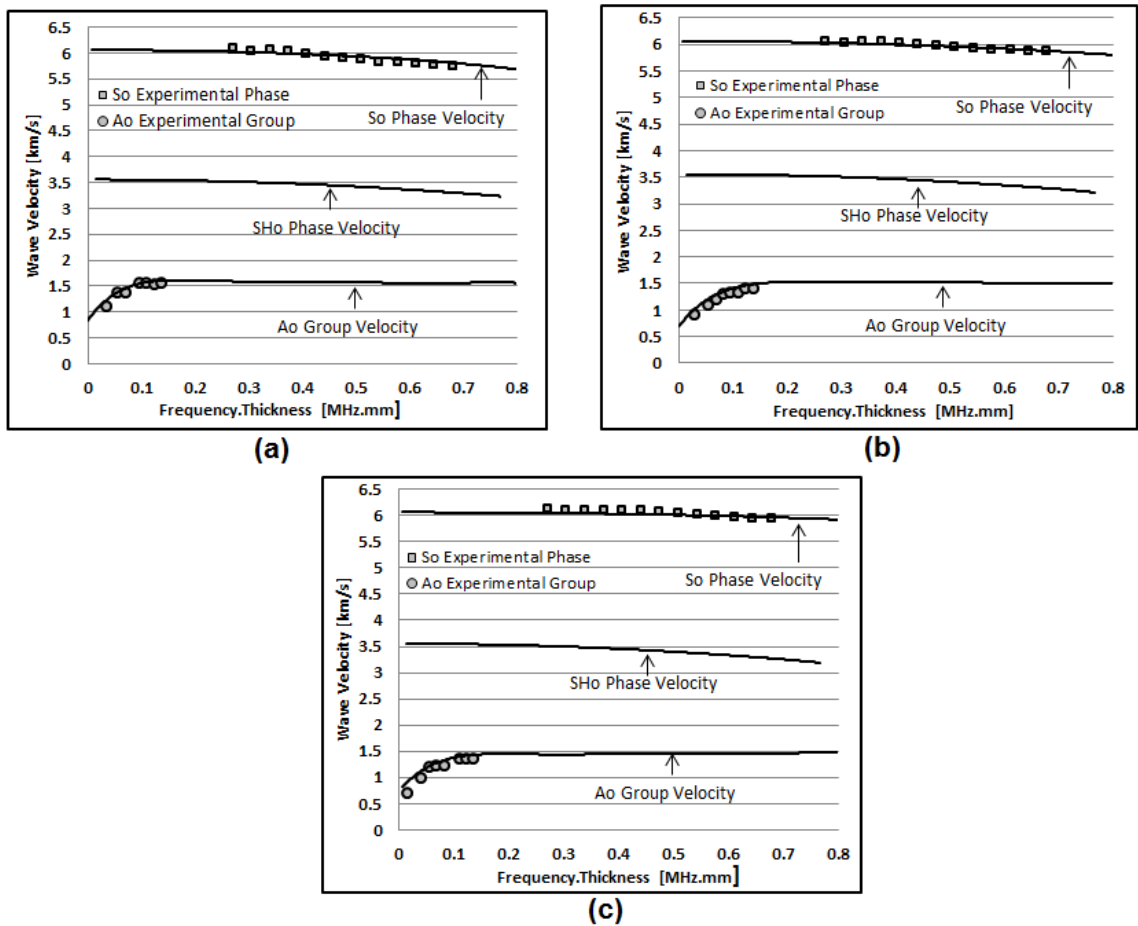


Figure 46: Dispersion curve for carbon-fibre epoxy at (a) 0°, (b) 45°, and (c) 90° sensor orientations, where solid lines represent the theoretically generated Lamb wave dispersion curves

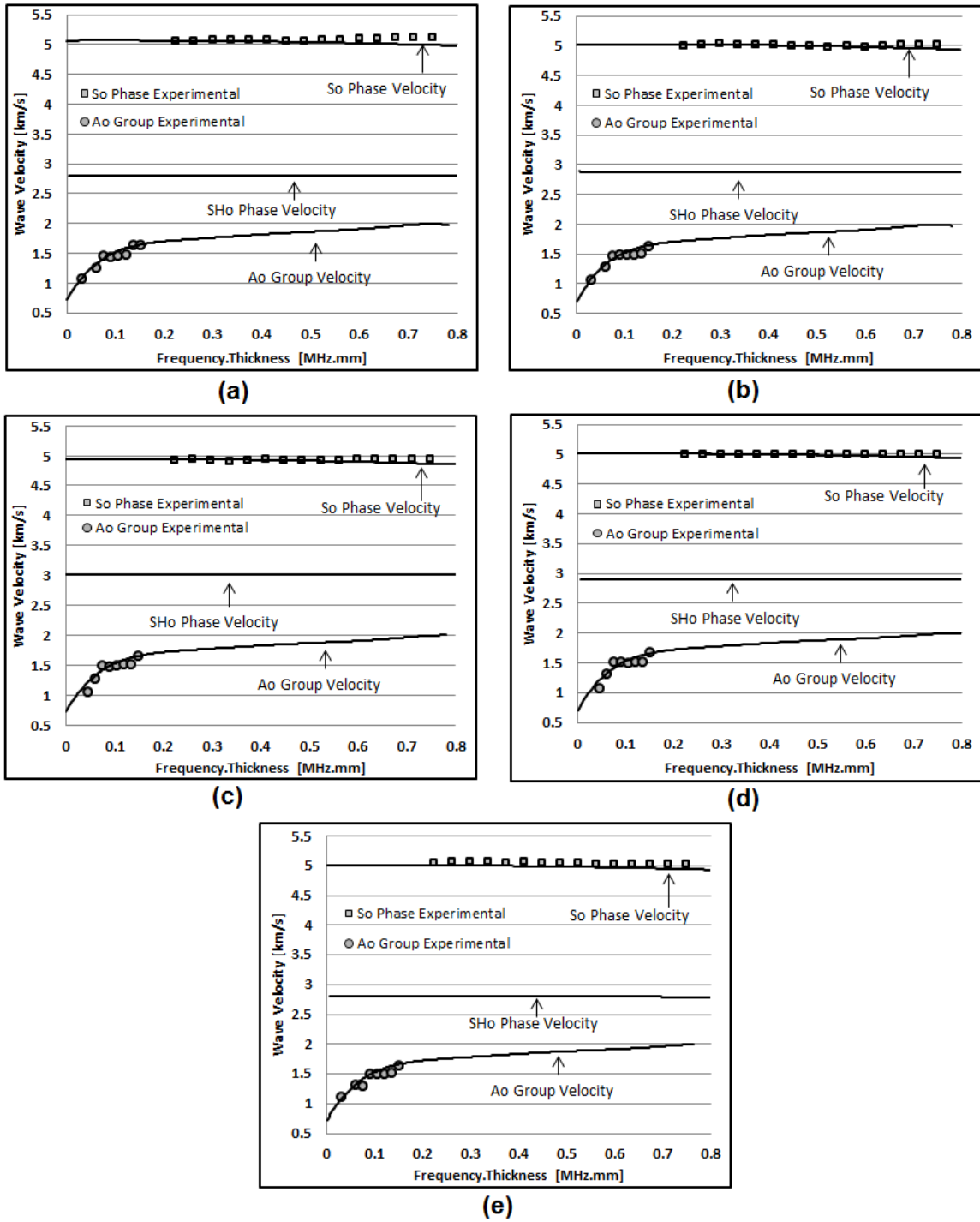


Figure 47: Dispersion curve for GLARE at (a) 0°, (b) 20°, (c) 45°, (d) 70°, and (e) 90° sensor orientations, where solid lines represent the theoretically generated Lamb wave dispersion curves

The largest differences between the experimental and theoretical results corresponded to 5.8% in 90° GLARE and 2.4% in 0° GLARE for anti-symmetric and symmetric Lamb waves respectively. The minor discrepancies found at higher frequencies in GLARE, for a 0° propagation angle can be explained by the difference in the stiffness of the aluminum between its rolling and transverse direction. In previous experiments by Rocha [B. Rocha, 2011], a difference of approximately 200 m/s was found to exist between the velocities of Lamb waves propagating in an isotropic aluminum panel in the plate rolling direction and the transverse direction. The error attributed to the anti-symmetric mode was due the proper extraction of group velocities, which can be seen as steps in both Figure 46 and Figure 47. The step was thought to be due to the complex wave propagation characteristics of Lamb waves in composites, but similar steps were also found in an isotropic aluminum panel disproving this hypothesis. The step was actually due to the wave tracking software tracing only the wave peaks; despite the fact that the actual group wave peak could be anywhere between the highest peak and the one adjacent to it. Other sources that may have contributed to the observed discrepancies include differences between the provided material properties and the actual properties of the lamina, accuracy limitations in the distance measurements between transducers (± 0.2 mm), surface bonding effects, and the effectiveness of the PZT transducers at higher frequencies. Through these results and the ones depicted in Figure 46 and Figure 47, it is evident that the proposed method predicts with considerable accuracy the Lamb wave dispersion curves for different types of materials, either a monoclinic or a combination of different types of symmetries.

2.2.7.1 Comparison with the classical laminated plate theory

As mentioned earlier in Section 2.2.3 one of the simplest and most commonly used methods to generate the Lamb wave dispersion curve for a composite laminate is to use the first-order Classical Laminate Plate Theory without considering the transverse shear effects. In this method the average elastic constants of a laminate are found by inverting the laminate ABD matrix and assuming an isotropic behavior in order to reduce the numerical complexity associated with anisotropy. For this comparison study, the previously used carbon-fibre epoxy was selected, whose material type and lay-up sequence is provided in Table 1 and the experimental setup and results are discussed in Section 2.2.7.

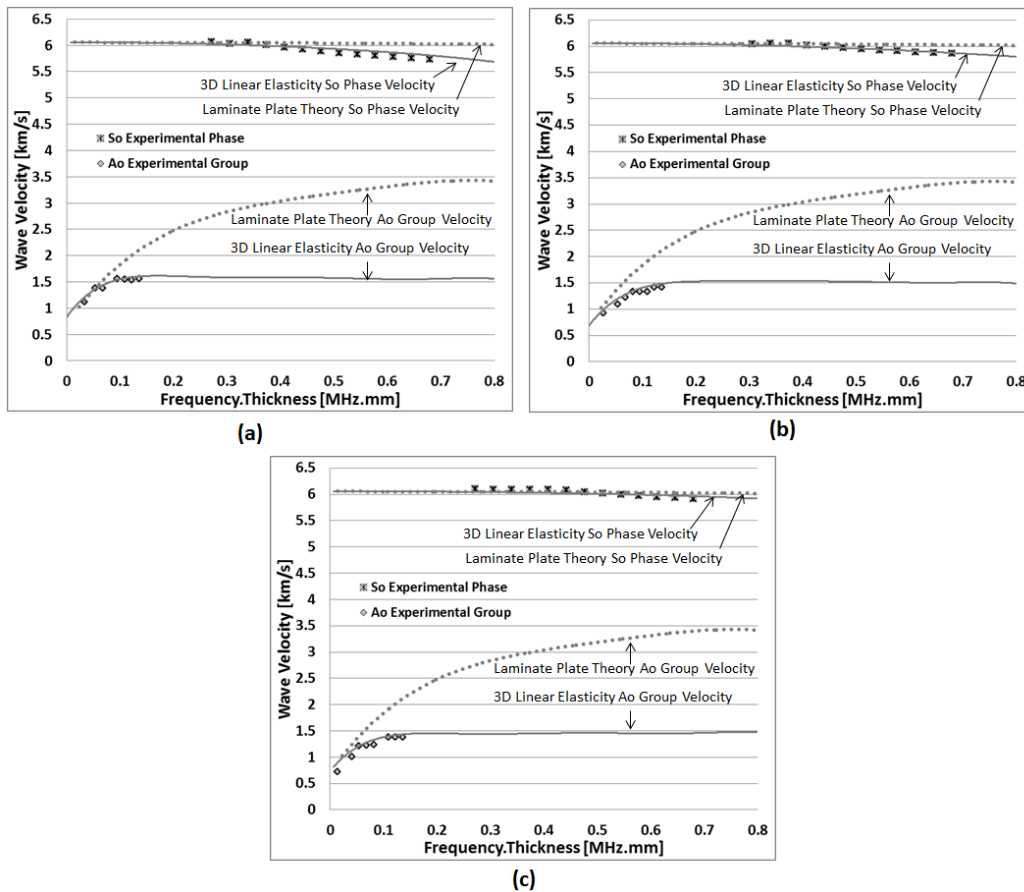


Figure 48: Comparison of 3D linear elasticity and classical laminate plate theory for Lamb wave travelling in (a) 0°, (b) 45°, and (c) 90°.

From Figure 48, it is evident that the experimental data follows the 3D linear elastic approach developed in this thesis closely as compared to the CLPT. The CLPT overestimated the fundamental anti-symmetric mode group velocity by a factor of two at higher frequency. CLPT also tend to remain constant for the symmetric wave phase velocity and failed to predict the drop off of the symmetric wave at higher frequency especially in 0° (Figure 48a) and 45° (Figure 48b) propagation angles. Therefore, it can be concluded that the analytical method presented in this thesis was able to better predict the Lamb waves' dispersion as compared to the first-order classical laminate plate theory.

CHAPTER 2 SUMMARY

In this chapter, an accurate solution method and a robust procedure for generating Lamb wave dispersion curves for an n-layered monoclinic and higher symmetric composite material is presented. The obtained solution compared positively with the experimental data using two different material types, an 8-layered carbon-fibre epoxy composite panel and a 7-layered fibre-metal laminate GLARE. For comparison purposes, the fundamental symmetric (S_o) and anti-symmetric (A_o) Lamb wave modes were excited at different frequencies between 20 kHz to 500 kHz and gathered for different propagation angles using the piezoelectric transducers. The phase and group velocity data were extracted for the S_o and A_o waves respectively by tracking the wave peaks/envelope using custom developed MATLAB based software. It was found that the presented 3D linear elasticity model followed the experimental data more accurately for both symmetric and anti-symmetric Lamb wave modes as compared to the classical laminate plate theory.

CHAPTER 3: EFFECTS OF LAMINA PROPERTIES ON LAMB WAVES

As discussed in Chapter 2, propagation characteristics of Lamb waves in composites are complex due to material anisotropy and strongly attenuative/dispersive behaviour of the waves, as compared to their metallic counterparts. Parameters of composite materials such as fibre volume fractions, layup sequence, and types of matrix/reinforcements used, strongly influence the wave propagation characteristics. Lamb waves in composite plates propagate in each direction with different velocities, with the shape of the wave front changing with frequency [W. J. Staszewski et al., 2004]. Therefore, in order to develop a reliable Lamb wave based SHM system for composites, it is necessary to understand how the dispersion and Lamb wave propagation changes due to presence of defects and damage, corresponding to changes in the material properties.

In this chapter some of the existing works on the propagation characteristic of Lamb wave due to change in material properties and environmental loadings are presented. Following the summary of the existing work, detail analysis on the effects of composite material properties variability, such as reductions in E_{11} , E_{22} , G_{12} , and density on Lamb waves' behaviour for three different laminate configurations are investigated. Beyond variability in material properties related to manufacturing processes, the aforementioned reductions are generally caused by the presence of defects, damage, and degradation associated with long-term environmental exposure and finding such defects/damage is the primary focus of SHM systems. Some of the typical damages in composites are discussed in Section 1.1.1, which are directly related to the change in material properties. For example: the presence of voids reduces the density; similarly,

fibre damage directly influences the E_{11} stiffness; whereas, the presence of damage in the matrix influences the E_{22} and G_{12} stiffness. It is also well known that fibre fracture occurs prior to total failure of the laminate. This fibre fracture causes changes in the material properties, i.e. fibre modulus, thus affecting the overall stiffness modulus of the composite [N. Pan et al., 1997].

3.1 EXISTING RESEARCH

Lamb wave based SHM systems are required to operate in harsh environments with variable applied loads, vibrations, and temperature variations if the structure is to be monitored during flight. Therefore, effects of these environmental variations on the propagation characteristic of Lamb waves need to be considered. The effect of applied stresses and temperature on phase and group velocities of an isotropic structure was considered by Dodson [J. C. Dodson, 2012], which showed that wave propagation is sensitive to the angle of the applied load. This is primarily due to the formation of an anisotropic behaviour in a material that is initially isotropic as a consequence of the applied load. However, the results found by Dodson [J. C. Dodson, 2012], demonstrated that the sensitivity to applied loads is frequency dependent but its variation is of less than 3 m/s for frequency range up to 60 kHz.

Dodson [J. C. Dodson et al., 2013] also considered the effect of only temperature variation on Lamb waves' propagation. This study demonstrated experimentally and analytically the thermal sensitivity of the dispersion curves and the effect of temperature changes on the wave speed and its dependency on frequency. The results showed changes in Lamb wave speed of up to 5

m/s/°C. Although, 5 m/s/°C does not seem to be a very high value, but an aircraft in operation would suffer temperature changes that might range from 25°C on the ground to -55°C during flight, which translate to a change in velocity of Lamb waves of approximately 400 m/s. Kessler [S. S. Kessler et al., 2002b] studied the effect of variability in material properties such as Young's modulus, density, and Poisson's ratio, and geometrical changes such as thickness, on the Lamb waves' behavior; thereby, creating relationships between material properties and the speed of Lamb waves.

As for the effect of density on the propagation of Lamb wave, an increase in the density of the material causes a reduction in the wave speed, since the wave speed is inversely related to the square root of density. The changes in the density of a composite material may be caused by the presence of trapped moisture and/or due to the presence of void/porosity during manufacturing.

Poisson's ratio variability seems to have little influence on the wave velocity; while the change in the thickness of the specimen has a proportional relationship with the Lamb wave propagation velocity. For example in a thicker specimen, the anti-symmetric A_o Lamb waves travel faster and show greater dispersive behaviour for a given range of actuation frequencies [S. S. Kessler et al., 2002b].

Thus, variability such as defects and damage, regardless of their type or origin, has an intrinsic effect on Lamb wave behaviour. Therefore, the presence of different types of damages in composite materials requires thorough understanding of their effects on Lamb waves' propagation behaviour for proper sensor selection and use of Lamb wave based SHM systems. Dispersion/propagation characteristics of Lamb waves are directly influenced by the variability in material properties, as previously suggested. However, the majority of the work regarding the effect of material properties has been done for isotropic materials. Therefore, detailed analyses on the effects of composite material properties variability, such as reductions in E_{11} , E_{22} , G_{12} , and density on Lamb waves' behaviour are investigated in the following sections.

3.2 EFFECTS OF CHANGES IN THE MATERIAL PROPERTIES

In this section, the effect of changes in the lamina material properties on the propagation characteristic of the fundamental symmetric (S_o) and anti-symmetric (A_o) Lamb wave modes are examined. Higher Lamb wave modes were not considered as they require higher excitation frequency, which corresponds to higher data acquisition rates. Also higher modes are extremely dispersive and multiple higher modes may be present at any given frequency amplifying the difficulty in extracting the proper velocity data. The information presented here can be used for selecting excitation frequency and proper Lamb wave modes, as part of a damage detection algorithm, optimizing/sizing piezoelectric transducers, configuring signal generation/acquisition systems, and characterizing material properties.

3.2.1 METHOD

A unidirectional carbon-fibre epoxy prepreg from Cytec industries (G40-800/5276-1) was used for this study, for which the material type and properties are provided in Table 2 and repeated here in Table 3. The propagation of Lamb waves in this prepreg was characterized and estimated analytically with the obtained results verified experimentally in Chapter 2. This prepreg was selected for the study as it represents one of the most commonly used composite materials for aerospace applications and also due to the fact that the propagation characteristics of Lamb wave have been proven both analytically and experimentally for this material in Chapter 2.

Table 3: Material properties for Cytec G40-800/5276-1 prepreg

Material Type: Transversely Isotropic [K. Fayazbakhsh et al., 2013]
$E_{11} = 143 \text{ GPa}$
$E_{22} = 9.1 \text{ GPa}$
$G_{12} = 4.8 \text{ GPa}$
$\mu_{12} = 0.3$
$\mu_{23} = 0.3$
Density = 1650 kg/m^3
Ply Thickness = 0.17 mm

As discussed earlier, parameters/mechanical properties of composites materials strongly influence the wave propagation characteristics, with this influence being non-linear. This implies that changes in different material properties affect the dispersion characteristic of S_o and A_o modes differently. In this study, the propagation of both S_o and A_o modes in three, 16-ply laminates constructed out of unidirectional carbon-fibre epoxy prepreg from Cytec industries (G40-800/5276-1) for which the material properties are given in Table 3 were analyzed. The layup sequences for the laminates are provided in Table 4.

Table 4: Laminate type and layup sequence

Laminate Type	Layup Sequence
Unidirectional	$[0_{16}]$
Cross-ply	$[0_2/90_2/0_2/90_2]_{\text{SYM}}$
Quasi-isotropic	$[0_2/45_2/90_2/-45_2]_{\text{SYM}}$

The change in the propagation characteristics of Lamb waves in the three laminates provided in Table 4 were analyzed for reductions in the tensile stiffness (E_{11}, E_{22}) and shear stiffness (G_{12}) by 5, 10, 15, and 30 percent off their original value. Similarly, density was reduced by 1, 2, 5, and 10 percent. The effects of changes in Poisson's ratios were not considered, since as it was found by Ryden [N. Ryden et al., 2003] and Kessler [S. S. Kessler et al., 2002b] previously that Lamb waves' propagations are not very sensitive to changes in Poisson's ratios of the host material.

Due to the fact that Lamb waves' velocity in a composite plate varies with the propagation direction, the laminates were analyzed at 0° , 20° , 45° , 70° , and 90° propagation angles to get a complete picture, for all the reductions mentioned above. A program developed in MATLAB (Figure 37) was used to generate the dispersion curves from the analytically derived set of equations for the fundamental anti-symmetric and symmetric Lamb wave modes. Only the fundamental modes were studied since these are the most commonly used modes for damage detection and material characterization as compared to the higher-order modes.

3.2.2 RESULTS

It is known that the symmetric wave stretches and compresses the plate cross-section in the direction of the wave propagation. Since the majority of the wave motion is along the wave direction, the symmetric wave mode is also called the extensional mode. In the anti-symmetric wave, the plate is bent, with the majority of the wave motion being perpendicular to the plate element. Therefore, the anti-symmetric wave mode is also known as flexural mode. This is true at frequencies below the ones in which the first higher-order modes are generated [NDT Resource Center, 2013b].

In the following sections the analytical dispersion and slowness curves of A_o and S_o Lamb wave modes due to changes in various material properties for unidirectional, cross-ply, and quasi-isotropic laminates are provided. For clarity, the slowness curves for the A_o mode are plotted for (0.1, 0.25, 0.5, 0.9) MHz.mm of the propagation frequency-thickness product, whereas only the slowness curves for (0.5, 0.9) MHz.mm are shown for S_o mode. This is because the S_o mode is not as dispersive as the A_o mode at lower frequency-thickness products, with very little differences being observed in such range.

3.2.2.1 Unidirectional laminate

The analytical dispersion curves for A_o and S_o are shown in Figure 49 to Figure 52. Similarly, the slowness curves for A_o and S_o are provided in Figure 53 and Figure 54, respectively.

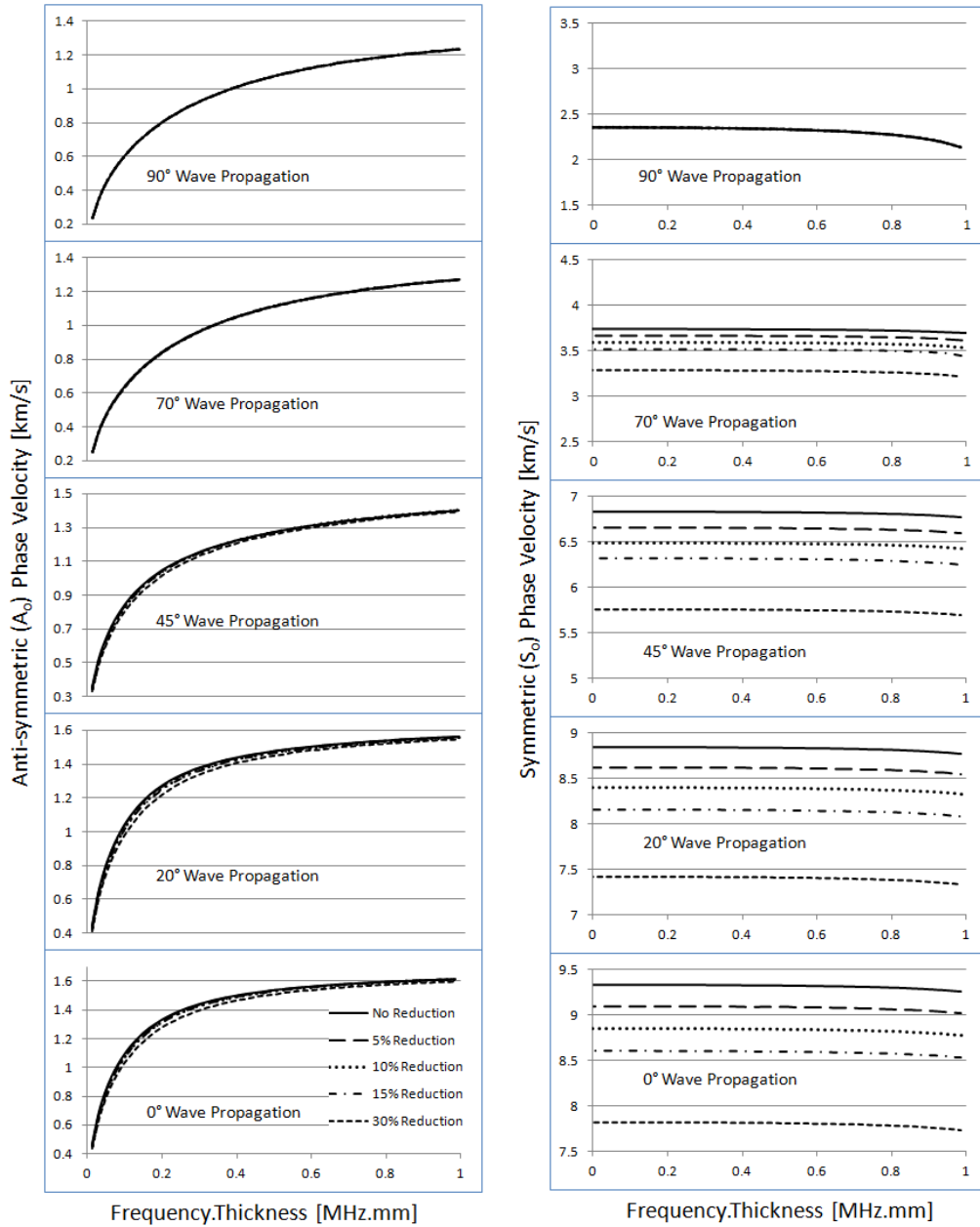


Figure 49: Effects of reducing E_{11} on the dispersion characteristic of A_0 and S_0 waves for unidirectional laminate

From Figure 49 it can be seen that the reduction in E_{11} affected the A_0 waves propagating at 45° and lower angles, with the propagation velocity of the waves reduced in the lower frequency-thickness product range below 0.5 MHz.mm. A similar effect could be observed for

the S_o mode, except the effect was negligible at 90° and grew towards 0° for all frequency-thickness product values since $E_{11} \gg E_{22}$. This suggests the use of S_o mode instead of A_o to detect damage associated with the reduction of E_{11} for unidirectional laminate at propagation angles below 90° .

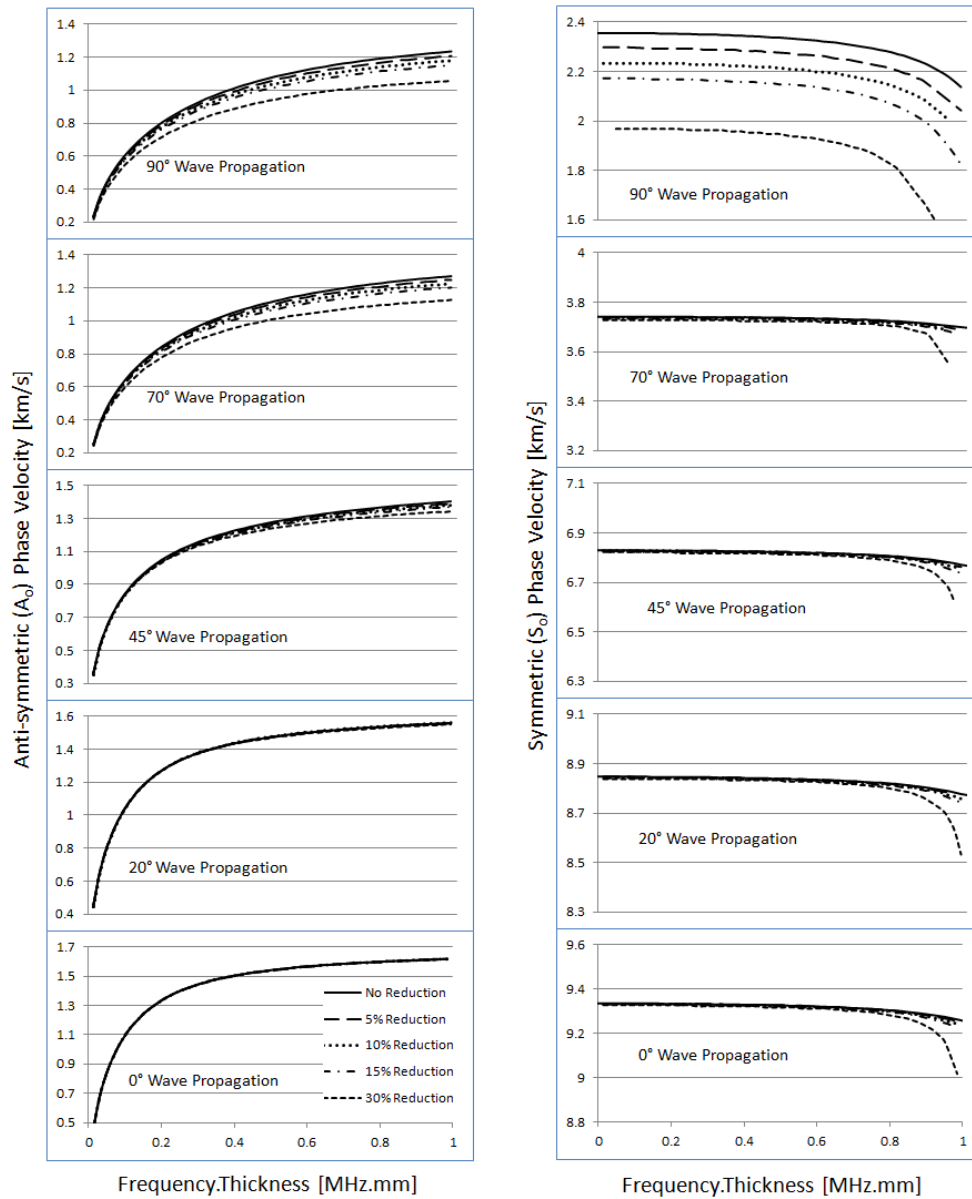


Figure 50: Effects of reducing E_{22} on the dispersion characteristic of A_o and S_o waves for unidirectional laminate

As shown in Figure 50, the reduction in E_{22} affected the A_o wave mode propagating at 45° and above, with the waves' propagation velocity being decreased. This effect increased as the wave propagation angle increased towards 90° in the frequency-thickness product range above 0.05 MHz.mm, with greater effects being observed at higher frequency-thickness values. For the S_o mode, the reduction in E_{22} only affected the waves propagating at 90° since E_{22} is dominant for the extensional effect at 90° , whereas E_{11} dominates the extensional effect at all other angles, since $E_{11} \gg E_{22}$. Beyond the observed reduction in the velocity for the S_o mode at 90° propagation direction, the reduction in E_{22} also caused the S_o dispersion curve to slope down towards the Rayleigh velocity at smaller values of the frequency-thickness product, for all propagating directions, making the S_o mode more dispersive. This effect can be explained by remembering that the laminate is transversely isotropic, meaning $E_{22} = E_{33}$, and therefore the reduction in E_{22} , and hence the reduction in E_{33} , increased the transverse dampening effect (decreased the transverse stiffness), thus reducing the starting frequency for higher modes, so the energy transferred from S_o to higher modes occurred at lower frequencies. Similarly, with $(E_{22} = E_{33})$ and $(E_{11} \gg E_{22}, E_{33})$, the transverse propagation of A_o at 90° was greatly affected as compared to lower angles where E_{11} is dominant. This suggests the use of S_o mode at 90° propagation angle at any frequency-thickness range and A_o mode at propagation angle above 45° at frequency-thickness of 0.2 MHz.mm or higher to detect damage associated with E_{22} in a unidirectional laminate.

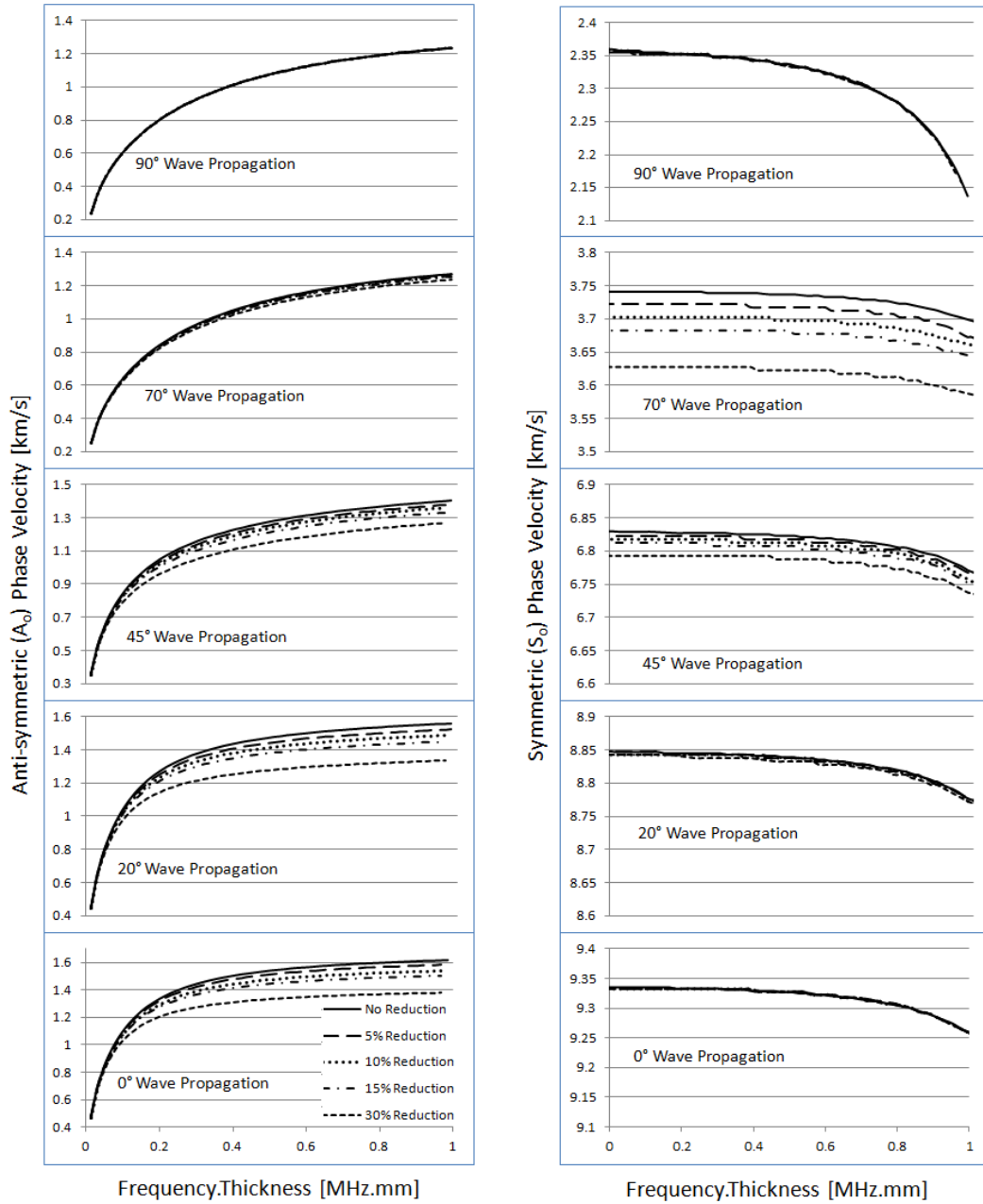


Figure 51: Effects of reducing G_{12} on the dispersion characteristic of A_0 and S_0 waves for unidirectional laminate

From Figure 51, it can be seen that the reduction in G_{12} affected the A_0 waves propagating below 90° for frequency-thickness product above 0.05 MHz.mm, with greater reductions in the

propagation velocity of the A_o waves being observed at higher values of such product. The G_{12} did not have an effect at 90° on the through-thickness deformation field for A_o ; therefore, the maximum effect can be seen at 0° . The S_o was not affected at both 0° and 90° because the laminate was transversely isotropic, i.e., no coupling effect was present between shear and extension at those angles of propagation. The reduction of the S_o propagation velocity could be observed for propagation directions of 45° and towards 90° , since $E_{22} \ll E_{11}$ the effect was pushed slightly from 45° towards 90° . This suggests the use A_o mode at or below 45° propagation angles at frequency-thickness product greater than 0.1 MHz.mm to detect damage associated with G_{12} in a unidirectional laminate.

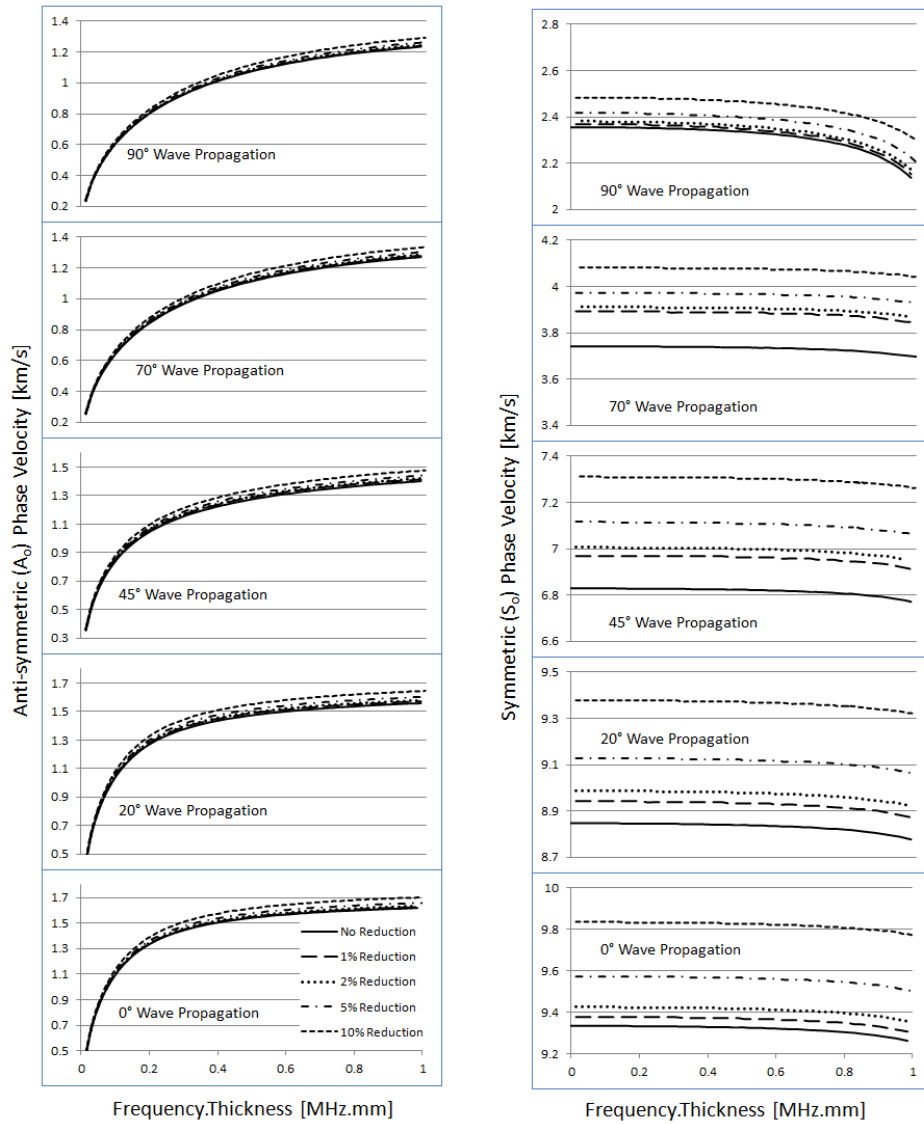


Figure 52: Effects of reducing density on the dispersion characteristic of A_0 and S_0 waves for unidirectional laminate

As expected, the reduction in density affected both A_0 and S_0 waves' propagation, with an observed increase in the wave propagation velocities along all directions and frequency-thickness range as shown in Figure 52. This increase also proves the inverse relationship between density and both A_0 and S_0 wave velocities and suggests the use of both A_0 and S_0 modes to find damage associated with the density.

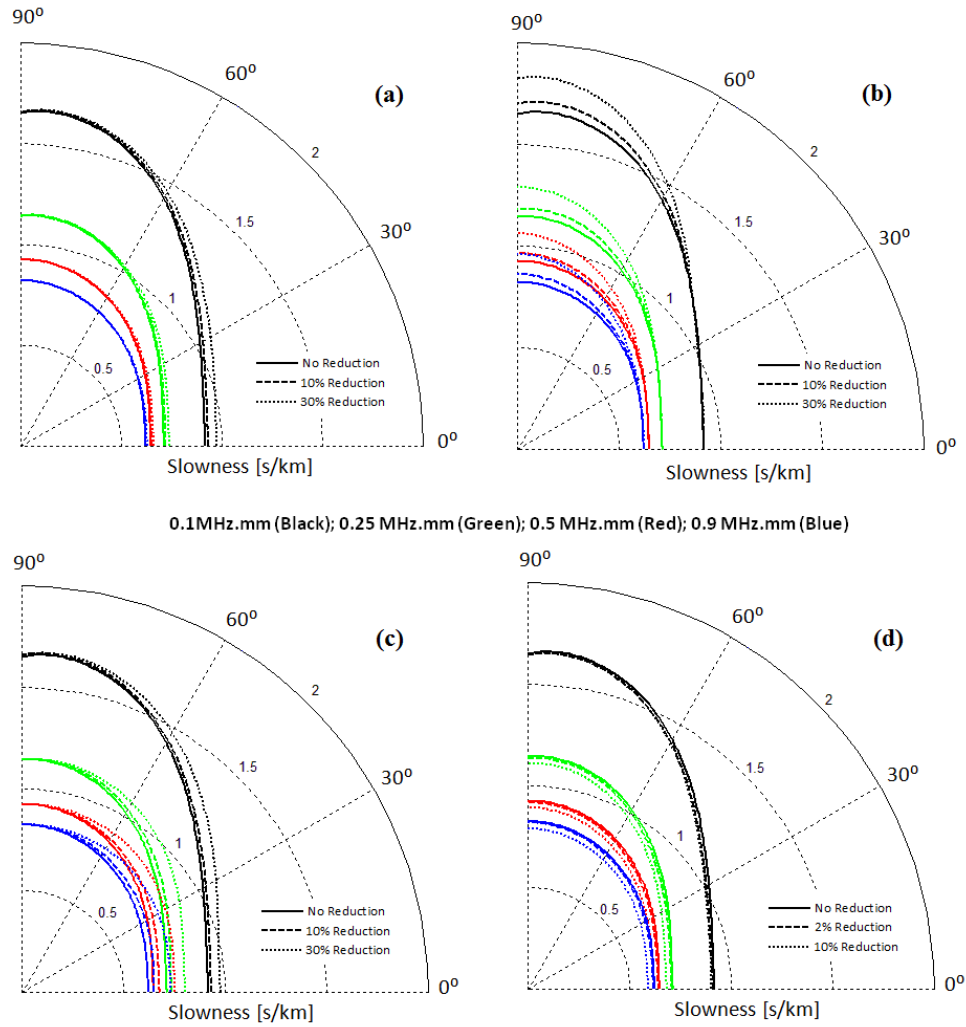


Figure 53: Effects of (a) E_{11} , (b) E_{22} , (c) G_{12} , and (d) density on the slowness of fundamental anti-symmetric Lamb wave propagating in the unidirectional laminate

From Figure 53 it can be summarized that the reduction in E_{11} (Figure 53a) and G_{12} (Figure 53c) affected the A_o wave travelling below 70° , where the effect was pronounced at lower frequency-thickness product (0.1 MHz.mm) for E_{11} and at higher frequency-thickness product for G_{12} . As for the reduction in E_{22} (Figure 53b), the A_o mode was affected at angles above 45° and equally in all frequency-thickness range above 0.1 MHz.mm. The change in density shifted the entire curve lower corresponding to increase in velocity as shown in Figure 53d.

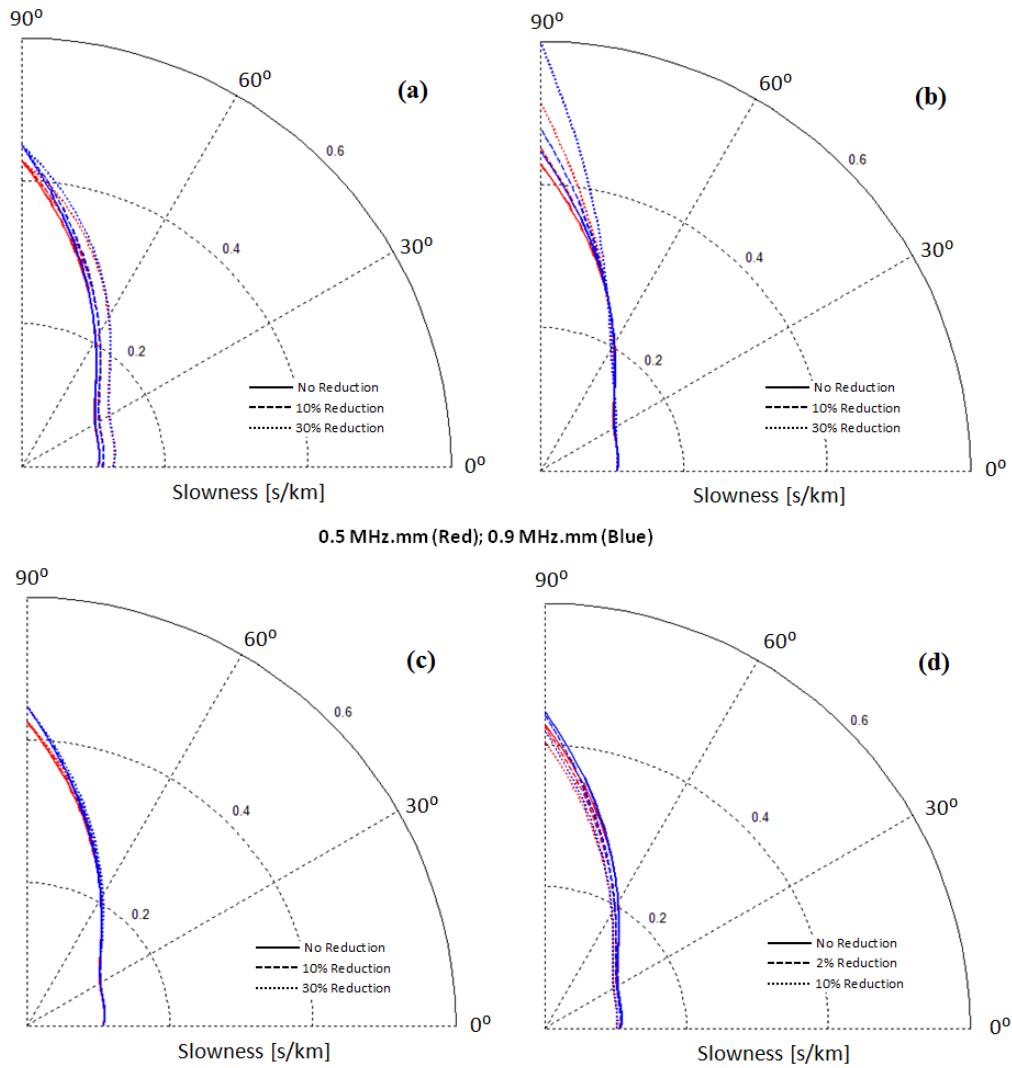


Figure 54: Effects of (a) E_{11} , (b) E_{22} , (c) G_{12} , and (d) density on the slowness of fundamental symmetric Lamb wave propagating in the unidirectional laminate

Figure 54 shows that the reduction in E_{11} (Figure 54a) affected the S_o wave travelling below 90° , whereas the reduction in E_{22} (Figure 54b) affected the wave travelling above 70° with an increase in the effect towards 90° . There was a negligible effect on S_o wave due to reduction in G_{12} (Figure 54c) and equal effect on S_o wave along all propagating direction due to change in density (Figure 54d).

3.2.2.2 Cross-ply laminate

The analytical dispersion curves for A_o and S_o are shown in Figure 55 to Figure 58 and the slowness curves for A_o and S_o are provided in Figure 59 and Figure 60, respectively for the cross-ply laminate.

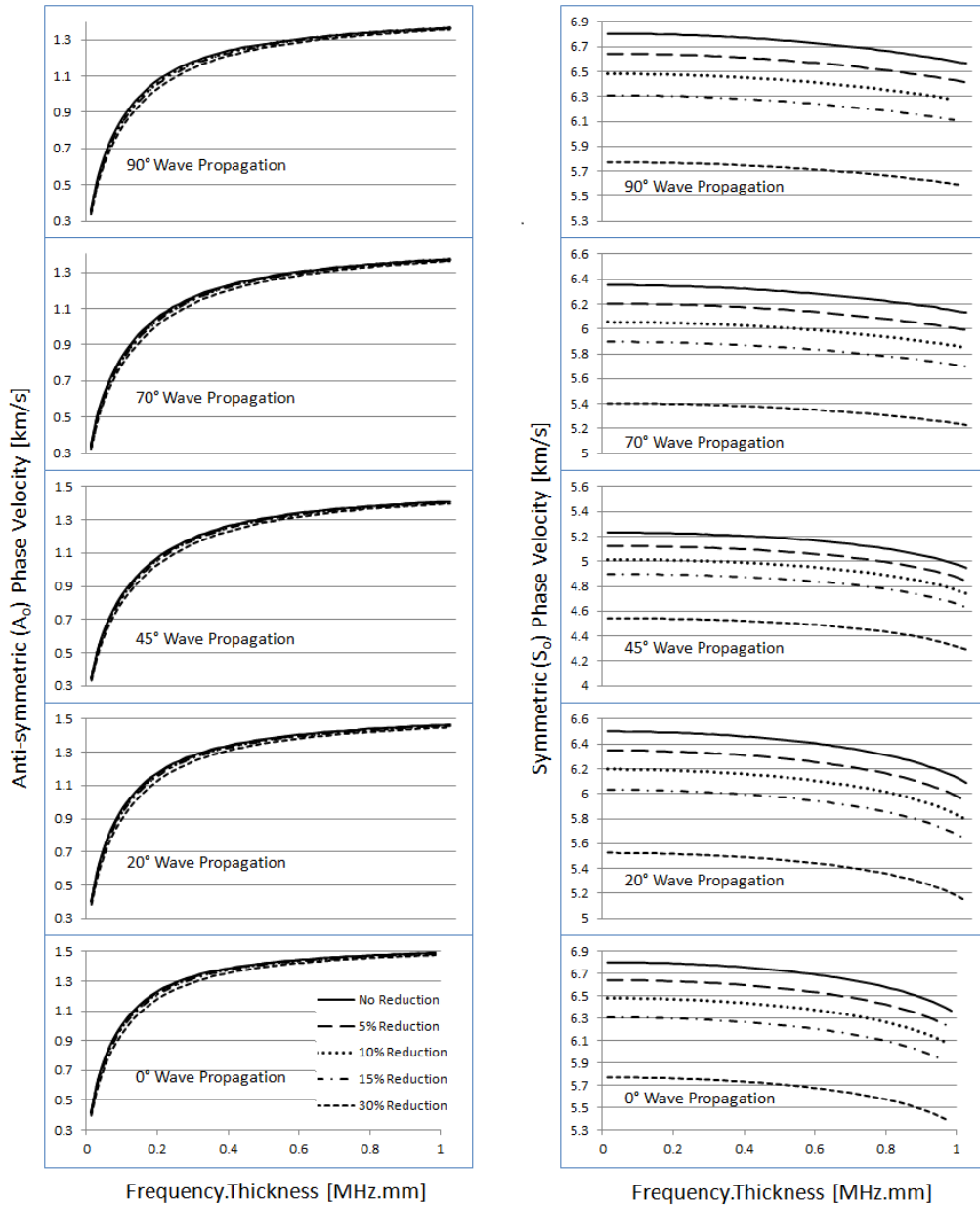


Figure 55: Effects of reducing E_{11} on the dispersion characteristic of A_o and S_o waves for cross-ply laminate

From Figure 55, it can be seen that the reduction in E_{11} marginally affected the A_o mode propagating in all directions in the lower frequency-thickness product range of below 0.5 MHz.mm. The effect of the reduction in E_{11} for the S_o mode can clearly be observed as a reduction in the propagation velocity for the waves of this mode, particularly towards 0° and 90° propagation angles, while smaller reductions in propagation velocity can be observed for 45° . In Figure 55, it can also be seen that the propagation velocity of the S_o mode tended towards the Rayleigh wave velocity at lower values of the frequency-thickness product for propagation directions approaching 0° . This was due to the outer plies in this cross-ply laminate being oriented at 0° (Table 4), and hence at 0° the damping effect is highest due to the reduction of E_{11} . This suggests the use of S_o mode at any direction and all frequency-thickness range, as compared to using A_o mode at any direction but limited to low frequency-thickness of 0.5 MHz.mm or lower to detect damage associate with E_{11} for a cross-ply laminate.

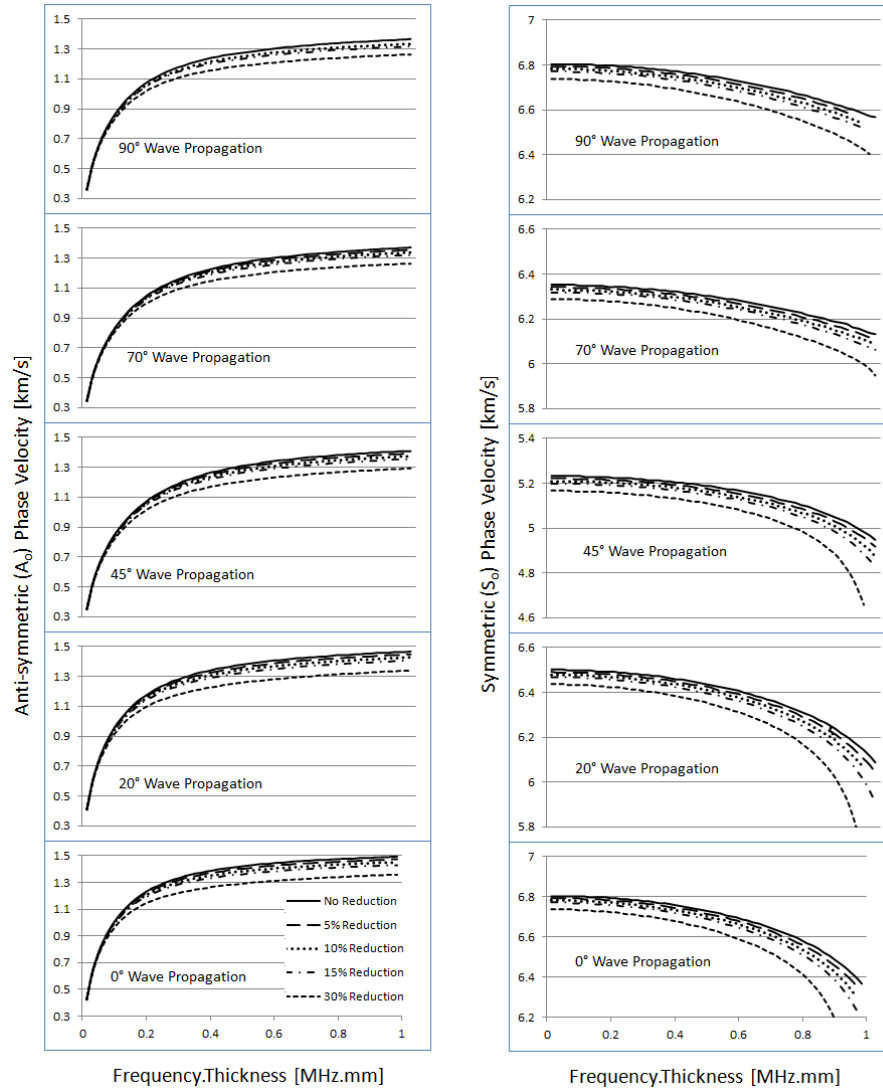


Figure 56: Effects of reducing E_{22} on the dispersion characteristic of A_o and S_o waves for cross-ply laminate

As shown in Figure 56, the reduction in E_{22} affected the A_o mode in all directions and this effect was higher at higher frequency-thickness product range. For the S_o mode, the reduction in E_{22} , hence the reduction in E_{33} , was found to be responsible for the propagation velocity of the S_o mode to tend towards Rayleigh velocity at lower values of the frequency-thickness products. This effect was observed to be stronger for propagation directions approaching 0°

with the explanation for this effect being similar to what was already explained for the reduction in E_{11} , due to the outer plies being oriented at 0° and playing a dominant role in this effect for the S_o waves. This suggests the use of S_o mode at any direction but at higher frequency-thickness product, as compared to the A_o mode, which can be used at any direction for any frequency-thickness product to detect damage associated with E_{22} for the cross-ply laminate.

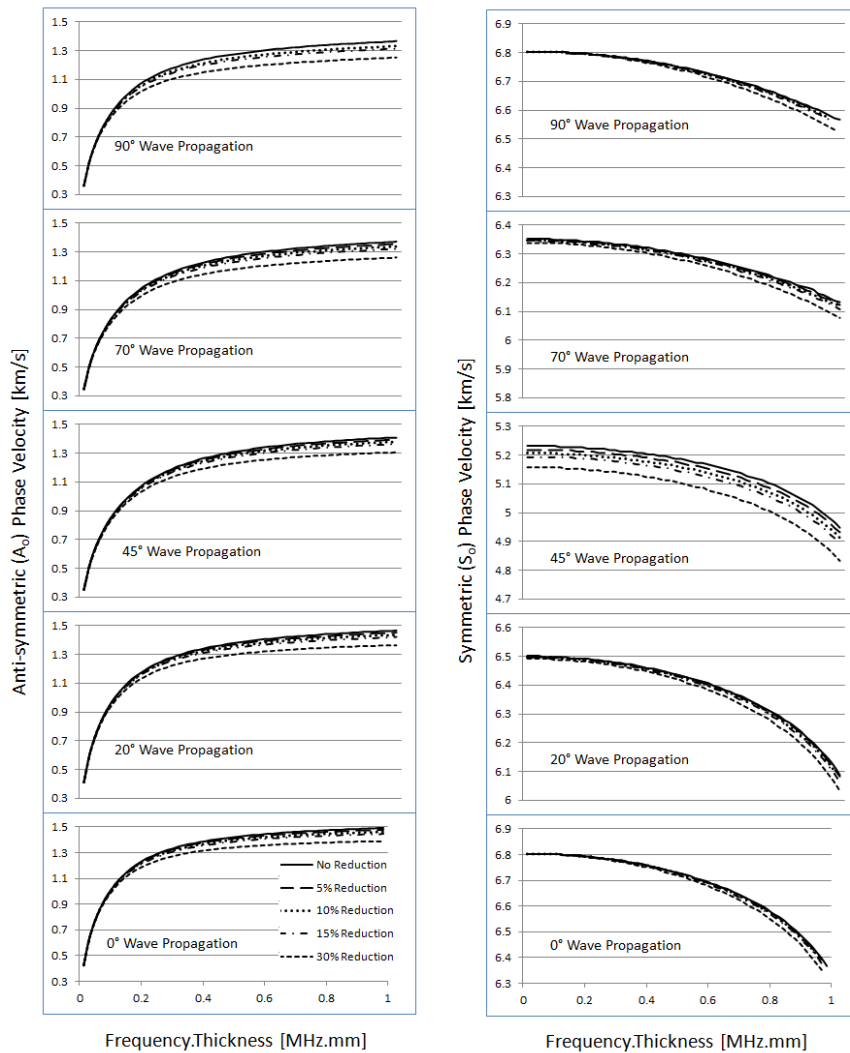


Figure 57: Effects of reducing G_{12} on the dispersion characteristic of A_o and S_o waves for cross-ply laminate

From Figure 57, it can be seen that the reduction in G_{12} affected the A_o mode in the higher frequency-thickness product range equally in all directions. As for the S_o mode, the effect of this reduction was observed to be strongest at 45° propagation angle, which was quickly reduced for the wave propagating away from 45° towards 90° or 0° as expected for a cross-ply laminate, where G_{12} is dominant in the $\pm 45^\circ$ orientation angle. This suggests the use of A_o mode over S_o mode to detect damage associated with G_{12} for a cross-ply laminate.

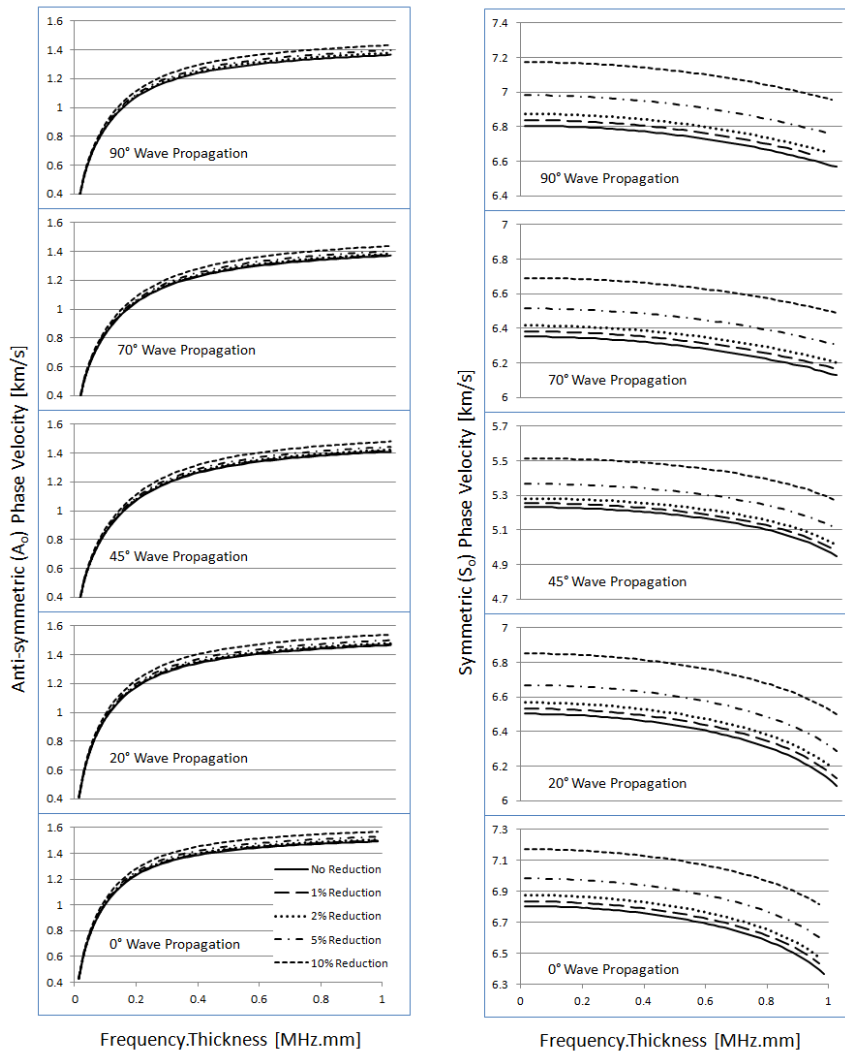


Figure 58: Effects of reducing density on the dispersion characteristic of A_o and S_o waves for cross-ply laminate

As shown in Figure 58, the effect of reducing density was similar to that for the unidirectional laminate, where the wave velocity increased for both A_o and S_o modes along all directions and frequency-thickness product ranges. This suggests the use of both A_o and S_o for detecting damage associated with density along any direction and all frequency-thickness ranges.

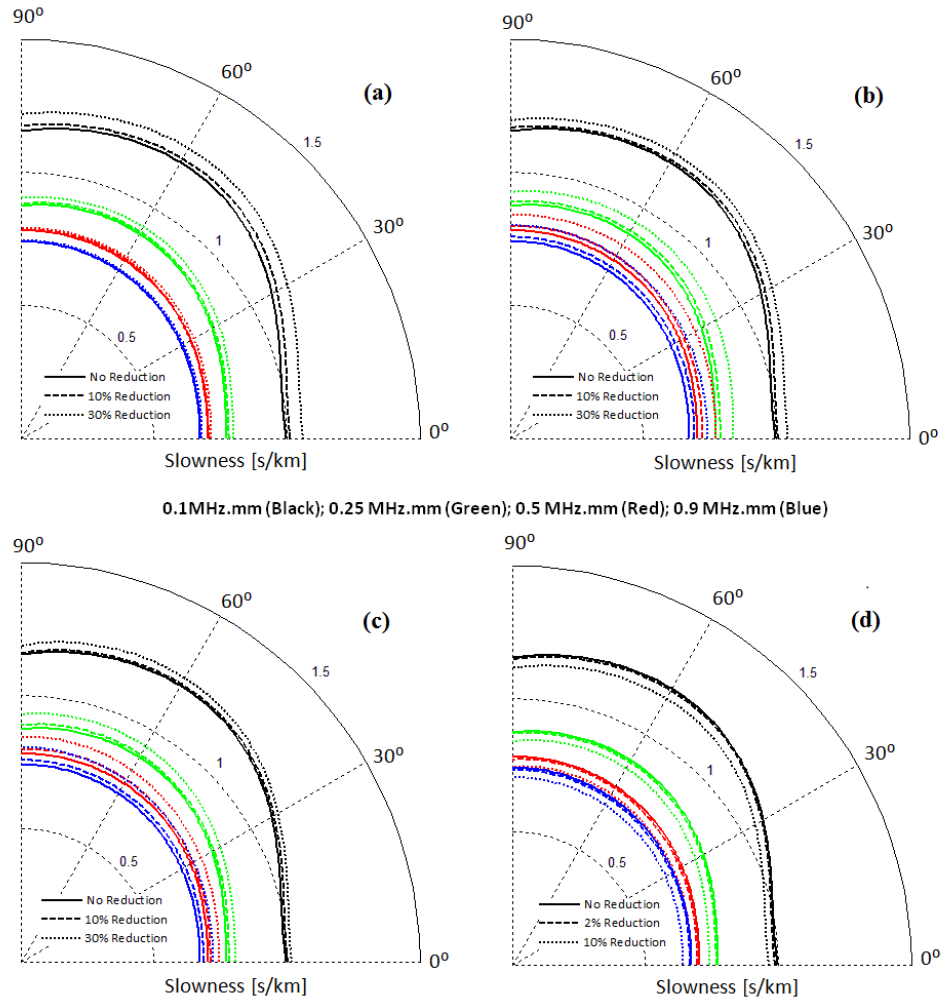


Figure 59: Effects of (a) E_{11} , (b) E_{22} , (c) G_{12} , and (d) density on the slowness of fundamental anti-symmetric Lamb wave propagating in the cross-ply laminate

As shown in Figure 59, the A_o wave was slower at 90° as compared to 0° , which was contrary to the expectation for a cross-ply laminate. This effect was due to the outer ply being oriented at

0° and since this is the farthest ply from the neutral-axis of the plate, the orientation of this ply will have an important effect on increasing the bending stiffness, hence increasing the A_o wave velocity in the 0° direction.

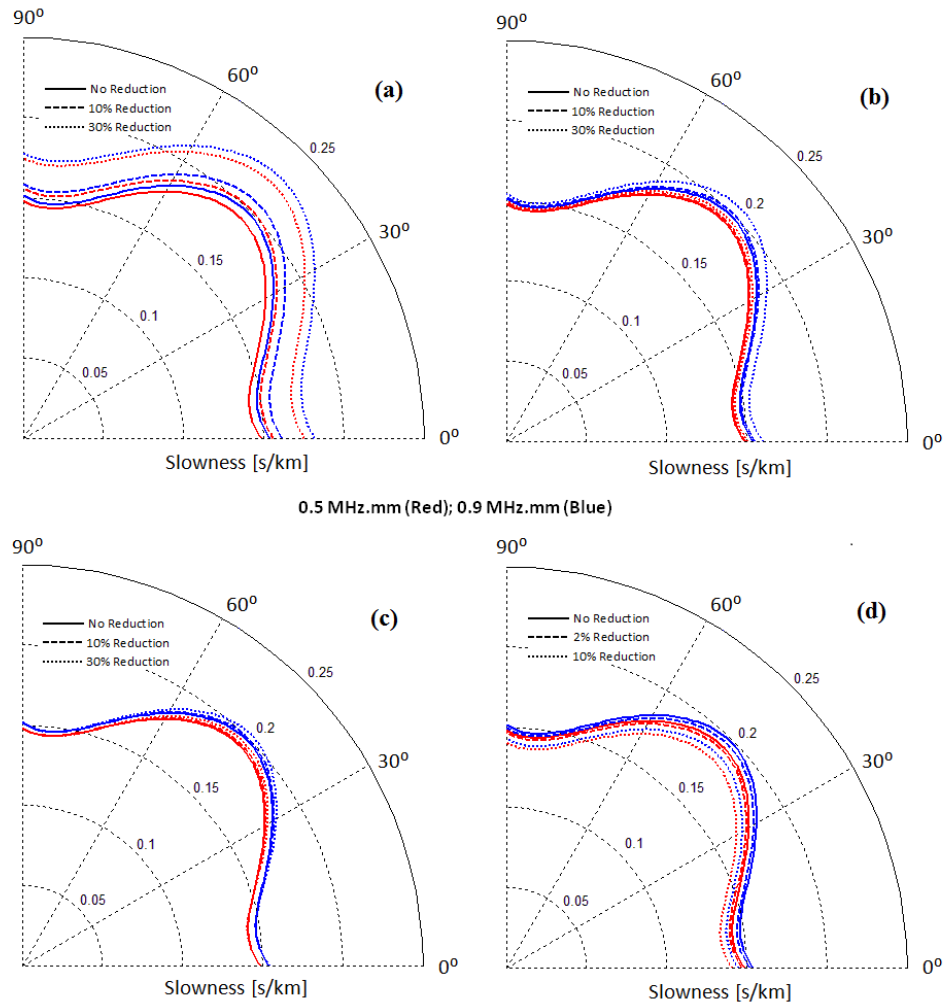


Figure 60: Effects of (a) E_{11} , (b) E_{22} , (c) G_{12} , and (d) density on the slowness of fundamental symmetric Lamb wave propagating in the cross-ply laminate

The slowness for S_o (Figure 60) was as expected, with the waves from this mode presenting lower propagation velocities at 45° and higher velocities towards 0° and 90°, since the plies were at 0° and 90° for the cross-ply laminate.

3.2.2.3 Quasi-isotropic laminate

The analytical dispersion curves for A_o and S_o are shown in Figure 61 to Figure 64 and the slowness curves for A_o and S_o are provided in Figure 65 and Figure 66, respectively.

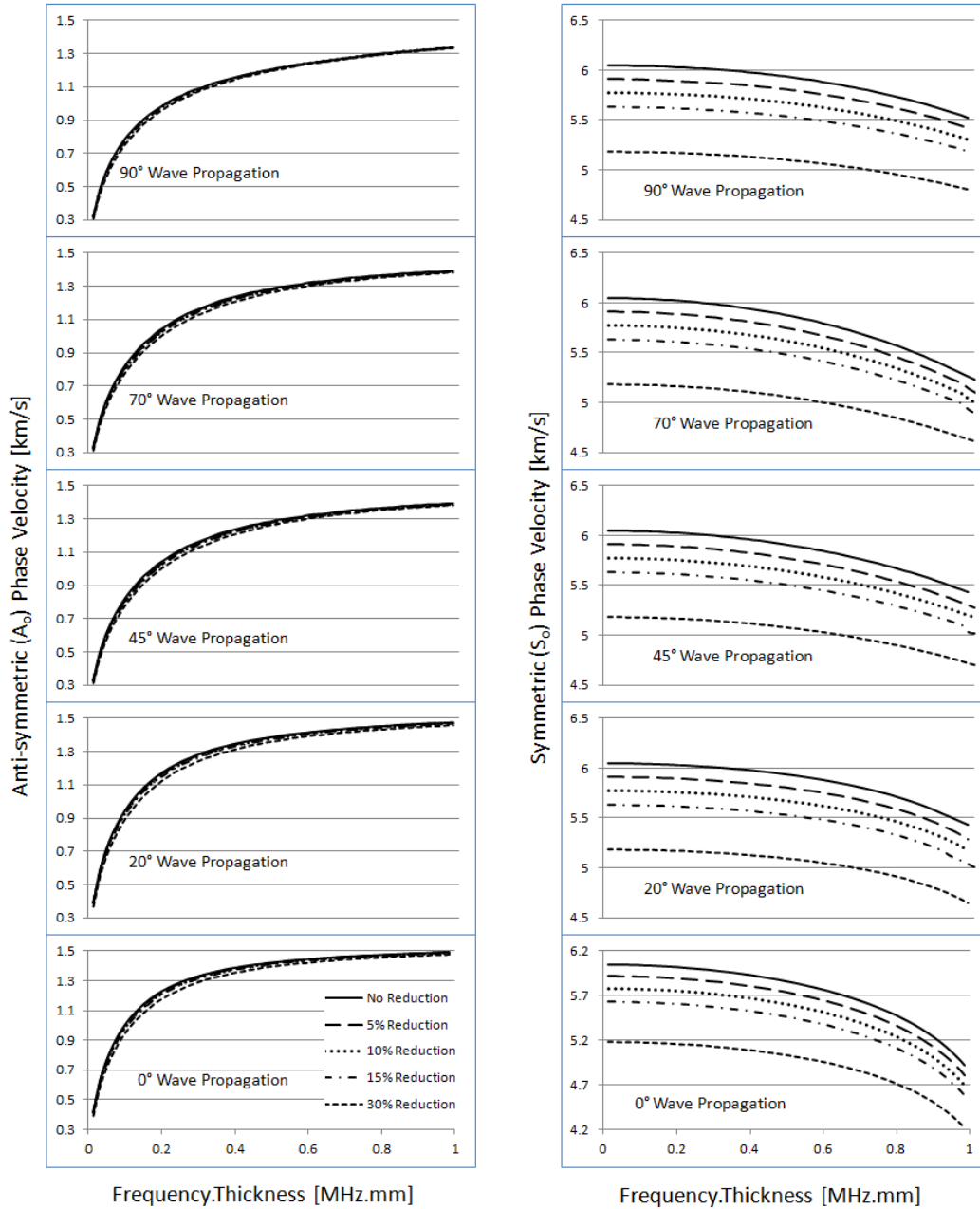


Figure 61: Effects of reducing E_{11} on the dispersion characteristic of A_o and S_o waves for quasi-isotropic laminate

As shown in Figure 61, the reduction in E_{11} affected the A_o waves propagating in all directions, for lower frequency-thickness product values ranging up to 0.5 MHz.mm. As for the S_o mode, the reduction in E_{11} affected the wave propagating in all directions equally, as expected for the quasi-isotropic laminate displaying in-plane isotropy. The drop-off in the dispersion curves of the S_o mode towards the Rayleigh velocity for 0° propagation angle happened at lower values of the frequency-thickness product. This can be explained by the higher dampening effect of the outer 0° oriented plies, forcing energy to be transferred from the S_o mode to the excitation of higher Lamb wave modes. This was confirmed by changing the ply stacking sequence of the laminate from $[0_2/45_2/-45_2/90_2]_{\text{SYM}}$ to $[90_2/45_2/-45_2/0_2]_{\text{SYM}}$ such that the outer plies were oriented at 90° , which shifted the sloping effect (at lower frequency-thickness products) towards the 90° propagation angle. This suggests the use of S_o mode over A_o mode to detect damage associated with E_{11} along all propagation directions and frequency-thickness products for a quasi-isotropic laminate.

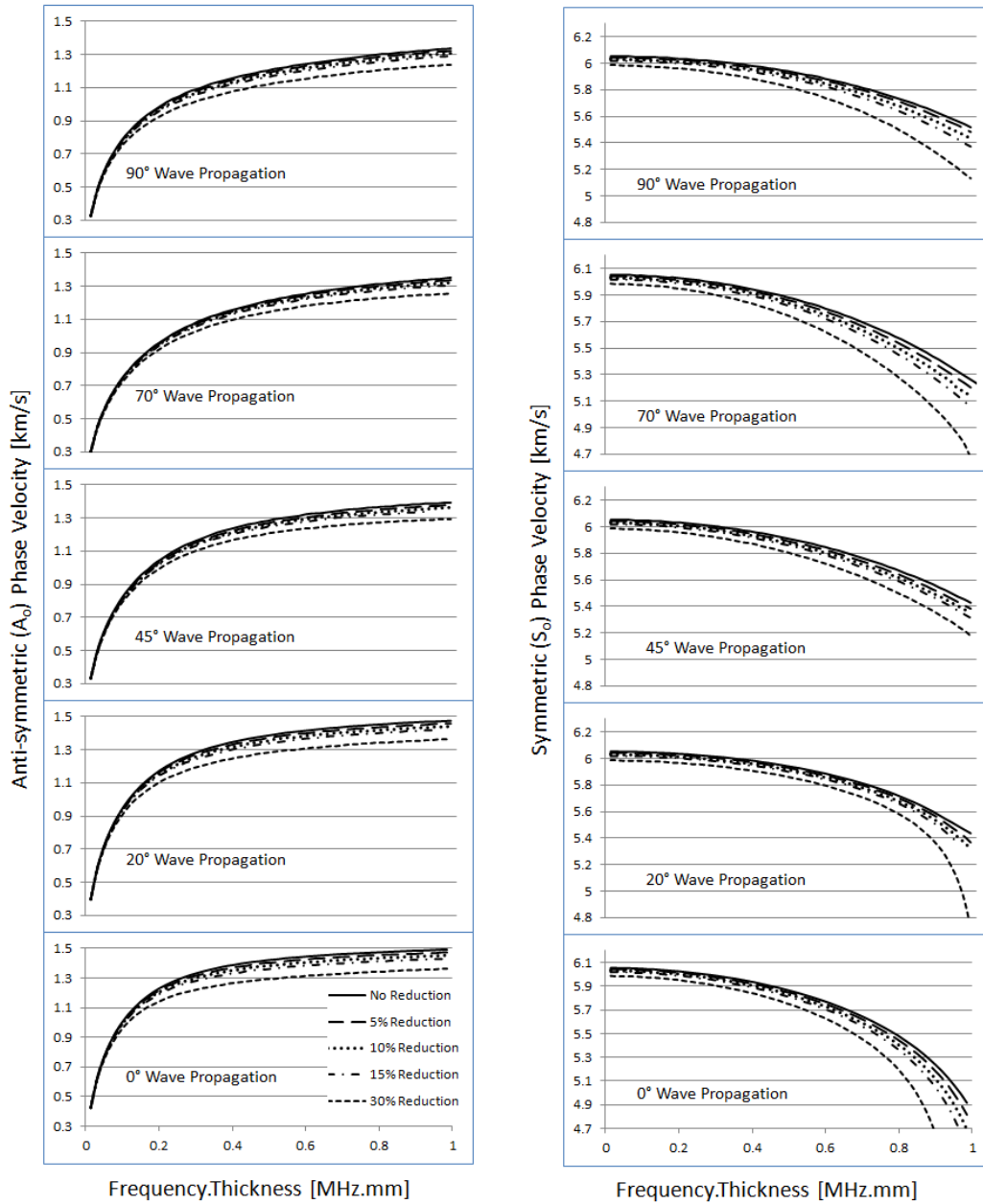


Figure 62: Effects of reducing E_{22} on the dispersion characteristic of A_0 and S_0 waves for quasi-isotropic laminate

From Figure 62, it can be seen that the reduction in E_{22} affected the A_0 mode in all directions and this effect was observed to be stronger at higher frequency-thickness products, this effect was similarly to the cross-ply laminate. The reduction in E_{22} also affected the S_0 mode in all

directions at higher values of the frequency-thickness product. The reduction in E_{22} was also found to be responsible for the propagation velocity of the S_o mode waves to tend towards the Rayleigh velocity at lower values of the frequency-thickness product, which can be explained similarly to the effect of the reduction in E_{11} for this quasi-isotropic laminate, with the outer plies playing a dominant role. This suggests the use of both A_o and S_o modes for all propagation angles, with limitation on the use of proper frequency-thickness products of 0.05 MHz.mm and higher for A_o and 0.6 MHz.mm and higher for S_o to detect damage associated with E_{22} for quasi isotropic laminate.

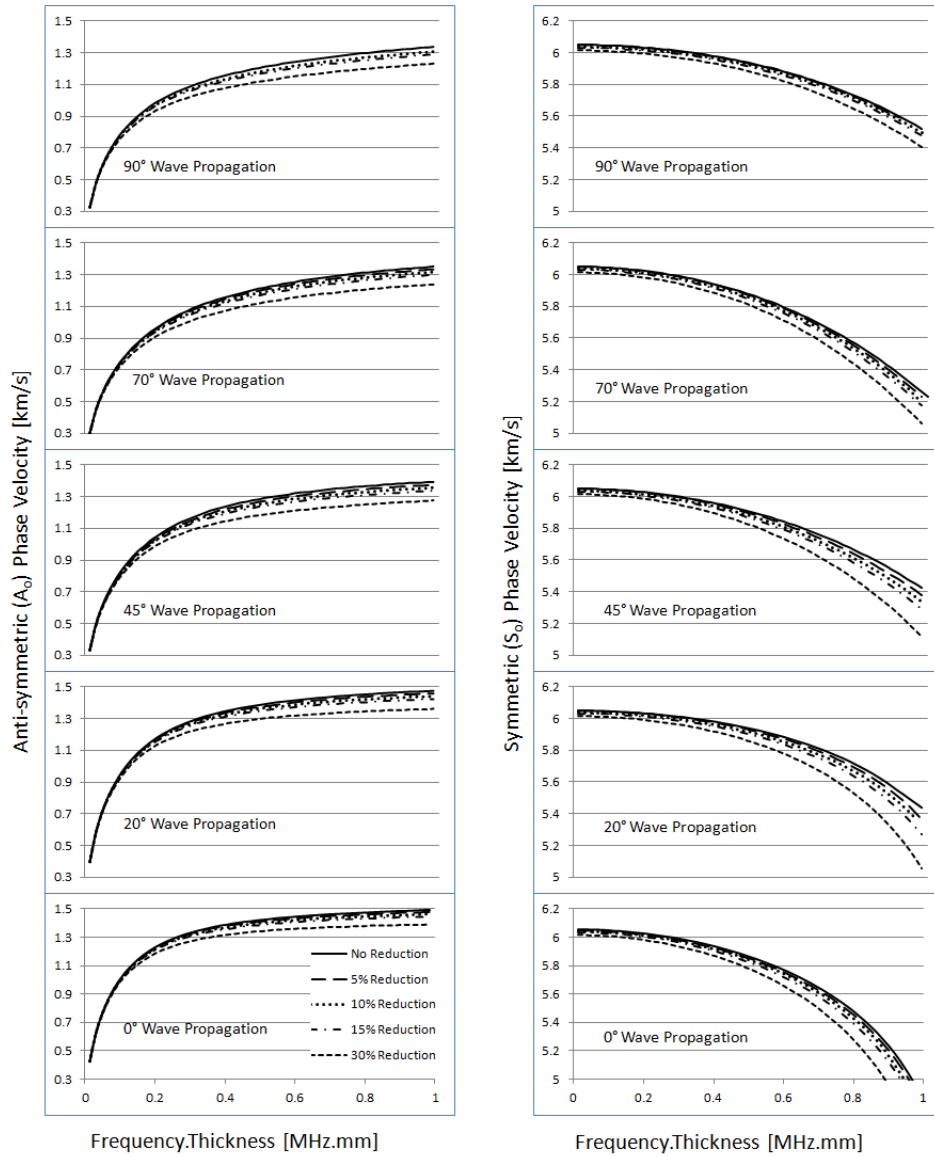


Figure 63: Effects of reducing G_{12} on the dispersion characteristic of A_o and S_o waves for quasi-isotropic laminate

As shown in Figure 63, the reduction in G_{12} affected the A_o mode in the higher frequency-thickness product range equally in all propagation directions. As for the S_o mode, the effect of the reduction in G_{12} could be observed towards high frequency-thickness products, being stronger for a propagation direction of 45° , and being weaker as the waves propagated towards

90° or 0° as expected for a quasi-isotropic laminate. This suggests the use of both A_o and S_o modes for all propagation angles, with limitation on the use of proper frequency-thickness products of 0.1 MHz.mm and higher for A_o and 0.4 MHz.mm and higher for S_o to detect damage associated with G_{12} for a quasi-isotropic laminate.

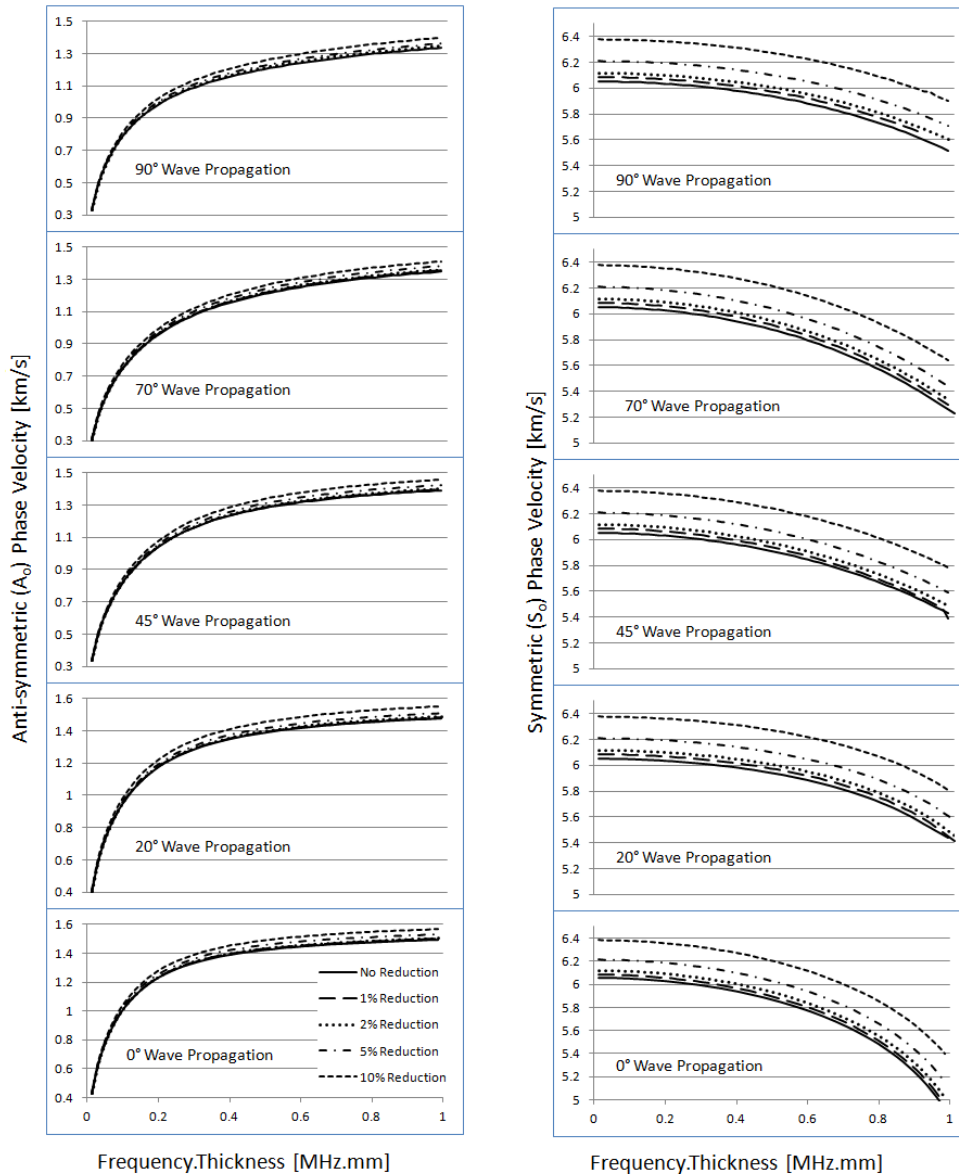


Figure 64: Effects of reducing density on the dispersion characteristic of A_o and S_o waves for quasi-isotropic laminate

As shown in Figure 64, the effect of reducing density was similar to that for the unidirectional and cross-ply laminate, where the wave velocity increased uniformly for both A_o and S_o modes along all propagation directions and frequency-thickness product range. This suggests the use of both A_o and S_o modes for detecting damage associated with density along any direction and all frequency-thickness ranges.

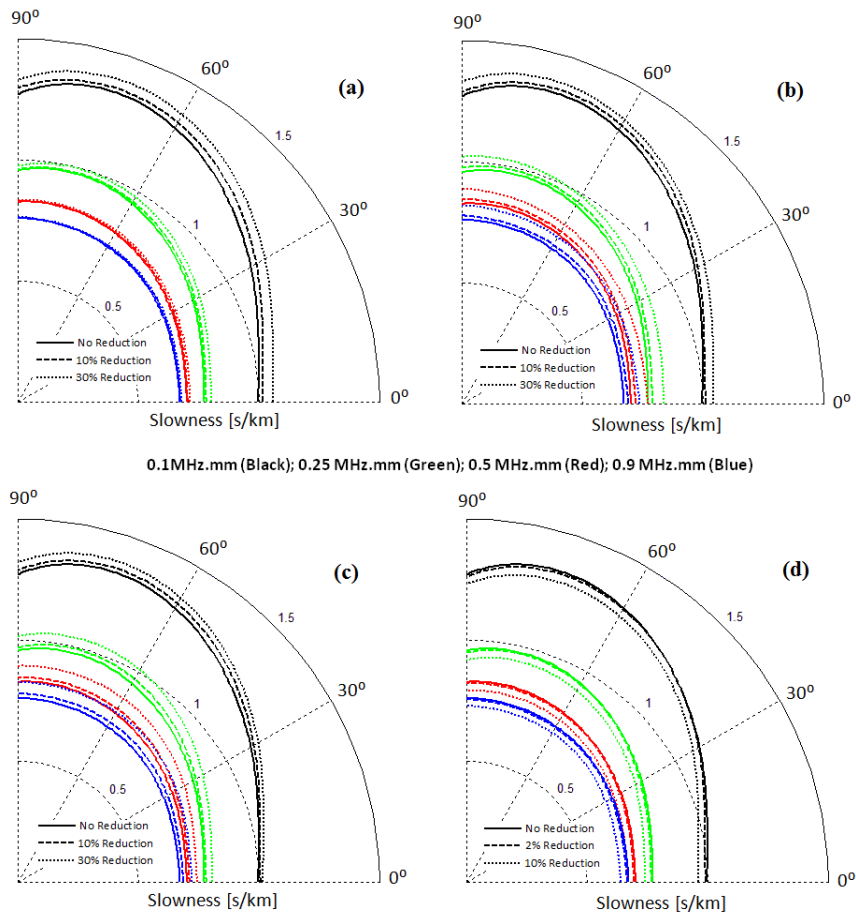


Figure 65: Effects of (a) E_{11} , (b) E_{22} , (c) G_{12} , and (d) density on the slowness of fundamental anti-symmetric Lamb wave propagating in the quasi-isotropic laminate

As shown in Figure 65, the A_o waves were slowest at 70° as compared to other angles of propagation direction, which was contrary to the expectation for a quasi-isotropic laminate. This

effect was again due to the four most outer plies being oriented at 0° and 45° , increasing the bending stiffness and hence increasing the A_o wave velocity between 0° and 45° .

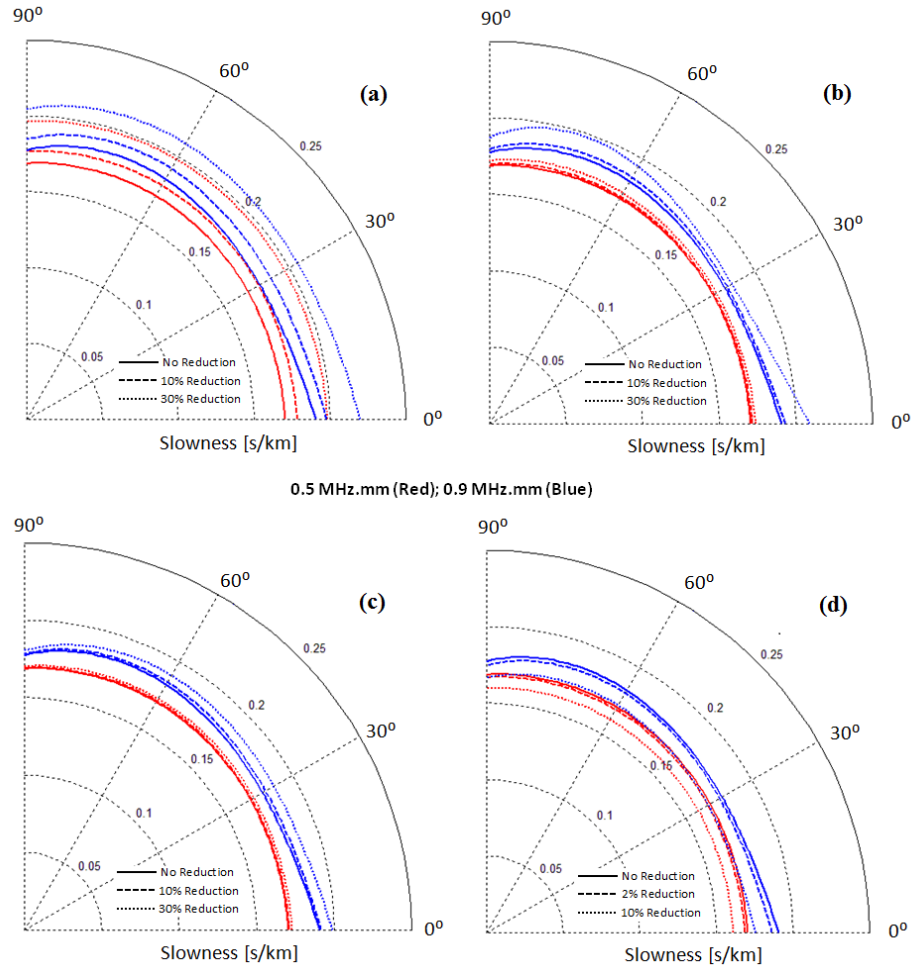


Figure 66: Effects of (a) E_{11} , (b) E_{22} , (c) G_{12} , and (d) density on the slowness of fundamental symmetric Lamb wave propagating in the quasi-isotropic laminate

Slowness for S_o (Figure 66) was as expected for the lower frequency-thickness product, which was comparable to the slowness curve for a wave propagating in an isotropic medium. However, for the higher frequency-thickness product, the S_o waves tend to slow down when propagating in directions approaching 0° , with the outer 0° ply playing a dominant role in this effect.

3.2.2.4 Summary of the results

The analytical method presented in Chapter 2 was used to determine the influence of changes in the material properties due to presence of defect/damage in the propagation characteristics of Lamb waves in composites. The result of this study is summarized in Table 5.

Table 5: Suggested Lamb wave modes to detect damage associated with E_{11} , E_{22} , G_{12} , and density

Laminate Type	Defect Associated with	Suggested Lamb wave mode	Propagation Angle	Frequency-thickness product range
Unidirectional	E_{11}	S_o mode	Below 90°	All
	E_{22}	S_o mode	At 90°	All
		A_o mode	Above 45°	0.2 MHz.mm or Higher
	G_{12}	A_o mode	45 and Below	0.1 MHz.mm or Higher
	Density	Both A_o and S_o	All	All
Cross-ply	E_{11}	S_o mode	All	All
		A_o mode	All	0.5 MHz.mm or Lower
	E_{22}	S_o mode	All	Effective at Higher range
		A_o mode	All	All
	G_{12}	A_o mode	All	0.05 MHz.mm or Higher
	Density	Both A_o and S_o	All	All
Quasi-isotropic	E_{11}	S_o	All	All
	E_{22}	S_o mode	All	0.6 MHz.mm or Higher
		A_o mode	All	0.5 MHz.mm or Higher
	G_{12}	S_o mode	All	0.4 MHz.mm or Higher
		A_o mode	All	0.1 MHz.mm or Higher
	Density	Both A_o and S_o	All	All

As presented in Table 5, overall the S_o mode was found to be sensitive to the fibre dominated properties (E_{11}), whereas the A_o mode was found to be sensitive to the matrix dominated properties (E_{22} , G_{12}). In addition, the S_o mode was sensitive to the matrix dominated properties at higher frequency-thickness products and the opposite was true for A_o mode waves, which were mainly sensitive to the fibre dominated properties at lower frequency-

thickness product ranges. This suggests the use of S_o and A_o modes for detecting fibre and matrix dominated damage, respectively. As for the presence of voids in a composite material are concerned, and considering the effect of these in changing the density of a material (for instance, as compared to the density values of a material used during design), it was found that both A_o and S_o modes were equally sensitive to the change in density; thus, any mode can be used for detecting voids. It was also interesting to observe the dominant effect of the outermost ply on the trend of the S_o mode waves' propagation velocity towards the Rayleigh velocity at lower frequency-thickness products, when the propagation angle was along the orientation of the dominant plies. This suggests the use of the S_o mode to find surface defects by observing the tendency of S_o mode velocity to go towards Rayleigh velocity. It is also to be noted that A_o and S_o modes are dominant at lower and higher frequency-thickness product ranges, respectively as described in Section 2.2.7. Therefore, it is desirable to use A_o mode waves for detecting damage at lower frequency-thickness product ranges as compared to S_o , for higher frequency-thickness products.

CHAPTER 3 SUMMARY

In this chapter, the effect on the Lamb wave propagation/dispersion due to changes in the material properties were analyzed for three different composite laminate types typically used in aerospace applications. The three laminates studied are unidirectional, cross-ply, and quasi-isotropic, all constructed out of 16-ply of unidirectional carbon-fibre epoxy prepregs. The analysis was done by reducing E_{11} , E_{22} , G_{12} by 5, 10, 15, 30 percent and density by 1, 2, 5, and 10 percent with the intent of representing defects and variability during manufacturing processes that might change the modulus of elasticity or material density. Since the Lamb waves' velocity in a composite laminate varies with the propagation direction, in order to get a complete picture, the laminates were analyzed at 0° , 20° , 45° , 70° , and 90° propagation angles, with all the aforementioned variations. A program developed in MATLAB, which was presented in Chapter 2 was used to generate the analytically derived dispersion curves for the fundamental anti-symmetric and symmetric Lamb wave modes.

CHAPTER 4: MATERIAL CHARACTERIZATION

In order to accurately solve the Lamb wave equations presented in Chapter 2 and to study the effect of variation in the material properties presented in Chapter 3, proper material property data are required. There are several techniques for determining material elastic properties. The most widely used are by conducting tensile, bending, torsion, and shear experiments. The aforementioned techniques can be destructive in nature and require a small subset of samples from the structure to be evaluated. To overcome this problem, non-destructive ultrasonic waves have been used to determine the elastic properties of materials. In this chapter, the theory of ultrasonic wave propagation, followed by numerical solution, and optimization methods based on non-linear least squared technique are presented to find the material properties non-invasively using the ultrasonic wave velocities. The method is then verified experimentally for isotropic metallic and transversely isotropic unidirectional composite specimens.

4.1 ULTRASONIC WAVE THEORY

As discussed in Chapter 2, bulk waves and guided waves are commonly used ultrasonic waves for NDE/SHM applications. In this section, the relationship between bulk wave velocities and material properties are derived. For this derivation, consider an anisotropic plate with thickness of $2h$ along with the associated co-ordinates shown in Figure 67. The anisotropic plate is assumed to be orthotropic, as most composite laminates exhibit orthotropic or higher degrees of symmetry along the principal axes.

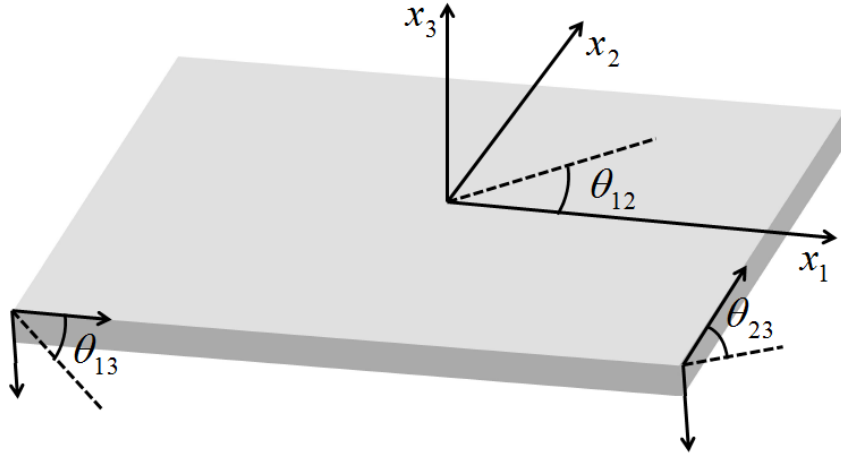


Figure 67: Orthotropic plate with the associate coordinates

The generalized stress-strain relationship for the orthotropic plate can be reduced from Eqn. (2.14) and is given by:

$$\begin{bmatrix} \sigma_{11} \\ \sigma_{22} \\ \sigma_{33} \\ \sigma_{23} \\ \sigma_{13} \\ \sigma_{12} \end{bmatrix} = \begin{bmatrix} c_{11} & c_{12} & c_{13} & 0 & 0 & 0 \\ c_{12} & c_{22} & c_{23} & 0 & 0 & 0 \\ c_{13} & c_{23} & c_{33} & 0 & 0 & 0 \\ 0 & 0 & 0 & c_{44} & 0 & 0 \\ 0 & 0 & 0 & 0 & c_{55} & 0 \\ 0 & 0 & 0 & 0 & 0 & c_{66} \end{bmatrix} \begin{bmatrix} \varepsilon_{11} \\ \varepsilon_{22} \\ \varepsilon_{33} \\ 2\varepsilon_{23} \\ 2\varepsilon_{13} \\ 2\varepsilon_{12} \end{bmatrix} \quad (4.1)$$

Strain and displacement relationship is given by Eqn. (2.4), which is repeated here:

$$\varepsilon_{ij} = \frac{1}{2} \left(\frac{\partial u_i}{\partial x_j} + \frac{\partial u_j}{\partial x_i} \right) \quad i=1,2,3; j=1,2,3 \quad (4.2)$$

Where, u_i is displacement and x_i represents direction

The displacement u_i is assumed to be simple harmonic with the form:

$$u_i = U_i e^{i(kn_j x_j - \omega t)} \quad (4.3)$$

Where, U_i is the displacement amplitude, k is the wave number, n_j is the unit vector, ω is the circular/angular frequency, and t is time

Taking the partial derivative of the displacement u_i with respect to direction x_i and time t and substituting the partials back into the equilibrium equations, Eqn. (2.18) to Eqn. (2.20) gives the well-known Christoffel equation, which can be written in a matrix form as:

$$\begin{bmatrix} \Lambda_{11} - \rho c_p^2 & \Lambda_{12} & \Lambda_{13} \\ \Lambda_{12} & \Lambda_{22} - \rho c_p^2 & \Lambda_{23} \\ \Lambda_{13} & \Lambda_{23} & \Lambda_{33} - \rho c_p^2 \end{bmatrix} \begin{Bmatrix} U_1 \\ U_2 \\ U_3 \end{Bmatrix} = 0 \quad (4.4)$$

Eqn. (4.4) is an eigenvalue problem of phase velocity c_p^2 , which defines three homogeneous linear equations for the displacement amplitudes (U_1, U_2, U_3) . The three solutions represent quasi-longitudinal, quasi-transverse-vertical, and transverse-horizontal waves propagating within the structure. For an orthotropic material the elements of Λ_{il} in Eqn. (4.4) are:

$$\begin{aligned} \Lambda_{11} &= c_{11}n_1^2 + c_{66}n_2^2 + c_{55}n_3^2 \\ \Lambda_{12} &= (c_{12} + c_{66})n_1n_2 \\ \Lambda_{13} &= (c_{13} + c_{55})n_1n_3 \\ \Lambda_{22} &= c_{66}n_1^2 + c_{22}n_2^2 + c_{44}n_3^2 \\ \Lambda_{23} &= (c_{23} + c_{44})n_2n_3 \\ \Lambda_{33} &= c_{55}n_1^2 + c_{44}n_2^2 + c_{33}n_3^2 \end{aligned} \quad (4.5)$$

The solution to Eqn. (4.4) and hence the phase velocities c_p^2 can be found by setting the determinant to be zero, which can be written as:

$$\begin{vmatrix} \Lambda_{11} - \rho c_p^2 & \Lambda_{12} & \Lambda_{13} \\ \Lambda_{12} & \Lambda_{22} - \rho c_p^2 & \Lambda_{23} \\ \Lambda_{13} & \Lambda_{23} & \Lambda_{33} - \rho c_p^2 \end{vmatrix} = 0 \quad (4.6)$$

Eqn. (4.6) can be further simplified by considering the waves propagating in the through-thickness direction along two-dimensional planes of symmetry (principal planes). For the wave propagating in the principal plane $(x_1 - x_3)$ along an angle θ_{13} measured with respect to the x_1 axis (Figure 67), the unit vector n_i can be expressed as:

$$n_i = (n_1, n_2, n_3) = (\cos \theta_{13}, 0, \sin \theta_{13}) \quad (4.7)$$

Therefore, Eqn. (4.6) can be reduced to:

$$\begin{vmatrix} \Lambda_{11} - \rho c_p^2 & 0 & \Lambda_{13} \\ 0 & \Lambda_{22} - \rho c_p^2 & 0 \\ \Lambda_{13} & 0 & \Lambda_{33} - \rho c_p^2 \end{vmatrix} = 0 \quad (4.8)$$

Where, the elements of Λ_{ij} is now given by:

$$\begin{aligned} \Lambda_{11} &= c_{11} \cos^2 \theta_{13} + c_{55} \sin^2 \theta_{13} \\ \Lambda_{13} &= (c_{13} + c_{55}) \cos \theta_{13} \sin \theta_{13} \\ \Lambda_{22} &= c_{66} \cos^2 \theta_{13} + c_{44} \sin^2 \theta_{13} \\ \Lambda_{33} &= c_{55} \cos^2 \theta_{13} + c_{33} \sin^2 \theta_{13} \end{aligned} \quad (4.9)$$

Eqn. (4.8) can be decomposed into three waves - transverse-horizontal (T), quasi-longitudinal (QL), and quasi-transverse-vertical (QT) waves or simply quasi-transverse, which are given as [A.

D. Degtyar et al., 1997]:

$$\begin{aligned} \rho c_{p(T)}^2 &= \Lambda_{22} \\ \rho c_{p(QL)}^2 &= \left(\frac{\Lambda_{11} + \Lambda_{33}}{2} \right) + \frac{\sqrt{(\Lambda_{11} - \Lambda_{33})^2 + 4\Lambda_{13}^2}}{2} \\ \rho c_{p(QT)}^2 &= \left(\frac{\Lambda_{11} + \Lambda_{33}}{2} \right) - \frac{\sqrt{(\Lambda_{11} - \Lambda_{33})^2 + 4\Lambda_{13}^2}}{2} \end{aligned} \quad (4.10)$$

The excitation/propagation of QL and QT waves at different wedge/propagation angles are shown in Figure 68. Referring to Figure 68, below the first critical angle both QL and QT waves are present. Whereas, between the first and the second critical angles only the QT wave is present at lower angles, while QT and Surface Waves (SW) are present at higher angles. Above the second critical angle only the SW are present.

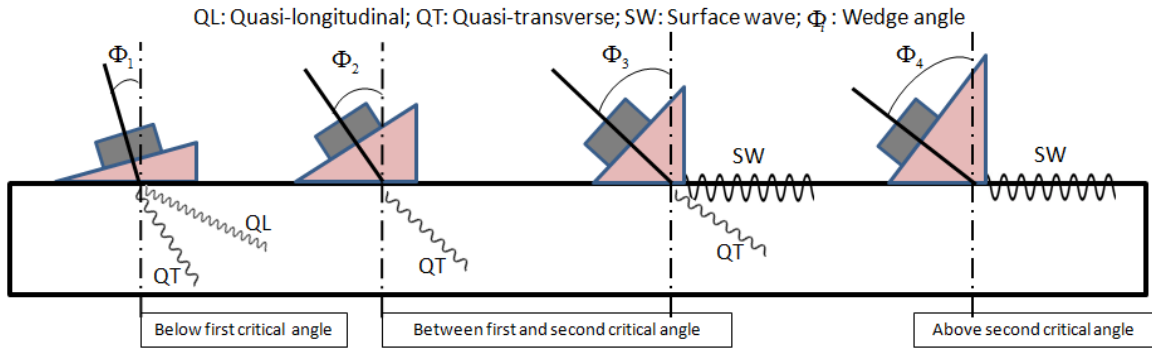


Figure 68: Modes of ultrasonic wave propagations at various wedge angles

Continuing with the derivation, similar process for $(x_1 - x_3)$ plane can be followed to find the equation for the wave propagating in the $(x_2 - x_3)$ plane of symmetry along the through-thickness angle θ_{23} measured with respect to the x_2 axis (Figure 67), for which the unit vector n_i can be expressed as:

$$n_i = (n_1, n_2, n_3) = (0, \cos \theta_{23}, \sin \theta_{23}) \quad (4.11)$$

Similar to $(x_1 - x_3)$ plane, three waves: transverse-horizontal (T), quasi-longitudinal (QL), and quasi-transverse (QT) waves exist for the $(x_2 - x_3)$ plane as well and are given by:

$$\begin{aligned}
\rho c_{p(T)}^2 &= \Lambda_{11} \\
\rho c_{p(QL)}^2 &= \left(\frac{\Lambda_{22} + \Lambda_{33}}{2} \right) + \frac{\sqrt{(\Lambda_{22} - \Lambda_{33})^2 + 4\Lambda_{23}^2}}{2} \\
\rho c_{p(QT)}^2 &= \left(\frac{\Lambda_{22} + \Lambda_{33}}{2} \right) - \frac{\sqrt{(\Lambda_{22} - \Lambda_{33})^2 + 4\Lambda_{23}^2}}{2}
\end{aligned} \tag{4.12}$$

Using the quasi-longitudinal or quasi-transverse-vertical wave propagating in the $(x_1 - x_3)$ plane, four linear elastic constants $(c_{11}, c_{13}, c_{33}, c_{55})$ can be found. Similarly, by considering the wave propagating in the $(x_2 - x_3)$ plane, four more constants $(c_{22}, c_{23}, c_{33}, c_{44})$ can be found, out of which (c_{33}) is repeated. Altogether seven out of nine constants for an orthotropic material can be found using the phase velocities of quasi-longitudinal or quasi-transverse-vertical waves propagating in the principal planes along $(x_1 - x_3)$ and $(x_2 - x_3)$. However, for computing (c_{12}, c_{66}) , wave travelling in the non-principal axes along an angle θ_{12} (Figure 69) must be considered [P. W. A. Stijnman, 1995], which reduces the orthotropic symmetry to monoclinic for which the stiffness matrix is given by Eqn. (2.14) and is repeated here:

$$\begin{bmatrix}
c_{11}' & c_{12}' & c_{13}' & 0 & 0 & c_{16}' \\
c_{12}' & c_{22}' & c_{23}' & 0 & 0 & c_{26}' \\
c_{13}' & c_{23}' & c_{33}' & 0 & 0 & c_{36}' \\
0 & 0 & 0 & c_{44}' & c_{45}' & 0 \\
0 & 0 & 0 & c_{45}' & c_{55}' & 0 \\
c_{16}' & c_{26}' & c_{36}' & 0 & 0 & c_{66}'
\end{bmatrix} \tag{4.13}$$

The terms for the monoclinic stiffness matrix $[c_{ij}']$ in Eqn. (4.13) can be found by multiplying the orthotropic stiffness matrix given by Eqn. (4.1) with the transformation matrix calculated using

the rotated angle θ_{12} by following the method suggested in Section 2.2.4.1. The superscript prime is used in order to differentiate it from the global coordinate of non-prime and local coordinate of superscript star used previously. The constants of the stiffness matrix $[c'_{ij}]$ are functions of $[c_{ij}]$ and the rotation angle θ_{12} , which are provided in Appendix B.

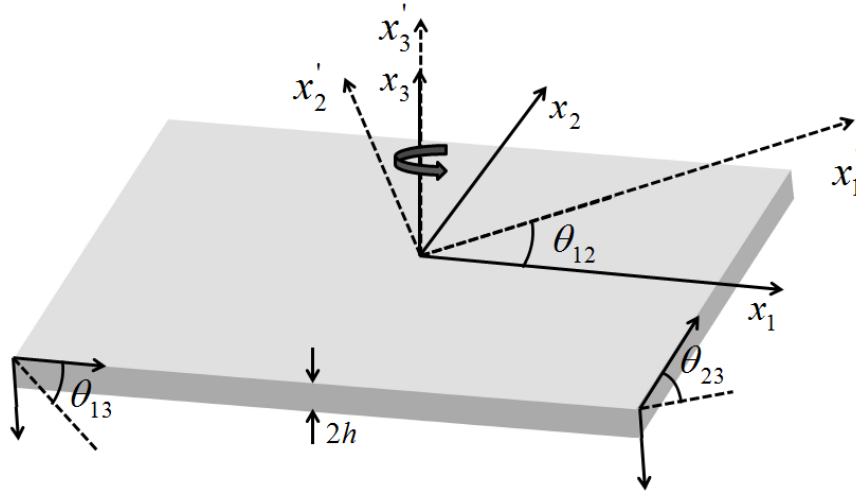


Figure 69: Anisotropic plate with rotated coordinate

To account for the monoclinic symmetry of the new stiffness matrix $[c'_{ij}]$, the terms Λ_{ij} in the Christoffel's equation given by Eqn. (4.5) has to be modified such that:

$$\begin{aligned}
 \Lambda'_{11} &= c'_{11} (n'_1)^2 + c'_{66} (n'_2)^2 + c'_{55} (n'_3)^2 + 2c'_{16} n'_1 n'_2 \\
 \Lambda'_{12} &= c'_{16} (n'_1)^2 + c'_{45} (n'_3)^2 + (c'_{12} + c'_{66}) n'_1 n'_2 \\
 \Lambda'_{13} &= (c'_{13} + c'_{55}) n'_1 n'_3 + (c'_{36} + c'_{45}) n'_2 n'_3 \\
 \Lambda'_{22} &= c'_{66} (n'_1)^2 + c'_{22} (n'_2)^2 + c'_{44} (n'_3)^2 + 2c'_{26} n'_1 n'_2 \\
 \Lambda'_{23} &= (c'_{36} + c'_{45}) n'_1 n'_3 + (c'_{23} + c'_{44}) n'_2 n'_3 \\
 \Lambda'_{33} &= c'_{55} (n'_1)^2 + c'_{44} (n'_2)^2 + c'_{33} (n'_3)^2 + 2c'_{45} n'_1 n'_2
 \end{aligned} \tag{4.14}$$

Where, (n'_1, n'_2) are the new unit vectors formed by rotating the original unit vectors (n_1, n_2) about x_3 axis by an angle θ_{12} (Figure 69)

Similar simplification as was done for the orthotropic symmetry discussed above by considering the wave travelling in the principal $(x_1 - x_3)$ and $(x_2 - x_3)$ planes can be repeated for the rotated monoclinic symmetry as well. This is done by considering the wave propagating in the $(x'_1 - x'_3)$ plane along the refracted angle θ'_{13} measured with respect to the x'_1 axis, for which the unit vector n'_i can be expressed as:

$$n'_i = (n'_1, n'_2, n'_3) = (\cos \theta'_{13}, 0, \sin \theta'_{13}) \quad (4.15)$$

By considering the wave propagating in the $(x'_1 - x'_3)$ plane the elements of Λ'_{ij} are reduced to:

$$\begin{aligned} \Lambda'_{11} &= c'_{11} (\cos \theta'_{13})^2 + c'_{55} (\sin \theta'_{13})^2 \\ \Lambda'_{12} &= c'_{16} \cos \theta'_{13} + c'_{45} (\sin \theta'_{13})^2 \\ \Lambda'_{13} &= (c'_{13} + c'_{55}) \cos \theta'_{13} \sin \theta'_{13} \\ \Lambda'_{22} &= c'_{66} (\cos \theta'_{13})^2 + c'_{44} (\sin \theta'_{13})^2 \\ \Lambda'_{23} &= (c'_{36} + c'_{45}) \cos \theta'_{13} \sin \theta'_{13} \\ \Lambda'_{33} &= c'_{55} (\cos \theta'_{13})^2 + c'_{33} (\sin \theta'_{13})^2 \end{aligned} \quad (4.16)$$

The elements of Λ'_{ij} given in Eqn. (4.16) are substituted back into the Christoffel's equation Eqn. (4.4) in order to find the eigenvalues and hence the three phase velocities. The three eigenvalues represent quasi-longitudinal, quasi-transverse, and transverse-horizontal waves propagating within the structure along the $(x'_1 - x'_3)$ plane.

In order to find the stiffness matrix using the search method discussed in Section 4.2, an algebraic expression is required to relate the phase velocities with the constants of $[\Lambda'_{ij}]$ matrix, similar to the one provided in Eqn. (4.10) and (4.12). For this reason, the method described by Koop [J. Koop, 2008] has been adopted to relate the stiffness constants to the phase velocities by analytically calculating the eigenvalues of the 3x3 Christoffel's matrix for which the constants Λ'_{ij} are provided in Eqn. (4.16).

In order to find the eigenvalues, Eqn. (4.6) takes on a polynomial form as:

$$\lambda^3 + M'_1\lambda^2 + M'_2\lambda + M'_3 = 0 \quad (4.17)$$

Where, λ is the eigenvalue, which is equal to (ρc_p^2) as given by Eqn. (4.6)

The coefficients $M'_{1,2,3}$ are given as:

$$\begin{aligned} M'_1 &= -\Lambda'_{11} - \Lambda'_{22} - \Lambda'_{33} \\ M'_2 &= \Lambda'_{11}\Lambda'_{22} + \Lambda'_{11}\Lambda'_{33} + \Lambda'_{22}\Lambda'_{33} - (\Lambda'_{12})^2 - (\Lambda'_{13})^2 - (\Lambda'_{23})^2 \\ M'_3 &= \Lambda'_{11}(\Lambda'_{23})^2 + \Lambda'_{22}(\Lambda'_{13})^2 + \Lambda'_{33}(\Lambda'_{12})^2 - \Lambda'_{11}\Lambda'_{22}\Lambda'_{33} - 2\Lambda'_{13}\Lambda'_{12}\Lambda'_{23} \end{aligned} \quad (4.18)$$

Defining:

$$\begin{aligned} p' &= (M'_1)^2 - 3M'_2 \\ q' &= -\frac{27}{2}M'_3 - (M'_1)^3 + \frac{9}{2}M'_1M'_2 \\ \beta &= \frac{1}{3} \arctan \left(\frac{\sqrt{(p')^3 - (q')^2}}{q'} \right) \end{aligned} \quad (4.19)$$

Finally, the eigenvalues are given by:

$$\begin{aligned}
 \rho(c'_{p(QL)})^2 = \lambda_1 &= \frac{\sqrt{p'}}{3} 2 \cos \beta - \frac{1}{3} M'_1 \\
 \rho(c'_{p(QT)})^2 = \lambda_2 &= -\frac{\sqrt{p'}}{3} (\cos \beta - \sqrt{3} \sin \beta) - \frac{1}{3} M'_1 \\
 \rho(c'_{p(T)})^2 = \lambda_3 &= -\frac{\sqrt{p'}}{3} (\cos \beta + \sqrt{3} \sin \beta) - \frac{1}{3} M'_1
 \end{aligned} \tag{4.20}$$

Eqn. (4.20) was evaluated and verified with the built in MATLAB function (*eig*) by comparing the eigenvalues of several randomly generated 3x3 symmetric matrices. In order to find the eigenvalues (λ_i) that are associated with the quasi-longitudinal and quasi-transverse waves propagating in the ($x'_1 - x'_3$) plane; Eqn. (4.20) was compared with the well-defined equations Eqn. (4.10) and Eqn. (4.12) for ($x_1 - x_3$) and ($x_2 - x_3$) planes respectively. Also the polarization (particle displacement) was examined using the eigenvectors of the associated eigenvalues. It was found that λ_1 , λ_2 , and λ_3 given by Eqn. (4.20) was associated with the quasi-longitudinal, quasi-transverse, and transverse-horizontal waves respectively.

The phase velocities can be readily calculated by using the aforementioned eigenvalues; however, group velocity is the one that is experimentally determined. Due to anisotropic nature of composites phase velocity vector propagating in the non-principal direction may not be equal to the group velocity vector [A. G. Every et al., 1990] as shown in Figure 70. In addition, material damping due to the use of viscoelastic polymer matrix can play a significant role in reducing the ultrasonic signal amplitude, thereby reducing the overall wave propagation distance.

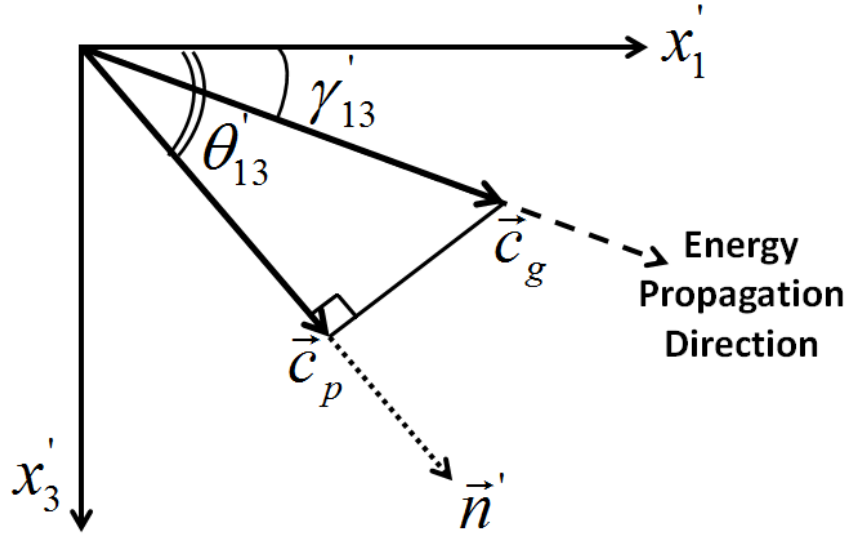


Figure 70: Propagation of phase and group velocity vectors in non-principal direction

Referring to Figure 70, the relationship between the group and the phase velocity vector is given by:

$$\begin{aligned} \vec{c}_p' &= \vec{c}_g' \cdot \vec{n}' \\ |\vec{c}_p'| &= |\vec{c}_g'| \cos(\theta'_{13} - \gamma'_{13}) \end{aligned} \quad (4.21)$$

Where, θ'_{13} the phase velocity angle and γ'_{13} is the group velocity angle measured experimentally

The equations presented in this section in conjunction with the experimentally determined group and phase velocities can be used to inversely calculate the stiffness constants for an orthotropic and higher symmetry specimen. In this dissertation, only isotropic metals and unidirectional composite laminates are considered for which a detailed method for inversely calculating and optimizing the stiffness constants is presented in the next section.

4.2 SEARCH ALGORITHM TO FIND ELASTIC CONSTANTS

Significant researches have been conducted and are described in the literature to inversely calculate and optimize the stiffness constants for composites using the measured phase/group velocities. Some of the most commonly used optimization methods include: Genetic Algorithms (GA) [K. Balasubramaniam et al., 1998], non-linear least square method [Y. C. Chu et al., 1994], or a combination of both [G. R. Liu et al., 2002]. Before using the experimental data to determine the stiffness constant, it is necessary to verify the optimization algorithm to be used for the inverse calculations. For this purpose, the built-in GA and Nonlinear Least Square (NLS) functions in MATLAB were evaluated at first to find the stiffness constants using the theoretically calculated phase velocities for an isotropic metal and transversely-isotropic unidirectional laminate with different wave propagation angles (number of wedges). It was found that the convergence of NLS method was superior to GA in this case; hence, the NLS method was chosen.

The built-in NLS method in MATLAB is based on minimizing the sum of square of the functions

$f_i(x)$ as:

$$\min_x f(x) = \min_x \sum_{i=1}^n f_i(x)^2 \quad (4.22)$$

In Eqn. (4.22), the functions $f_i(x)$ to be minimized are given by Eqn. (4.10) and Eqn. (4.12) for finding the stiffness constants $(c_{11}, c_{13}, c_{33}, c_{55})$ and $(c_{22}, c_{23}, c_{33}, c_{44})$ respectively by minimizing the error between the calculated and experimental phase velocities of quasi-longitudinal and quasi-transverse waves as:

$$\min \sum_{i=1}^n \left[(V_{P_{Calculated}})_i - (V_{P_{Measured}})_i \right]^2 \quad (4.23)$$

The sensitivity analysis of the NLS method to the random perturbation in the data was studied for isotropic metallic and unidirectional composite laminates, for which the results are presented in the following sections.

4.2.1 SENSITIVITY ANALYSIS FOR ISOTROPIC MATERIAL

The non-linear least squared algorithm was first verified on an isotropic aluminum Al 2024-T6 having the material properties of Young's modulus ($E = 72.4$ GPa), shear modulus ($G = 27.2$ GPa), Poisson's ratio ($\mu = 0.33$), and density ($\rho = 2780$ kg/m³) [ASM Al 2024-T6, 2014] for which the phase velocities were calculated analytically using Eqn. (4.10) by considering the quasi-longitudinal and quasi-transverse waves propagating at $\theta_{12} = 0^\circ$ along θ_{13} at [60/65/70/75/80/85/90] and [25/30/35/40/45/50/55] degrees respectively (Figure 69). Different propagating angles were needed to excite the quasi-longitudinal (QL) and quasi-transverse (QT) waves as shown in Figure 68. Figure 71 shows the flow chart of the method used to initially calculate the stiffness constants ($c_{11}, c_{13}, c_{33}, c_{55}$).

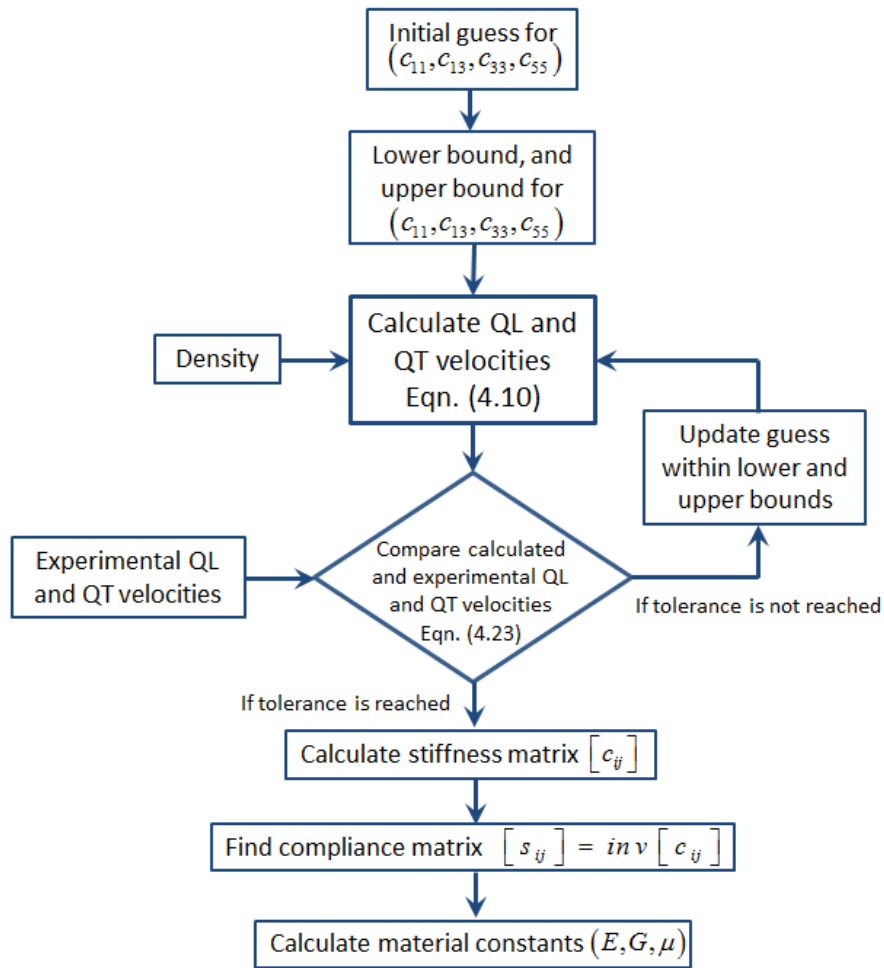


Figure 71: Non-linear least square method to calculate isotropic material constants

The wave velocities were then randomly perturbed by 0.5, 1, 2, and 5 percent from their original values to generate a total of ten data points for each perturbation. This study was performed in order to find out how the number of experimental readings, the number of propagation angles, and the effect of random variation in the experimental data influence the convergence of the material stiffness constants. The results, as shown in Figure 72 to Figure 74 for E , G , and μ respectively can be used to select the minimum number of propagation angles; hence, the minimum number of wedges needed to generate the quasi-longitudinal and quasi-transverse waves for an isotropic solid.

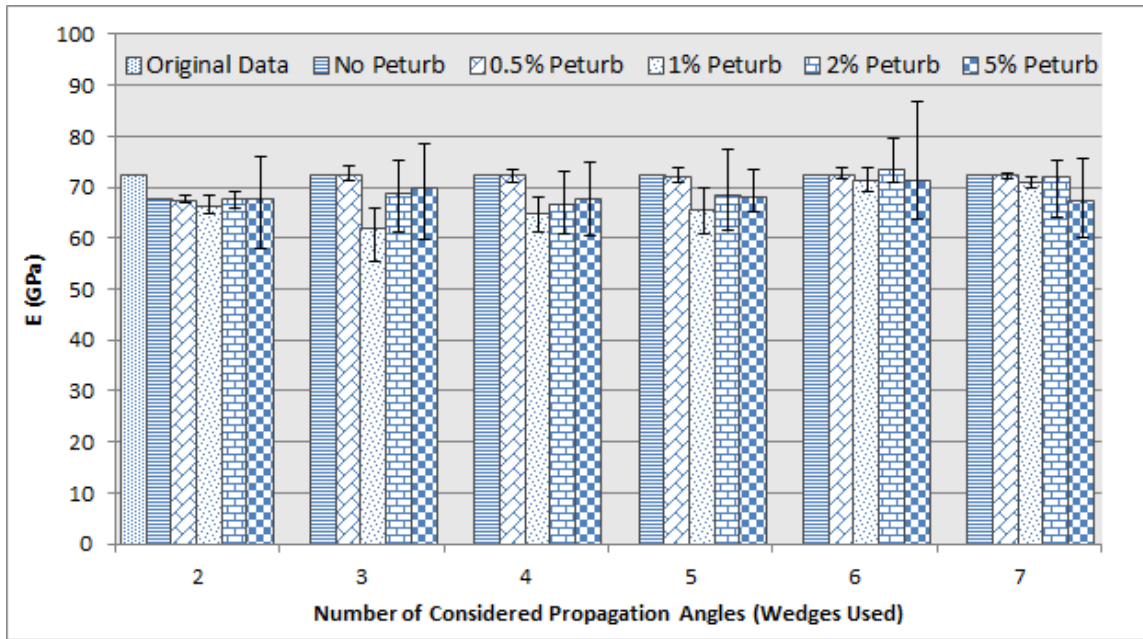


Figure 72: Initial convergence summary of Al 2024-T6 elastic stiffness (E)

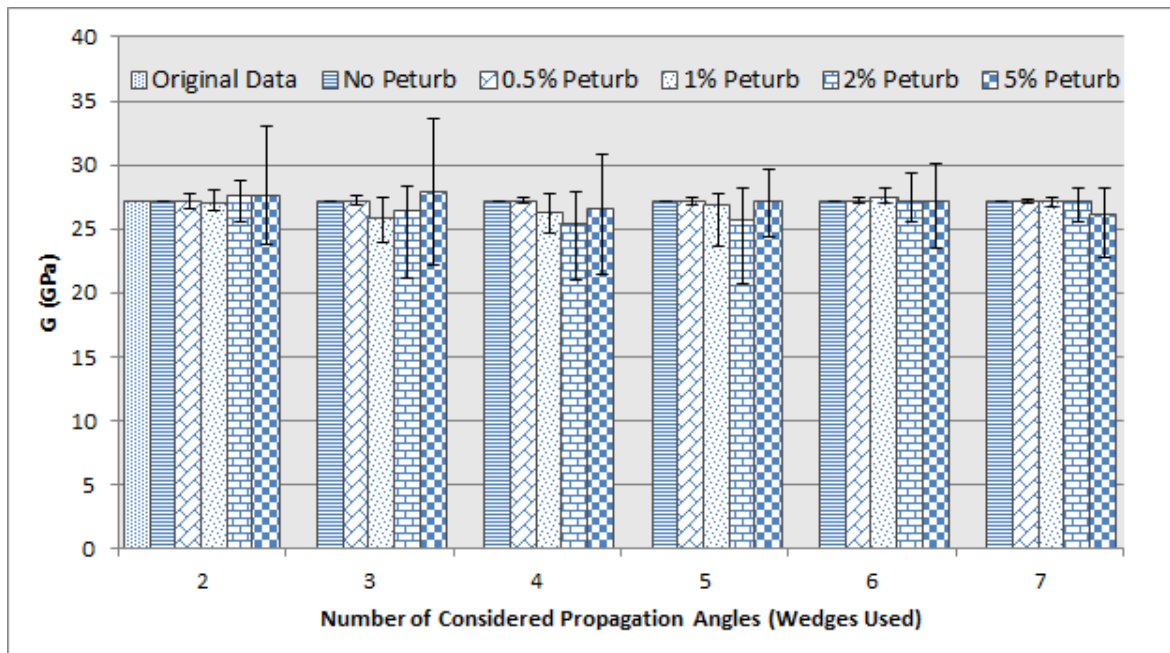


Figure 73: Initial convergence summary of Al 2024-T6 shear stiffness (G)

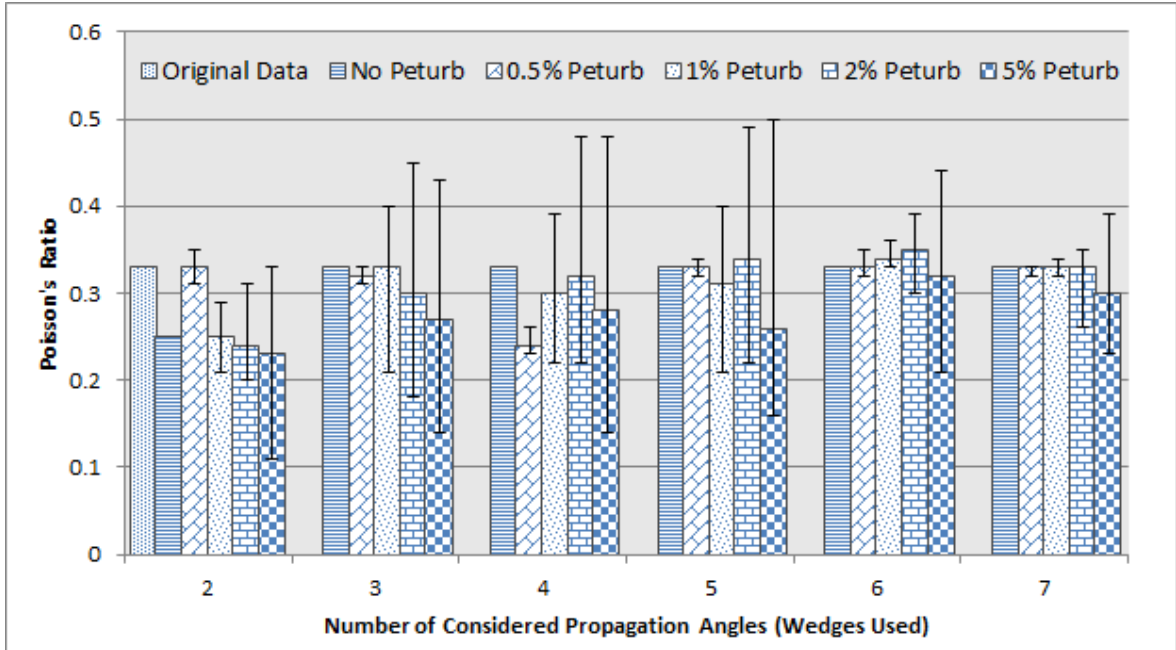


Figure 74: Initial convergence summary of AI 2024-T6 Poisson's ratio (μ)

From Figure 72 to Figure 74 above, it can be seen that there is a direct relationship between the number of propagation angles used and the convergence of the elastic constants for random perturbation of 2% and higher. It was found that the number of data considered for an average (three or ten data points) had very minimal effect in the convergence. The algorithm did not converge even without any perturbation if only two perturbations angles were considered, suggesting the need of at least three angles for the experiments. As can be seen from Figure 72 and Figure 74, the error associated with the data scatter of E and μ respectively was higher compared to G , which is shown in Figure 73.

An improvement in the least-squared algorithm for an isotropic material presented above was performed by comparing the stiffness matrix constants (c_{11}, c_{33}). Knowing that c_{11} should equal

to c_{33} for an isotropic material, a bisection method was implemented to minimize the difference between c_{11} and c_{33} by letting the other two variables (c_{13}, c_{55}) change between the upper and lower bounds to satisfy the imposed equality condition. The improved optimization method shown in Figure 75, in turn greatly improved the convergence results.

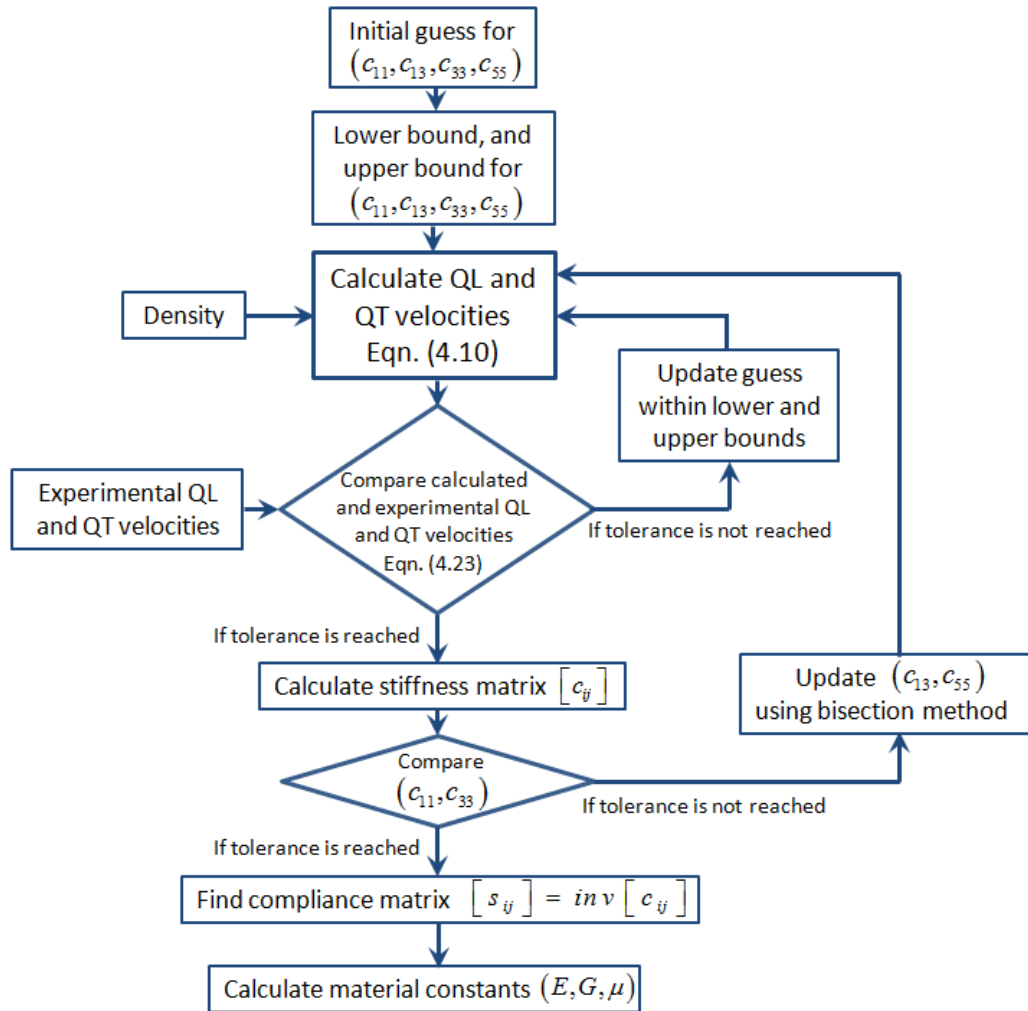


Figure 75: An improved method to calculate isotropic material stiffness constants

The convergence summary and the data scatter plot after implementing the bisection method on the same sets of data used previously are shown in Figure 76 to Figure 78.

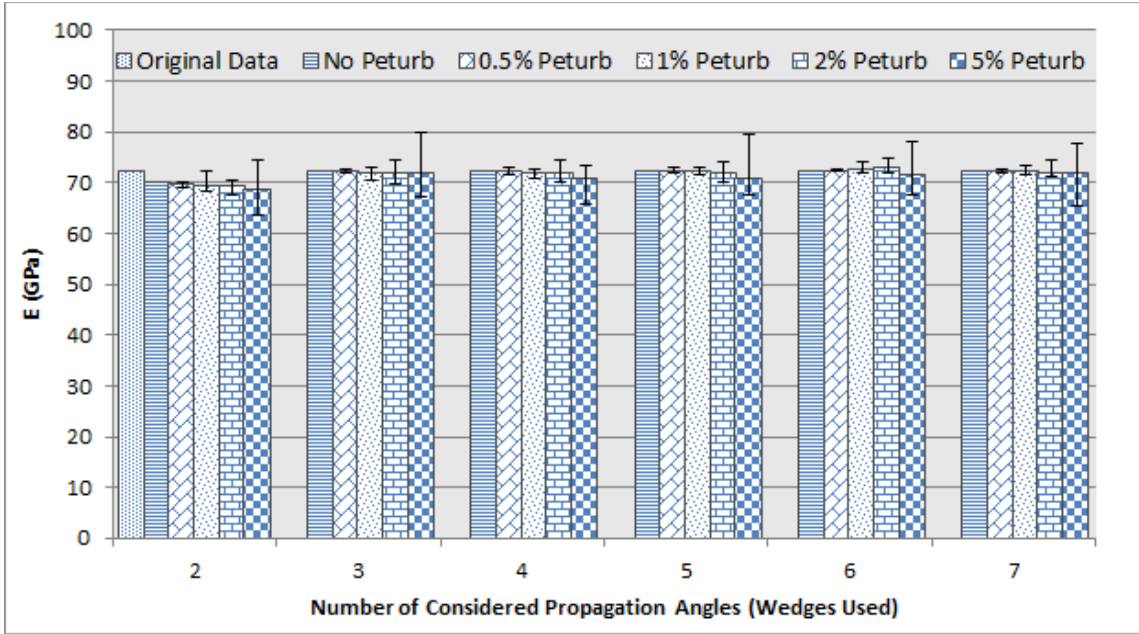


Figure 76: Convergence of AI 2024-T6 elastic stiffness (E) after implementing improved algorithm

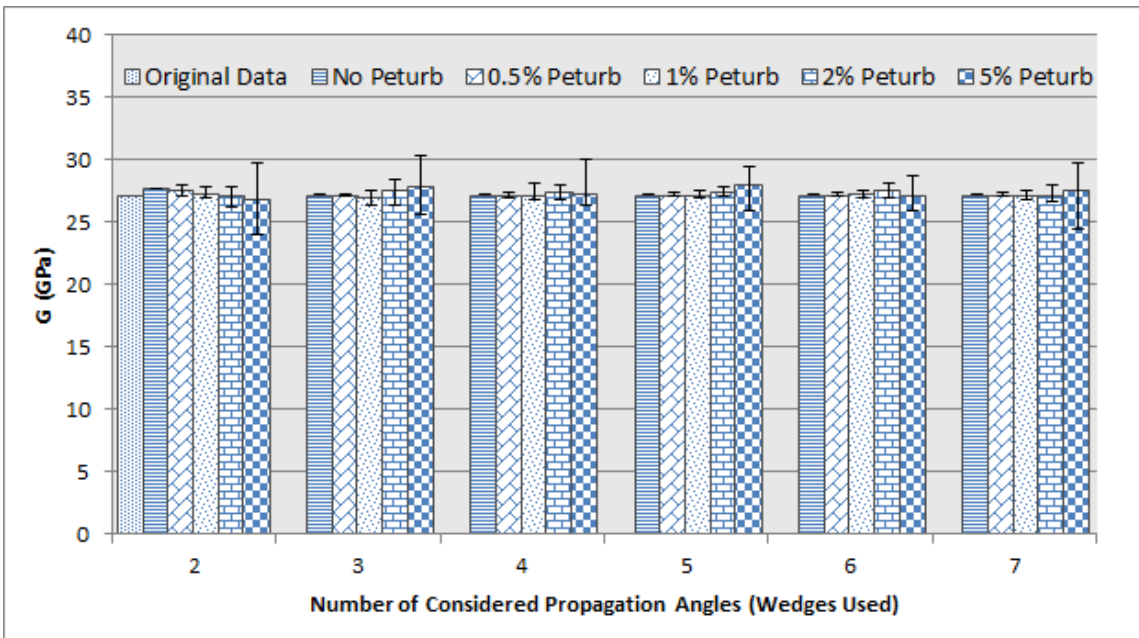


Figure 77: Convergence of AI 2024-T6 shear stiffness (G) after implementing improved algorithm

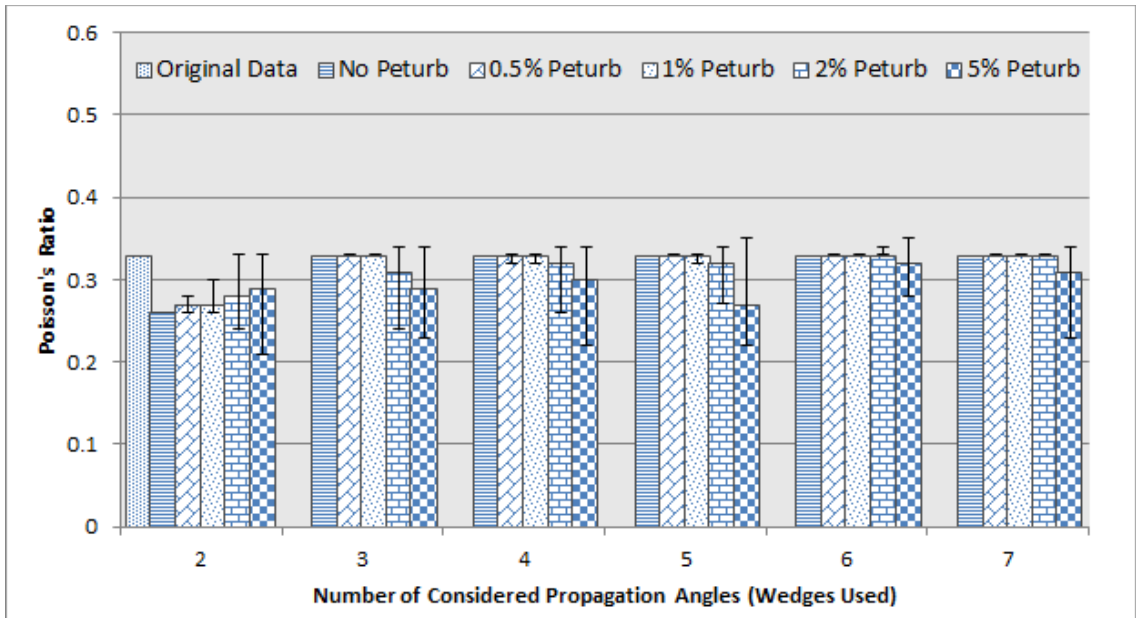


Figure 78: Convergence of Al 2024-T6 Poisson's ratio (μ) after implementing improved algorithm

It is evident from Figure 76 to Figure 78 that implementing the bisection search has greatly improved the convergence results and managed to reduce the number of required propagation angles from six to only three in order to counteract up to 1% random errors. It can be seen that the refined algorithm still did not converge if only two propagation angles were considered. Hence, a minimum of three propagation angles (three wedges) are required for both quasi-longitudinal and quasi-transverse waves. Similar results were found when the algorithm was tested on an isotropic Ti-6Al-4V alloy for which the results are provided in Appendix C.

4.2.2 SENSITIVITY ANALYSIS FOR UNIDIRECTIONAL COMPOSITE LAMINATE

The algorithm was then tested on a previously used unidirectional composite laminate (G40-800/5276-1) for which the material properties are provided in Table 3. The quasi-longitudinal and quasi-transverse waves' phase velocities for this laminate were calculated analytically using

Eqn. (4.10) and Eqn. (4.12) for $\theta_{12} = 0^\circ$ and $\theta_{12} = 90^\circ$ respectively, along the propagation angles of θ_{13} and θ_{23} at [60/65/70/75/80/85/90] and [25/30/35/40/45/50/55] degrees (Figure 69). Figure 79 shows the flow chart of the method used to initially calculate the stiffness constants $(c_{11}, c_{13}, c_{33}, c_{55})$ and $(c_{22}, c_{23}, c_{33}, c_{44})$ by considering the waves along $\theta_{12} = 0^\circ$ and $\theta_{12} = 90^\circ$ respectively.

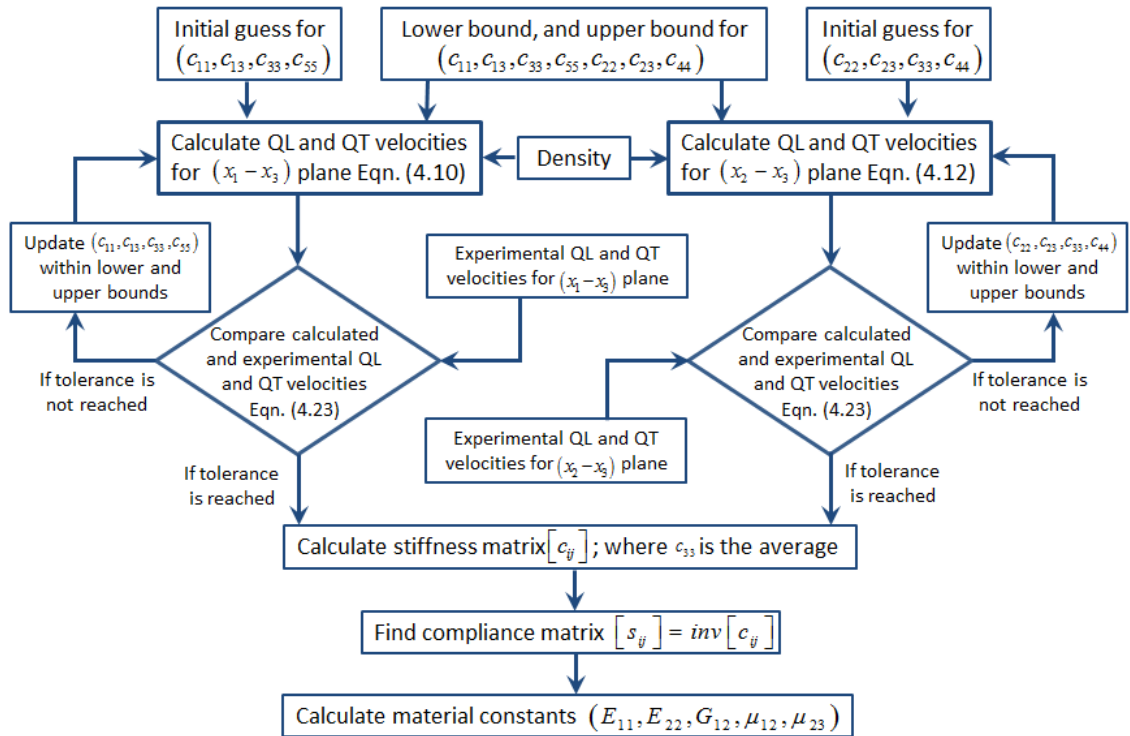


Figure 79: Flow chart to calculate stiffness constants of a unidirectional composite laminate

The wave velocities were then randomly perturbed by 0.5, 1, 2, and 5 percent from their original values to generate a total of ten data points for each perturbation as was previously done for the isotropic material. Similar to the isotropic case, the results as shown in Figure 80 to Figure 84 for E_{11} , E_{22} , G_{12} , and Poisson's ratios (μ_{12}, μ_{23}) can be used to select the minimum

number of propagation angles; hence, the minimum number of wedges needed to generate the quasi-longitudinal and quasi-transverse waves for a unidirectional laminate.

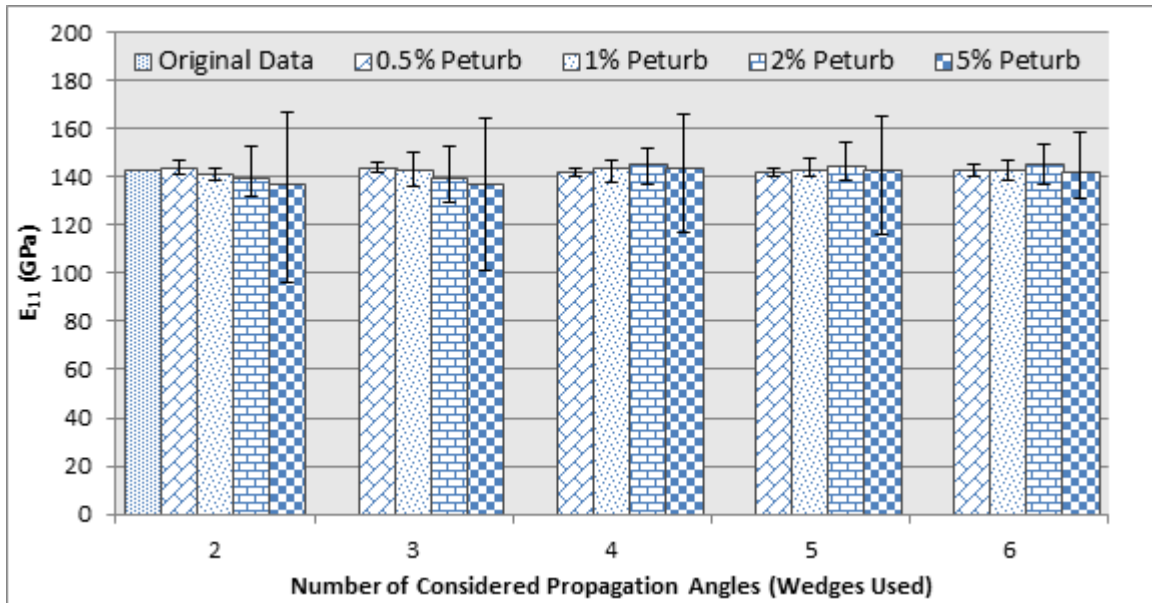


Figure 80: Initial convergence summary of E_{11}

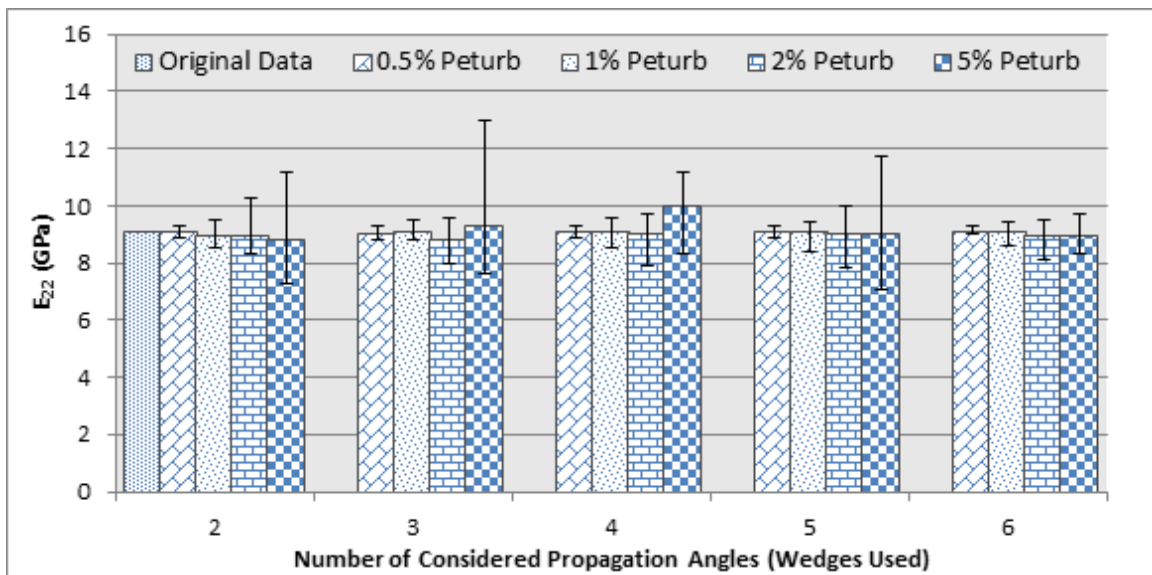


Figure 81: Initial convergence summary of E_{22}

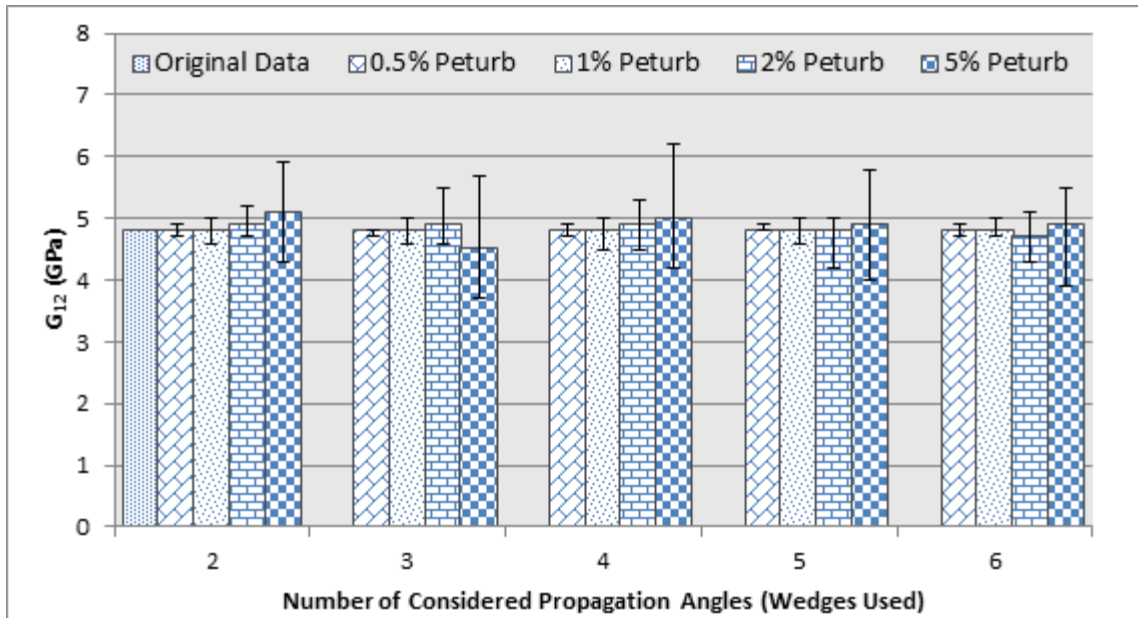


Figure 82: Initial convergence summary of G_{12}

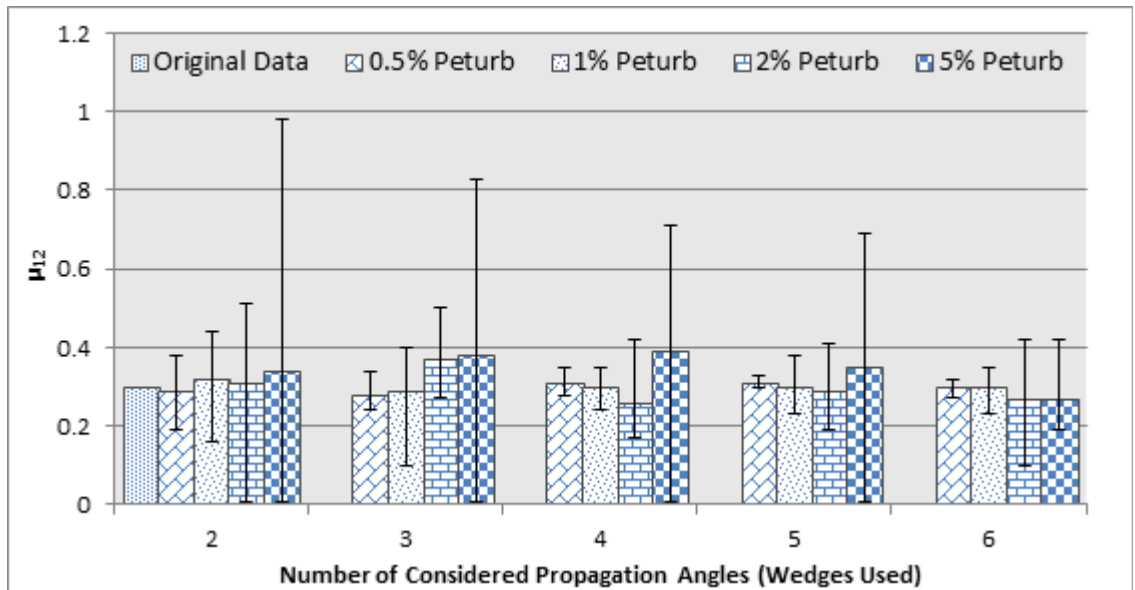


Figure 83: Initial convergence summary of μ_{12}

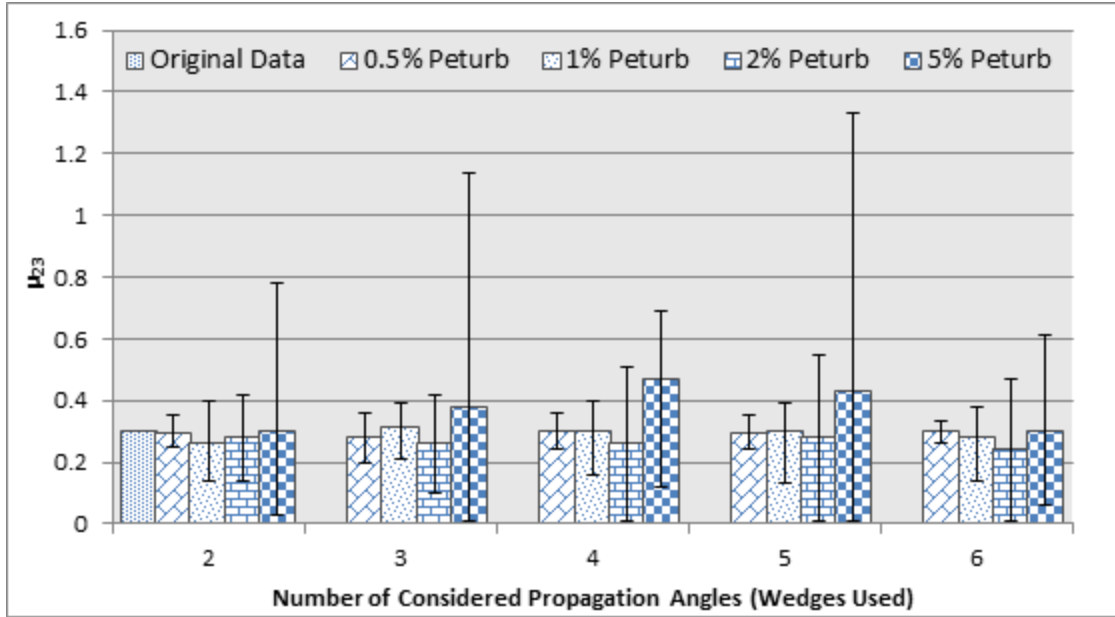


Figure 84: Initial convergence summary of μ_{23}

From Figure 80 to Figure 84 above, it can be seen that unlike for isotropic material the algorithm converged even when only two wedges were considered. This suggests the minimum number of required wedges to be only two each for quasi-longitudinal and quasi-transverse waves for $(x_1 - x_3)$ and $(x_2 - x_3)$ planes. The method presented in Figure 79 was susceptible to the change in initial guess and lower and upper bounds. The error associated with the data scatter of Poisson's ratio was higher as compared to the tensile and shear stiffness. Therefore, an improvement in the least-squared algorithm for the unidirectional laminate presented above was performed by comparing and equating the stiffness matrix constants (c_{33}) calculated using the waves propagating in the $(x_1 - x_3)$ and $(x_2 - x_3)$ planes. Also knowing that c_{22} should be equal to c_{33} for a transversely isotropic material; a bisection method was implemented in two steps. First, the difference between the calculated c_{33} from two different wave propagation planes were minimized. Then, the minimized stiffness constant c_{33} was further compared with

c_{22} in order to reduce the difference. During the minimization process the other variables ($c_{11}, c_{13}, c_{23}, c_{55}, c_{44}$) were let to freely change between the upper and lower bounds to satisfy the equality condition. The flow chart of the improved search method is shown in Figure 85.

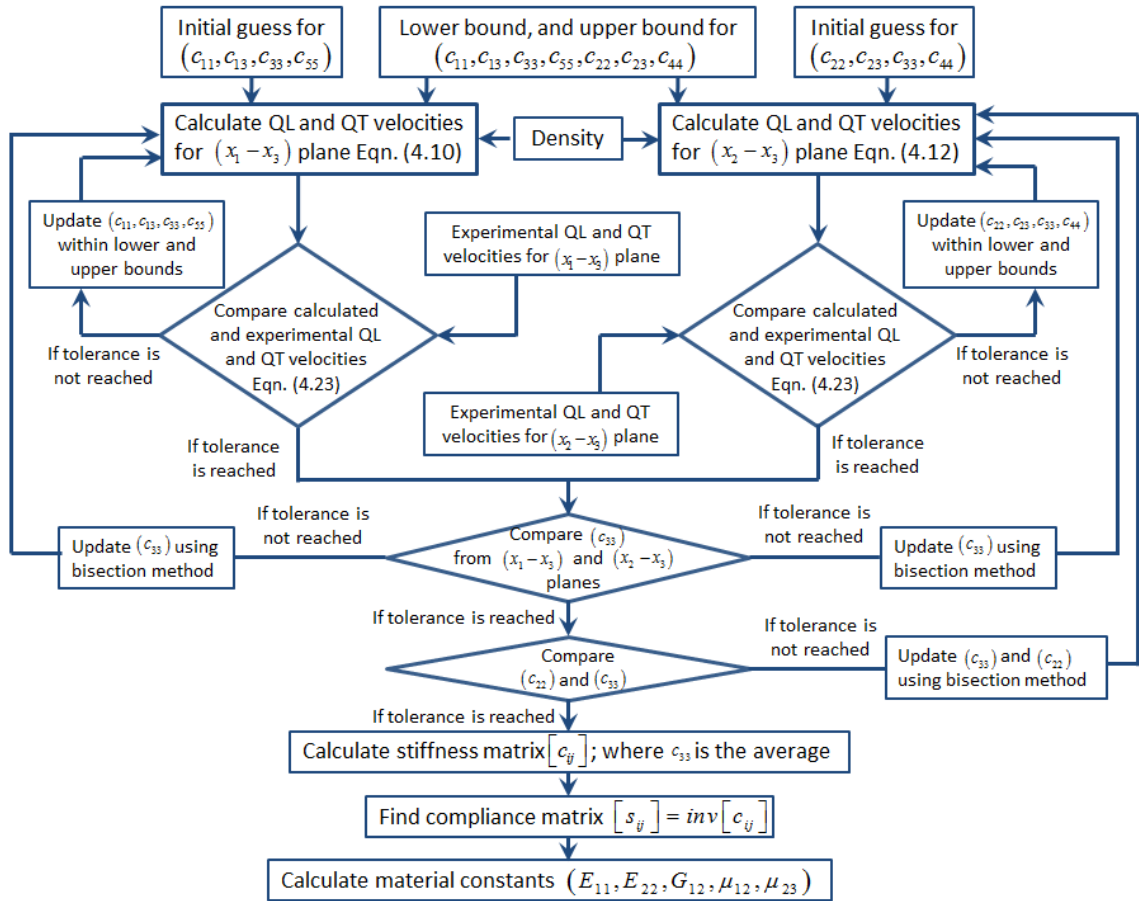


Figure 85: Improved method to find stiffness constant of transversely isotropic material

This method in turn greatly improved the convergence results especially for E_{22} and μ_{23} as shown in Figure 87 and Figure 90 respectively. The other stiffness constants E_{11} (Figure 86), G_{12} (Figure 88), and μ_{12} (Figure 89) were not significantly changed as compared to the initial method shown in Figure 79.

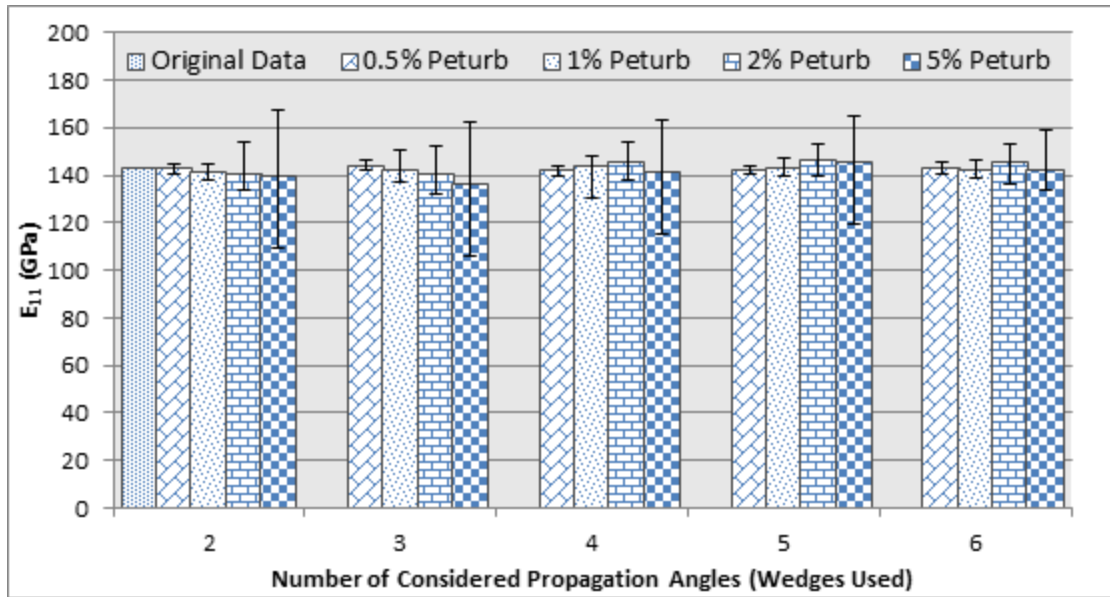


Figure 86: Convergence summary of E_{11} after implementing improved algorithm

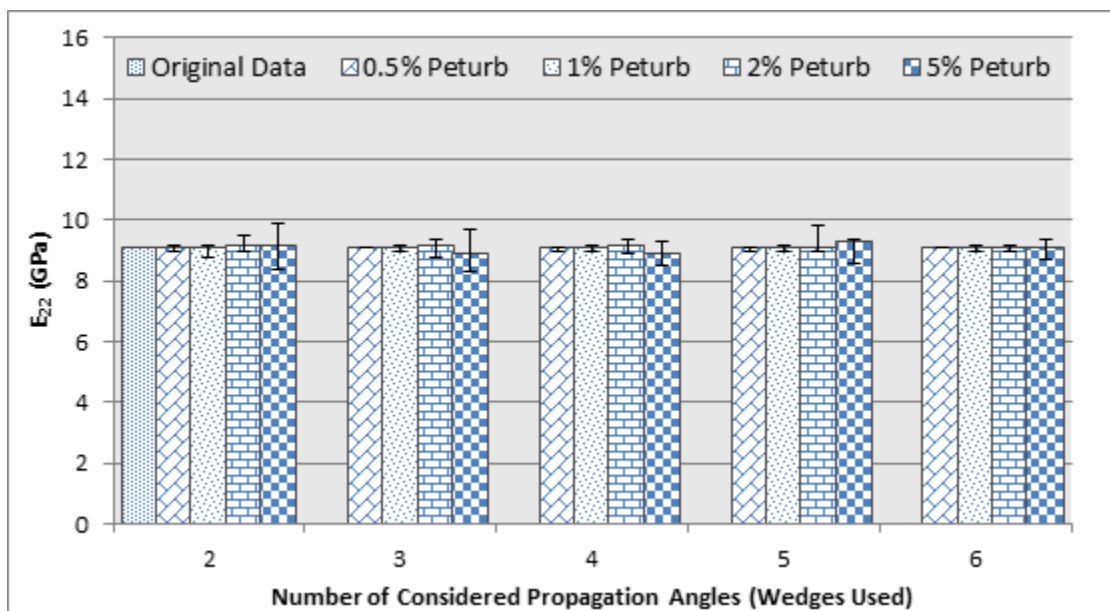


Figure 87: Convergence summary of E_{22} after implementing improved algorithm

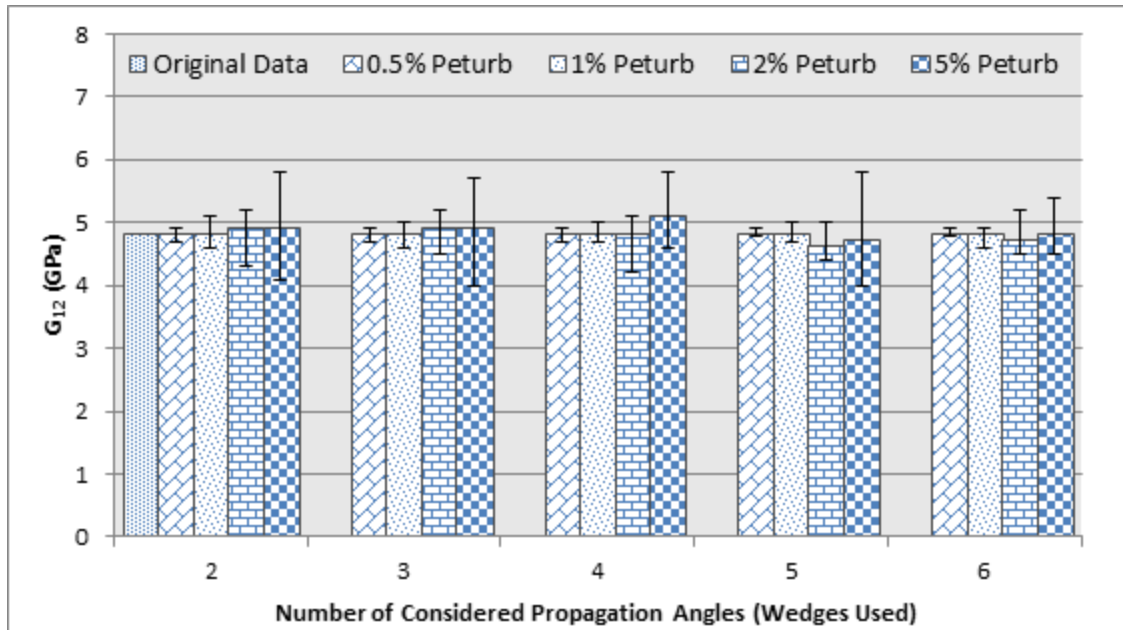


Figure 88: Convergence summary of G_{12} after implementing improved algorithm

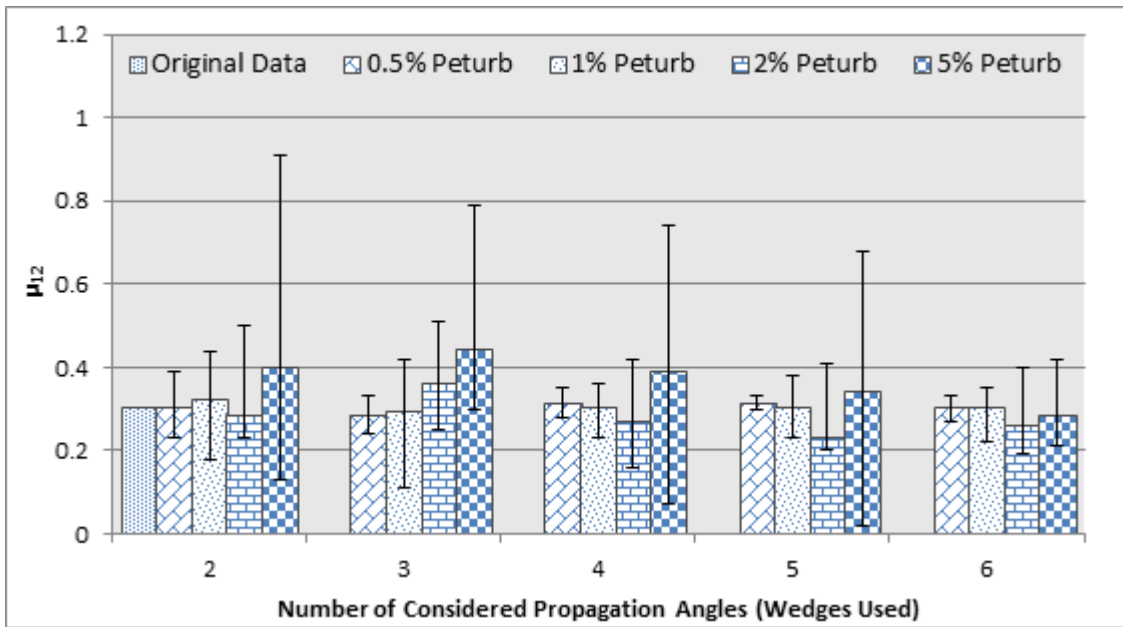


Figure 89: Convergence summary of μ_{12} after implementing improved algorithm

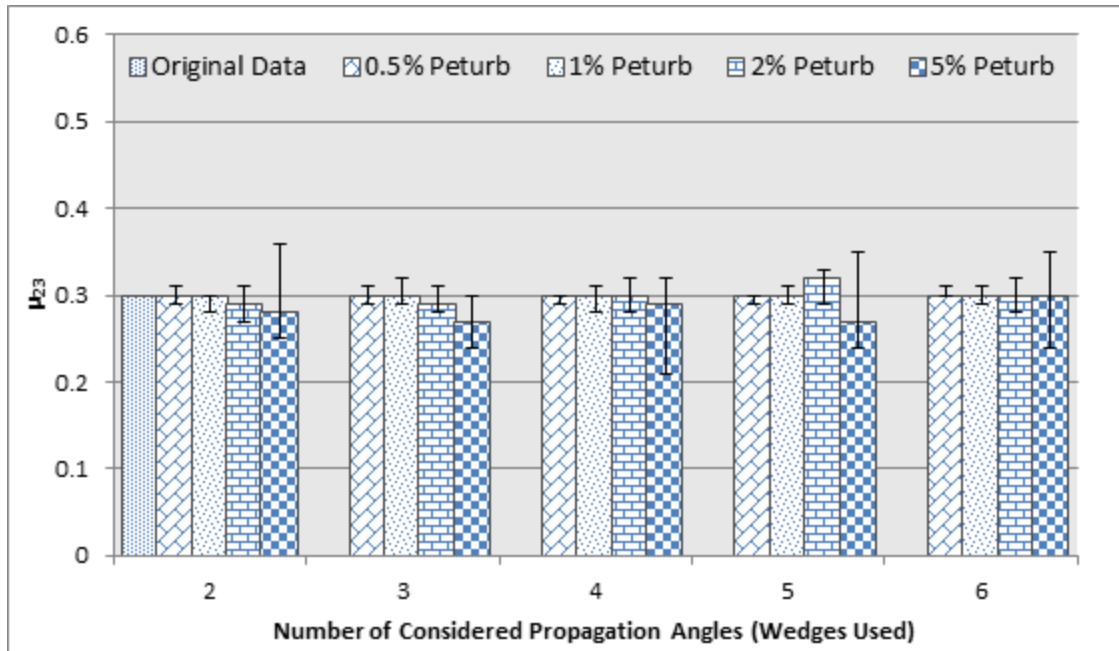


Figure 90: Convergence summary of μ_{23} after implementing improved algorithm

From Figure 86 to Figure 90 above, it is evident that a minimum of two wedges each to generate quasi-longitudinal and quasi-transverse waves are required. The improved method was not susceptible to change in initial guesses and search bounds. Similar results were found when the algorithm was tested on a different transversely isotropic material for which the results are provided in Appendix D.

4.3 EXPERIMENTAL VERIFICATION

The most commonly used methods for determining the stiffness constants for an isotropic solid consists of directly measuring the pure longitudinal and shear wave velocities across the thickness using pulse-echo [E. P. Papadakis, 1998] or through transmission [E. E. Franco et al., 2011] technique and relating the velocities to the stiffness constants E , G , and μ [ASTM

E494-10, 2010]. Whereas for transversely isotropic media the stiffness constants are calculated using the ultrasonic phase velocities that are based on: (i) cutting the specimen in a predetermined plane or (ii) by using an immersion technique. In the cutting technique, the samples are cut along a predetermined direction and the ultrasonic wave velocities are measured along those directions to directly calculate the stiffness constants [W. C. Van Buskirk et al., 1986]. In the immersion techniques the sample is immersed in a water/liquid where quasi-longitudinal and quasi-transverse waves are generated at different oblique angles to the liquid-solid interface by rotating the specimen [P. W. A. Stijnman, 1995] as shown in Figure 91. In order to find the wave propagation angle, the ultrasonic receiver can be translated vertically to receive the signal at the maximum strength.

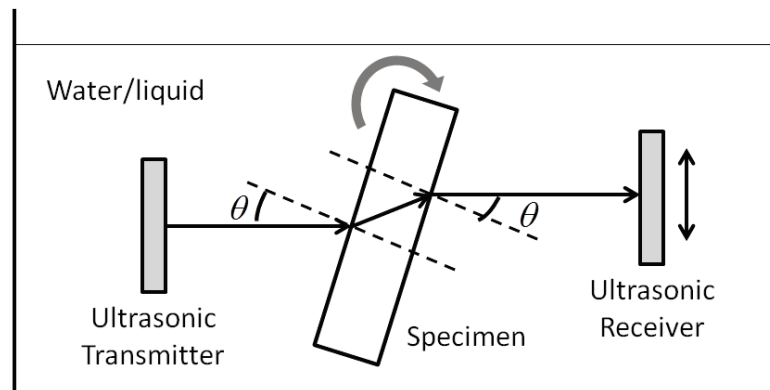


Figure 91: Schematic of the immersion method

One major drawback of the aforementioned methods is that small samples from the material or structure being analyzed with access to both surfaces are required. To overcome this problem, a one-sided method based on the ultrasonic wave propagation theory as discussed in Section 4.1 is experimentally verified. The method consists of generating and receiving quasi-longitudinal and quasi-transverse waves at proper angle of incidence (Figure 68) using the number of angled wedges as suggested by the search/sensitivity analysis presented in Section 4.2.

4.3.1 EXPERIMENTAL SETUP AND DATA ACQUISITION

Two different thicknesses of isotropic aluminum Al 7050-T7451 and one transversely isotropic unidirectional composite laminate constructed out of Cycom 977-2-12k-HTA prepreg were experimentally tested to verify the analytical and optimization routines presented in Section 4.2.1 and 4.2.2 respectively. The experimental schematic and setup is shown in Figure 92 and is described in the following paragraph.

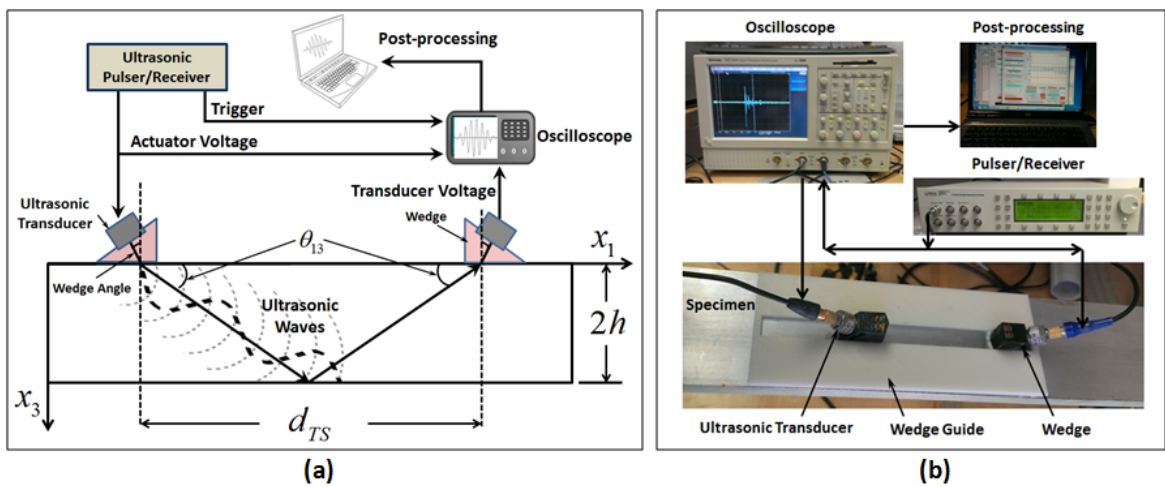


Figure 92: Experimental (a) schematic and (b) setup to generate and gather ultrasonic waves

UTEX UT340 pulser/receiver system was used to send high voltage (100 V) at short pulses to a Panamatrix 5MHz/0.25"/C543-SM ultrasonic transducers as well as a trigger signal to start the Tektronix TDS-5104 digital oscilloscope. The ultrasonic wave generated by the pulse signal propagates through the sample in an angle and gets reflected from the back surface; another ultrasonic transducer of the same kind then picks up the reflected signal. The distance (d_{TS}) between the actuating and sensing transducers were varied in a straight line with the help of a wedge guide in order to capture the maximum signal strength received by the sensing

transducer. Once the maximum signal strength was received, data were acquired at a rate of 125 MS/s and exported to MATLAB as a (.mat) file for post-processing. Custom software was developed in MATLAB to post-process the data and extract the ultrasonic wave velocity as shown in Figure 93.

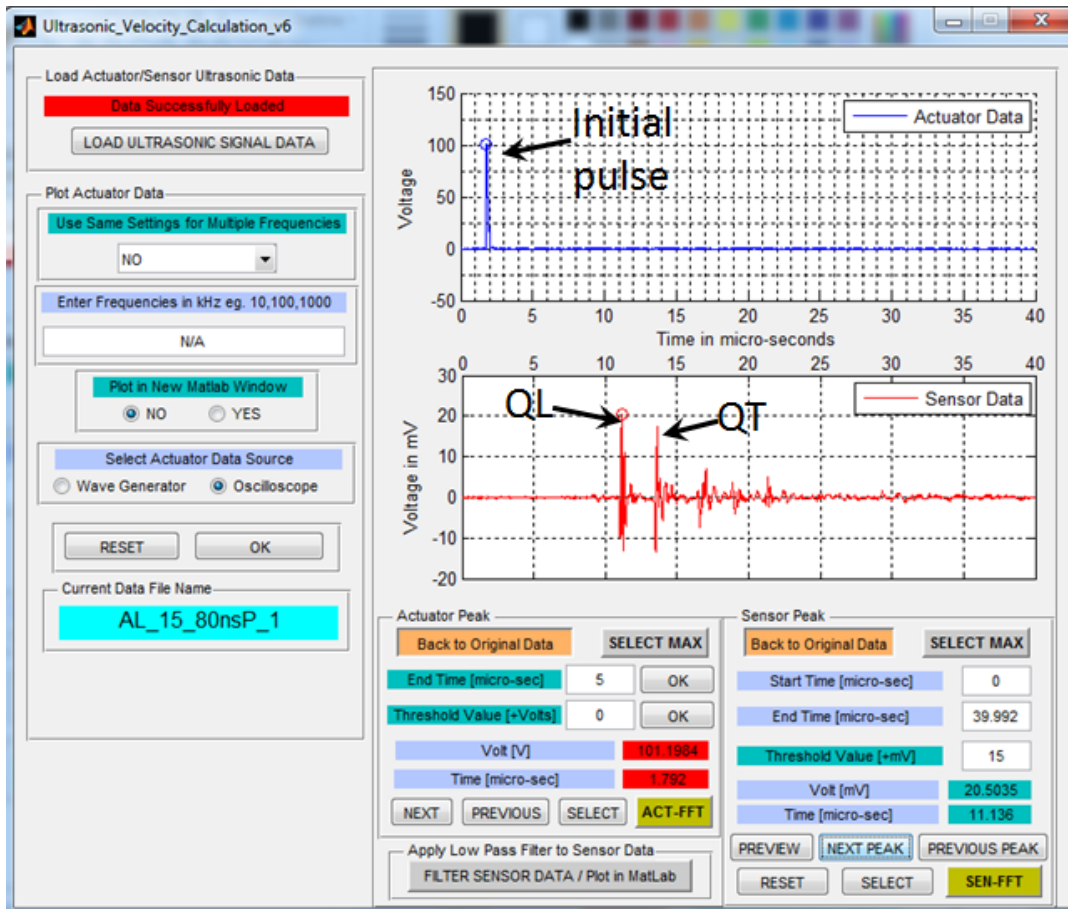


Figure 93: Custom MATLAB GUI showing initial pulse, QL and QT waves generated by 15° wedge

Custom-made wedges were used to excite QL and QT waves for isotropic and unidirectional composite specimen. The wedges were designed and printed in Stratasys Dimension 3D printer with the holes filled with Westsystem 105 Epoxy resin and 205 Fast-hardener. The methods followed to make the wedges are shown in Figure 94.

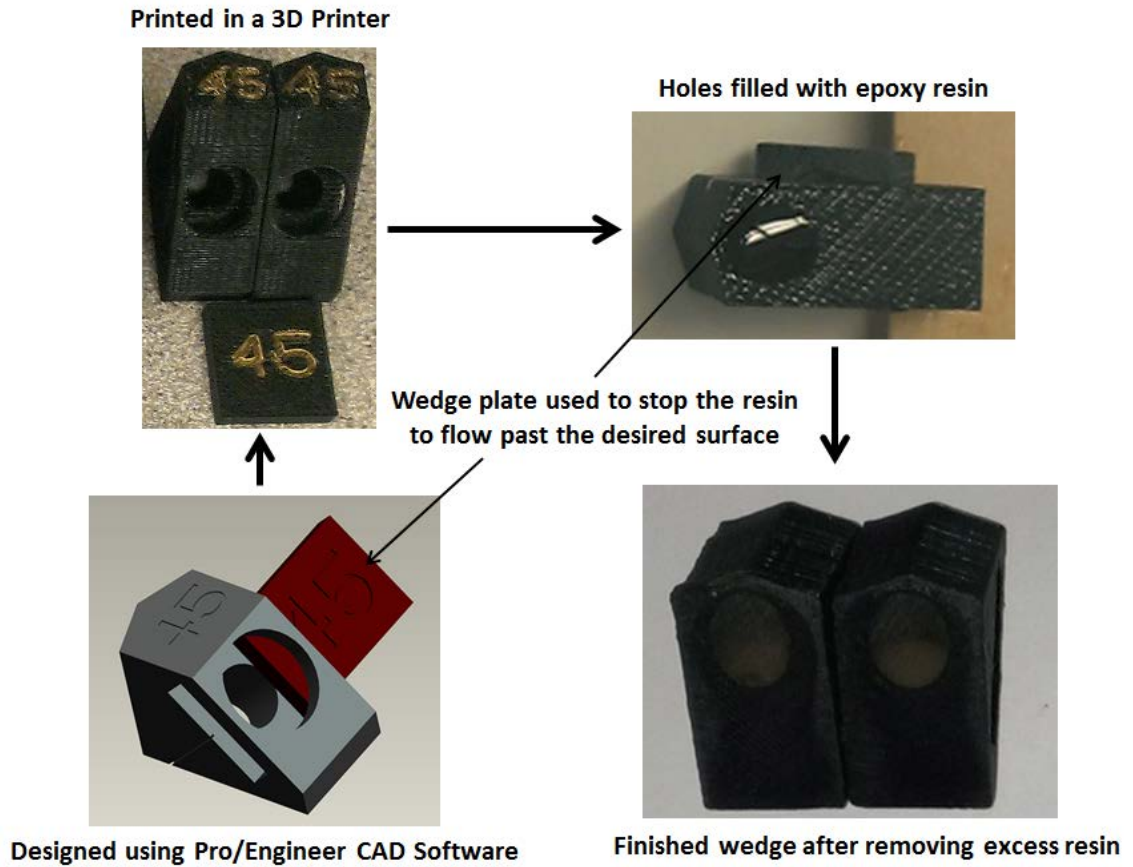


Figure 94: Method followed to fabricate the custom wedges

Acquired signals were calibrated to incorporate for the time taken by the ultrasound to travel through the wedge and into the sample. This was done by measuring the time for the ultrasound to travel from the actuating transducer to the sensing transducer for all sets of wedges. It was also found that there was a delay of approximately 0.2 micro-seconds between the pulse generated by the pulser/receiver and the ultrasound generated by the transducer. This was due to the time-delay or rise-time for the piezo-electric element used in the transducer to react to the applied short high voltage pulse. The time-of-travel was found by tracking the peak of the initial pulse and the wave signal received by the receiving transducer as shown in Figure 93. The total delay time was added to the acquired initial pulse time when calculating the wave velocity.

4.3.2 EXPERIMENTAL RESULTS FOR ISOTROPIC AL 7050-T7451

The two samples of isotropic aluminum Al 7050-T7451 measuring 254 mm by 50.8 mm with thicknesses of 5 mm and 12.7 mm were experimentally tested using the ultrasonic method presented in this thesis. Stiffness constants for the Al 7050-T7451 sample cut from the same block was experimentally determined previously at Delft University of Technology (TU Delft) by Lotz [T. Lotz, 2014] using tensile tests following the ASTM standard [ASTM E8M-04, 2004]. The quasi-longitudinal and quasi-transverse waves were generated and acquired using three different angled wedges as suggested by the sensitivity analysis. An average of three data points were taken for each velocity measurements. The summary of the measured QL and QT velocities using different wedges for the isotropic Al 7050-T7451 is provided in Table 6.

Table 6: Measured QL and QT velocities and propagation angles of Al 7050-T7451 specimen

Wave Mode	5 mm Sample		12.7 mm Sample	
	Propagation Angle θ_{13} (Figure 67)	Wave Velocity (m/s)	Propagation Angle θ_{13} (Figure 67)	Wave Velocity (m/s)
QL	37.2°	6247.3	46.9°	6188.9
QL	60.0°	6200.6	60.8°	6188.7
QL	90.0°	6278.2	90.0°	6235.3
QT	40.2°	3033.0	32.3°	3041.7
QT	42.6°	3060.7	39.8°	3057.6
QT	48.6°	3069.7	46.8°	3076.5

The velocity data provided in Table 6 was used to inversely calculate the material constants provided in Table 7 using the improved algorithm for the Al 7050-T4451 sample.

Table 7: Measured material properties of Al 7050-T7451

	E (GPa)	Poisson's ratio	G (GPa)	Density (kg/m ³)
Published [MIL-HDBD-5, 2001]	71.7	0.33	26.9	2825
Measured using Tensile Test [T. Lotz, 2014]	70.2	0.33	26.4	Not Measured
Measured using ultrasonic techniques presented above				
12.7 mm sample (Using improved algorithm)	71.8	0.34	26.7	2830 (Measured)
5 mm sample (Using improved algorithm)	71.7	0.35	26.6	2830 (Measured)

It can be seen from Table 7 that the results obtained using the non-destructive ultrasonic method were consistent for both thick (12.7mm) and thin (5mm) samples with minor discrepancy in the Poisson's ratio. The values for E and G measured using the ultrasonic method were closer to the published data as compared to the values using the tensile testing. However, the Poisson's ratio was slightly off as compared to both mechanical testing and the published value.

4.3.3 EXPERIMENTAL RESULTS FOR TRANSVERSELY ISOTROPIC

For finding the stiffness constants of a transversely isotropic laminate, a panel constructed out of 24 layers of unidirectional Cycom 977-2-12k-HTA prepreg was tested using the ultrasonic technique along with the tensile test. The overall dimension of the sample was 300 mm by 300 mm with an average thickness of 6 mm. The density of the sample was measured to be 1700 kg/m³. The quasi-longitudinal and quasi-transverse waves were generated and acquired using three different angled-wedges instead of two as suggested by the sensitivity analysis due to the variation in sample thickness. The QL and QT waves were measured at two different planes

corresponding to 0° and 90° angles with respect to the fibre orientation. An average of three data points were taken for each velocity measurements. The summary of the measured QL and QT velocities using different angled wedges for the transversely isotropic composite laminate is provided in Table 8.

Table 8: Summary of the measured QL and QT velocities of the transversely isotropic specimen

Wave Mode	$\theta_{12} = 0^\circ$ (Figure 67)		$\theta_{12} = 90^\circ$ (Figure 67)	
	Propagation Angle (θ_{13})	Wave Velocity (m/s)	Propagation Angle (θ_{23})	Wave Velocity (m/s)
QL	23.9°	8334.8	45.6°	2801.0
QL	27.0°	8179.0	34.0°	2755.6
QL	90.0°	2800.5	90.0°	2800.5
QT	65.7°	2422.6	43.9°	1637.5
QT	66.4°	2447.6	43.1°	1640.9
QT	70.9°	2501.2	37.7°	1676.5

The velocity data provided in Table 8 was used to inversely calculate the material constants provided in Table 9 using the improved algorithm provided in Figure 85. Once the ultrasonic velocity data were obtained, the panel was then waterjet cut to produce four coupons measuring 25.4 mm (1 inch) by 254 mm (10 inch) each for tensile testing on a MTS-810 Material Test System using a displacement controlled mode of 2 mm/min. Two coupons from 0° and 90° fibre orientations were used to measure E_{11} and E_{22} respectively. Coupon from 0° was instrumented with Tee strain gage (CAE-06-125WT-350) to determine the in-plane Poisson's ratio μ_{12} ; whereas, MTS-643.12E-24 extensometer was used to measure the induced strains due to applied loads on rest of the coupons for calculating E_{11} and E_{22} stiffness. Transverse Poisson's ratio μ_{23} and shear stiffness G_{12} could not be measured due to limitations in the as constructed panel. Results from the tensile tests are also presented in Table 9.

Table 9: Measured material properties of transversely isotropic sample

	E_{11} (GPa)	E_{22} (GPa)	G_{12} (GPa)	μ_{12}	μ_{23}
Measured using ultrasonic technique with improved algorithm	127.3	11.8	13.4	0.56	0.27
Measured using tensile test	119.6	10.9	Not Measured	0.33	Not Measured

It can be seen from Table 9, that the results obtained using the non-destructive ultrasonic method and the improved algorithm presented in this thesis were consistent with the tensile tests with minor discrepancy in the E_{11} (6.4%) and E_{22} (8.3%). However, the ultrasonic method over-predicted the in-plane Poisson's ratio μ_{12} by about 70% and no data were available to compare μ_{23} and G_{12} . This discrepancy can be explained due to the panel thickness variation of approximately ± 0.5 mm corresponding to the percent error in the propagating wave between 1.2 to as high as 7.8 percent as presented in Table 10 and Table 11 for $\theta_{12} = 0^\circ$ and 90° respectively.

Table 10: Change in QL and QT velocities due to ± 0.5 mm thickness variation for $\theta_{12} = 0^\circ$

Wave Mode	Angle (θ_{13})	Wave Velocity (m/s) (+0.5 mm)	Wave Velocity % Error	Wave Velocity (m/s) (-0.5 mm)	Wave Velocity % Error
QL	23.9°	8438.1	1.2	8237.7	1.2
QL	27.0°	8306.5	1.6	8058.7	1.4
QL	90.0°	3011.0	7.5	2590.0	7.8
QT	65.7°	2571.4	6.2	2275.7	6.1
QT	66.4°	2599.5	6.2	2297.6	6.1
QT	70.9°	2666.2	6.6	2337.9	6.5

Table 11: Change in QL and QT velocities due to ± 0.5 mm thickness variation for $\theta_{12} = 90^\circ$

Wave Mode	Angle (θ_{23})	Wave Velocity (m/s) (+0.5 mm)	Wave Velocity % Error	Wave Velocity (m/s) (-0.5 mm)	Wave Velocity % Error
QL	45.6°	2912.1	4.0	2693.3	3.8
QL	34.0°	2823.8	2.5	2688.4	2.5
QL	90.0°	3011.0	7.5	2590.0	7.8
QT	43.9°	1701.2	3.9	1579.4	3.6
QT	43.1°	1692.2	3.2	1572.0	4.2
QT	37.7°	1722.0	2.7	1625.6	3.0

On top of thickness variation, errors were accumulated from the manufactured wedges and the distance measured between the two transducers. As presented in Figure 86 to Figure 90, even after implementing the improved algorithm, 5% random error in the input velocity data had significant effect on μ_{12} (Figure 88) as compared to the other constants. However, despite the presence of experimental error higher than 5%, the ultrasonic method provided in this thesis had an excellent agreement with the tensile tests for E_{11} and E_{22} . Therefore, it can be concluded that the ultrasonic method and the improved algorithm works well if the error in the experimental data can be reduced to less than 1%. This can be done by controlling the laminate thickness, using better wedges, and precisely measuring the distance between the two ultrasonic transducers.

CHAPTER 4 SUMMARY

In this chapter, an *in-situ* method for measuring the material properties with access to only one side of the specimen is presented. The technique uses generating and receiving quasi-longitudinal and quasi-transverse waves at different angles using different angled wedges commonly used in shear wave non-destructive testing applications. First, the analytical equations were derived for an isotropic and transversely isotropic material. Then, an inverse method based on the non-linear least square technique was used to calculate the stiffness constants using the ultrasonic wave velocities. A sensitivity analysis was performed by randomly perturbing the velocity data and observing its effect on the calculated stiffness constants. An improved algorithm was proposed and tested to reduce the effects of the random errors. Based on the sensitivity analysis a minimum number of propagation angles required to inversely calculate the stiffness constants were presented. The method was then experimentally verified on an isotropic aluminum 7050-T7451 with two different thicknesses and a transversely isotropic composite sample fabricated using 24 plies of unidirectional Cycom 977-2-12k-HTA prepreg.

CHAPTER 5: THESIS CONCLUSIONS

Literature review showed that most work regarding the analytical derivations of Lamb wave equations was performed for orthotropic and higher symmetric laminate. Adopting an orthotropic and higher symmetry may not be true, if the actuators and sensors are installed in a non-principal direction, which gives rise to a lower monoclinic symmetry. The work in this dissertation has addressed this shortcoming by providing a full derivation of Lamb wave equations for n-layered monoclinic composite laminates. The derivation was based on 3D linear elasticity theory considering displacement fields along all three directions and partial wave technique, which takes into account the superposition of three upward, and three downward travelling waves to satisfy the boundary conditions. The equations from each layer were combined using the Global Matrix (GM) approach. A robust method for numerically solving the derived Lamb wave equations was proposed and successfully verified experimentally on two different material types, an 8-layered carbon-fibre epoxy composite panel and a 7-layered fibre-metal laminate GLARE. The Global Matrix became numerically unstable when the Lamb wave propagation angle was along the principal axes, where six waves were combined with four waves due to the decoupling effect. This instability was eliminated by subtracting the material orientation by 1° , which ensured the presence of six waves travelling along the plane at any given material and sensor angles. Due to the tuning effects, the anti-symmetric wave was found to be dominated in the lower frequencies as compared to the higher frequencies where the symmetric wave was the dominant one. In addition, the experimental data followed the 3D linear elastic approach developed in this dissertation more closely as compared to the classical laminate plate theory, which over predicted the wave velocities at higher frequency-thickness

products. Therefore, it can be concluded that the analytical and numerical method presented in this dissertation was able to accurately predict the Lamb waves' dispersion behaviour.

The experimentally proven numerical methods for solving the derived Lamb wave equations were used to study the effect on the Lamb wave propagation/dispersion due to changes in the material properties. The study was performed on three different composite laminate types - unidirectional, cross-ply, and quasi-isotropic by reducing E_{11} , E_{22} , G_{12} by 5, 10, 15, 30 percent and density by 1, 2, 5, and 10 percent with the intent of representing defects. The laminates were analyzed at 0° , 20° , 45° , 70° , and 90° propagation angles. As expected, the propagation characteristic of Lamb waves was dissimilar in different directions due to changes in the material properties for different laminate types. It was found that the S_o mode was sensitive to the fibre dominated properties; whereas, the A_o mode was sensitive to the matrix dominated properties at all frequency-thickness product ranges. In addition, the S_o mode was sensitive to the matrix dominated properties at higher frequency-thickness products; whereas, the A_o mode was sensitive to the fibre dominated properties at lower frequency-thickness product ranges. Therefore, S_o and A_o modes can be used for detecting fibre and matrix dominated damage respectively. As for the change in density created by formation of voids, both A_o and S_o modes were equally sensitive at all frequency-thickness range. It was also suggested to use S_o mode to find surface defects by observing the tendency of S_o mode velocity to go towards Rayleigh wave velocity at lower frequency-thickness range. It was found that the propagation/dispersion of Lamb waves was susceptible to even the slightest difference in the material properties, which

could be observed by selecting the proper symmetric and/or anti-symmetric modes along with the propagation directions and frequency-thickness products for their excitation. Therefore, the results from this study can be used to determine the influence of changes in the material properties due to presence of defect/damage in the propagation characteristics of Lamb waves in composites. Not only can the determination of these effects be very important for material characterization, but also these can be extremely relevant for the establishment of reliable SHM systems for composite materials, considering that defects, damage, and degradation introduces changes in local and global material properties which can have a detrimental effect on safety.

Another novelty brought from this work is the exploration of an *in-situ* method for measuring material properties with access to only one side of the specimen. The method consists of generating, acquiring, and analyzing the quasi-longitudinal (QL) and quasi-transverse (QT) waves propagating through the thickness. For this purpose, the analytical equations for orthotropic and higher symmetry materials were derived; however, only transversely isotropic and isotropic materials were further analyzed. The analysis consisted of using a non-linear least square technique to inversely calculate the stiffness constants from the QL and QT wave velocities. In order to find the effect of experimental errors, sensitivity analysis was performed by randomly perturbing the QL and QT wave velocities by 0.5, 1, 2, and 5 percent from their original values and observing their effects on the calculated stiffness constants. Based on the initial sensitivity analysis, an optimization routine was proposed by comparing and equating the stiffness matrix constants (c_{11}, c_{33}) for isotropic and (c_{22}, c_{33}) for transversely isotropic material. It was found that the proposed optimization routine greatly improved the convergence of E , G , and μ for isotropic material; whereas, only E_{22} and μ_{23} were significantly improved for a transversely

isotropic material. It was also confirmed that the change in initial guesses and upper bounds had no effects on the final results of the improved algorithm, thereby proving its robustness. The presented analytical equations and optimization routine were verified experimentally on an isotropic aluminum Al 7050-T7451 with two different thicknesses and a Cycom 977-2-12k-HTA transversely isotropic composite fabricated using a 24 plies unidirectional prepreg. For the Al 7050-T7451 sample, the stiffness constants obtained from the presented method was compared against the published values in the literature and experimentally determined value using tensile tests. The results were consistent for both thick (12.7 mm) and thin (5 mm) isotropic Al 7050-T7451 samples with minor discrepancy in the Poisson's ratio. As for the transversely isotropic material, the experimental results were compared against the tensile tests performed on the cut out of the same sample. It was found that E_{11} and E_{22} agreed well with the presented ultrasonic method and the tensile test, despite having excess of 5% experimental error due to variation in sample thickness. However, for the in-plane Poisson's ratio μ_{12} , the discrepancy was about 70% between the ultrasonic method and the tensile test. This is because μ_{12} is very sensitive to the random error as compared to other stiffness constants found by the sensitivity analysis. No data were available for comparing the transverse Poisson's ratio μ_{23} and shear stiffness G_{12} . Therefore, it can be concluded that the ultrasonic material characterization method presented in this dissertation is less sensitive to the isotropic material as compared to the transversely isotropic material. For transversely isotropic material the ultrasonic method works well if the experimental errors can be reduced to less than 1%.

CHAPTER 6: FUTURE RECOMMENDATIONS

Successful implementation of Lamb wave for damage detection as a part of a SHM system depends on a thorough understanding of the underlying physics behind its propagation characteristics. The work presented in this dissertation has provided the means to derive and numerically solve the Lamb wave equations, which can be used for transducer sizing, optimize transducer placement, select proper Lamb wave modes', and excitation frequency. However, there are still lots of work needed to be done before a Lamb wave based SHM system can be incorporated in an aircraft. Some of the future recommendations include:

- Expanding the analytical method presented in this thesis to take into account the effects of temperature, humidity, and load. This is important if the system is to be used to monitor damage nucleation/growth in flight because aircraft in flight will experience different temperature and loading conditions as compared to being on the ground or inside a hangar.
- Incorporating viscoelastic behaviour of composites, which can not only change the Lamb waves' dispersive behaviour but also govern the maximum distance Lamb waves can travel; hence, dictating the transducers' placement. Viscoelastic behaviour can be taken into account by finding the loss modulus of the material and integrating it into the analytical expression derived in this thesis.
- Analysing the response of piezoelectric element used to generate Lamb wave to the applied voltage/frequency in order to better predict the excitation signal without having to use an intermediate sensor.

As for the material characterization using the ultrasonic wave, following are some of the recommendations for future work:

- Improve upon the experimental error by automating or precisely controlling the excitation and acquisition angles. Automation can also be used to detect the maximum signal strength. This is because the method presented in this thesis provides an accurate results if the experimental errors are less than 1%.
- Expand the proposed method to test on orthotropic materials. For this, the off axis waves' group velocities instead of phase velocities are required for the analytical expressions presented in this thesis.

Going forward, the analytical method can be expanded to create a finite element model that can be used to simulate the Lamb wave propagation within the structure. The finite element model can be used to study the interaction of Lamb waves with damage in a complex structure, thus reducing cost and time for experiments and implementations. The simulation results can also be used for sensor selection and optimization. Once proven reliable, the method can be employed from the earliest stage of the airframe life. The sensors can be permanently installed at the optimized location within the airframe in an array. This can be used as an initial quality control mechanism to determine pass/fail criteria by testing the propagation of Lamb wave within the region and comparing the results with the analytical/simulation models. If the airframe is found to be within the specifications, this initial information can also be used as a baseline for any further assessments. Damage can be detected as a shift in the baseline signal. During the service life, the material properties can be evaluated using the ultrasonic method and can be fed back

into the simulation for evaluation proposes and to support continuing airworthiness. Thus, the analytical methods presented in this dissertation can be used from beginning to an end of airframe lifecycle as a part of an improved Lamb wave based SHM system.

REFERENCES

- A. A. Baker, S. Dutton, D. Kelly (2004), Composite materials for aircraft structures, AIAA, Virginia.
- A. D. Degtyar, S. I. Rokhlin (1997), Comparison of elastic constant determination in anisotropic materials from ultrasonic group and phase velocity data, *Journal of Acoustical Society of America*, 102(6):3458-3466.
- A. G. Every, W. Sachse (1990), Determination of the elastic constants of anisotropic solids from acoustic-wave group-velocity measurements, *The American Physical Society*, 42(13):8196-8207.
- A. H. Nayfeh (1989), Free wave propagation in plates of general anisotropic media, *Journal of Applied Mechanics*, 56(4):881-886.
- A. H. Nayfeh (1991), The general problem of elastic wave propagation in multilayered anisotropic media, *Journal of Acoustical Society of America*, 89(4):1521-1531.
- A. H. Nayfeh (1995), *Wave propagation in layered anisotropic media with applications to composites*, Elsevier, New York.
- A. H. Shah, S. K. Datta (1982), Harmonic waves in a periodically laminated medium, *International Journal of Solids and Structures*, 18(5):397-410.
- A. J. Fawcett, G. D. Oakes (2006), Boeing composite airframe damage tolerance and service experience, Power-Point presentation, Boeing Commercial Airplanes.
- A. Kapadia (2011), *Nondestructive testing of composite materials*, National Composite Network Best Practice Guide.
- A. M. Rubin, K. L. Jerina (1994), Evaluation of porosity in composite aircraft structures, *Mechanics of Composite Materials*, 30(6):587-600.
- A. Manohar (2012), *Quantitative nondestructive testing using infrared thermography*, PhD Dissertation, University of California - San Diego.
- A. N. Vorontsov, G. Kh. Murzakhanov, V. N. Shchugorev (1989), Delamination failure of composite structures, *Mechanics of Composite Materials*, 25(6):723-737.
- A. Raghavan (2007), *Guided-wave structural health monitoring*, PhD Dissertation, University of Michigan.

A. Vary, J. Summerscales (1990), Acousto-ultrasonic, Non-destructive testing of fiber-reinforced plastics composites, Volume 2, Elsevier.

A. Wilson (2002), Assets maintenance management, Industrial Press Inc., New York.

APC International (2011), Piezoelectric ceramics principles and applications, APC International, Ltd.

APC International (2012), Physical and piezoelectric properties of APC materials, Product Information Sheet.

ARP6461 (2013), Guidelines for Implementation of structural health monitoring on fixed wing aircraft, SAE International.

ASM, Aluminum Al-2024-T3 (2013), Aerospace Specification Metals Inc, Online: <http://asm.matweb.com/search/SpecificMaterial.asp?bassnum=MA2024T3>, Accessed: 2 Feb 2013.

ASM, Aluminum Al-2024-T6 (2014), Aerospace Specification Metals Inc, Online: <http://asm.matweb.com/search/SpecificMaterial.asp?bassnum=MA2024t6>, Accessed: Feb 4, 2014.

ASTM E2533-09 (2009), Standard guide for nondestructive testing of polymer matrix composites used in aerospace applications, ASTM International.

ASTM E494-10 (2010), Standard practice for measuring ultrasonic velocity in materials, ASTM International.

ASTM E8M-04 (2004), Standard test method of tension testing of metallic materials at room temperature, ASTM International.

Aviation Safety Network (1985), Accident description Japan Air Lines Flight 123, Online: <http://aviation-safety.net/database/record.php?id=19850812-1>, Accessed: 17 Mar 2014.

B. G. Kumar, R. P. Singh, T. Nakamura (2002), Degradation of carbon fiber-reinforced epoxy composites by ultraviolet radiation and condensation, *Journal of Composite Materials*, 36(24):2413-2421.

B. Pavlakovic, M. Lowe, D. Alleyne, and P. Cawley (1997), DISPERSE: A general purpose program for creating dispersion curves, 23rd Symposium on Quantitative NDE, 185-192.

B. Rocha (2011), Structural health monitoring of aircraft structures, PhD Dissertation, University of Lisbon.

- B. Rocha, C. Silva, A. Suleman (2010), Structural health monitoring system using piezoelectric networks with tuned Lamb waves, *Journal of Shock and Vibration*, 17(4):677-695.
- B. Tang, E. G. Henneke II (1989), Long wavelength approximation for Lamb wave characterization of composite laminates, *Research in Nondestructive Evaluation*, 1(1):51-64.
- Bittech Inc., Development of Woodpecker, Online: www.wp632.com, Accessed: Jun 12, 2013.
- C. Dong (2011), Model development for the formation of resin-rich zones in composite processing, *Composites Part A: Applied Science and Manufacturing*, 42(4):419-424.
- C. G. Drury, J. Watson (2002), Good practices in visual inspection, *FAA/Human Factors in Aviation Maintenance*.
- C. Potel, J. F. De Belleval (1993), Propagation in an anisotropic periodically multilayered medium, *Journal of Acoustical Society of America*, 93(5):2669-2677.
- C. R. Farrar, N. A. J. Lieven (2007), Damage prognosis: The future of structural health monitoring, *Philosophical Transactions of The Royal Society A*, 356:623-632.
- C. T. Sun, J. D. Achenbach, G. Herrmann (1968), Continuum theory of a laminated medium, *Journal of Applied Mechanics*, 35(3):467-475.
- CAA-CAP 562 (2005), Civil Aircraft Airworthiness Information and Procedures.
- CATT Flyer, Computer-aided tap-testing, Advanced Structural Imaging, Inc.
- Ch. E. Katsikeros, G. N. Labeas (2009), Development and validation of a strain-based structural health monitoring system, *Mechanical Systems and Signal Processing*, 23:372-383.
- D. E. Chimenti, A. H. Nayfeh (1985), Leaky Lamb wave in fibrous composite laminates, *Journal of Applied Physics*, 58(12):4531-4538.
- D. Kugler, T. J. Moon (2002), Identification of the most significant processing parameters on the development of fiber waviness in thin laminates, *Journal of Composite Materials*, 36(12):1451-1479.
- D. Montalvao, N. M. M. Maia, A. R. R. Ribeiro (2006), A review of vibration-based structural health monitoring with special emphasis on composite materials, *The Shock and Vibration Digest*, 38(4): 295-324.
- D. Roach (2007), Improving in-service inspection of composite structures, *Commercial Aircraft Composite Repair Committee (CACRC)*.

D. Roach (2009), Real time crack detection using mountable comparative vacuum monitoring sensors, *Smart Structures and Systems*, 5(4):317-328.

D. W. Hoepfner (2011), Fretting fatigue considerations in Holistic Structural Integrity Based Design Processes (HOLSIP) - A continuing evolution, *Tribology International*, 44:1364-1370.

E. E. Franco, J. M. Meza, F. Buiocchi (2011), Measurement of elastic properties of materials by the ultrasound through-transmission technique, *DYN*, 168:59-64.

E. P. Papadakis (1998), Ultrasonic wave measurements of elastic moduli E, G, μ for product development and design calculations, *American Society for Testing and Materials*, 26(3):240-246.

F. C. Campbell (2010), *Structural composite materials*, ASM International.

FAA-23.573 (2002), *Damage tolerance and fatigue evaluation of structure*.

FAA-AC-20-107B (2009), *Composite aircraft structure*, Advisory Circular.

FAA-AC-43.13-1B (2008), *Acceptable methods, techniques and practices – Aircraft inspection and repair*, Advisory Circular.

FAA-AC-43-204 (1997), *Visual inspection for aircraft*, Advisory Circular.

FAA-AR-09-4 (2009), *Effects of disbonds, lightning strikes, and low-velocity, impact damage on adhesively bonded composite joints*, Final Report.

FAA-H-8083-30 (2008), *Inspection fundamentals*, Aviation Maintenance Technician Handbook.

G. Neau (2003), *Lamb waves in anisotropic viscoelastic plates, study of the wave fronts and attenuation*, PhD Dissertation, Imperial College.

G. Park, H. Sohn, C. R. Farrar, D. J. Inman (2003), Overview of piezoelectric impedance-based health monitoring and path forward, *Shock and Vibration Digest*, 35(6):451-463.

G. R. Liu, J. Tani, K. Watanabe, T. Ohyoshi (1990), Lamb wave propagation in anisotropic laminates, *Journal of Applied Mechanics*, 57:923-929.

G. R. Liu, X. Han, K. Y. Lam (2002), A combined genetic algorithm and nonlinear least squares method for material characterization using elastic waves, *Computer Methods in Applied Mechanics and Engineering*, 191:1909-1921.

H. Hu (2007), Physical aging in long term creep of polymeric composite laminates, *Journal of Mechanics*, 23(3)245-252.

H. Lamb (1917) On waves in an elastic plate, Proceedings of the Royal Society, Mathematical, Physical and Engineering Sciences, 93:114-128.

H. Sohn, C. R. Farrar, F. M. Hemez, D. D. Shunk, D. W. Stinemat, B. R. Nadler (2003), A review of structural health monitoring literature: 1996-2001, Los Alamos National Laboratory Report, LA-13976-MS.

I. A. Viktorov (1967), Rayleigh and Lamb waves: Physical theory and applications, Plenum Press, New York.

I. Ihara (2008), Ultrasonic sensing: Fundamentals and its application to nondestructive evaluation, sensors, advancements in modeling, design issues, fabrication, and practical applications, Springer, Berlin.

IASA (2005), China Airlines Flight CI-611 Crash Report Released, Online: http://www.iasa.com.au/folders/Safety_Issues/FAA_Inaction/CI-611finalreport.html, Accessed: 17 Mar 2014.

IHS (2014), Jane's all the world's aircraft: Development & production, Online Database.

J. C. Dodson (2012), Guided wave structural health monitoring with environmental considerations, PhD Dissertation, Virginia Polytechnic Institute and State University.

J. C. Dodson, D. J. Inman (2013), Thermal sensitivity of Lamb waves for structural health monitoring applications, Journal of Ultrasonics, 53: 677-885.

J. D. N. Cheeke (2002), Fundamentals and applications of ultrasonic waves, CRC Press, New York.

J. D. Pearson, M. A. Zikry, M. Prabhugoud, K. Peters (2007), Global-local assessments of low-velocity impact damage in woven composites, Journal of Composite Materials, 41(23):2759-2783.

J. F. Laliberté (2002), Investigation of low-velocity impact damage in fibre-metal-laminates, PhD Dissertation, Carleton University.

J. J. Scholey, P. D. Wilcox, M. R. Wisnom, and M. I. Friswell (2010), Quantitative experimental measurements of matrix cracking and delamination using acoustic emission, Composites: Part A, 41(5):612-623.

J. Koop (2008), Efficient numerical diagonalization of Hermitian 3x3 matrices, International Journal of Modern Physics C, 19(3):523-535.

J. L. Rose (1999), Ultrasonic waves in solid media, Cambridge University Press, New York.

- J. M. Berthelot (1982), Effect of fiber misalignment on the elastic properties of oriented discontinuous fiber composites, *Fiber Science and Technology*, 17:25-39.
- J. M. Park, J. W. Kong, D. S. Kim, D. J. Yoon (2005), Nondestructive damage detection and interfacial evaluation of single-fibers/epoxy composites using PZT, PVDF and P(VDF-TrFE) copolymer sensors, *Composite Science and Technology*, 65(2):241-256.
- J. M. Whitney, C. T. Sun (1973), A higher order theory for extensional motion of laminated composites, *Journal of Sound and Vibration*, 30(1):85-97.
- J. R. Lhota, G. C. Panos, E. C. Johnson (1994), Ultrasonic backscatter technique for corrosion detection in solid rocket motors, Aerospace Report No. TR-94(4464)-1, The Aerospace Corporation.
- J. W. S. Rayleigh, (1885) On waves propagated along the plane surfaces of an elastic solid, *Proceedings of the London Mathematical Society*, London, UK.
- K. Balasubramaniam, N.S. Rao (1998), Inversion of composite material elastic constants from ultrasonic bulk wave phase velocity data using genetic algorithms, *Composite Part B*, 29(B):171–180.
- K. Fayazbakhsh, M. A. Nik, D. Pasini , L. Lessard (2013), Defect layer method to capture effect of gaps and overlaps in variable stiffness laminates made by automated fiber placement, *Composite Structures*, 97:245-251.
- K. L. Verma (2008), On the wave propagation in layered plates of general anisotropic media, *International Journal of Engineering and Applied Sciences*, 4(8):444-450.
- K. Vanclooster, S. V. Lomov, I. Verpoest (2009), On the formability of multi-layered fabric composites, *Metallurgy and Materials Engineering, ICCM-17*.
- L. Cook (2009), Visual inspection reliability for composite aircraft structures, PhD Dissertation, Cranfield University.
- L. E. Mujica, J. Vehi, W. Staszewski, K. Worden (2008), Impact damage detection in aircraft composites using knowledge-based reasoning, *Structural Health Monitoring*, 7(3):215-230.
- L. Knopoff (1964), A matrix method for elastic wave problems, *Bulletin of the Seismological Society of America*, 54:431-438.
- L. P. Kollár and G. S. Springer (2003), *Mechanics of composite structures*, Cambridge University Press, New York.

- L. P. Solie, B. A. Auld (1973), Elastic waves in free anisotropic plates, *Journal of Acoustical Society of America*, 54(1):50-65.
- L. Wang, F. G. Yuan (2007a), Lamb wave propagation in composite laminates using a higher-order plate theory, *Nondestructive Characterization for Composite Materials*, Proc SPIE, 6531.
- L. Wang, F. G. Yuan (2007b), Group velocity and characteristic wave curves of Lamb waves in composites: Modeling and experiments, *Composites Science and Technology*, 67:1370-1384.
- M. Anderson (2012), Phased array testing basic theory for industrial applications, *NDT Field Guides*, Olympus NDT.
- M. Calomfirescu (2008), Lamb waves for structural health monitoring in viscoelastic composite materials, *Science-Report*, Berlin.
- M. Hagenbeek (2005), Characterization of fiber metal laminates under thermo-mechanical loadings, PhD Dissertation, Delft University of Technology.
- M. J. S Lowe, P. Cawley, B. N. Pavlakovic (2004), A general purpose computer model for calculating elastic waveguide properties with application to non-destructive testing, *Surface Waves in Anisotropic and Laminated Bodies and Defects Detection*, 241-256.
- M. J. S. Lowe (1995), Matrix techniques for modeling ultrasonic waves in multilayered media, *IEEE Transactions on Ultrasonics, Ferroelectrics and Frequency Control*, 42(4):525-542.
- M. M. Derriso, F. K. Chang (2006), Future of structural sensing for aerospace applications, *The Defense Technical Information Center*, ADA479860.
- M. M. Reda Taha, A. Noureldin, J. L. Lucero, T. J. Baca (2006), Wavelet transform for structural health monitoring: A compendium of uses and features, *Structural Health Monitoring*, 5(3):267-297.
- M. Majumder, T. K. Gangopadhyay, A. K. Chakraborty, K. Dasgupta, D. K. Battacharya (2008), Fiber Bragg gratings in structural health monitoring – Present status and applications, *Sensors and Actuators A: Physical*, 147(1):150-164.
- M. Martinez, B. Rocha, M. Li, G. Shi, A. Beltempo, R. Rutledge, M. Yanishevsky (2012) Load monitoring of aerospace structures using micro electro mechanical systems (MEMS), *SMASIS 2012, ASME 2012 Conference of Smart Materials, Adaptive Structures and Intelligent Systems*, Georgia.

M. R. Vanlandingham, R. F. Eduljee, J. W. Gillespie Jr. (1999), Moisture diffusion in epoxy system, *Journal of Applied Polymer Science*, 71(5):787-798.

M. R. Wisnom (1993), Analysis of shear instability in compression due to fiber waviness, *Journal of Reinforced Plastics and Composites*, 12:1171-1189.

MIL-HDBD-5 (2001), *Metallic materials and elements for aerospace vehicle structures*, Table 3.7.4.0(b1): Design mechanical and physical properties of 7050 aluminum alloy plate.

N. Dube (2007), Introduction to phased array ultrasonic technology applications: R/D tech guideline, *Advanced Practical NDT Series*, Olympus.

N. Pan, H. C. Chen, J. Thompson, M. K. Inglesby, S. Khatua, X. S. Zhang, S. H. Zeronian (1997), The size effects on the mechanical behaviour of fibers, *Journal of Materials Science*, 32(9): 2677-2685.

N. Ryden, Ch. B. Park, P. Ulriksen, R. D. Miller (2003), Lamb wave analysis for non-destructive testing of concrete plate structures, 9th EAGE/EEGS Meeting, September.

National Instruments (2013), *Measuring strain with strain gages*, White Papers, National Instruments.

NDT Resource Center (2010), Wave propagation, Online: <http://www.ndt-ed.org/EducationResources/CommunityCollege/Ultrasonics/Physics/wavepropagation.htm>, Accessed: Apr 20, 2010.

NDT Resource Center (2013a), Ultrasonic data presentation, Online: <http://www.ndt-ed.org/EducationResources/CommunityCollege/Ultrasonics/EquipmentTrans/DataPres.htm>, Accessed: Nov 25, 2013.

NDT Resource Center (2013b), Modes of sound wave propagation. Online: www.ndt-ed.org/EducationResources/CommunityCollege/Ultrasonics/Physics/modepropagation.htm, Accessed Oct 3, 2013.

NDT Resource Center (2014), Computed tomography, Online: <http://www.ndt-ed.org/EducationResources/CommunityCollege/Radiography/AdvancedTechniques/computedtomography.htm>, Accessed: Feb 24, 2014.

Netcomposites (2013), Interactive knowledge base on NDE of composites, Online: <http://www.netcomposites.com/ikb>, Accessed: May 9, 2013.

P. E. Mix (2005), *Introduction to nondestructive testing: A training guide*, Wiley, New Jersey.

- P. Gayathri, K. Umesh, R. Ganguli (2010), Effect of matrix cracking and material uncertainty of composite plates, *Reliability Engineering and System Safety*, 95:716-728.
- P. Kudela, W. Ostachowicz, and A. Zak (2008), Damage detection in composite plates with embedded PZT transducers, *Mechanical Systems and Signal Processing*, 22(6):1327-1335.
- P. Vaara, J. Leinonen (2012), Technology survey on NDT of carbon-fiber composites, Series B Reports, Kemi-Tornio University of Applied Sciences.
- P. W. A. Stijnman (1995), Determination of the elastic constants of some composites by using ultrasonic velocity measurements, *Composites* 26(8):597-604.
- R. D. Finlayson, M. Friesel, M. Carlos, P. Cole, J. C. Lenain (2000), Health monitoring of aerospace structures with acoustic emission and acousto-ultrasonic, 15th World Conference on NDT, Rome.
- R. D. Mindlin (1960a), Waves and vibrations in isotropic elastic plates, *Structural Mechanics*, 199-232.
- R. D. Mindlin (1960b), *Structural mechanics*, Pergamon, New York.
- R. G. Liptai (1972), Acoustic emission from composite materials, *Composite Materials: Testing And Design (Second Conference)*, ASTM, 285-298.
- S. Abrate (1991), Matrix cracking in laminated composites: A review, *Composites Engineering*, 1(6):337-353.
- S. Beeby, G. Ensell, M. Kraft, N. White (2004), *MEMS mechanical sensors*, Artech House Inc., Norwood.
- S. K. Datta, A. H. Shah, R. L. Bratton, T. Chakraborty (1988), Wave propagation in laminated composite plates, *Journal of Acoustical Society of America*, 83(6):2020-2026.
- S. S. Kessler (2002a), Piezoelectric-based in-situ damage detection of composite materials for structural health monitoring systems, PhD Dissertation, Massachusetts Institute of Technology.
- S. S. Kessler, S. M. Spearing, C. Soutic (2002b), Damage detection in composite materials using Lamb wave methods, *Smart Material and Structures*, 11(2): 269-278.
- S. W. Dowbling, C. R. Farrar, M. B. Prime (1998), A summary review of vibration-based damage identification methods, *Shock and Vibration Digest*, 30(2):91-105.

- S. Wang, D. D. L. Chung (2002), Effect of moisture on the interlaminar interface of a carbon fiber polymer-matrix composite, studied by contact electrical resistivity measurement, *Composite Interfaces*, 9(5):453-458.
- T. Lotz (2014), Development of a consistent experimental method to study residual stress effects on fatigue crack growth, Master's Thesis, Delft University of Technology.
- T. R. Hay (2004), Aspects of guided waves in structural health monitoring, PhD Dissertation, Pennsylvania State University.
- V. Antonucci, A. Cusano, M. Giordano, J. Nasser, L. Nicolais (2005), Cure-induced residual strain build-up in a thermoset resin, *Composites: Part A*, 37:592-601.
- V. Dayal, V. K. Kinra (1989), Leaky Lamb waves in an anisotropic plate I: An exact solution and experiments, *Journal of Acoustical Society of America*, 85(6):2268-2276.
- V. Giurgiutiu (2008), *Structural health monitoring with piezoelectric wafer sensors*, Elsevier, Burlington.
- V. K. Goel L. Ferrara (2008), Basic science symposium II: MEMS technology, *SAS Journal*, 2(2):120-129.
- V. V. Bolotin (1996), Delaminations in composite structures: Its origin, buckling, growth and stability, *Composites: Part B*, 27(B):129-145.
- W. C. Van Buskirk, S. C. Cowin, R. Carter (1986), A theory of acoustic measurement of the elastic constants of a general anisotropic solid, *Journal of Materials Science*, 21:2759-2762.
- W. J. Staszewski (2002), Intelligent signal processing for damage detection in composite materials, *Composites Science and Technology*, 62(7-8):941-950.
- W. J. Staszewski, C. Boller, G.R. Tomlinson (2004), *Health monitoring of aerospace structures smart sensor technologies and signal processing*, John Wiley & Sons Ltd., Chichester.
- W. T. Thomson (1950), Transmission of elastic waves through a stratified solid medium, *Journal of Applied Physics*, 21:89.
- WichiTech RD³, RD³ digital electronic tap hammer, Operation Manual.
- X. E. Gros, K. Ogi, K. Takahashi (1998), Eddy current, ultrasonic C-scan and scanning acoustic microscopy testing of delaminated quasi-isotropic CFRP materials: A case study, *Journal of Reinforced Plastics and Composites*, 17(5):389-405.
- X.P.V. Maldague 2002, Introduction to NDT by active infrared thermography, *Materials Evaluation*, 60(9):1060-1073.

- Y. Bar-Cohen (2000a), Emerging NDT technologies and challenges at the beginning of the third millennium, Part 1, *Material Evaluation* 58(1):17-26.
- Y. Bar-Cohen (2000b), Emerging NDT technologies and challenges at the beginning of the third millennium, Part 2, *Material Evaluation* 58(2):141-150.
- Y. C. Chu, S. I. Rokhlin (1994), A method for determination of elastic constants of a unidirectional lamina from ultrasonic bulk velocity measurements on [0/90] cross-ply composites, *Journal of Acoustical Society of America*, 96(1):342-352.
- Y. Li, R. B. Thompson (1990), Influence of anisotropy on the dispersion characteristics of guided ultrasonic plate modes, *Journal of Acoustical Society of America*, 87(5):1911-1931.
- Y. Lingyu, V. Giurgiutiu (2005), Advanced signal processing for enhanced damage detection with piezoelectric wafer active sensors, *Smart Structures and Systems*, 1(2).
- Y. Y. Hung 1999, Applications of digital shearography for testing of composite structures, *Composites: Part B*, 30:765-773.
- Y. Y. Hung, C.Y. Liang (1979), Image shearing camera for direct measurements of surface strains, *Applied Optics*, 18(7):1046-1051.
- Y. Zou, L. Tong, G. P. Steven (2000), Vibration-based model-dependent damage (delamination) identification and health monitoring for composite structures – A review, *Journal of Sound and Vibration*, 230(2): 357-378.
- Z. C. Xi, G. R. Liu (2001), *Elastic waves in anisotropic laminates*, CRC Press.
- Z. Su, L. Ye (2004), An intelligent signal processing and pattern recognition technique for defect identification using an active sensor network, *Smart Materials and Structures*, 13(4):957.
- Z. Su, L. Ye, Y. Lu (2006), Guided Lamb waves for identification of damage in composite structures: A review, *Journal of Sound and Vibration*, 295(3-5):753-780.
- Z. Tian, L. Yu (2014), Lamb wave frequency-wavenumber analysis and decomposition, *Journal of Intelligent Material Systems and Structures*, In-Press, DOI: 10.1177/1045389X14521875.
- Z. Yongbo, F. Huimin (2011), On the longitudinal compressive strength prediction of unidirectional laminated composites based on an improved model, *Polymer Composites*, 32(11):1817-1826.

APPENDIX A: CONSTANTS FOR COEFFICIENT (D_i)

$$D_1 = c_{55}c_{44}c_{33} - c_{45}^2c_{33} \quad (A.1)$$

$$D_2 = \left(c_{55}c_{66}c_{33} + 2c_{45}^2c_{13} - c_{55}c_{36}^2 - 2c_{13}c_{44}c_{55} + 2c_{45}c_{36}c_{13} \right) k_1^2$$

$$+ \left(-2c_{16}c_{45}c_{33} - c_{13}^2c_{44} + c_{11}c_{44}c_{33} \right. \\ \left. + \left(-c_{55}c_{23}^2 + c_{55}c_{22}c_{33} - 2c_{26}c_{45}c_{33} - 2c_{55}c_{23}c_{44} + c_{66}c_{44}c_{33} \right) k_2^2 \right. \\ \left. + \left(2c_{55}c_{26}c_{33} + 2c_{45}c_{36}^2 + 4c_{45}^2c_{36} + 2c_{16}c_{44}c_{33} + 2c_{45}c_{23}c_{13} \right. \right. \\ \left. \left. - 4c_{55}c_{36}c_{44} - 2c_{13}c_{44}c_{36} - 2c_{55}c_{36}c_{23} - 2c_{45}c_{66}c_{33} - 2c_{45}c_{12}c_{33} \right) k_2k_1 \right. \\ \left. + \left(c_{45}^2 - c_{55}c_{44} - c_{55}c_{33} - c_{44}c_{33} \right) \rho\omega^2 \right) \quad (A.2)$$

$$D_3 = \left(-2c_{11}c_{36}c_{45} + c_{11}c_{66}c_{33} - c_{13}^2c_{66} + 2c_{16}c_{36}c_{13} + 2c_{16}c_{36}c_{55} \right) k_1^4$$

$$+ \left(-c_{11}c_{36}^2 + c_{11}c_{44}c_{55} - c_{16}^2c_{33} - c_{11}c_{45}^2 - 2c_{13}c_{66}c_{55} + 2c_{16}c_{45}c_{13} \right) k_1^4$$

$$+ \left(-2c_{11}c_{36}c_{44} + 2c_{16}c_{23}c_{55} + 2c_{12}c_{36}c_{55} - 4c_{13}c_{26}c_{55} + 2c_{16}c_{44}c_{13} \right. \\ \left. + 2c_{16}c_{23}c_{13} + 2c_{12}c_{36}c_{13} - 2c_{16}c_{12}c_{33} - 2c_{13}^2c_{26} + 2c_{11}c_{26}c_{33} \right. \\ \left. + 2c_{45}c_{12}c_{13} - 2c_{11}c_{36}c_{23} - 4c_{16}c_{45}^2 - 2c_{11}c_{45}c_{23} + 4c_{16}c_{44}c_{55} \right) k_2k_1^3$$

$$+ \left(c_{45}^2 + 2c_{13}c_{55} - c_{55}c_{66} + 2c_{36}c_{45} - c_{11}c_{44} - c_{11}c_{33} \right) k_1^2\rho\omega^2$$

$$+ \left(+c_{36}^2 - c_{55}c_{44} - c_{66}c_{33} + 2c_{16}c_{45} + c_{13}^2 \right) k_1^2\rho\omega^2$$

$$+ \left(2c_{16}c_{26}c_{33} + 4c_{12}c_{36}c_{45} - 2c_{16}c_{36}c_{23} + 2c_{12}c_{23}c_{55} + 2c_{66}c_{44}c_{13} \right. \\ \left. + 2c_{66}c_{23}c_{55} + 2c_{12}c_{44}c_{13} - 2c_{26}c_{36}c_{13} + 2c_{66}c_{23}c_{13} - 2c_{26}c_{45}c_{13} \right. \\ \left. - c_{23}^2c_{11} - c_{12}^2c_{33} - c_{13}^2c_{22} - 4c_{45}^2c_{66} - 2c_{45}^2c_{12} + 2c_{36}^2c_{12} \right. \\ \left. - 2c_{12}c_{66}c_{33} - 2c_{16}c_{45}c_{23} - 2c_{16}c_{36}c_{44} + 2c_{12}c_{44}c_{55} - 2c_{26}c_{36}c_{55} \right. \\ \left. + 2c_{12}c_{23}c_{13} - 2c_{13}c_{22}c_{55} + c_{11}c_{22}c_{33} - 2c_{11}c_{23}c_{44} + 4c_{66}c_{44}c_{55} \right) k_2^2k_1^2$$

$$+ \left(2c_{36}c_{44} + 2c_{36}c_{23} + 2c_{45}c_{12} + 2c_{45}c_{66} + 2c_{13}c_{45} + 2c_{45}c_{23} \right) k_2k_1\rho\omega^2$$

$$+ \left(-2c_{16}c_{33} - 2c_{16}c_{44} - 2c_{55}c_{26} + 2c_{55}c_{36} - 2c_{26}c_{33} + 2c_{13}c_{36} \right) k_2k_1\rho\omega^2$$

$$+ \left(4c_{55}c_{26}c_{44} - 4c_{16}c_{23}c_{44} + 2c_{12}c_{44}c_{36} - 2c_{13}c_{22}c_{36} + 2c_{12}c_{23}c_{36} \right. \\ \left. + 2c_{12}c_{23}c_{45} - 2c_{13}c_{22}c_{45} + 2c_{26}c_{23}c_{55} - 2c_{26}c_{12}c_{33} + 2c_{26}c_{44}c_{13} \right. \\ \left. - 2c_{55}c_{22}c_{36} + 2c_{16}c_{22}c_{33} + 2c_{26}c_{23}c_{13} - 2c_{16}c_{23}^2 - 4c_{26}c_{45}^2 \right) k_2^3k_1$$

$$+ \left(-c_{36}^2c_{22} - c_{45}^2c_{22} - c_{26}^2c_{33} - c_{23}^2c_{66} + c_{66}c_{22}c_{33} + c_{55}c_{22}c_{44} \right. \\ \left. - 2c_{66}c_{23}c_{44} - 2c_{36}c_{22}c_{45} + 2c_{26}c_{44}c_{36} + 2c_{26}c_{23}c_{36} + 2c_{26}c_{23}c_{45} \right) k_2^4$$

$$+ \left(c_{23}^2 + c_{36}^2 + c_{45}^2 - c_{55}c_{44} - c_{55}c_{22} + 2c_{36}c_{45} \right) k_2^2\rho\omega^2$$

$$+ \left(+2c_{26}c_{45} - c_{66}c_{33} - c_{66}c_{44} - c_{22}c_{33} + 2c_{23}c_{44} \right) k_2^2\rho\omega^2$$

$$+ \left(c_{33} + c_{44} + c_{55} \right) \rho^2\omega^4$$

$$\begin{aligned}
D_4 = & (c_{11}c_{66}c_{55} - c_{16}^2c_{55})k_1^6 \\
& + (-2c_{16}c_{12}c_{55} + 2c_{11}c_{66}c_{45} + 2c_{11}c_{26}c_{55} - 2c_{16}^2c_{45})k_2k_1^5 \\
& + \left(\begin{aligned} & -2c_{12}c_{66}c_{55} + c_{11}c_{66}c_{44} + 2c_{16}c_{26}c_{55} + c_{11}c_{22}c_{55} \\ & -4c_{16}c_{12}c_{45} + 4c_{11}c_{26}c_{45} - c_{12}^2c_{55} - c_{16}^2c_{44} \end{aligned} \right) k_2^2k_1^4 \\
& + (c_{16}^2 - c_{55}c_{66} - c_{11}c_{55} - c_{11}c_{66})k_1^4\rho\omega^2 \\
& + \left(\begin{aligned} & -2c_{11}c_{45} - 2c_{11}c_{26} + 2c_{16}c_{12} \\ & -2c_{55}c_{26} - 2c_{16}c_{55} - 2c_{45}c_{66} \end{aligned} \right) k_2k_1^3\rho\omega^2 \\
& + \left(\begin{aligned} & -2c_{12}^2c_{45} + 2c_{16}c_{22}c_{55} + 2c_{11}c_{22}c_{45} + 2c_{11}c_{26}c_{44} \\ & + 4c_{16}c_{26}c_{45} - 4c_{12}c_{66}c_{45} - 2c_{16}c_{12}c_{44} - 2c_{26}c_{12}c_{55} \end{aligned} \right) k_2^3k_1^3 \\
& + (c_{11} + c_{55} + c_{66})k_1^2\rho^2\omega^4 \\
& + \left(\begin{aligned} & c_{12}^2 - c_{66}c_{44} - c_{55}c_{66} - c_{55}c_{22} - c_{11}c_{22} - c_{11}c_{44} \\ & + 2c_{12}c_{66} - 2c_{16}c_{26} - 4c_{16}c_{45} - 4c_{26}c_{45} \end{aligned} \right) k_2^2k_1^2\rho\omega^2 \\
& + \left(\begin{aligned} & -4c_{26}c_{12}c_{45} + 4c_{16}c_{22}c_{45} - 2c_{12}c_{66}c_{44} + 2c_{16}c_{26}c_{44} \\ & + c_{11}c_{22}c_{44} + c_{66}c_{22}c_{55} - c_{26}^2c_{55} - c_{12}^2c_{44} \end{aligned} \right) k_2^4k_1^2 \\
& + (2c_{66}c_{22}c_{45} - 2c_{26}c_{12}c_{44} + 2c_{16}c_{22}c_{44} - 2c_{26}^2c_{45})k_2^5k_1 \\
& + \left(\begin{aligned} & -2c_{16}c_{22} + 2c_{26}c_{12} - 2c_{26}c_{44} \\ & -2c_{16}c_{44} - 2c_{45}c_{66} - 2c_{22}c_{45} \end{aligned} \right) k_2^3k_1\rho\omega^2 \\
& + (2c_{16} + 2c_{45} + 2c_{26})k_2k_1\rho^2\omega^4 \\
& + (c_{22} + c_{44} + c_{66})k_2^2\rho^2\omega^4 \\
& + (c_{26}^2 - c_{22}c_{44} - c_{66}c_{22} - c_{66}c_{44})k_2^4\rho\omega^2 \\
& + (c_{66}c_{22}c_{44} - c_{26}^2c_{44})k_2^6 - \rho^3\omega^6
\end{aligned} \tag{A.4}$$

APPENDIX B: CONSTANTS FOR THE STIFFNESS MATRIX $[c'_{ij}]$

$$c'_{11} = (c^2 c_{11} + s^2 c_{12})c^2 + (c^2 c_{12} + s^2 c_{22})s^2 + 4c^2 s^2 c_{66}$$

$$c'_{12} = (c^2 c_{11} + s^2 c_{12})s^2 + (c^2 c_{12} + s^2 c_{22})c^2 - 4c^2 s^2 c_{66}$$

$$c'_{13} = c^2 c_{13} + s^2 c_{23}$$

$$c'_{16} = -(c^2 c_{11} + s^2 c_{12})cs + (c^2 c_{12} + s^2 c_{22})cs + 2csc_{66}(c^2 - s^2)$$

$$c'_{22} = (s^2 c_{11} + c^2 c_{12})s^2 + (s^2 c_{12} + c^2 c_{22})c^2 + 4c^2 s^2 c_{66}$$

$$c'_{23} = s^2 c_{13} + c^2 c_{23}$$

$$c'_{26} = -(s^2 c_{11} + c^2 c_{12})cs + (s^2 c_{12} + c^2 c_{22})cs - 2csc_{66}(c^2 - s^2)$$

$$c'_{33} = c_{33}$$

$$c'_{36} = -csc_{13} + csc_{23}$$

$$c'_{44} = c^2 c_{44} + s^2 c_{55}$$

$$c'_{45} = cc_{44}s - sc_{55}c$$

$$c'_{55} = s^2 c_{44} + c^2 c_{55}$$

$$c'_{66} = -(-csc_{11} + csc_{12})cs + (-csc_{12} + csc_{22})cs + (c^2 - s^2)^2 c_{66}$$

Where c and s are cosine and sine respectively of propagation angle θ_{12} (Figure 67)

APPENDIX C: CONVERGENCE STUDY OF ISOTROPIC TI-6AL-4V

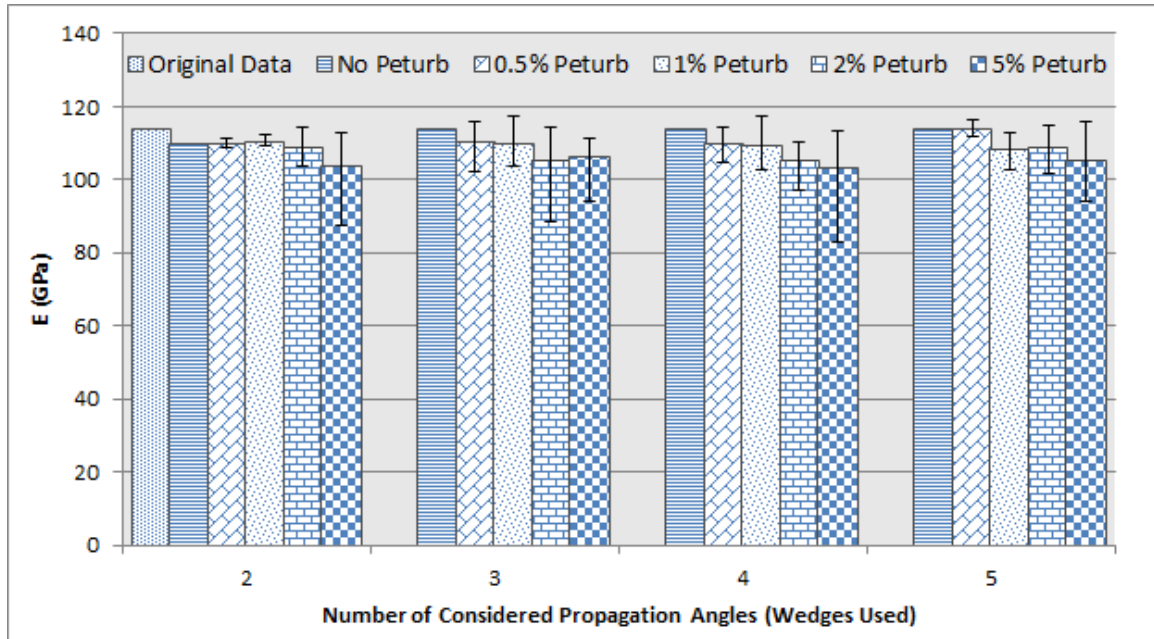


Figure C1: Initial convergence of Ti-6Al-4V elastic stiffness (E)

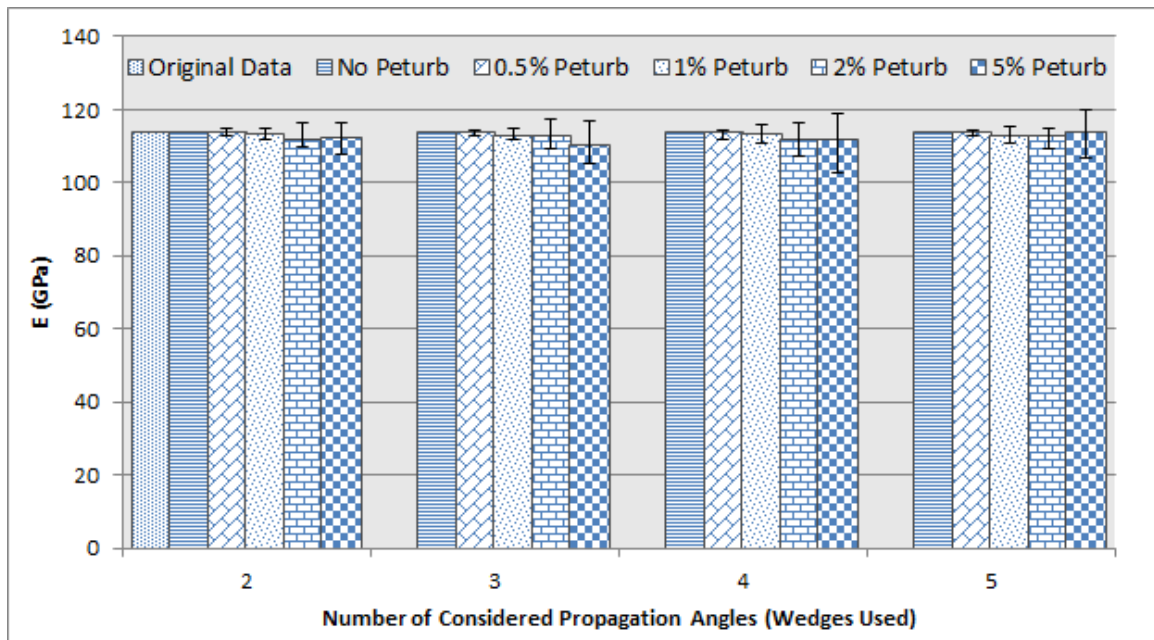


Figure C2: Convergence of Ti-6Al-4V elastic stiffness (E) after implementing improved algorithm

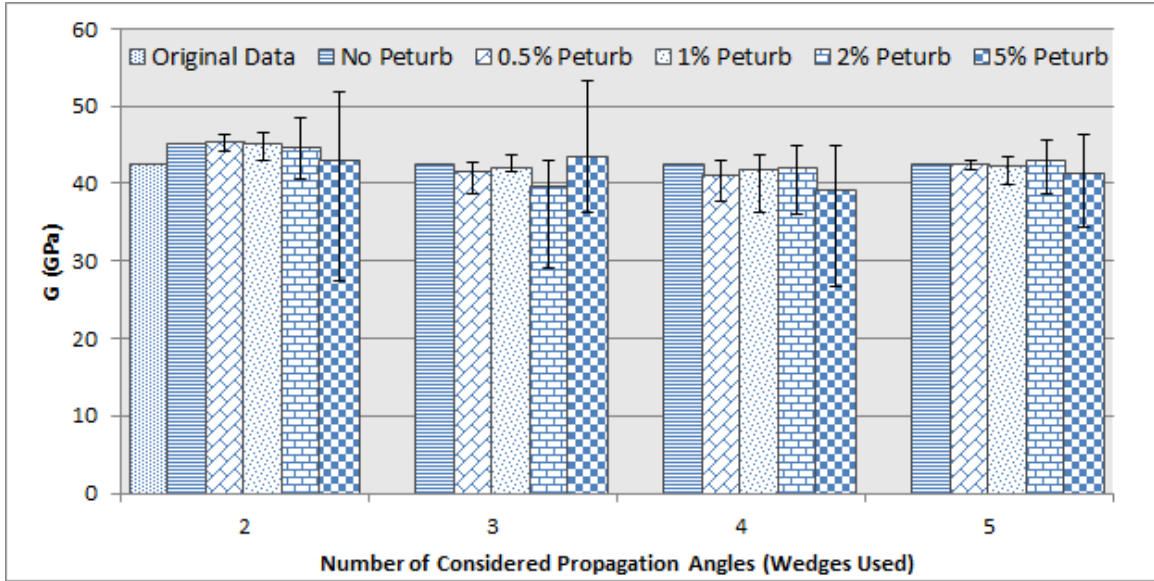


Figure C3: Initial convergence of Ti-6Al-4V shear stiffness (G)

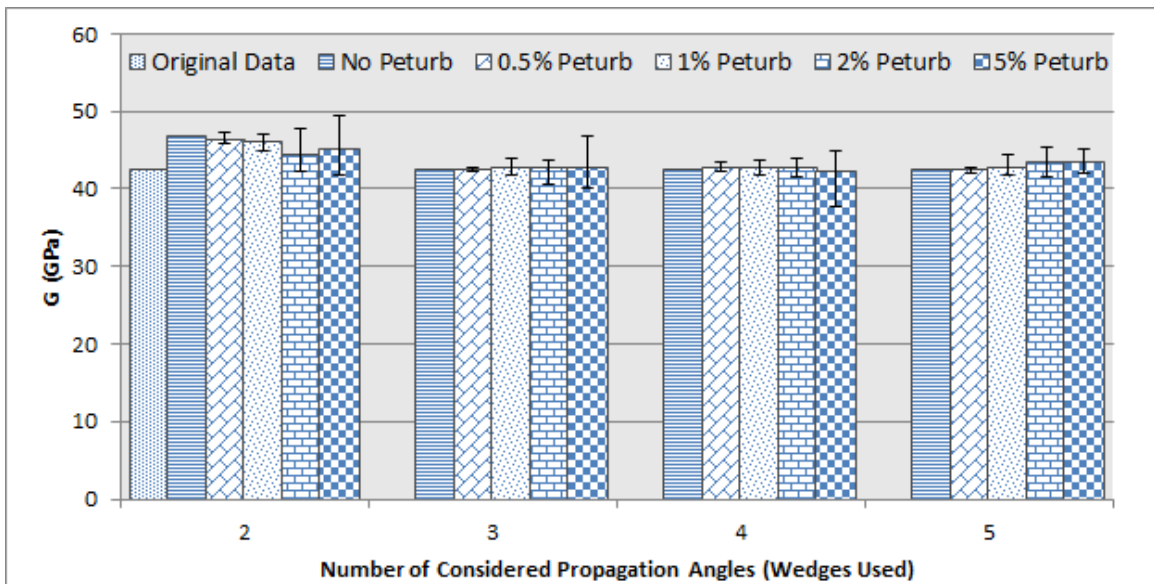


Figure C4: Convergence of Ti-6Al-4V shear stiffness (G) after implementing improved algorithm

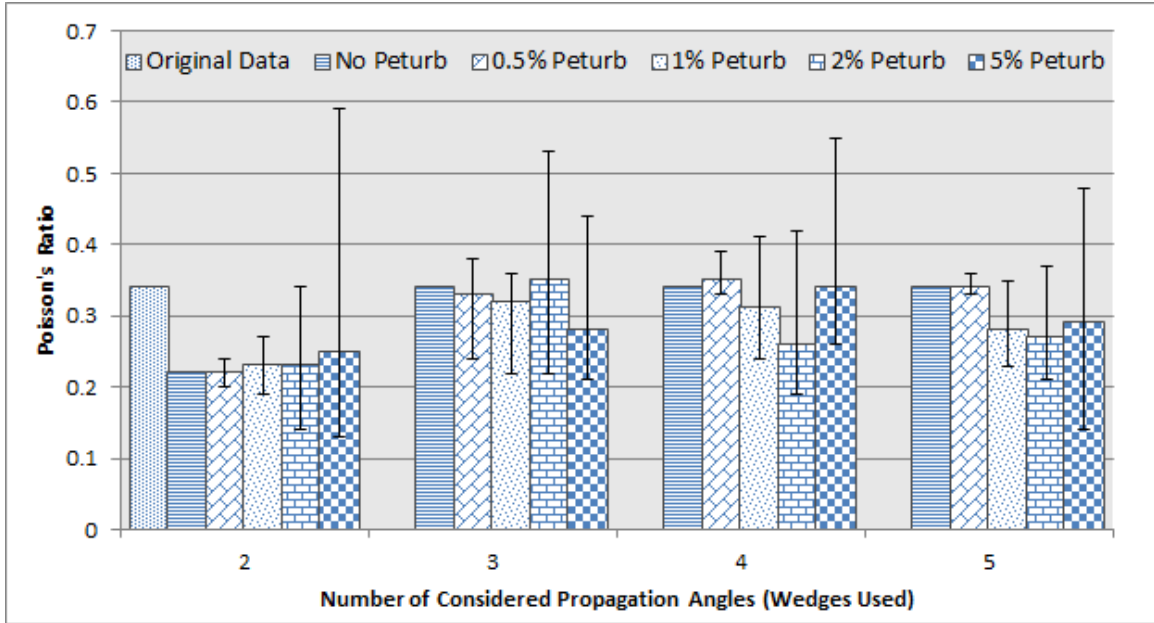


Figure C5: Initial convergence of Ti-6Al-4V Poisson's ratio (μ)

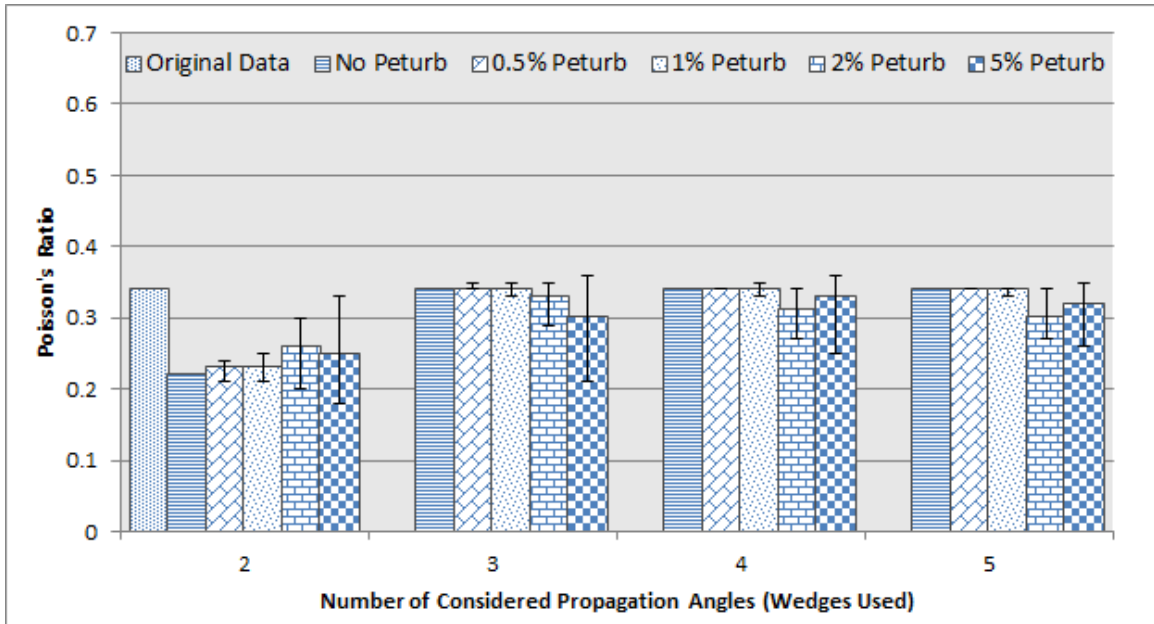


Figure C6: Convergence of Ti-6Al-4V Poisson's ratio (μ) after implementing improved algorithm

APPENDIX D: CONVERGENCE STUDY OF UNIDIRECTIONAL LAMINATE

Table D1: Material properties used for the sensitivity study [L. Wang et al., 2007b]

E_{11}	E_{22}	G_{12}	μ_{12}	μ_{23}	Density
127.6 GPa	11.3 GPa	5.97 GPa	0.30	0.34	1578 kg/m ³

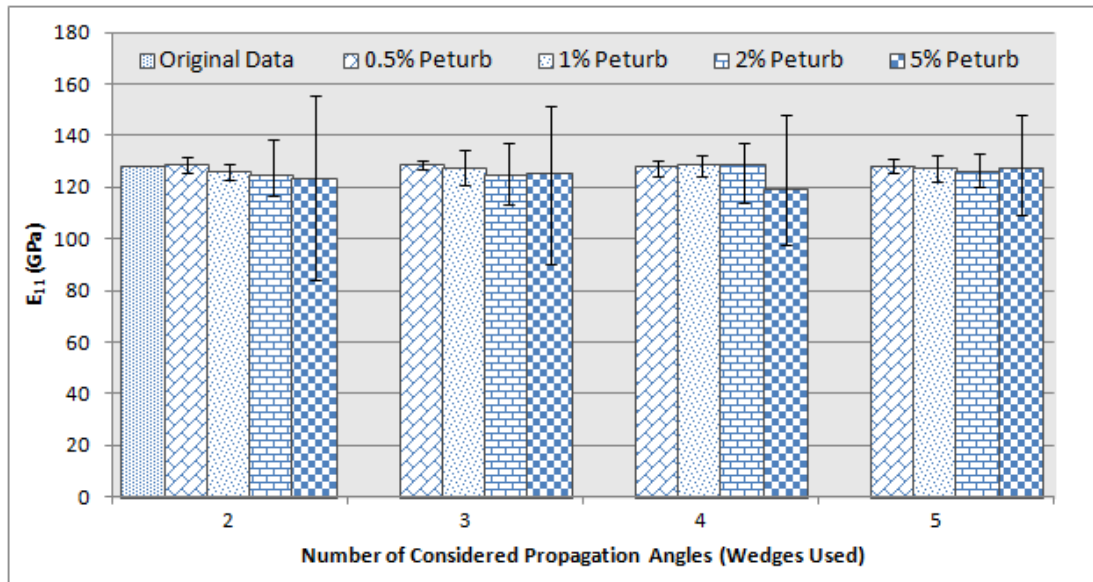


Figure D1: Initial convergence of elastic stiffness (E_{11})

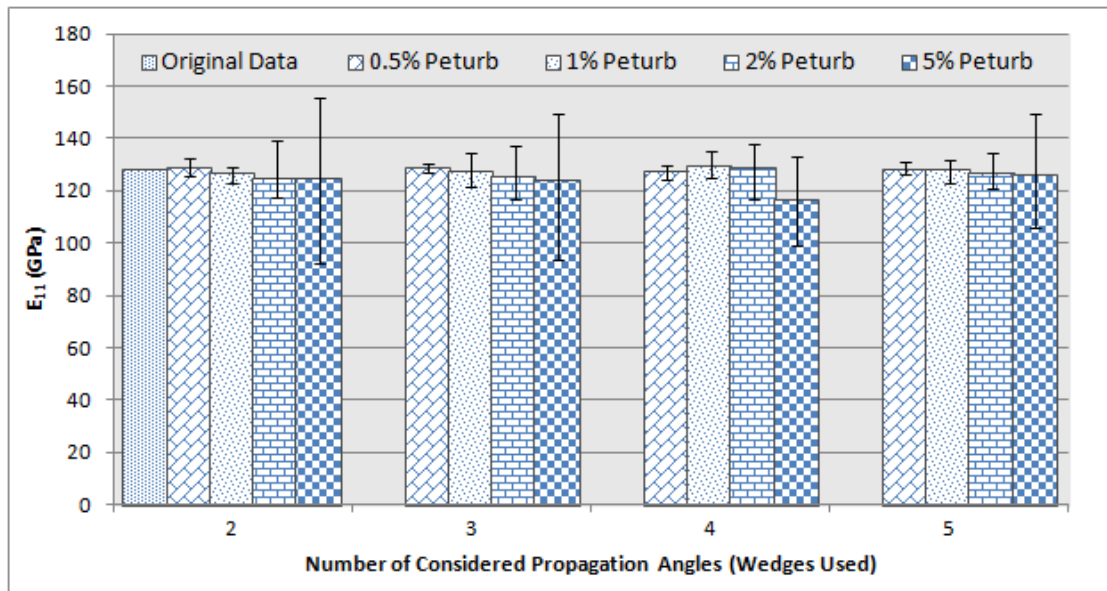


Figure D2: Convergence of elastic stiffness (E_{11}) after implementing improved algorithm

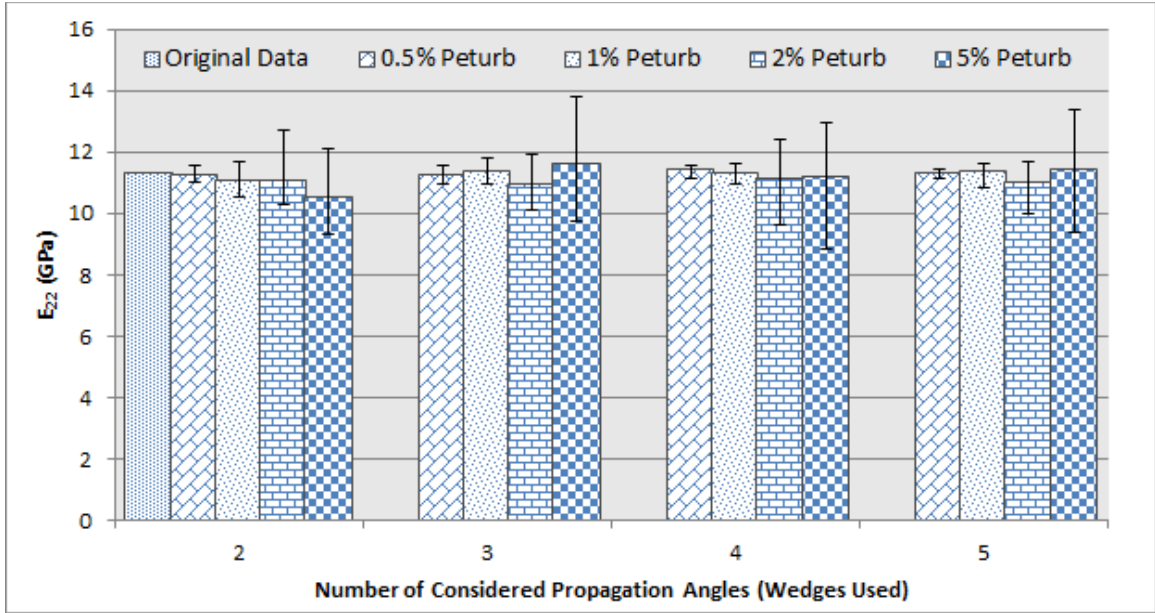


Figure D3: Initial convergence of elastic stiffness (E_{22})

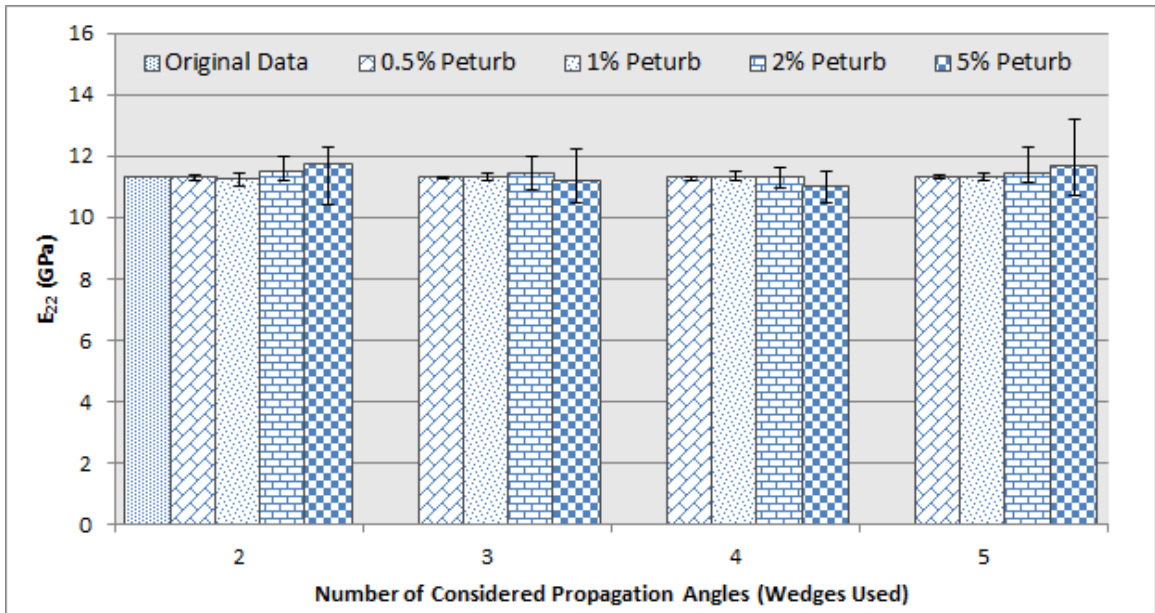


Figure D4: Convergence of elastic stiffness (E_{22}) after implementing improved algorithm

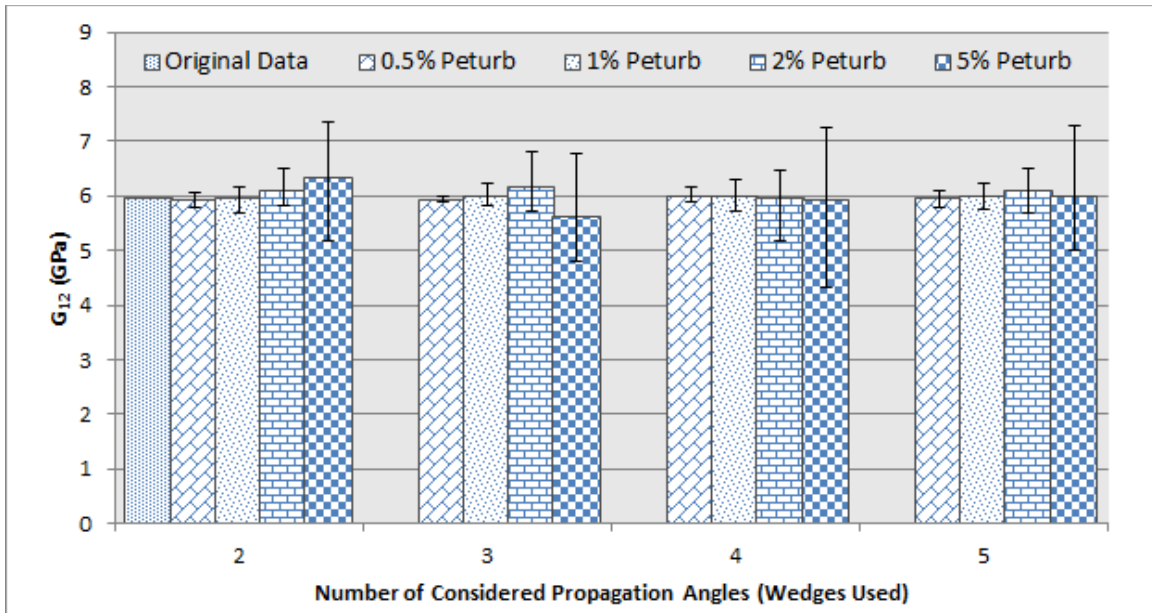


Figure D5: Initial convergence of shear stiffness (G_{12})

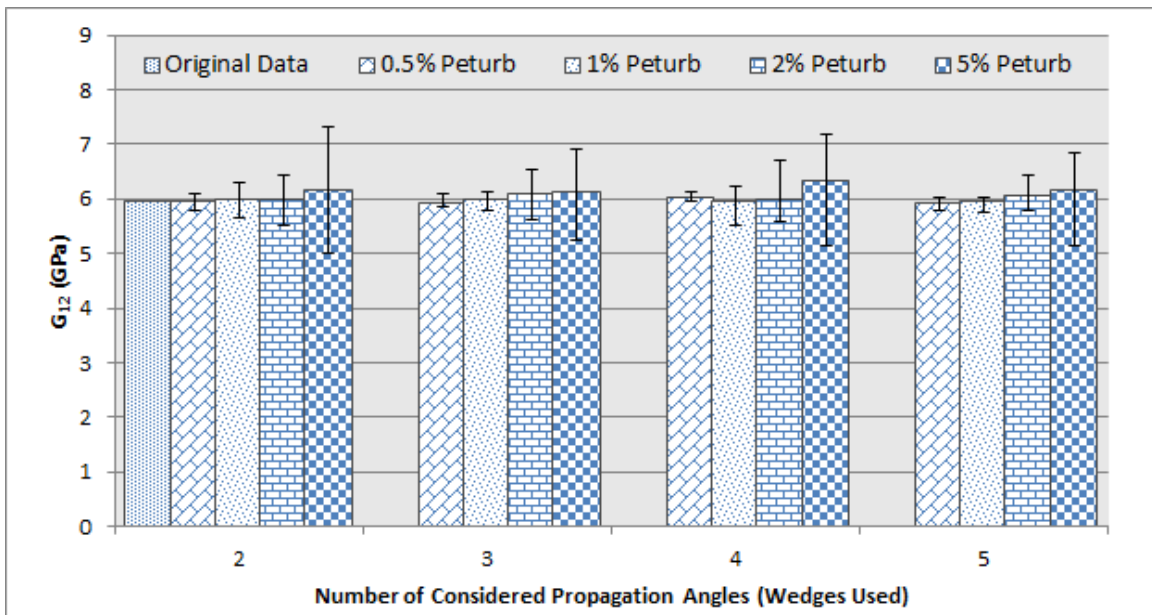


Figure D6: Convergence of shear stiffness (G_{12}) after implementing improved algorithm

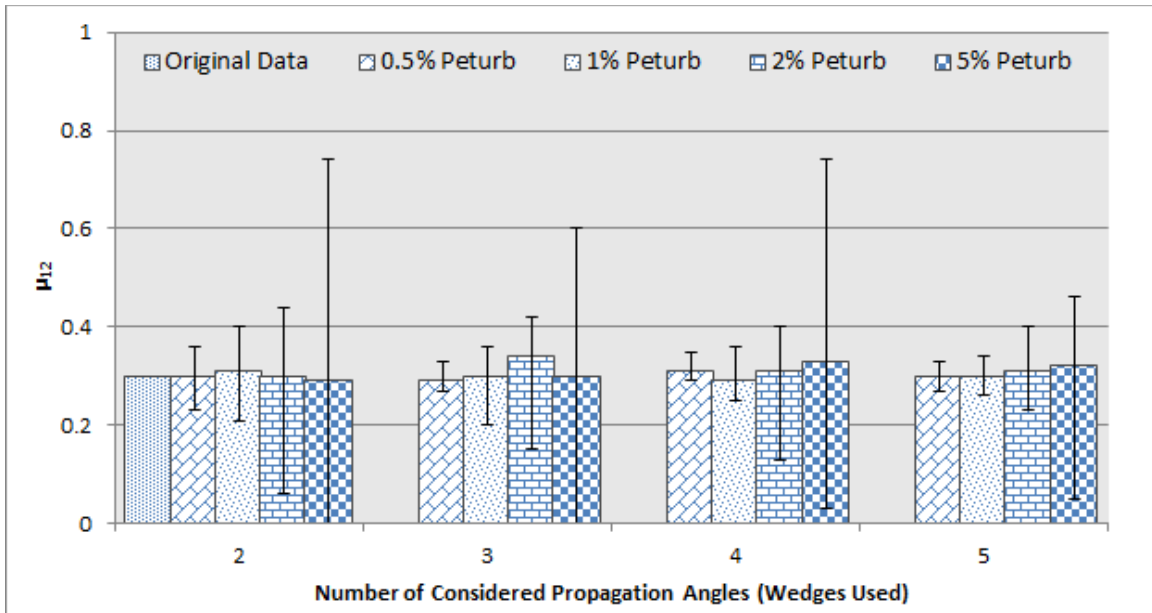


Figure D7: Initial convergence of Poisson's ratio (μ_{12})

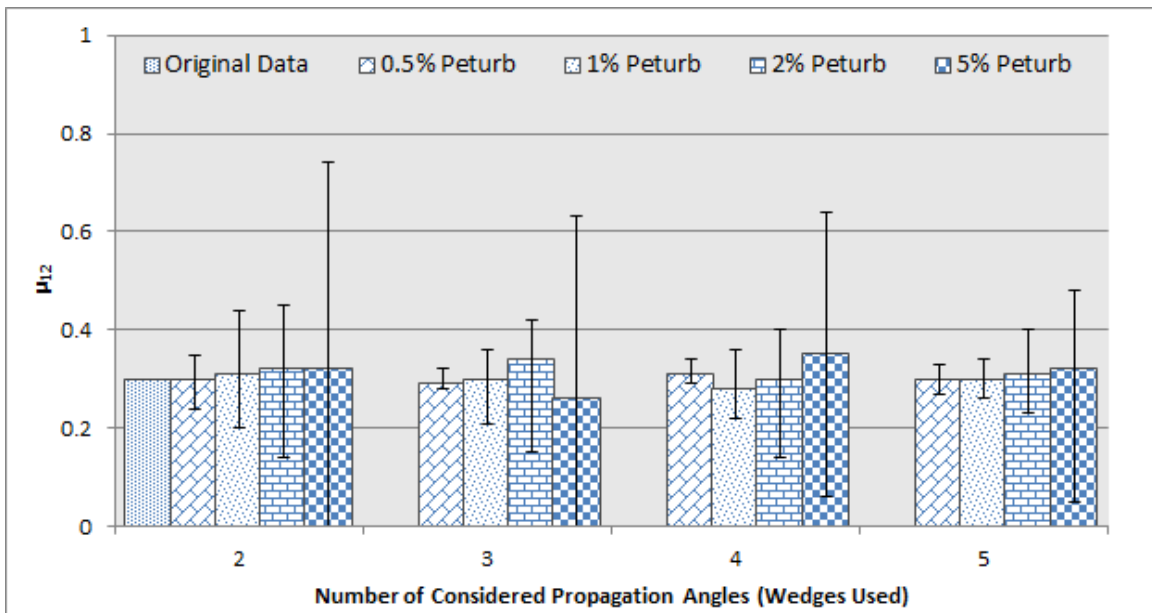


Figure D8: Convergence of Poisson's ratio (μ_{12}) after implementing improved algorithm

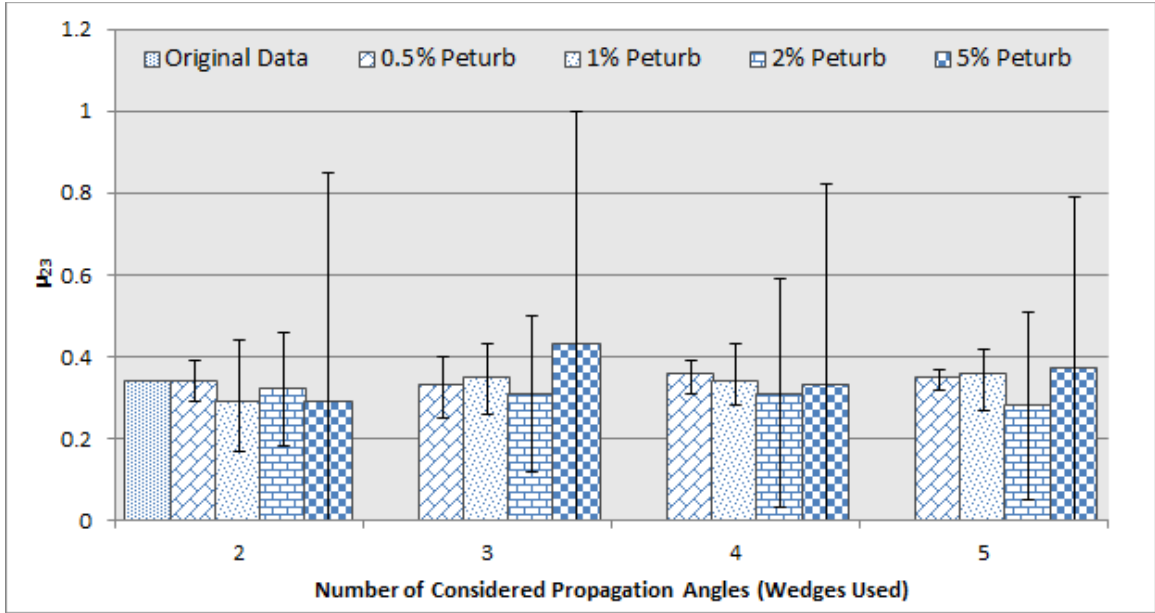


Figure D9: Initial convergence of Poisson's ratio (μ_{23})

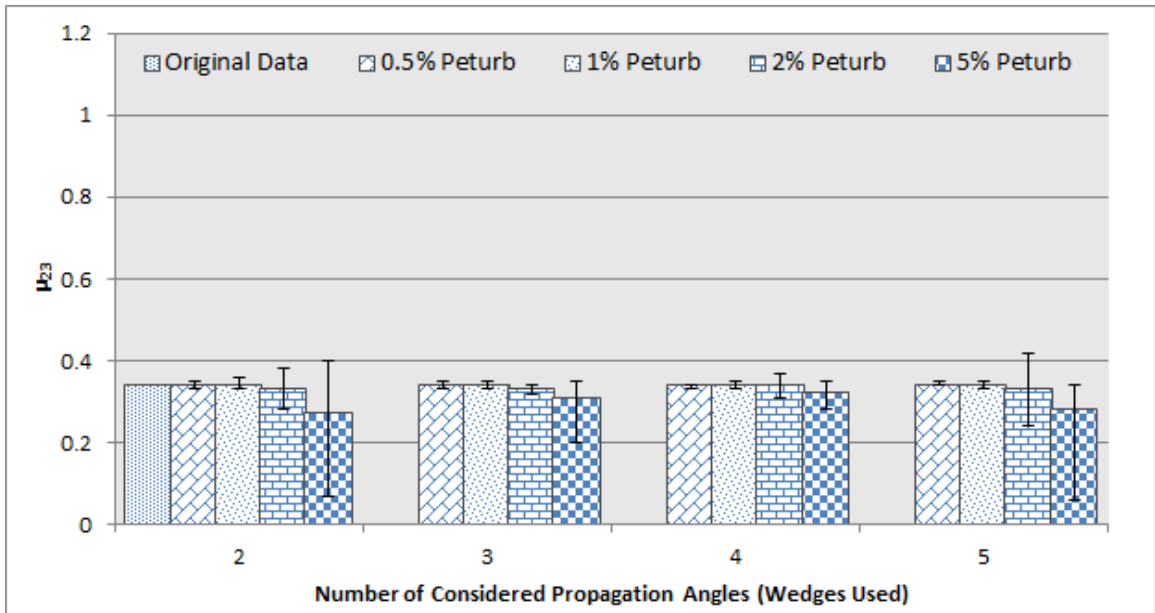


Figure D10: Convergence of Poisson's ratio (μ_{23}) after implementing improved algorithm